Computational Chemistry of Supramolecular Systems

-

Ab Initio and DFT Studies

Von der Fakultät für Mathematik, Informatik und Naturwissenschaften der RWTH Aachen University zur Erlangung des akademischen Grades einer Doktorin der Naturwissenschaften genehmigte Dissertation

vorgelegt von

Diplom-Chemikerin
Verena Moha, geb. Gossen

aus Stolberg (Rhld.)

Berichter: Univ.-Professor Dr. rer. nat. M. Albrecht
apl. Professor Dr. rer. nat. G. Raabe

Tag der mündlichen Prüfung: 03.08.2012

Diese Dissertation ist auf den Internetseiten der Hochschulbibliothek online verfügbar.

To my parents

It doesn't matter how beautiful your theory is,
it doesn't matter how smart you are.
If it doesn't agree with experiment, it's wrong.

Richard Feynman

The computational studies of this thesis have been performed from september 2009 until January 2012 at the Institute of Organic Chemistry at the RWTH Aachen university under the supervision of Prof. Dr. Markus Albrecht and Prof. Dr. Gerhard Raabe.

Parts of the described results have already been published:

1. "Anion-π Interactions in Salts with Polyhalide Anions: Trapping of I_4^{2-}" - M. Müller, M. Albrecht, V. Gossen, T. Peters, A. Hoffmann, G. Raabe, A. Valkonen, K. Rissanen, *Chem. Eur. J.* **2010**, *16*, 12446.

2. "Induced Fit in Chiral Recognition: Epimerization upon Dimerization in the Hierarchical Self-Assembly of Helicate-type Titanium(IV) Complexes"- M. Albrecht, E. Isaak, M. Baumert, V. Gossen, G. Raabe, R. Fröhlich, *Angew. Chem. Int. Ed.* **2011**, *50*, 2850.

3. "Cooperativity of H-bonding and anion- interaction in the binding of anions with neutral -acceptors" - M. Giese, M. Albrecht, T. Krappitz, M. Peters, V. Gossen, G. Raabe, A. Valkonen, K. Rissanen: *Chem. Comm.*, DOI: 10.1039/C2CC34748B.

Parts of the described results were part of bachelor thesis:

1. S. Mommer, Bachelor thesis **2010**, RWTH Aachen (chapter 5.1)

2. R.Kozik, Bachelor thesis **2010**, RWTH Aachen (chapter 5.1)

My greatful thanks go to Prof. Dr. Markus Albrecht for the interesting topic, his continuous interest in the process of this work, and for the left liberties.

My grateful thanks go to Prof. Dr. Gerhard Raabe for his continous interest in the process of this work, his support with questions regarding the field of theoretical chemistry, and for being my co-advisor.

Contents

1 Introduction **1**
1.1 Supramolecular Chemistry 1
1.2 Project Aim 8
1.3 Computational Details 11
1.4 CD Measurements 14

2 Anion - π Interactions **16**
2.1 Studies of Interactions with Anions 16
2.2 Studies of Interactions with Dianions 20

3 Mononuclear Complexes **26**
3.1 Mononuclear Complexes with Pincer Ligands 26
3.2 Mononuclear Complexes with Triscatecholate-Based Ligands 45
3.3 Dimerization of Triscatecholate-Based Complexes 51
3.4 TD-DFT studies of Triscatecholate-Based Complexes 56

4 Binuclear Complexes **129**
4.1 Homodinuclear Complexes with Alkyl-Bridged Dicatecholate-Ligands . 129
4.2 Homodinuclear Complexes with Imino-Bridged Ligands 139
4.3 Heterodinuclear Complexes with Bishydroxychinoline-Based Ligands . . 145
4.4 Heterodinuclear Complexes with Dicatecholate-Based Ligands 153

5 Tetranuclear Complexes **164**
5.1 Tetranuclear Helicates 164
5.2 Molecular Tetrahedra 185

6 Summary **194**

A References **197**

Acronyms and Abbreviations

AO	atomic orbital
a.u.	atomic energy units (Hartrees)
B3LYP	Becke Three Parameter Hybrid
c	velocity of light
cam	coulomb-attenuating method
cat	catecholate
CD	circular dichroism
DF	density functional
DFT	density functional theory
DMSO	dimethyl sulfoxide
ECP	electron core potential
fac	facial
GGA	generalized gradient approximation
h	Planck's constant
HEG	homogeneous electron gas
HF	Hartree Fock
HOMO	highest occupied molecular orbital
KS	Kohn Sham
λ	wavelength
LDA	local density approximation
LP	lone pair
LUMO	lowest unoccupied molecular orbital
MDF	Dirac-Fock relativistic
MeOH	methanol

mer	meridional
MMFF	Merck Molecular force field
MO	molecular orbital
MP2	Møller-Plesset perturbation to the second order
MWB	molecular weight basis
N_A	Avogadro's number
NBO	natural bond orbital
occ	occupied
Ψ	spin orbital
R	rotational strength
RY	Rydberg
SDD	Stuttgart Dresden potential
TD	time dependent
THF	tetrahydrofuran
TZVP	triple-zeta valence polarization
virt	virtual

1 Introduction

1.1 Supramolecular Chemistry

The existence of intermolecular forces was postulated by Johannes Diderik van der Waals in 1873.[1] The basic concepts within supramolecular chemistry were established by Nobel laureate Hermann Emil Fischer, who suggested more detailed principles of the interactions between molecular units.[2]

Later, in 1987, Jean-Marie Lehn defined supramolecular chemistry as "chemistry beyond the molecules" in his nobel lecture. This chemistry focuses on the highly selective reversible non-covalent interactions [i] which lead to the spatial organization or association of two or more species. According to Jean-Marie Lehn, "its development requires the use of all resources of molecular chemistry combined with the designed manipulation of non-covalent interactions".[3] Examples for such interactions are hydrogen bonds (e.g. DNA and protein structure),[4] electrostatic interactions between ions or dipoles (e.g. crown ether),[5] van-der-Waals-interactions[6] (e.g. rotaxanes and catenanes),[7] hydrophobic and hydrophilic forces (e.g. cyclodextrins and calixarene),[8] π-stacking (e.g. consecutive base pairs in DNA),[9] or coordinative bonds (e.g. helicates).[10] Consequently, there is a fundamental contrast between classical chemistry, which deals with covalently bonded molecules, and supramolecular chemistry treating non-covalent intermolecular and intramolecular interactions.

Already in the 1960's, Pedersen observed the ring closure of an open chain to form the crown ether "18-crown-6". If cations are present as templates, (Figure 1) the ion is located in the center and interacts with the polar molecule. Not only the crown ethers are prominent examples of a supramolecule but also DNA, enzymes, cryptands, siderophores, helicates, rotaxanes, and many others.[11] All of them show unique properties which can only be observed via the interaction as a supramolecule.

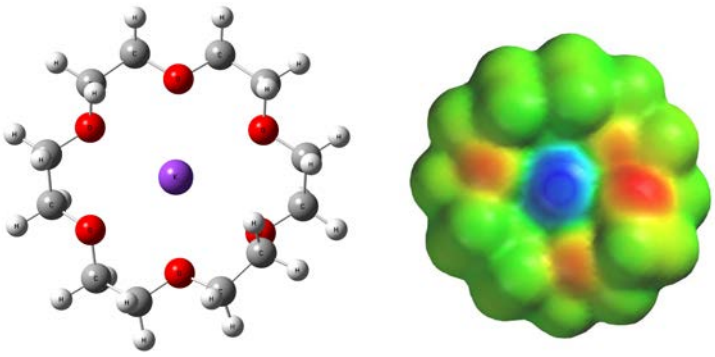

Fig. 1: *18-Crown-6 coordinating a potassium ion, right: electrostatic potential of the density.*

[i] Within supramolecular chemistry, the term "non-covalent bonds" is used for interactions, which do not follow the general concept of simple bonds between atoms ("each part contributes one electron to a two-electron bond"). Examples are hydrogen bonds and coordinative bonds of ligands to metal ions. A more exact description of the "non-covalent" interactions would be "weak" bonds or "weak" interactions, as these take the covalent part of the bond into account.

Two different principles are of great importance in the field of supramolecular chemistry. One phenomenon is the lock-and-key principle (E. Fischer 1894)[12] which is based on molecular recognition. The selective geometric and electronic complementarity between host and guest molecules is crucial for this event.

P. Ehrlich termed the interacting parts within this phenomenon "receptor" (host) and "substrate" (guest). This is of great importance as it often occurs in biological systems.[13] The principle is illustrated in Figure 2. In 1958, Daniel Koshland defined the more complex "induced fit" model describing the enzyme-substrate interaction.[14] This model assumes that an enzyme has a rather flexible structure which interacts with the substrate and reshapes until substrate and enzyme are finally bonded.

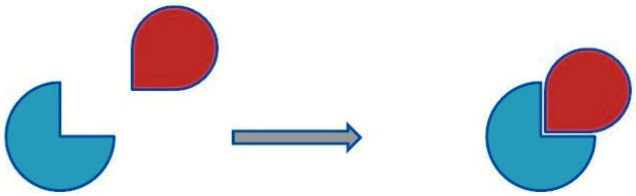

Fig. 2: *Lock-and-key principle.*

The other phenomenon is self-assembly. The single components adopt a defined arrangement resulting in an assembly, which is directed through non-covalent as well as electrostatic interactions (e.g. metal coordination, hydrogen bonds, and van-der-Waals or π-π interactions).[15] In 1987, J. M. Lehn (definition of supramolecular chemistry), C. J. Petersen (molecular recognition), and D. J. Cram (host-guest chemistry) received the Nobel price for their "development and use of molecules with structure-specific interactions of high selectivity, i.e. molecules that can "recognize" each other and choose with which other molecules they will form complexes".[16]

"*Pedersen, Lehn, and Cram laid the foundations of what is today one of the most active and expanding fields of chemical research, a field for which Cram has coined the term host-guest chemistry while Lehn calls it supramolecular chemistry.*"
The Royal Swedish Academy of Sciences.[17]

Since then, the interest in this field has widely spread, as important advances were made: supramolecular coordinations are one-pot syntheses with high yields. The resulting complexes show special properties because of their reversible non-covalent interactions, like the removal of false connections with the help of self-repairing mechanisms.[18]

The field of supramolecular chemistry is interdisciplinary, as the design of complex supramolecular structures requires cooperation between different parts of science. The synthesis of the receptors for example is a part of organic chemistry, while physical chemistry allows to study the interactions with the help of theoretical and experimental methods. Also biochemists are highly interested in this field since many biological processes start with the recognition and binding of substrates.[15]

1.1.1 Anion-π Interaction

In general, the attractive non-covalent π-π interactions between aromatic rings play a significant role in chemical and biological recognition.[19] An example is the π-stacking of aryl rings, which stabilizes the DNA double helix,[20] the packing of aromatic molecules in crystals, the conformational preferences of polyaromatic macrocycles and the tertiary structure of proteins.[21] While the π-π and the cation-π interaction are well known, the non-covalent anion-π interaction were much less investigated.[22]

The nucleophilic character of anions leads to the assumption of repulsive interactions with the aromatic π clouds. However, an attractive interaction exists and is determined by dispersion forces and ion-induced polarization.[23] The electrostatic term can be explained by the permanent quadrupole moment of the aromatic ring. By adding electron-withdrawing groups to the aromatic ring, the quadrupole moment increases leading to the attractive anion-π interaction.

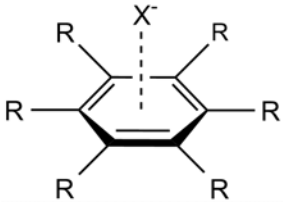

Fig. 3: *η^6-Anion-π complex, X^-: anion, R: electron-withdrawing group.*

Figure 3 shows a typical arrangement resulting from anion-π interaction. The anion may be a halogenid for example. One example for the electron withdrawing group (R) is fluorine (Figure 4).

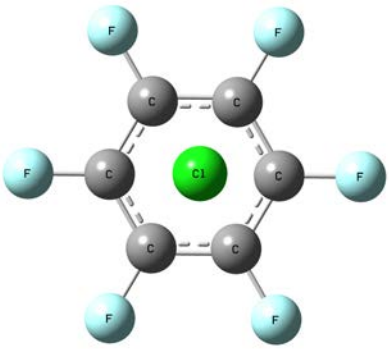

Fig. 4: *η^6-Anion-π complex, X^-: Cl^-, R: fluorine.*

The phenomenon of anion-π interaction was detected for the first time with π-electron-poor aromatic rings and anions. Afterwards, several calculations showed that interactions between systems such as fluorobenzene derivates and anions lead to attractive forces.[24]

1.1.2 Helicates



Fig. 5: *Helicity in nature, sea shell.*

Helices are fascinating and aesthetical attractive topological motives (Figure 5).[25] The term "helix" comes from the Greek word "$\varepsilon\lambda\iota\xi$" (twist, coil). Helices were discovered on a molecular level in several biological and chemical structures. Examples are α helices of peptides,[26] triple helices of collagen,[27] inorganic materials like zinc oxide, and the well-known example DNA. The structure of DNA was described by James D. Watson and Francis Crick in 1953 based on X-ray studies by Rosalind Franklin and Raymond Gosling.[28] Within the DNA, the π stacking of the basepairs stabilizes the structure. In artificial systems, non-covalent interactions are often used for the coordination at metal ions.[29]

A class of such compounds are the helicates, where the word "helicate" is derived from "helix". In such a complex, one or more ligands are wrapping around two or more metal centers leading to a chiral compound as the ligands can bind to the center in two different ways which results in structures that are image and mirror image.[30] Therefore, helicates are an example for intermolecular self-assembly.[ii]

Work on helicates had been done even before the term was coined, but a wide expansion in this field did not occur until the late 1980's followed by a rapid growth in the late 1990's.[31] Historically, helicates were observed in 1937, when Burstall and Morgan reported on a Ag(I) complex with unexpected stability against oxidation.[32] Later, this phenomenon could be explained by the helical structure of this complex as Edwin C. Constable and coworkers were able to obtain crystal structures.[33]

[ii] The term "self-assembly" describes the combination of species into an organized structure without external influence. Within the field of supramolecular chemistry, this concept is of great importance as one primary goal is the formation of defined structures within assemblies with the help of non-covalent interactions.

In 1958, Busch described the first triple-stranded metal complex,[34] in 1976 Stuckmeier reported about a bidentate helical zinc(II) complex,[35] and in 1985 Raymond published a bidentate triple-chained helical iron(III) complex.[36]

In general, metals with preferred tetrahedral or octahedral coordination geometry and two or three bidentate ligands can form mononuclear complexes with either Δ (right-handed propeller twist) or Λ (left-handed propeller twist) configuration (Figure 6).

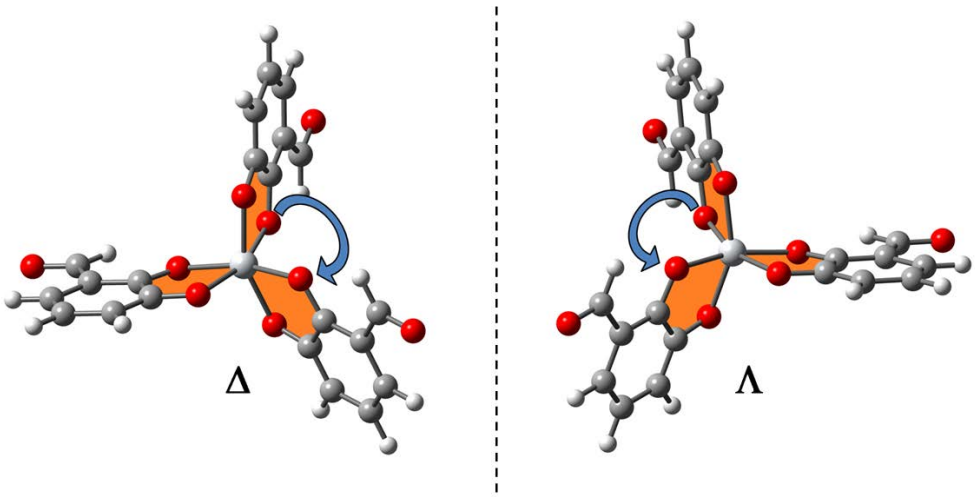

Fig. 6: Δ *(right-handed propeller twist) and* Λ *(left-handed propeller twist) form of a helicate with Ti(IV) and three bidentate ligands.*

One example for such a mononuclear coordination compound is the triscatecholate gallium(III) complex. In Figure 7 the complex formation between metal ion and ligand forming the monomeric triscatecholate complex is illustrated.

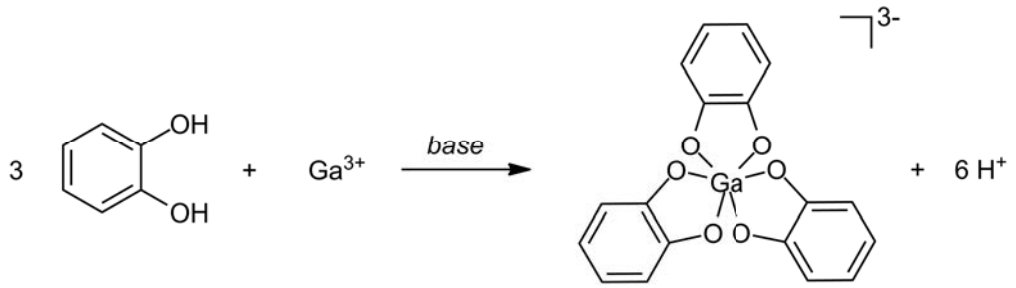

Fig. 7: *Formation of the triscatecholate gallium(III) complex.*

Larger structures like binuclear complexes can be obtained from *bis*-bidentate ligands and metal ions which favor six-fold-coordination and octahedral geometry. The metal centers are coordinated by the bidentate groups at the ends of the three ligands.[37] Binuclear complexes are able to form helicates having either a $\Delta\Delta$ or a $\Lambda\Lambda$ configuration. A $\Lambda\Delta$ or a $\Delta\Lambda$ configuration leads to a *meso*-helicate with an intermolecular plane of symmetry (Figure 8).

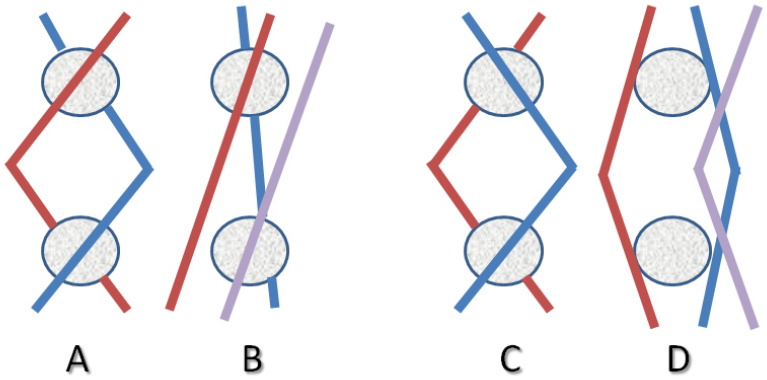

Fig. 8: *Form A (with two ligands): helicate, form B (with three ligands): helicate, form C (with two ligands): meso helicate, and form D (with three ligands): meso helicate.*

With spacers like methylene groups, an interesting class of helicates can be formed. These alkyl-bridged-triple-stranded helicates are of great importance as they provide an internal cavity. Therefore, guest species like alkali cations can be bonded.[38]

Additionally, the alkyl spacer can influence the relative configuration of the metal complex units. As such complexes prefer the zigzag conformation, a spacer with an odd number of methylene units forms a *meso*-helicate and one with an even number leads to a helicate (Figure 9).[39]

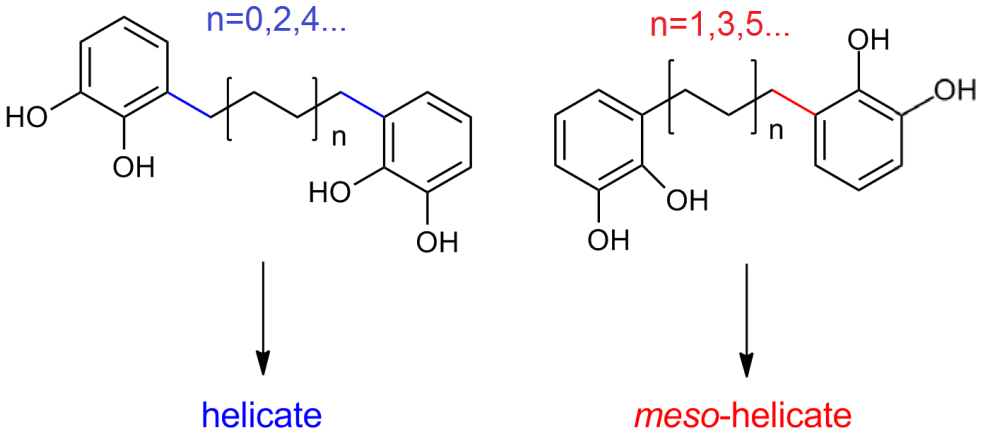

Fig. 9: *Influence of the chain length of the spacer to the stereo chemistry of self-assembly, blue: helicate form with an even number of methylene units, red: meso-helicate form with an odd number of methylene units.*

Furthermore, the control of stereochemistry is possible for larger complexes like helicates from imino-bridged ligands. Binuclear ligands with metal binding sites at a distance of about 20 Å lead to a *meso*-helicate if a central CH_2 unit is placed in a fixed spacer, while a $(CH_2)_2$ unit in the same position leads to a helicate (Figure 10).[40]

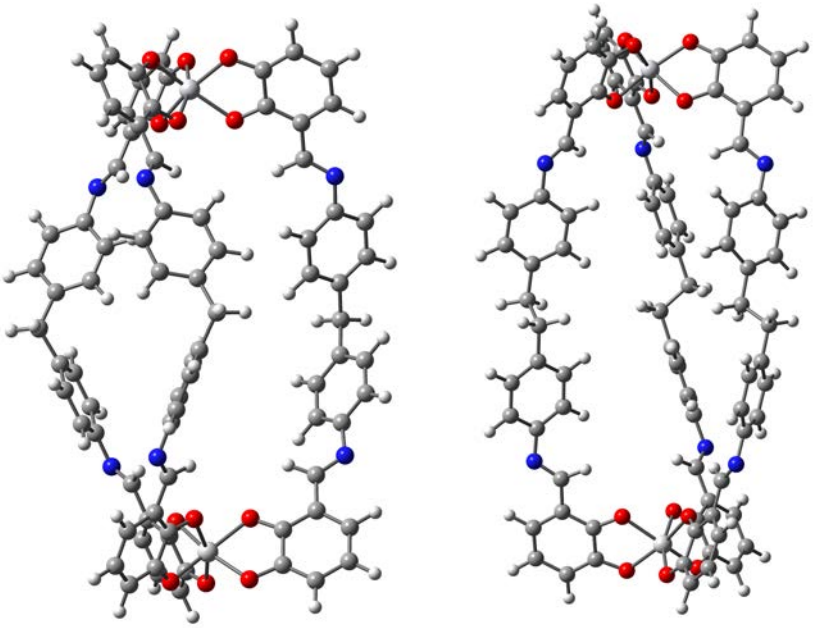

Fig. 10: *Meso-helicate (left) and helicate (right) from imino-bridged ligands.*

Bigger internal cavities than those found within the presented helicates can be obtained in larger systems like molecular tetrahedra.

1.1.3 Molecular Tetrahedra

Tetrahedra represent a simple geometrical body for a molecular container with a big internal cavity. Molecular M_4L_4 tetrahedra, which will be discussed within the framework of this thesis, are container molecules with a high symmetry. The molecular self-assembly of triangular ligands with chelating units and suitable metal ions leads to such molecular tetrahedra (Figure 11).[41]

One way to synthesize a molecular tetrahedron is to combine six linear ligands with two metal binding sites and four metal cations resulting in a M_4L_6 tetrahedron. A second way leads to M_4L_4 tetrahedra through the combination of four ligands with three metal binding sites, an idealized C3 axis, and four metal cations.[42] One example for a suited ligand is presented in Figure 12. This ligand has the required three binding sites as three catechol units are[43]

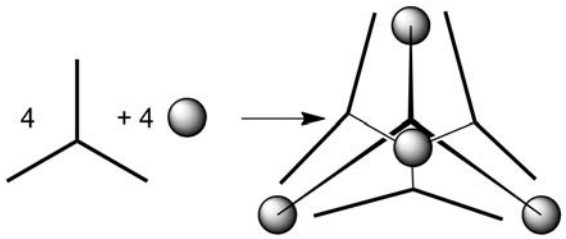

Fig. 11: *M_4L_4 tetrahedron, reaction path with four ligands and four metal centers.*

The obtained cavity of a molecular tetrahedron is able to bind guests,[44] to stabilize reactive intermediates[45] or to run chemical reactions inside the tetrahedron.[46]

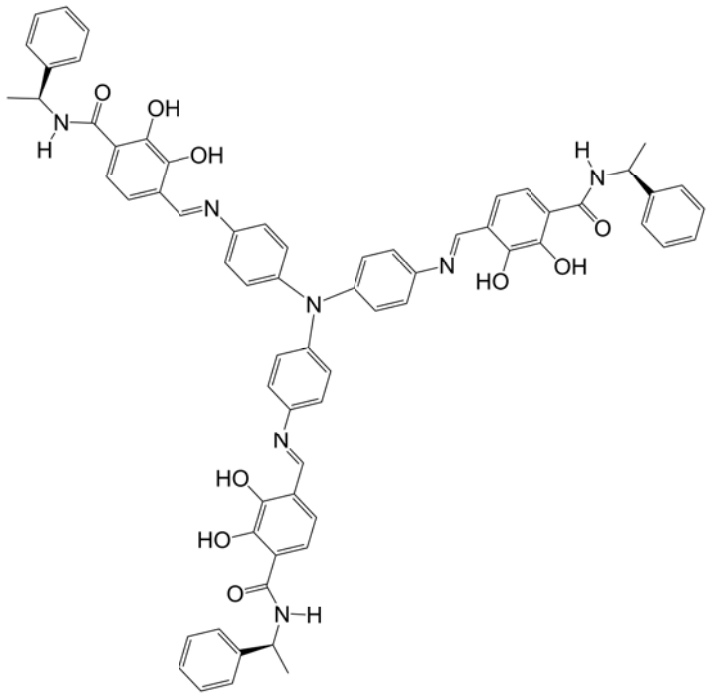

Fig. 12: *Ligand with three chelating units for the formation of a molecular tetrahedron with four metal centers.*[43]

1.2 Project Aim

The goal of this project is to use the methods of computational chemistry to describe supramolecular systems. In the beginning, the geometry of relatively small model systems will energetically be optimized and compared with expermintally obtained results. Due to the small size, methods like MP2 and basis sets of a high quality like 6-311++g** can be used at this level. Later on, bigger and more complex systems will be studied with the help of density functional (DF) methods. The combined results should then lead to a better understanding of already existing systems and should guide the design of new ones.

´ We start with the analysis of anion interactions with the π systems of aromatic rings. These molecules are relatively small but require high-level ab initio calculations. Within cavities formed by electron-deficient aromatic rings, anions which are not stable in the gas phase like the tetraiodide dianion can be stabilized. With the help of computational chemistry, the structure of the anion and its dominating intermolecular interaction will be investigated.

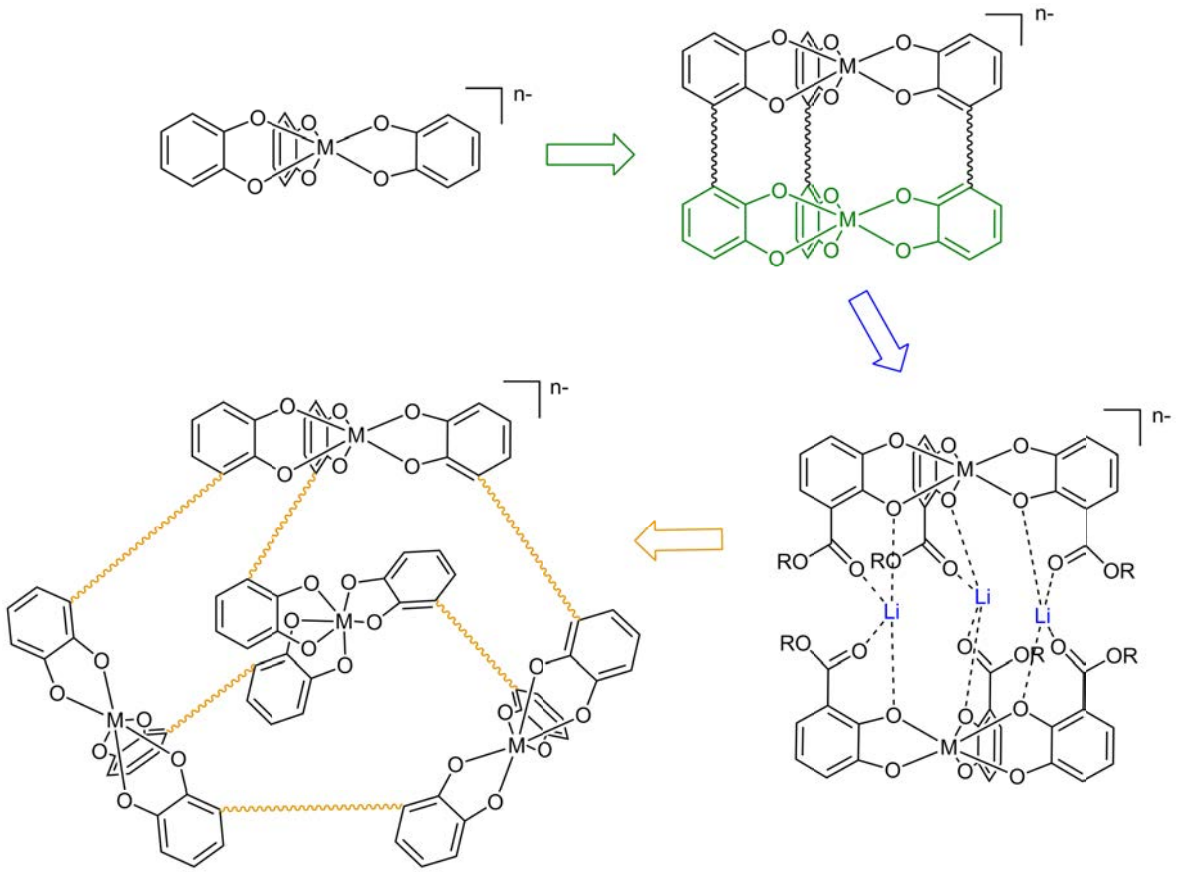

Fig. 13: *The four steps of increasing the complexity of the calculated systems.*

Following this, interactions between cations and larger systems like the ones presented in Figure 13 are studied. As those systems are bigger than the molecules studied in the "anion-π section" and therefore contain more interacting atoms, methods based on the density functional theory (DFT) are used.[47] The increase in complexity of the systems is shown in Figure 13. The first step is a triscatecholate complex with only one metal center, the second a binuclear complex with an alkylic spacer, the third a hierarchical formed lithium-bridged helicate, and the final step is a molecular tetrahedron.

In the second step, the different diastereomeres (helicate and *meso*-helicate) for tetra anionic titanium(IV) or hexa anionic gallium(III) complexes will be studied regarding the influence of the spacer (methylene versus ethylene versus propylene). The calculation of transition states for the non-dissociative conversion of the diastereomers will be compared to experimental results as earlier experiments led to the conclusion that the barriers of isomerization of complexes depend on the size of the different spacers.[48] The results of the calculations will provide an insight into the underlying mechanism. Insertion of different cations (templates) into the cavity of the binuclear complexes is also important as they also have an influence on the isomerization. The enlargement of the studied systems results in binuclear complexes with imino-bridged ligands (Figure 14).

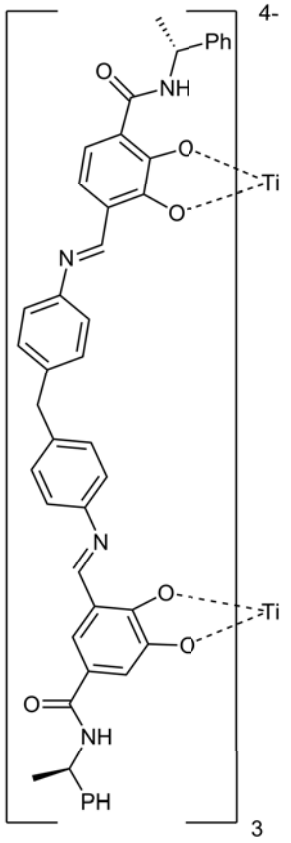

Fig. 14: *Binuclear complex with imino-bridged ligands.*

In the third step, the hierarchically formed lithium-bridged helicates will be energetically optimized and emphasis will be put on the stereochemical induction of the monomeric towards the dimeric complexes. Complexes with different stereogenic centers at the α-, β-, or γ-position will be examined. The studied complexes have aldehyde, ketone or ester functions in the 3-position. Previous studies showed that the cooperation of two monomers results in a dimer depending on the choice of solvent (methanol or DMSO) and different stereogenic centers (α, β or γ). This phenomenon will be examined closely with the help of time-independent as well as time-dependent DF-based methods. As new compounds, which have not been examined theoretically so far, gallium(III) complexes with different chiral substituents will be studied.

In the fourth and last step, bigger systems like the M_4L_4 tetrahedra are of interest. Especially the mechanical coupling between the metal complex units is important. Also the possible isomerization paths of the complexes ($\Lambda\Lambda\Lambda\Lambda \rightarrow \Lambda\Lambda\Lambda\Delta \rightarrow \Lambda\Lambda\Delta\Delta \rightarrow \Lambda\Delta\Delta\Delta \rightarrow \Delta\Delta\Delta\Delta$) will be examined theoretically.

1.3 Computational Details

For the theoretical studies on supramolecular systems, different quantum-chemical methods will be used: for example Hartree-Fock, MP2 (Møller-Plesset perturbation theory to the second order), or dispersion corrected DFT. To obtain reasonable starting geometries to be used in the minimization of the energy of the different complexes, their structures have to be optimized with the help of methods implemented in programs like Spartan'08[49] or Chemdraw3D.[50] Both programs provide methods which allow force field calculations to locate stationary points on the corresponding potential energy surfaces. Subsequently, the obtained starting geometries will be optimized with the help of the Gaussian09 suite of programs[51] or Turbomole[52] employing different functionals and basis sets, beginning with small sets of contracted gaussian functions like 6-31g and later on with 6-311g*, including polarization functions on heavy atoms, or even larger ones like 6-311++g**, depending on the computational requirements (time and storage) for the current complex and taking into account the polarity of the system.

Each structure is pre-optimized with the MMFF forcefield[53] employing the Monte Carlo algorithm as implemented in the Spartan'08 set of routines. The resulting structures are then used as starting points for all other calculations.

The first systems which will be analyzed involve anion-π interactions. To obtain accurate results, theoretical treatment of such systems requires high-level ab initio calculation. It is essential that electron correlation is taken into account, for example with the Møller-Plesset perturbation theory.[54] Thus, the MP2 method will be used to study these systems.

For the theoretical investigation of the interaction between metal center and ligands, the DF-based methods will be used. Possible functionals are B3LYP (Becke Three Parameter Hybrid)[55] and PBE1PBE (the 1996 pure functional of Perdew, Burke and Ernzerhof, as made into a hybrid by Adamo).[56] In the case of systems with large intramolecular distances, other DFT methods have to be used which properly handle the long-range correlation energy. Some of the new methods that take the dispersion energy into account employ long-range-corrected functionals like e.g. LC-wPBE.[57] cam-B3LYP is the long-range-corrected version of B3LYP using the Coulomb-attenuating method[58] to include long range exchange, and WB97XD is a method developed by Head-Gordon and coworkers including empirical dispersion.[59]

To compare the theoretically obtained structures with the complexes experimentally studied in solution, CD-spectra will be measured. With the results of time-dependent (TD)-DFT calculations, such spectra can be obtained theoretically and analyzed.

1.3.1 Ab Initio Methods

The most important post-HF *ab initio* method which was used within this thesis, is the Møller-Plesset perturbation theory.[60] The ground state energy is expanded in a Taylor series:[61]

$$E_0 = E^{(0)} + \lambda E^{(1)} + \lambda^2 E^{(2)} + \lambda^3 E^{(3)} + ... \tag{1}$$

In this equation, $E^{(0)} + E^{(1)}$ is the energy obtained at the self-consistent field (SCF) level of the Hartree-Fock formalism. The terms $\lambda^x E^{(x)}$ with x≥2 describe the correlation energy. For the Møller-Plesset perturbation energy to the second order (MP2),[60] the expansion is terminated after $E^{(2)}$. The result is:

$$E^{(2)} = -\underbrace{\sum_{a}^{occ}\sum_{b}^{occ}}_{b>a}\underbrace{\sum_{r}^{virt}\sum_{s}^{virt}}_{s>r} \frac{|\left\langle \psi_a(i)\psi_b(j), \frac{e^2}{r_{ij}}[\psi_r(i)\psi_s(j) - \psi_s(i)\psi_r(j)]\right\rangle|^2}{\epsilon_r + \epsilon_s - \epsilon_a - \epsilon_b} \tag{2}$$

ψ are the spin orbitals, e the elementary charge (the charge of the electron is -e), r_{ij} the distance between two electrons. a and b are indices for the occupied spin orbitals, and r and s stand for the virtual spin orbitals. ϵ is the energy of the corresponding spin orbitals. The summation runs over the occupied and virtual spin orbitals, respectively.[62]

1.3.2 Density Functional Theory

The basis of the density functional theory (DFT) is the concept postulated by Hohenberg and Kohn[63] that the electronic energy of the ground state can be described by its electron density. The advantage of this method in contrast to those which employ the wave function like the Hartree-Fock theory in which the complexity increases exponentially (N^4) with the number of electrons is that instead of 3N+N coordinates (3N spatial and N spin coordinates), only three coordinates have to be taken into account since the electron density only depends on the three spatial coordinates x, y, and z. It could be proved that a varied density leads to another ground state. But the exact functional, combining the energy of the ground state and the density, could not be found so far. Thus, one aim of the research in the field of DFT-based methods is to find approximate functionals which give the energy of the electron density as accurately as possible.[64]

Different from the density functional theory in its original orbital-free formulation, the Kohn-Sham (KS) version of DFT falls back on an orbital representation which strongly reminds of the one within the Hartree-Fock theory. Similar to that approach the KS scheme results in a set of one electron equations which, similar to the HF equations, have to be solved iteratively, resulting in the so-called Kohn-Sham orbitals and

the corresponding eigenvalues.[61] The fundamental difference between the HF and the KS method is that the latter method includes a certain amount of correlation in that the system is brought to self consisting in presence of a functional that describes correlation as well as exchange and is, therefore, called "correlation-exchange" functional. Thus the KS eigenfunctions (KS orbitals) and eigenvalues are not directly comparable to those obtained from strict application of HF theory but rather to those obtained by semiempirical HF-like SCF methods.

The theory of Kohn and Sham (KS)[65] includes a term for the kinetic energy, as well as the electron-nuclei and the electron-electron repulsion. Therefore, the Hamilton operator can be described as follows:

$$H_\lambda = T + V_{ext}(\lambda) + \lambda V_{ee} \quad with \quad 0 \leq \lambda \leq 1 \tag{3}$$

V_{ext} in equation (**3**) is the operator of the potential energy excluding the electron electron repulsion which is included in the term V_{ee}. T is the kinetic energy. The energy is calculated iteratively employing a Slater determinant[66] consisting of the Kohn-Sham ϕ_i. The approximated density ρ_{approx} can be specified like this:

$$\rho_{approx} = \sum_{i=1}^{N} |\phi_i|^2 \tag{4}$$

N is in equation (**4**) the number of electrons which is equal to the number of one-electron orbitals.

$$E_{DFT}[\rho] = T_S[\rho] + E_{ne}[\rho] + J[\rho] + E_{xc}[\rho] \tag{5}$$

E_{ne} in equation (**5**) is the electron-core attraction, and $J[\rho]$ is the Coulomb energy. The subscript S in the kinetic energy T_S indicates that this part of the kinetic energy was calculated from a Slater determinant. The remaining kinetic energy is included into the exchange-correlation-term $E_{xc}[\rho]$. Equation (**6**) for the exchange-correlation energy, $E_{xc}[\rho]$, includes the difference between the total kinetic energy $T[\rho]$ and the kinetic energy derived by the Slater determinant. In addition, it gives the difference between the electron-electron correlation energy $E_{ee}[\rho]$ and the Coulomb interaction $J[\rho]$.

$$E_{xc}[\rho] = \underbrace{(T[\rho] - T_S[\rho])}_{kinetic\ correlation\ energy} + \underbrace{(E_{ee}[\rho] - J[\rho])}_{correlation\ and\ exchange\ energy} \tag{6}$$

The task obtaining orbital-free models, is to find functionals for the approximation of the kinetic, exchange and correlation energy. In contrast to this, within the KS theory only approximations for the exchange-correlation energy have to be found.[56]

In the early 1920's, Thomas and Fermi studied the homogeneous electron gas (HEG).[67] Derived from this, a class of local density approximations (LDA) to the exchange-correlation energy functional was found. These functionals only depend upon the value

of the electronic density at the coordinate where the functional is evaluated and the wave function is expressible in terms of plane waves. This leads to an exchange energy density which is proportional to $\rho^{1/3}$ if the density is constant. Therefore, the kinetic and exchange densities of the non-interacting HEG can be described in the following way:

$$T[\rho] = 2.87 \int [\rho]^{5/3}(r)dr \tag{7}$$

and

$$E_x[\rho] = -0.74 \int [\rho]^{4/3}(r)dr \tag{8}$$

The local exchange correlation energy per electron $E_{xc}[\rho]$ can be approximated as a function ϵ_{xc} of the local charge density $\rho(r)$ like this:

$$E_{xc}[\rho] \approx \int \rho(r)\epsilon_{xc}(\rho(r))dr \tag{9}$$

ϵ_{xc} in equation (**9**) can be interpreted as the exchange and correlation energy of the HEG of the density $\rho(r)$. This is the local density approximation LDA. It consists of exchange ($\epsilon_x(\rho)$) and correlation ($\epsilon_c(\rho)$) contributions:

$$\epsilon_{xc}(\rho) = \epsilon_x(\rho) + \epsilon_c(\rho) \tag{10}$$

Within the LDA, an approximation for the exchange hole is made which has a number of unphysical properties.[68] The resulting energy functional of the generalized gradient approximation (GGA) depends on the electron density and also on its gradient.[69] The GGA functional is shown in equation (**11**).

$$E_{xc}(\rho) \approx \int \rho(r)\epsilon_{xc}(\rho, \nabla\rho)dr \tag{11}$$

Application of the GGA gives better results for molecular geometries and ground state energies.

1.4 CD Measurements

Circular dichroism (CD) measurement is an important tool to investigate the spatial structure of a molecule. The following behaviour of the circularly polarized light is taken advantage of: if circularly polarized light passes through an optically active substance, the extinction coefficients of the left and right polarized waves are different resulting in different absorbances.[70]

$$\Delta A = A_L - A_R \tag{12}$$

A is the absorption of the light, L stands for left-polarized and R for right-polarized light. The difference between the absorptions can be obtained from experiment and results in the CD spectrum. With the help of Lambert-Beer's law the expression can be changed into:

$$\Delta A = (\epsilon_L - \epsilon_R)cl \tag{13}$$

ϵ_L and ϵ_R are the molar extinction coefficients for left- and right-circularly-polarized light. c is the molar concentration of the chiral molecule and l is the path length of the cuvette in cm. Thereby, the molar dichroism is given by:

$$\Delta\epsilon = \epsilon_L - \epsilon_R \tag{14}$$

The computational results obtained with the TD-DFT method give the excited states of a molecule and, thereby, the electric and magnetic transition moments, which can then be used to calculate the rotational strengths as the imaginary part of the scalar product of these moments. Thus, the rotational strength associated with a transition form the ground state Ψ_0 to the excited state Ψ_e is given by:

$$R_{0e} = Im(\langle \Psi_0 | \widehat{\mu} | \Psi_e \rangle \cdot \langle \Psi_e | \widehat{m} | \Psi_0 \rangle) \tag{15}$$

In equation (**26**), $\widehat{\mu}$ and $\widehat{m}$ are the electric and magnetic moment operator. The relation between the rotational strength and the measured $\Delta\epsilon$ is:[71]

$$R_{exp} = \frac{hc}{32\pi^3 N_A} \int \frac{\Delta\epsilon}{\lambda} d\lambda = 2.205 \cdot 10^{-39} \int \frac{\Delta\epsilon}{\lambda} d\lambda \tag{16}$$

In equation (**27**) λ is the wavelength, h is Planck's constant, c is the velocity of light in vacuo, and N_A is Avogadro's number.

The comparison of the results from the TD-DFT calculations and the measured spectra provides information about the geometric structure of the complex and sometimes also about the molecule's dynamics in the chosen solvents. Especially in supramolecular chemistry, this is an important aspect, as interactions with solvents play an important role. One example for this is the template chemistry.

The CD measurements presented in this thesis were performed at room temperature with an ANV 62DS CD spectrometer.

2 Anion - π Interactions

MP2-based quantum-chemical studies on the interactions between π-electron-poor aromatic rings and anions were performed within the work group of Prof. Lüchow before.[72] The chapter on the study of these interactions presented in this thesis is divided into two parts. In the first part the interactions of a π-system with an anion, which carries one negative charge are studied. The second part deals with the interaction with a dianion. As free dianions like I_4^{2-} are normally not stable, the stabilizing effect by π-systems is of great interest.

2.1 Studies of Interactions with Anions

As a starting point for the study of the interactions of aromatic systems with anions, the interactions of bromide, chloride, and iodide with hexafluorobenzene were investigated. The calculations were performed at the MP2 level of theory with the 6-311++g** contraction of gaussians as basis set. For calculations involving iodide, the ECP MWB46 was used. With this method, the influence of the size of spherical ions was studied. For the influence of the shape of the anion, BF_4^- and PF_6^- were chosen (Figure 16).[73]

In general, there are five major possible ways of a spherical anion to interact with an aromatic system:[72]

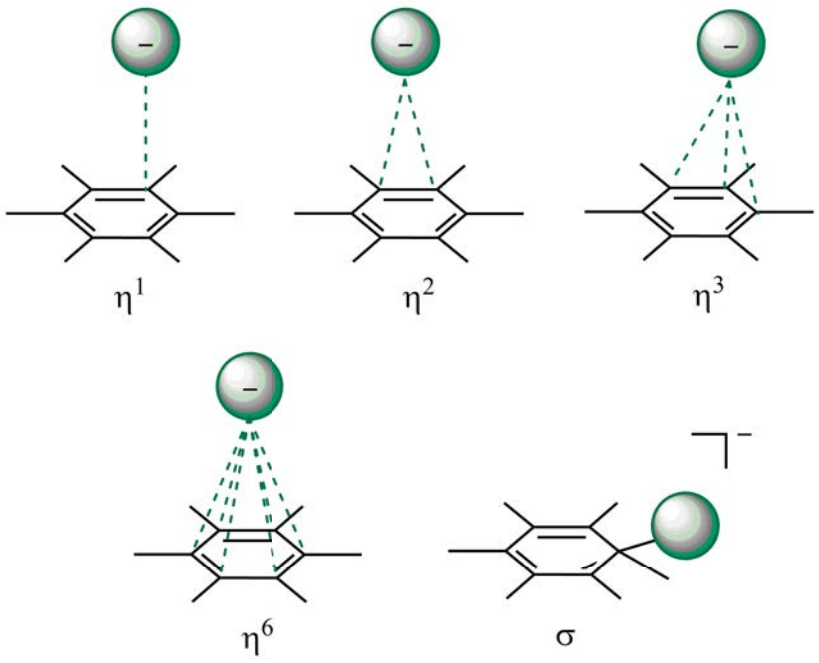

Fig. 15: *Different possibilities for the position of an anion interacting with an aromatic system.*

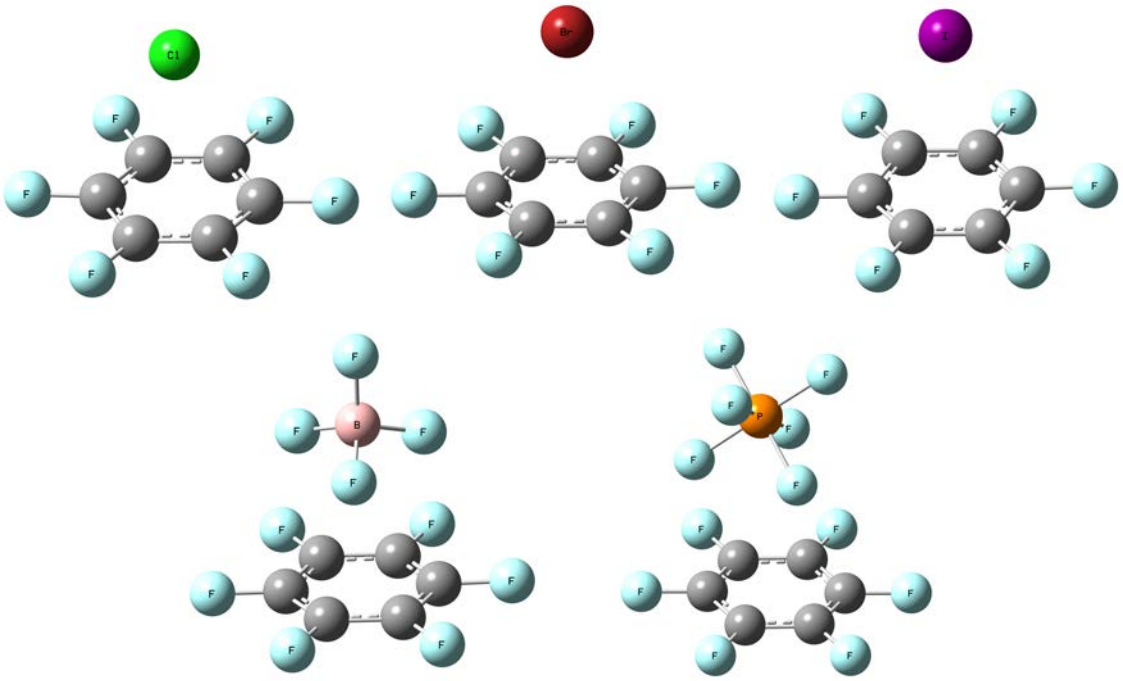

Fig. 16: *With MP2/6-311++g** optimized geometries of the complexes with Cl^-, Br^-, I^-, BF_4^-, and PF_6^-.*

anion	distance* in Å	coordination
Cl^-	3.40	η^6
Br^-	3.55	η^6
I^-	3.80	η^6
BF_4^-	3.63	η^6
PF_6^-	3.85	η^2

Table 1: *Average distances (C−anion) and coordination type for the optimized geometries with different anions, *the numbers are average distances between the center of the anion and the six C-atoms of the aromatic ring; method: MP2/6-311++g**.*

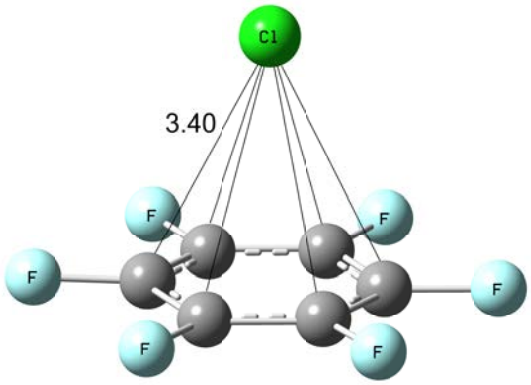

Fig. 17: *With MP2/6-311++g** optimized geometry of the complex with Cl^-, average C−Cl^- distance: 3.40 Å; grey: C, blue: F, green: Cl.*

With spherical ions like Cl^-, Br^- and I^-, the distance to the aromatic ring increases with the radius of the ion. Therefore, I^- has the largest distance to the center of the

aromatic ring (Table 1). With other ions like BF_4^- and PF_6^-, the coordination of the aromatic ring is not always symmetric like it is in the η^6 case. Due to its shape, PF_6^- for example is η^2 coordinated.

Similar calculations were performed previously[74] at the MP2/6-31++g** level of theory. The obtained equilibrium distance R_e of 3.155 Å for the interaction between C_6F_6 and Cl^- and 3.214 Å for the interaction between C_6F_6 and Br^- are very similar to the calculations presented in this thesis ($C_6F_6 \cdots Br^-$: 3.214 Å and $C_6F_6 \cdots Cl^-$: 3.098 Å). The differences are caused by the different computational methods.

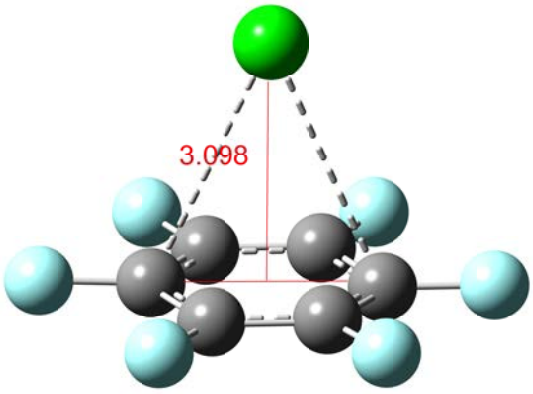

Fig. 18: *With MP2/6-311++g** optimized geometry of the complex of C_6F_6 with Cl^-, aromatic ring$-Cl^-$ distance: 2.098 Å.*

In the next step, the interaction of an anion with a more complex system with three aromatic rings (complex **1**) was analyzed. The structure of the chosen complexing molecule and the computationally obtained geometry are shown in Figure19.

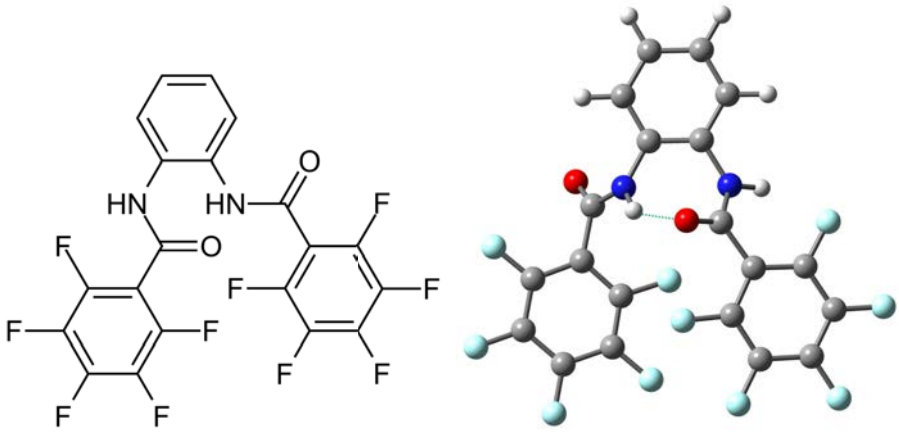

Fig. 19: *MP2/6-311++g**-optimized geometry of the acceptor part of complex **1**; grey: C, blue: F, dark blue: N, red: O, white: H, green dashed line: hydrogen bridge.*

The acceptor part of the complex can adopt two different conformations. Both of them are considered within the calculation. The first conformer (Figure 20 left) has one C=O$\cdots$H$-$N hydrogen bridge and the anion is located above one of the electron-deficient aromatic rings (C_1). Within the second possibility (C_{2v}), the electron-deficient

rings are approximately parallel to each other. Therefore, the anion can interact with both of the rings (Figure 20 right). Within this conformation two interactions with hydrogens are possible.

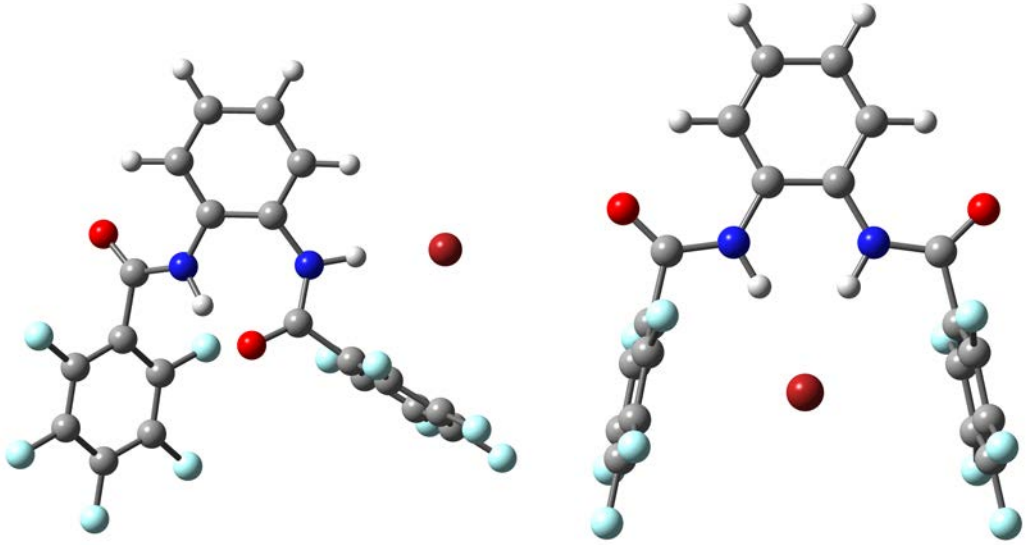

Fig. 20: *MP2/6-31g*-optimized geometry of the complex **1** with Br^- attached, two possible conformers; grey: C, blue: F, dark blue: N, red: O, white: H, dark red: Br.*

Calculations on the MP2/6-31g* level of theory with Br^- as anion show, that the structure adopting C_{2v} symmetry is energetically favored (Figure 20). The C_1 conformer results in a total energy of −4588.782676 a.u and the C_{2v} in a total energy of −4588.792078 a.u., which leads to a difference of 5.90 kcal/mol.

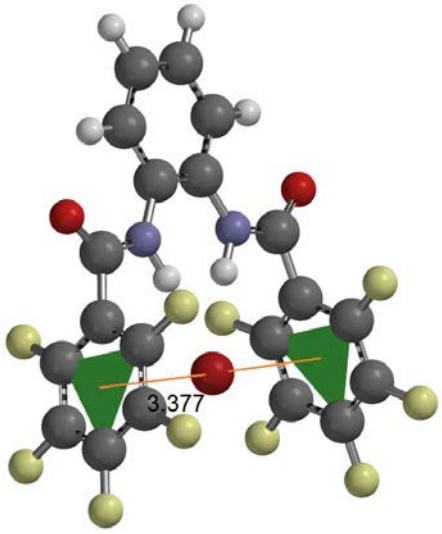

Fig. 21: *MP2/6-311++g**-optimized geometry of the complex **1**, distance between the center of the pentafluorophenyl unit (C_6F_5) and the anion (Br^-) in orange.*

On the MP2/6-311++g** level of theory, the C_6F_5−Br^- distance is 3.377 Å (Figure 21) and the C_6F_5−Cl^- distance is 3.224 Å. As in the first part of this study, these results show that a smaller anion leads to smaller distances (Table 2).

anion	distance to C_6F_5 in Å	distance to N−H in Å	energy in a.u.
Cl^-	3.224	2.065	−2479.563790
Br^-	3.377	2.321	−4592.368950

Table 2: *Comparison of the two conformers of complex **1** with different anions attached, level of theory: MP2/6-311++g**.*

The performed calculation on anion-π interactions answer the question, which conformer of complex **1** is energetically favored, if an anion is present. This result helps to understand in which way anions can be stabilized within a cavity. To study this further, calculations on interactions with dianions were carried out.

2.2 Studies of Interactions with Dianions

Previously, Schneider, Frontera, Deyà, and others reported on interactions between electron-deficient aromatic rings and dianions like tetraiodide. With the help of theoretical and experimental methods, they could demonstrate the existence of π interactions with polyiodide anions. However, correlation energy was omitted in their calculations,[75] and although the electrostatic contribution to the energy of interaction will probably play the most important role, it is doubtful that correlation effects can be neglected. Thus, the starting point for the study of interactions with dianions were calculations on the MP2 level of theory.

For this study, the structure of the I_4^{2-}-anion from the crystal of bisphosphonium salts was chosen.[76] Within the solid state, the dianion undergoes an interaction with the π system and is stabilized in the cavity of electron-demanding pentafluorophenyl units. This rarely observed phenomenon was studied with the help of calculations at the MP2/LANL2DZ level to analyze the structure of the anion and its dominating intramolecular interactions.[77]

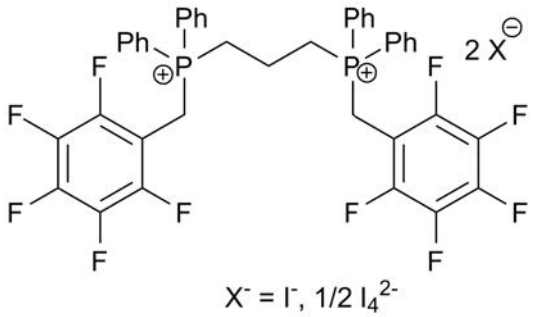

Fig. 22: *Structure of the synthesized tweezer-type diphosphonium salt with two electron demanding pentafluorophenyl units **1**.*

Figure 22 shows the structure of the diphosphonium salt with two pentafluorophenyl units, which crystallizes together with the iodide dianion located between the planes of the aromatic rings.

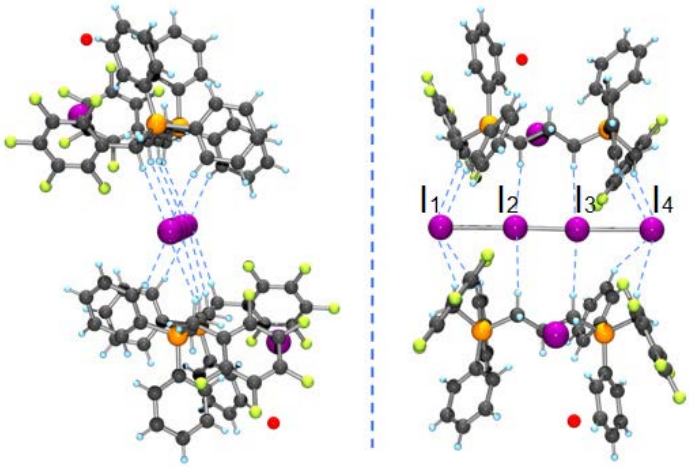

Fig. 23: *Different views of complex* ***1****, solid state structure*[76] *showing the linear tetraiodide anion stabilized by multiple CH-hydrogen bond interactions (black: C, blue: H, green: F, orange: P, magenta: I).*

As can be seen in Figure 23, the cavity stabilizes the anion by CH-hydrogen bonds from the benzylic and phenylic substituents to the terminal I-atoms and between the alkyl spacer and the central iodines. Additionally, the terminal iodine atoms are capped by C_6F_5 units of adjacent phosphonium cations.

- CH$-$I$_{terminal}$ = 2.943-3.308 Å
- CH$-$I$_{internal}$ = 3.251-3.271 Å

Within the I_4^{2-} dianion interatomic distances of 2.826 Å (central bond) and 3.403 Å (terminal bonds) are observed. The energy of this dianion was calculated at the MP2 level of theory. The result is -44.820147 a.u. In order to find the best combination of functional and basis set, further calculations at various levels of theory were carried out.

	basis set a		basis set b	
method or functional	I2$-$I3	I1$-$I2, I3$-$I4	I2$-$I3	I1$-$I2, I3$-$I4
full MP2	3.094	3.608	3.055	3.712
B3LYP	3.160	3.571	3.128	3.604
BP86	3.203	3.540	3.177	3.560
B3PW91	3.128	3.505	3.098	3.536
MPW1PW91	3.107	3.484	3.076	3.515
PBE1PBE	3.104	3.474	3.073	3.507

Table 3: *Optimized geometrical data of* I_4^{2-} *at various levels of theory, distances are given in Å, basis set a = LANL2DZ and b = SDD/MWB46.*

The use of different basis sets and functionals in the calculations (Table 3) show, that the functional PBE1PBE[78] with the LANL2DZ basis set gives the smallest difference of 0.342 Å (central bond) and 0.111 Å (terminal bonds) to the structure of the dianion

in the solid state. Despite this fact, the calculation with MP2 and the LANL2DZ basis set is supposed to be the most accurate one, as it includes the electron correlation by means of Rayleigh-Schrödinger perturbation theory probably more precisely.

The optimization with MP2 leads to a total energy of −44.831644 a.u., which is 7.21 kcal/mol lower than the energy of the tetraiodide anion obtained with the same method employing the experimental structure. The central bond is 0.268 Å and the terminal bonds are 0.205 Å shorter than the bonds of the solid state structure. This might be due to the fact that MP2 slightly overestimates long range correction. The optimized molecule is slightly bent (C_{2v}, I−I−I=179.2°). Another local minimum of $D_{\infty h}$ symmetry was located only 0.03 kcal/mol above the C_2 structure.

To investigate the nature of the bonds within the optimized structure of I_4^{2-}, a NBO (Natural Bond Orbital)-analysis[79] was carried out.

donor NBOs	occupation	acceptor NBOs	occupation	E^2
BD I2−I3	1.99809	RY* I1/I4	0.00112	0.89
LP I1/I4	1.75671	BD* I2-I3	0.48252	25.1
LP I1/I4	1.99987	BD* I2-I3	0.48252	0.86
LP I1/I4	1.85727	RY* I2/I3	0.00049	0.07
LP I1/I4	1.85727	RY* I2/I3	0.00012	0.20

Table 4: *Occupation of the Natural Bond Orbitals (E^2 in kcal mol^{-1}). Donor NBOs are π-type lone pairs of iodine, BD: bonding orbital, LP: lone pair, RY: Rydberg orbital, *anti-bonding, E^2: stabilization energy, associated with delocalization.*

The highest stabilization energy (E^2) of −25.1 kcal/mol (Table 4) results from interactions of the lone pairs at the terminal iodine atoms with the smallest occupation of 1.76 electrons, and the BD* orbital of the central I−I bond. Analysis of the NBO result shows that this stabilization results from an interaction of one lone pair per atom (degenerate HOMO 14 and 15) with the π* orbital (16) of the central I−I bond (LUMO) as shown in Figure 24. Consequently, the occupation numbers of these lone pairs are reduced and the acceptor NBOs carry up to 0.48 e.

Within the framework of the NBO method there is neither a π nor a σ bond between the terminal iodine atoms and the central I_2 unit. Respectively, each of the terminal iodine atoms carries four lone pairs and is negatively charged while the central I_2 unit is approximately neutral. This result matches Hassel's interpretation of the iodide dianion as a charge transfer complex of two donating iodide anions and an accepting iodine molecule.

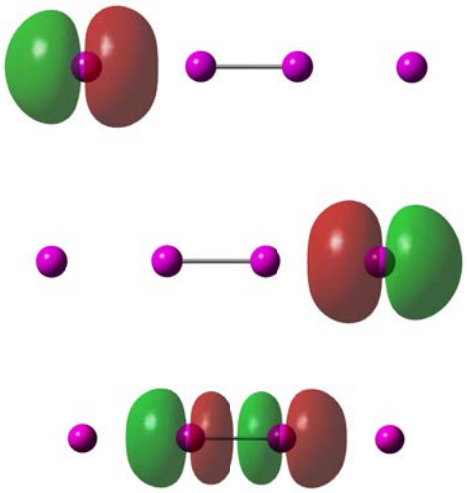

Fig. 24: *Molecular orbital (MO) 14, 15 (HOMO degenerate) and 16 (LUMO) of* I_4^{2-}.

Figure 24 shows the relevant molecular orbitals of the optimized structure. In order to study the strength of the terminal bonds, the energies of the possible reactions of I_2 with two I^- to I_4^{2-} were calculated (Figure 25).

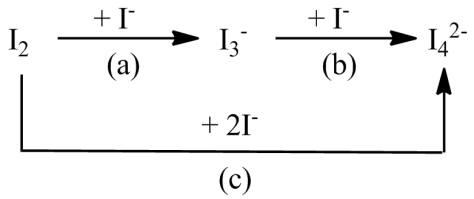

Fig. 25: *possible reactions to the product* I_4^{2-}.

	E_{tot}	ϵ_0	$E_{tot} + \epsilon_0$
I_4^{2-}	−44.831645	0.000727	−44.830918
	−44.831656	*0.000778*	*−44.830878*
I_3^-	−33.655768	0.000798	−33.654970
I_2	−22.354634	0.000407	−22.354227
$I_2^{-\cdot}$	−22.447444	0.000235	−22.447208
I^-	−11.247857		

Table 5: *Total energies at the MP2/LANL2DZ level. The numbers in italics are the energies of the less stable linear structure (Hartree,* ϵ_0 *is the zero point energy).*

The numbers in table 5 show that reaction (a) of I_2 with a single I^- to I_3^- is exoenergetic (−33.2 kcal/mol) and (b) of I_3^- with I^- to I_4^{2-} endoenergetic (+45.1 kcal/mol). This very high value of reaction (b) demonstrates the low barrier to fragmentation of the tetraiodide dianion. Moreover, further calculations show that I_4^{2-} is separated from its reactants by a barrier of only 0.013 kcal/mol, which provides an explanation for the instability of the free I_4^{2-} dianion.

Another way of the fragmentation of I_4^{2-} is the one into two radicals ($I_2^- \cdot$). Compared to the fragmentation of I_4^{2-} into I_3^- and one I^-, $I_2^- \cdot$ is a less stable product with a total energy of −44.894416 a.u. instead of −44.903625 a.u..

To obtain the potential curve in Figure 26, the distance between the terminal iodine atoms (I1−I2) was increased form 3.5 Å to 3.9 Å. The maximum energy corresponds to the transition state for the reaction (b).

The bond length at the transition state of dissociation of the bond between the terminal iodide atoms I1−I2 is 3.78 Å. At this distance I3−I4 and the central atoms I2−I3 are 3.50 Å and 3.09 Å. The optimized transition state is very slightly bent: I1−I2−I3 = 179.1° and I2−I3−I4 = 179.3°. This result is comparable to the slight bent within the optimized minimum structure.

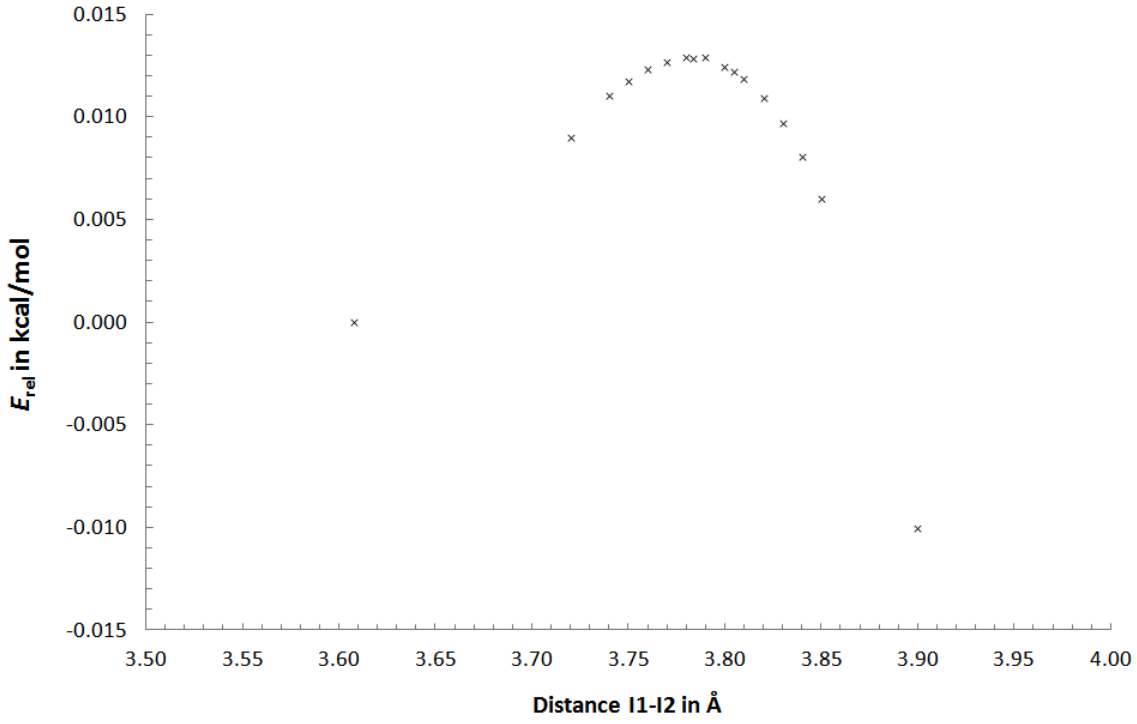

Fig. 26: *Variation of the distance I1−I2 from 3.5 Å to 3.9 Å and deviation of energy (E_{rel}) of the resulting structures to I_4^{2-} in kcal/mol, Maximum: with MP2 and LANL2DZ optimized transition state for the reaction of I_3^- with I^-.*

Figure 27 shows the potential curve of the endoenergetic reaction of I_3^- to I_2 and I^- with a reaction energy of +33.2 kcal/mol. The distance between I1−I2 was varied from 3.0 Å to 6.5 Å. It reveals the stable character of I_3^-. Therefore, the fragmentation of I_4^{2-} would be easy, and its product I_3^- is stable.

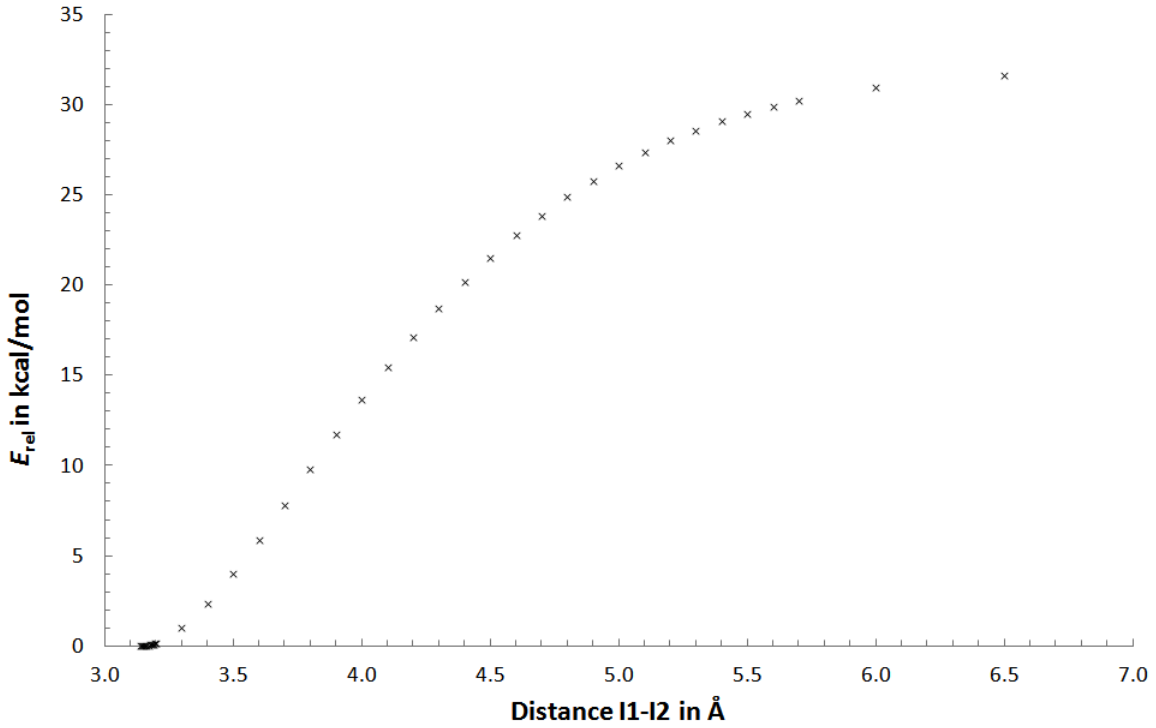

Fig. 27: *Dependence of the energy of I_3^- as a function of the distance I1−I2 between 3.0 Å and 6.5 Å, with MP2 and LANL2DZ optimized structures in each step as a model for the reaction of I_3^- to I_2 and I^-.*

The calculations reveal the weakly bonded character of I_4^{2-} with a very low barrier of fragmentation to I_3^- and I^- and long terminal I−I bonds of 3.608 Å. This result is underlined by a NBO analysis. Since the dianion could only be observed in the solid state it is evident that I_4^{2-} has to be stabilized in the interior of appropriate cavities. In the studied case, such a cavity is formed by a tweezer-type diphosphonium salt with two electron demanding pentafluorophenyl units. The anion-π interactions are supposed to stabilize I_4^{2-} in the solid state. They allow the isolation of the crystal containing the tetraiodide dianion. Therefore, this study shows that even unstable dianions like I_4^{2-} can exist, if a suitable cavity is present.

3 Mononuclear Complexes

3.1 Mononuclear Complexes with Pincer Ligands

Complexes with pincer ligands have the special ability to coordinate not only the metal ion but also several other counter ions, solvent molecules or bigger molecules. As the effective coordinating nature of rare earth metal ions was elucidated in earlier studies, metals like Y(III), La(III) or Eu(III) were chosen, and molecules containing phenanthroline as hexadentate ligands. The resulting structures of the complexes are presented in Figure 28.

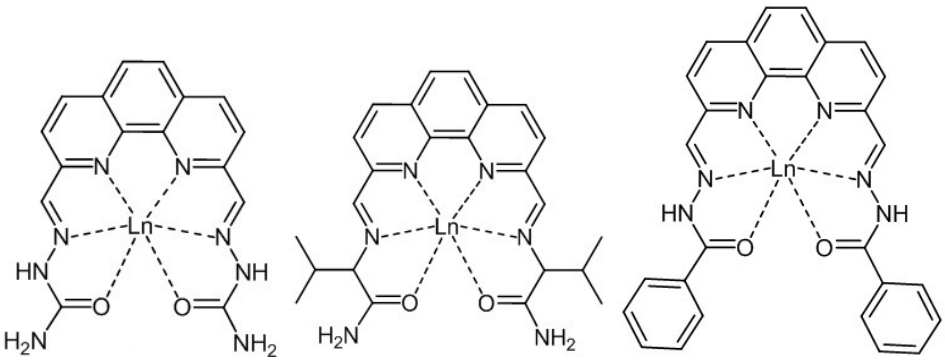

Fig. 28: *Synthesized Ln(III) complexes* **2**, **3** *and* **4** *with phenanthroline and different semicarbazones, Ln(III)=Y(III), La(III), Eu(III).*

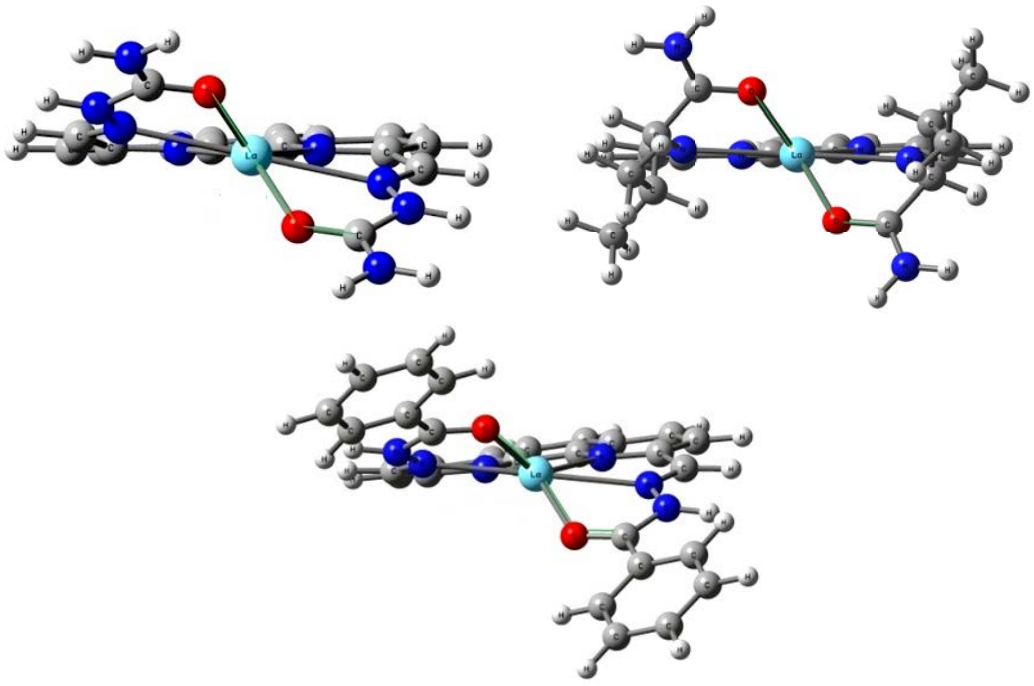

Fig. 29: *Dihedral angles of the structurally optimized complexes* **2**, **3** *and* **4**; *(O,La,O,C):* $\alpha(1) = -111.08°$, $\alpha(2) = -103.53°$, $\alpha(3) = -106.77°$; *method: PBE1PBE/TZVP.*

To analyze the structure and the capacity as a sensor for anions and cations of these complexes, a computational study was carried out. Spartan with the MMFF

force field was used for the initial conformational search. The obtained structures were then energetically optimized with Gaussian‘09 on the PBE1PBE/TZVP level of theory. For the lanthanide ions, the combination of the SDD basis set and effective core potential MWB28 was used. The computationally analyzed complexes in their optimized structures are shown in Figure 29.

Due to the different sterical demands of the substituents, the resulting dihedral angles α(O,La,O,C) vary from $-111.08°$ up to $-103.53°$. The different angles lead to varying environments of the metal ion in the three analyzed complexes. This might be an important aspect of the presented complexes regarding their behaviour in catalytic reactions. The energetically optimized structure of complex **1** with Y(III) instead of La(III) is presented in Figure 30. The structure has a dihedral angle α(O,Y,O,C) of -93.52°.

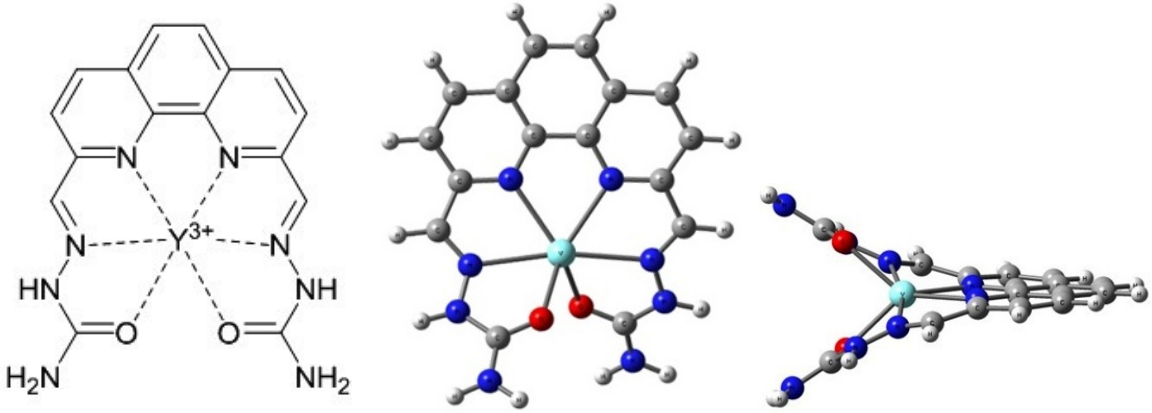

Fig. 30: *Geometry of complex 2 optimized with PBE1PBE/TZVP and SDD/MWB28 for Y(III).*

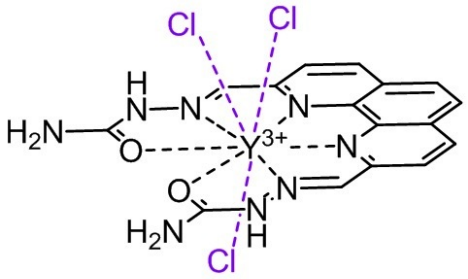

Fig. 31: *Complex 2 with Y(III) and three Cl^- atoms.*

The chosen complexes have different positions, where chloride ions or solvent molecules can be attached. Three of these possibilities were chosen for the calculations (Figure 31): two ions can be positioned on the top of the molecule and one below, which is due to the “bending” of the ligand. The crystal structure shows that two DMSO molecules and one Cl^- anion are directly attached (Figure 32). Two other Cl^- are in a higher coordination sphere and have a larger distance to the metal cation.

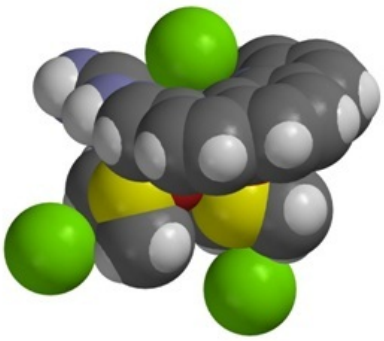

Fig. 32: *Solid state structure of the Y(III) complex with three solvent molecules (DMSO) and three Cl^- atoms (green).*

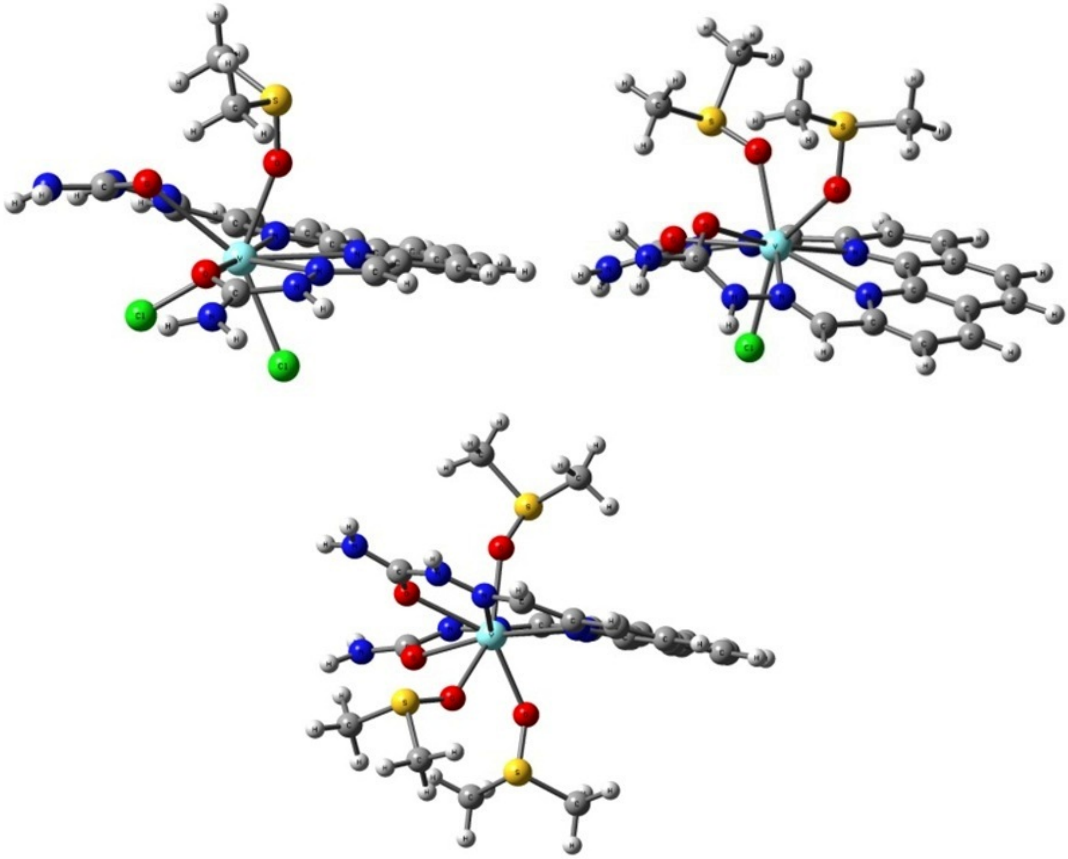

Fig. 33: *Optimized structure of complex **2** with one, two and three solvent molecules, method: PBE1PBE/TZVP and SDD/MWB28 for Y(III).*

The optimized structures in Figure 33 show the important influence of the attached molecules on the geometry of the central complex, especially on the "bending" of the ligands. Different O−O distances between the carbonyl groups of the ligands result depending on the number of solvent molecules. They differ between 2.66 Å (three Cl^-) and 2.82 Å (one DMSO and two Cl^-).

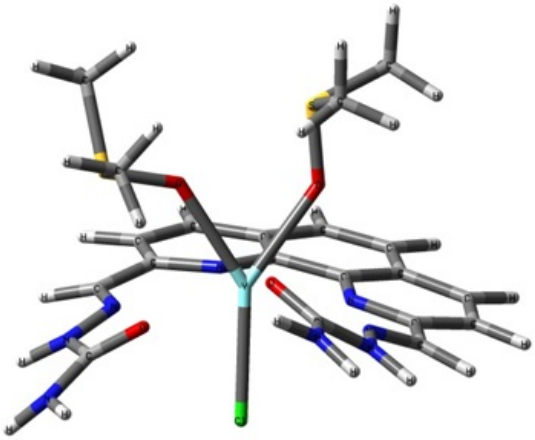

Fig. 34: *Complex 2 with two DMSO and one Cl^- (green), "out of plane bending" of the ligand.*

The optimized geometry of the complex with one Cl^- and two DMSO, which is close to the solid state structure, has an O−O distance between the two carbonyl groups of the complex of 2.70 Å (Figure 34).

- **Time Dependent Calculations**

All TD-DFT calculations were carried out at the B3LYP/TZVP and SDD/MWB (Ln(III)) level of theory. From the results of these calculations, CD spectra as well as UV/VIS spectra can be derived. Especially the CD spectra are of great interest for the complexes with chiral ligands. The metal center is coordinated either in the Λ or Δ form and the ligand has a (S) or (R) chiral rest. Comparison of the calculated and measured CD spectra will reveal structural information on the complexes.

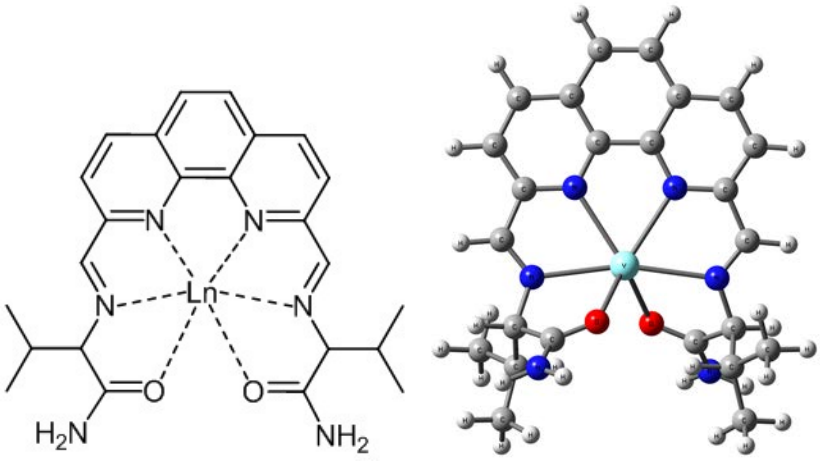

Fig. 35: *Optimized geometry of Y(III) complex 3, method: PBE1PBE/TZVP and SDD/MWB28 for Y(III).*

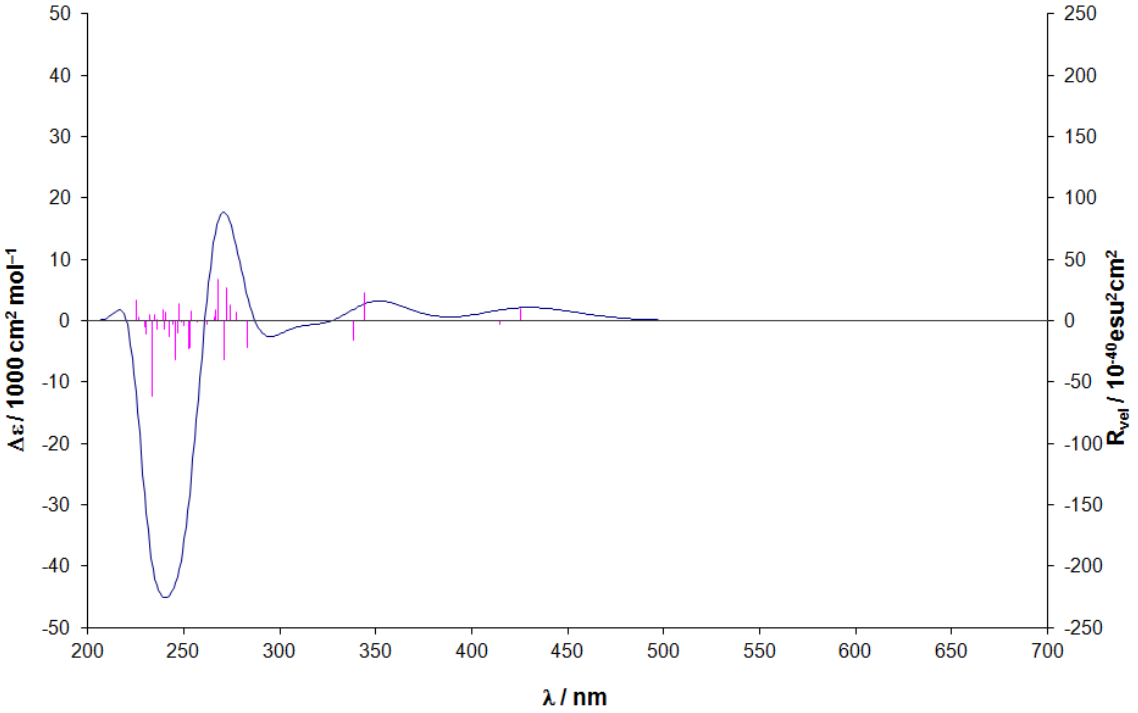

Fig. 36: *With B3LYP/TZVP calculated CD spectrum of Y(III) complex **3**, without Cl^- ions attached.*

The calculated CD spectrum of complex Y(III) **3** shows a negative Cotton effect at 240 nm and a positive Cotton effect at 260 nm. Some minor Cotton effects are found at higher wavelength (Figure 36). The list of the strongest rotational strengths presented in Table 6 reveals that some of the most intense transitions take place from the HOMO−3 and HOMO−2 to the LUMO or LUMO+1 from the ligand to the metal center. The transition between MO 106 and MO 121 has the strongest rotational strength. The coefficient for this transition is 0.35226 corresponding a contribution to the state of about 25%.

Rotational Strength/ 10^{-40}esu^{2}cm^2	Wavelength/ nm	transition
27.176	272.47	116 -> 120 n -> π^*,σ^*
−31.893	270.83	117 -> 121 n, π -> π^*,σ^*
33.495	267.68	116 -> 120 n -> π^*,σ^*
−31.618	245.88	113 -> 121 n, π -> π^*,σ^*
−61.862	233.25	106 -> 121 n, π -> π^*,σ^*

Table 6: *Rotational strength of the strongest transitions of the TD-DFT calculation of the Y(III) complex **3**.*

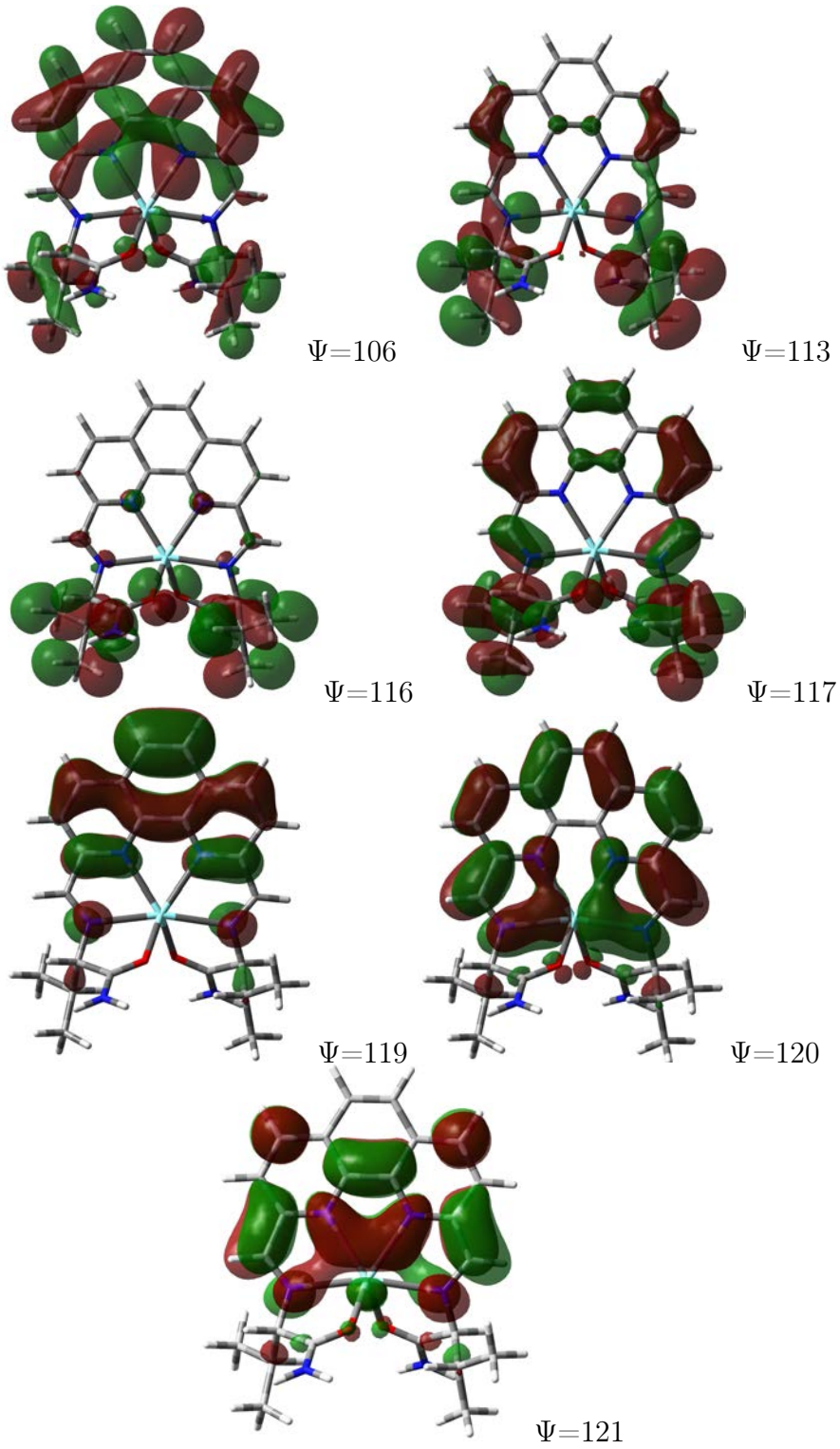

Fig. 37: *Kohn-Sham molecular orbitals* Ψ *of the Y(III) complex* ***3****, HOMO:* Ψ *=119, LUMO:* Ψ *=120.*

Figure 37 shows that orbitals at the O atoms of the ligand participate strongly in the transitions. They have large coefficients at MO 106, 116 and 117, which are the source orbitals for many transitions with strong rotational strengths between 230 and 275 nm. The corresponding coefficients for these strong transitions are 0.49057 (116 -> 120), 0.54555 (117 -> 121), 0.40613 (116 -> 120), and 0.35226 (106 -> 121).

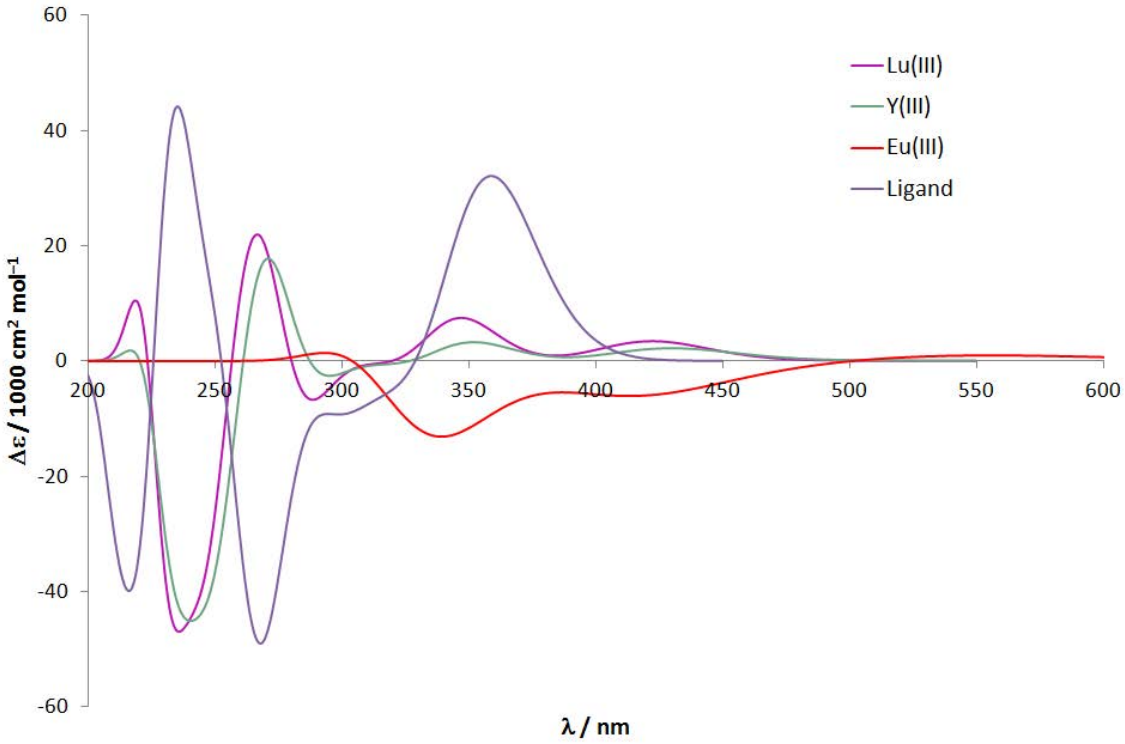

Fig. 38: *Comparison of the different calculated CD spectra with Lu(III), Y(III), Eu(III) and the ligand, without counter ions, method: TDDFT/B3LYP/TZVP//PBE1PBE/TZVP.*

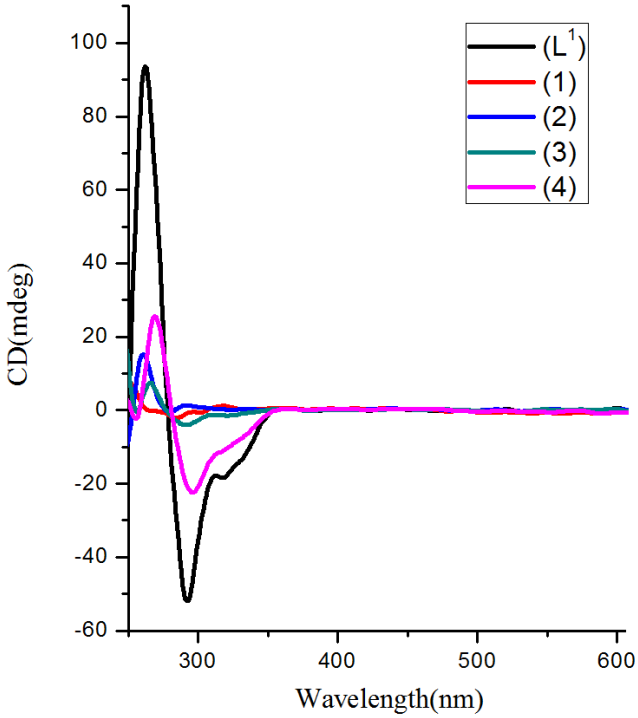

Fig. 39: *Measured CD spectra, solvent: MeOH, L^1 = ligand, (1) = Eu complex, (2) = Tb complex, (3) = Y complex, (4) = Lu complex, data from Prof. P.S. Subramanian, Central Salt and Marine Chemicals Research Institute, India.*

As the distances between the O-atoms and the different metals (Eu (2.267 Å), Y (2.240 Å), Tb (2.227 Å) Lu (2.195 Å)) vary, the resulting CD-spectra have different

shapes for different metals. The LCAO coefficients at the O atoms of the states resulting in the strong transition seem to play an important role. The O-atoms take part in most of the strong transitions (see Figure 37 Ψ=106, 113, 116, 117, and 121) and they seem to influence the shape of the spectrum, as the O−O distance is the main structural difference between the complexes with the metals Eu, Y, Tb, and Lu (Figure 38).

Qualitatively, the measured spectra (Figure 39) shows the same shapes of the curves as their calculated counterparts (Figure 38). As expected for the complex with Eu(III), the spectra of the complexes show a positive Cotton effect at about 270 nm and a negative Cotton effect at about 300 nm.

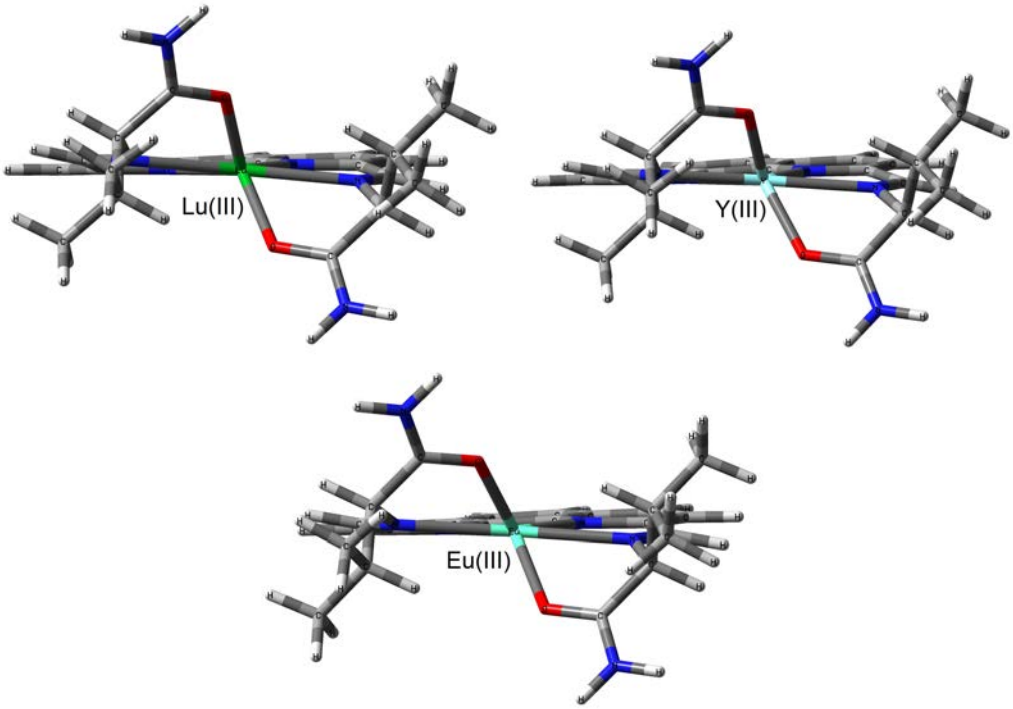

Fig. 40: *Optimized geometry of complex **3** with Lu, Y, and Eu, dihedral angle (O,M,O,C) (Lu) = −87.93°, (Y) = −90.63° and (Eu) = −93.18°, method: PBE1PBE/TZVP.*

Figure 40 illustrates the differences between the three energetically optimized structures. Depending on the metal the dihedral angle O-M-O-C varies from −87.93° to −93.18°. In complex **2**, Y(III) has one Cl^- ion and two solvent molecules (DMSO) attached. The dihedral angle ((O,Y,O,C) = −93.52°) offers enough space for the coordination of three chloride anions. Complex **3** with Y(III) has a dihedral angle of −90.63°, which offers less space. Therefore, it is most likely that in this case only one Cl^- ion is coordinated.

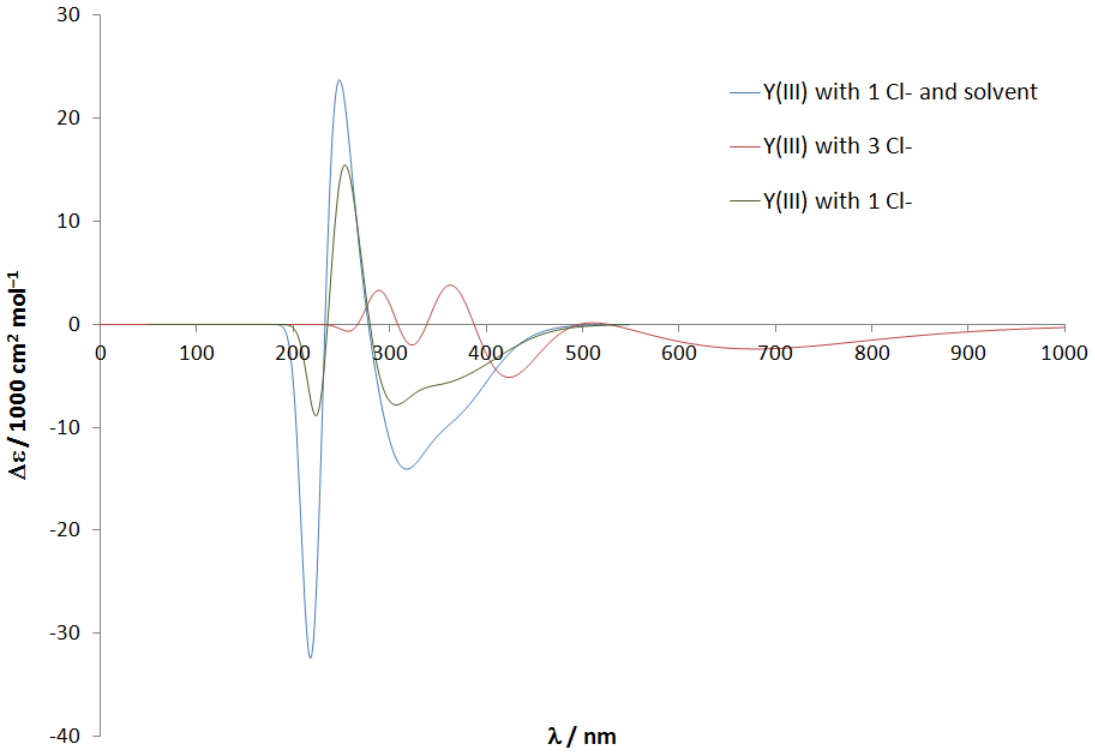

Fig. 41: *Comparison of the resulting CD spectra, Y(III) complex **3** with one Cl^- ion attached (green), with three Cl^- ions (red), solvent=DMSO included by the CPCM method (blue), method: TDDFT/B3LYP/TZVP//PBE1PBE/TZVP.*

If three Cl^- ions are attached to Y(III), the resulting CD spectrum (Figure 41) has a different shape than the one of the complex with only one Cl^- ion. The TDDFT calculation including solvent effects (CPCM, solvent=DMSO) leads to more intense rotational strengths but to the same shape of the curves. The structure being used for this TD calculation was optimized including solvent effects.

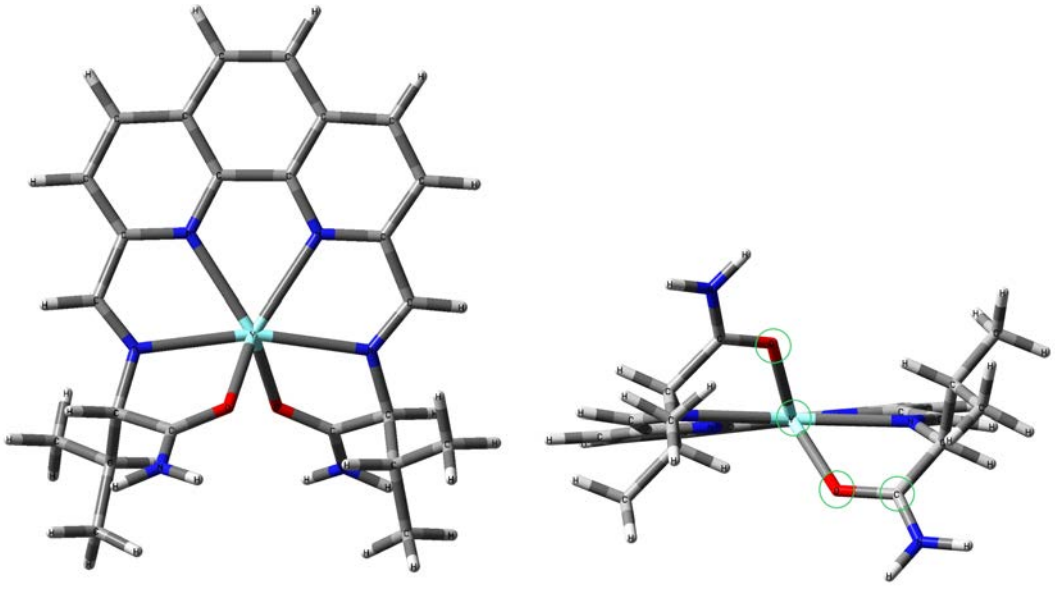

Fig. 42: *Optimized geometry of complex **3** without Cl^- ions, dihedral angle (O,Y,O,C) = −90.63° (marked in green); blue: N, red: O, light blue: Y(III); method: PBE1PBE/TZVP.*

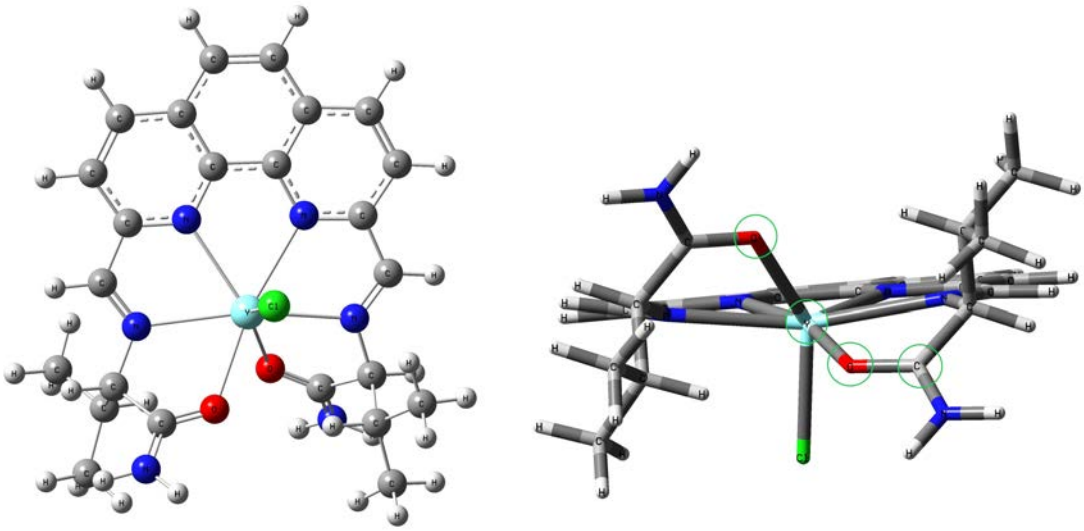

Fig. 43: *Optimized geometry of complex **3** with one Cl^- ion, dihedral angle (O,Y,O,C) = −99.86° (marked in green); blue: N, red: O, light blue: Y(III); method: PBE1PBE/TZVP.*

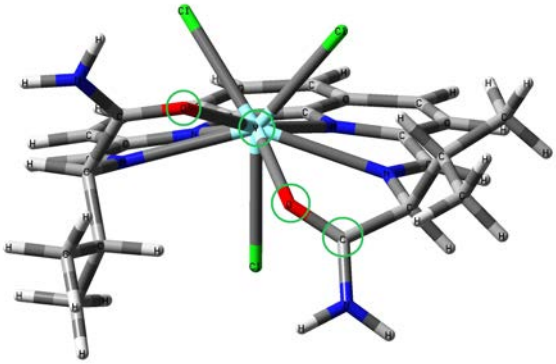

Fig. 44: *Optimized geometry of complex **3** with three Cl^- ions, dihedral angle (O,Y,O,C)= −170.34° (marked in green); blue: N, red: O, light blue: Y(III); method: PBE1PBE/TZVP.*

The comparison of the optimized structures (Figure 44) shows that the dihedral angle is larger with three Cl^- ions attached (−170.34° instead of −99.86° with one Cl^- ion).

The calculated CD spectra of complex **3** with Lu(III) (Figure 45) show a similar shape compared to the CD spectrum with Y(III) (Figure 41). The largest change in the shape of the blue curve compared to the other spectra (red and green) is due to the presence of three Cl^- ions. This underlines the profound impact of the counter ions on the CD spectra.

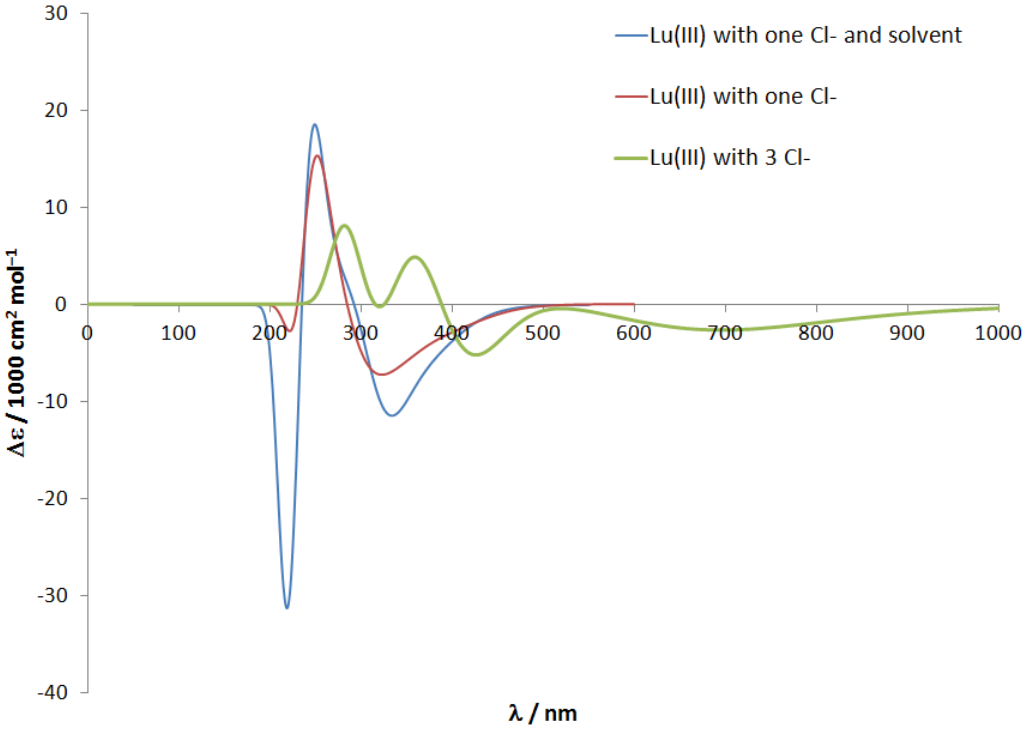

Fig. 45: *Comparison of the resulting CD spectra, Complex **3** with Lu(III) and one Cl^- attached (red), with three Cl^- (green), solvent = DMSO included by the CPCM method (blue); method: TDDFT/B3LYP/TZVP//PBE1PBE/TZVP.*

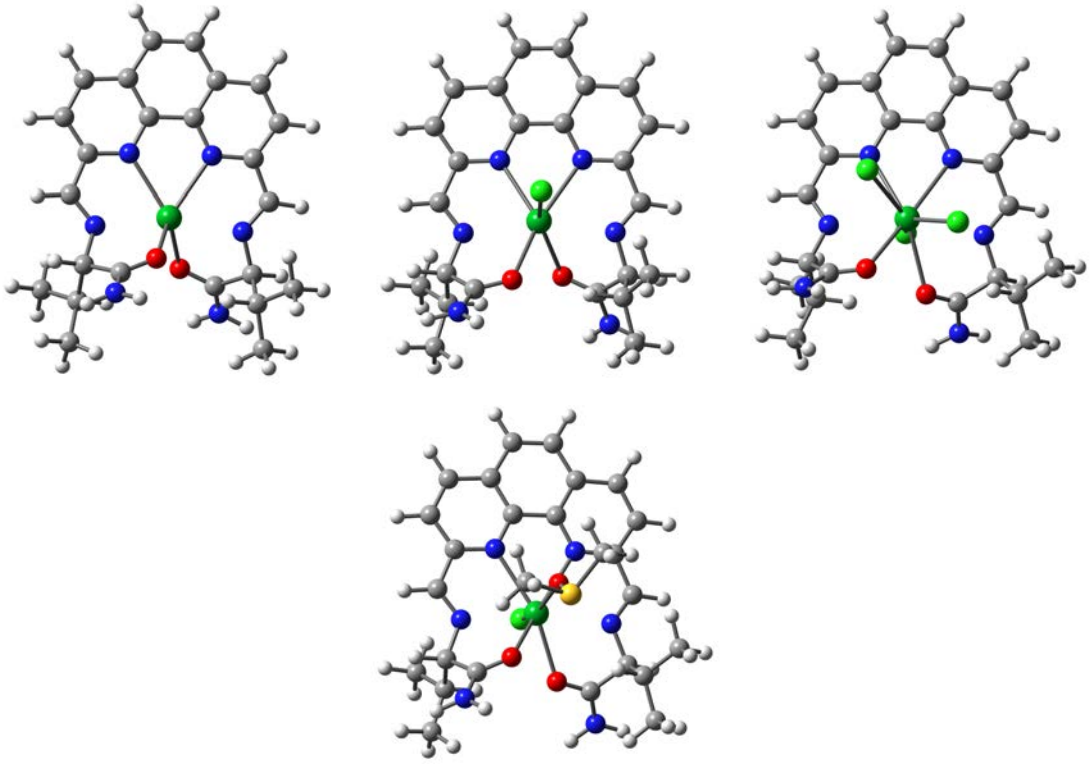

Fig. 46: *Optimized geometries of complex **3** with Lu(III) and different numbers of counter ions and solvent molecules; red: O, yellow: S, dark green: Lu(III), green: Cl, blue: N; method: PBE1PBE/TZVP.*

With the help of calculated UV spectra, the influence of the counter ions was further investigated. The structures of complex **3** with Lu(III) and different numbers of counter ions (Cl^-) are presented in Figure 46.

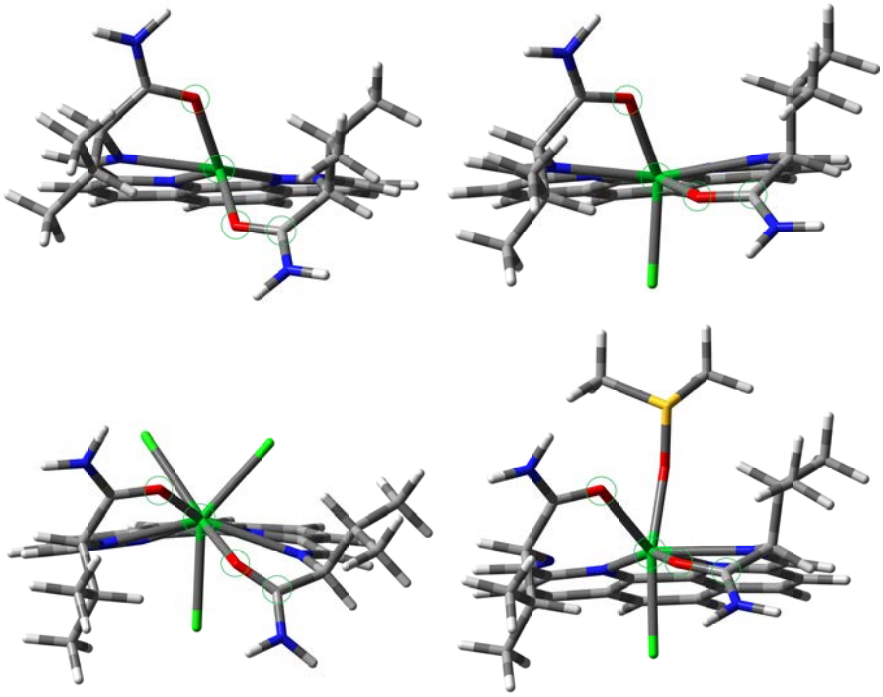

Fig. 47: *Optimized geometries of complex **3** with Lu(III) and different numbers of counter ions and solvent molecules; red: O, yellow: S, dark green: Lu(III), green: Cl, blue: N; dihedral angle O-Lu-O-C (marked in green): complex without Cl^-: −89.56°, with one Cl^-: − 110.77°, with three Cl^-: −169.42°, and with one Cl^- and one DMSO molecule: −142.79°; method: PBE1PBE/TZVP.*

Figure 47 shows that the complex **3** with Lu(III) with three Cl^- ions has largest dihedral angle (O-Lu-O-C: −160.42°) of the presented structures. The smallest angle has the complex without Cl^- ions (O-Lu-O-C: −89.56°). The O−O distances are 3.28 Å (complex without Cl^- ions), 2.86 Å (complex with one Cl^- ion), 2.70 Å (complex with three Cl^- ions), and 2.72 Å (complex with one Cl^- ion and one DMSO molecule). The distances of the metal center to the N atoms of the aromatic part of the ligand are 2.43 Å (complex without Cl^- ions), 2.47 Å (complex with one Cl^- ion), 2.63 Å (complex with three Cl^- ions), and 2.52 Å (complex with one Cl^- ion and one DMSO molecule). These numbers reveal that the complex with one Cl^- and one DMSO molecule has the largest distances between the two O atoms of the ligand as well as the largest one between the metal center and the N atoms of the aromatic part.

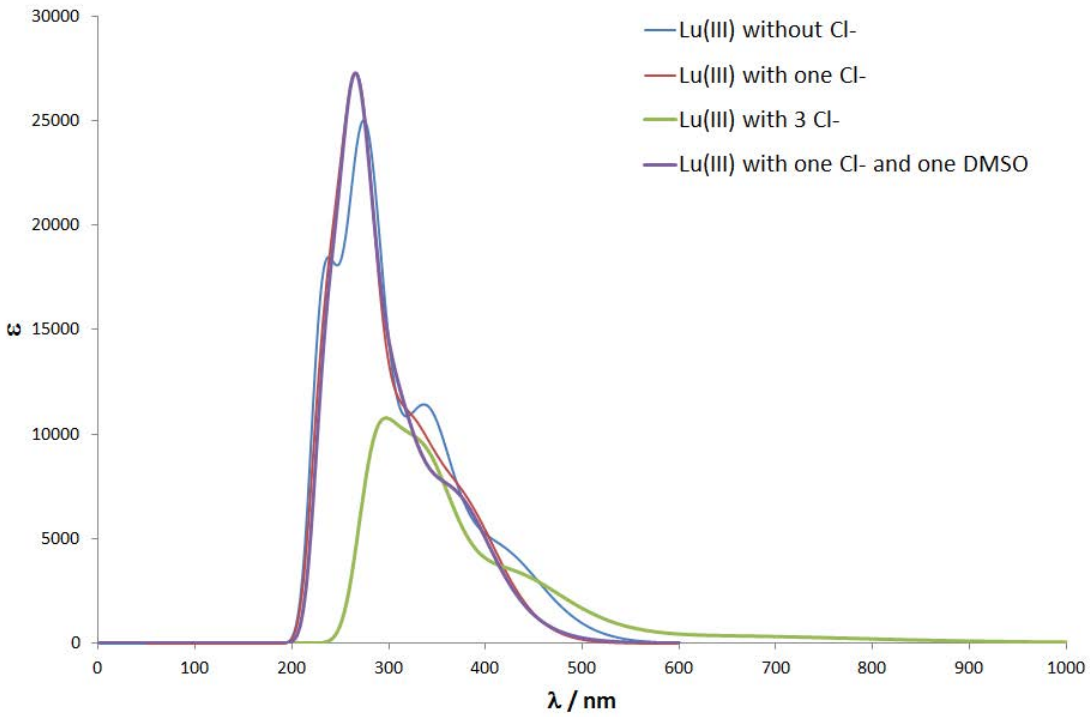

Fig. 48: *Comparison of the resulting UV spectra, Complex **3** with Lu(III); method: TDDFT/B3LYP/TZVP//PBE1PBE/TZVP.*

The UV/VIS spectra of Lu(III) without Cl^- and with one Cl^- ion show nearly the same shape. The spectrum of the complex without a counter ion has a slightly more intense peak at 260 nm than the one with a single Cl^- ion. The spectrum with one Cl^- ion and one DMSO has a shape which is identical to the one with one Cl^- ion. The only significant difference can be noticed with three Cl^- ions. The peak at 300 nm is significantly less intense than the corresponding peak in the spectra of the complexes with one, two, and one Cl^- plus one DMSO molecule. Moreover, this peak is slightly shifted to the red. The strongest transition in this spectrum is the one at 343 nm which is dominated by a transition from the MO 138 to the MO 147 (Figure 49). Since the spectral curves of the complexes involving one Cl^- and one DMSO molecule are essentially indistinguishable it appears that it is less the nature of the attached species but rather the geometrical changes that causes the differences in the spectral curves.

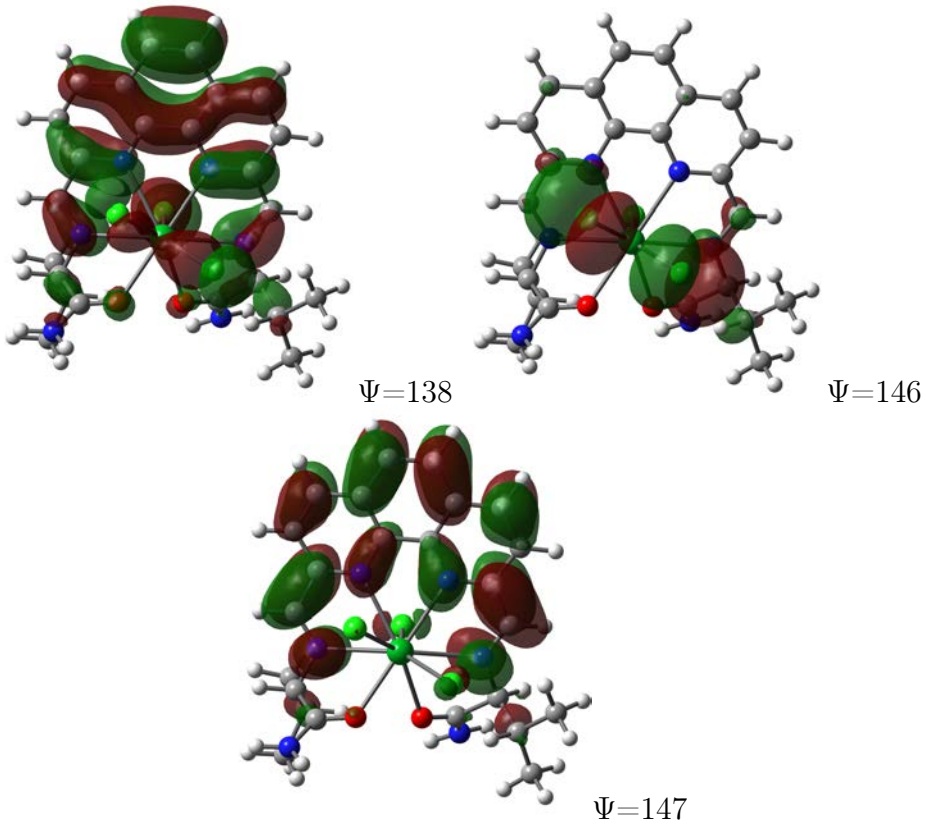

Fig. 49: *Kohn-Sham molecular orbitals Ψ of complex* ***3*** *with Lu(III) and three* Cl^-*, HOMO: Ψ =146, LUMO: Ψ =147.*

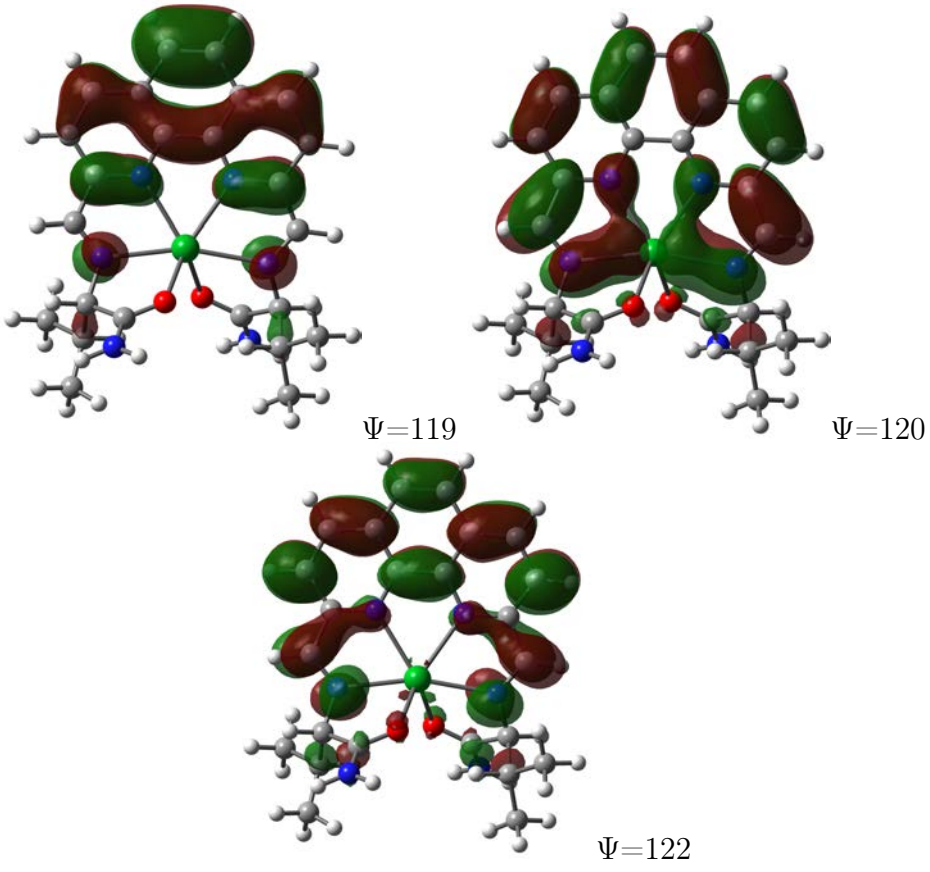

Fig. 50: *Kohn-Sham molecular orbitals Ψ of complex* ***3*** *with Lu(III), HOMO: Ψ =119, LUMO: Ψ =120.*

The transition with the highest intensity of the spectrum obtained for the bare cationic complex without counter ions is the one at 282 nm and occurs from the MO 119 to the MO 122 between the HOMO and the LUMO+2. The main transition of the complex with three Cl^- ions occurs between the energetically very low HOMO-8 and the LUMO (coefficient: 0.41036) and between HOMO-5 and LUMO+2 (coefficient: 0.40899) at a wavelength of 342 nm.

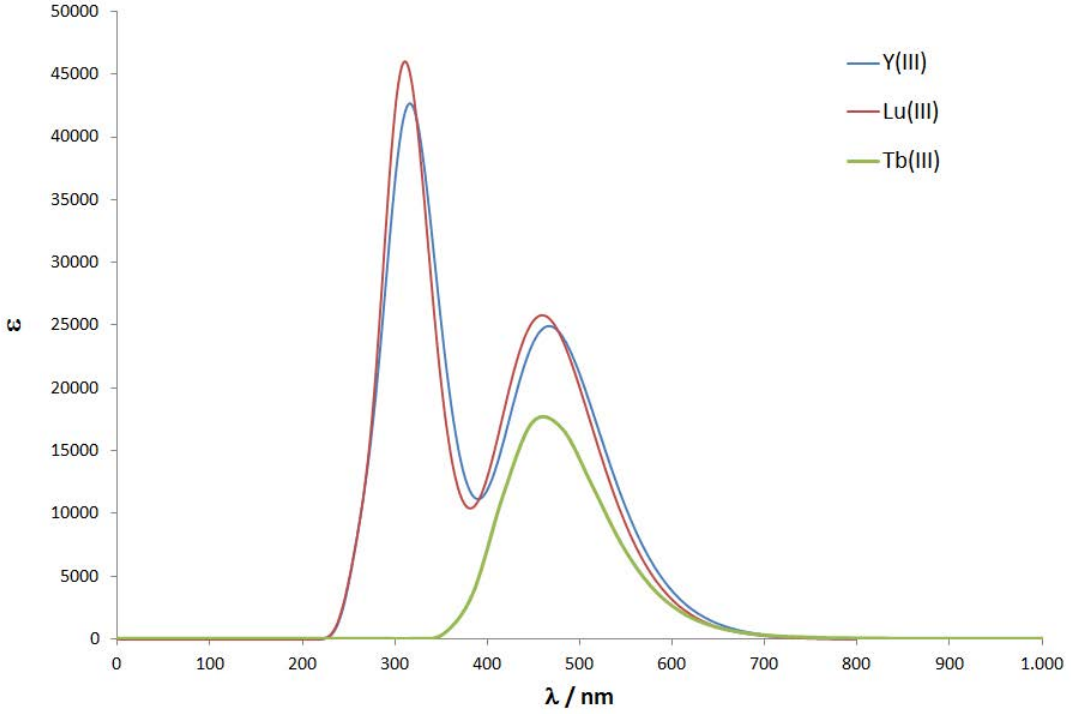

Fig. 51: *Comparison of the resulting UV spectra, ligand **4** with Y(III), Tb(III) and Lu(III); method: TDDFT/B3LYP/TZVP//PBE1PBE/TZVP.*

Ligand **4** with Y(III) or Lu(III) results in an UV spectrum with two maxima which are shown in Figure 51. The first maximum appears at 320 nm and the second one at about 450 nm. The corresponding transitions take place between the two phenyl rings and the scaffold of the pincer ligand. At 461 nm the transition of the complex with Y(III) is between MO 124 and MO 128 and at 321 nm it is between MO 125 and MO 131. For the complex with Lu(III) the transition at a wavelength of 454 nm takes place between MO 140 and MO 144 and at a wavelength of 320 nm between MO 141 and MO 144. In Figure 52 and 53 the corresponding MOs are presented.

The spectrum with Tb(III) has only one maximum and a smaller oscillator strength. Due to the larger distances within this complex (ionic radius of Tb(III): 100 pm)[80] and the resulting different structure compared to the complexes with the other metals Y(III) and Lu(III) (see Figure 55 and 56) the transition between the two aromatic parts of the ligand does not occur. There is only one major transition between MO 138 and MO 145 at a wavelength of 451 nm.

The comparison of the ionic radii (Tb(III) 100 pm < Y(III) 93 pm ≤ Lu(III) 93 pm)[80] shows that the radii of Y(III) and Lu(III) are the same leading to similar shapes of the UV spectra, while Tb(III) having a larger ionic radius shows only one maximum in the UV spectrum of the corresponding complex.

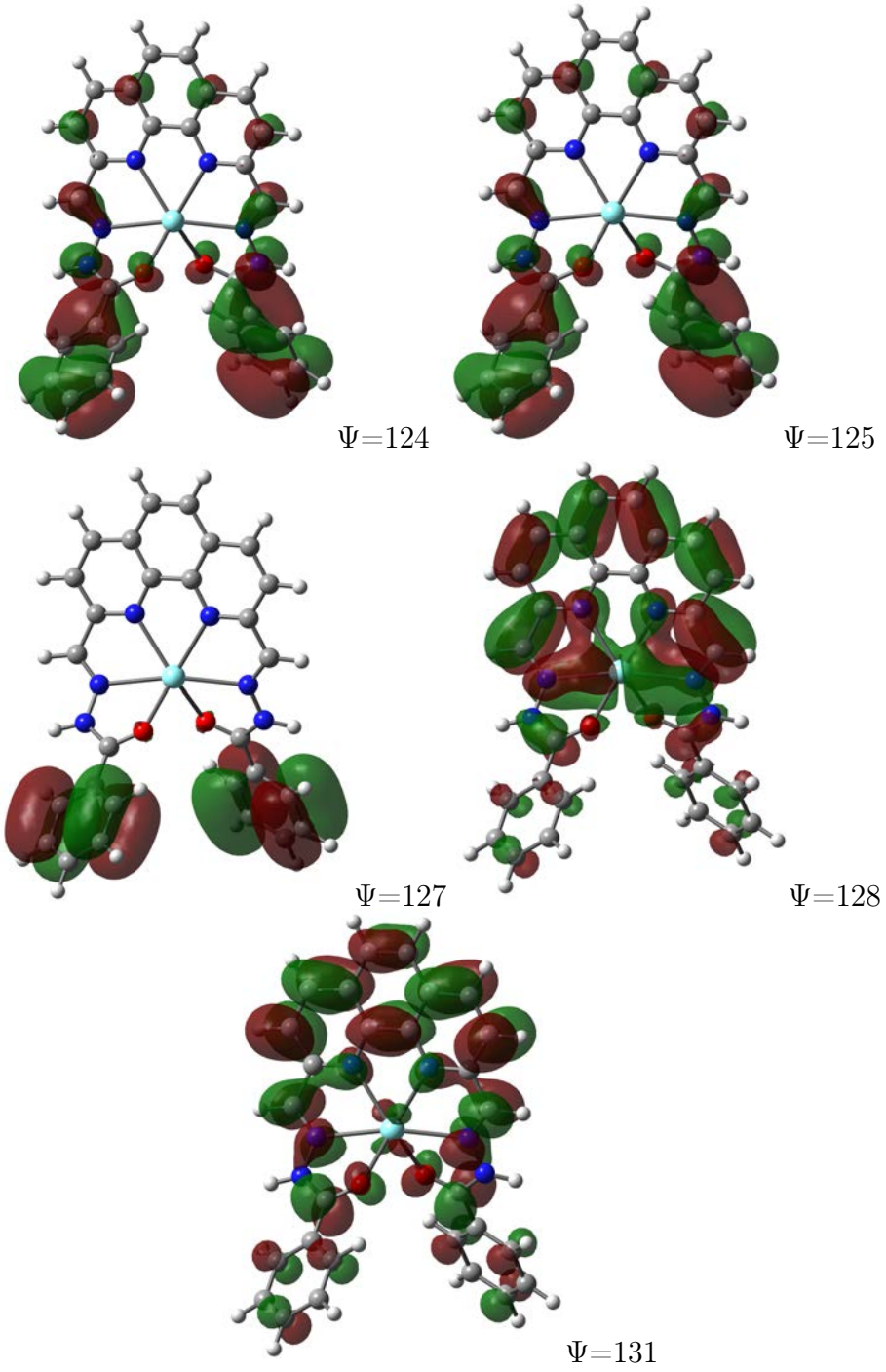

Fig. 52: *Kohn-Sham molecular orbitals Ψ of complex 4 with Y(III), HOMO: Ψ =127, LUMO: Ψ =128.*

Metal Center	Wavelength/ nm	Oscillator Strength	transition
Y(III)	461.17	0.4415	124 ->128 π -> π^*
	320.59	0.6105	125 ->131 π -> π^*
Lu(III)	453.69	0.4437	140 ->144 π -> π^*
	319.57	0.4524	141 ->146 π -> π^*
Tb(III)	450.97	0.2064	138 ->145 π -> π^*

Table 7: *Oscillator strengths of the strongest transitions of the TD-DFT calculation of ligand **4** with Y(III), Lu(III), Tb(III); method: TDDFT/B3LYP/TZVP//PBE1PBE/TZVP.*

The HOMO (Ψ =127) of complex **4** with Y(III) has the largest coefficients at the phenyl rings, while the LUMO (Ψ =128) is widely located at the phenanthroline part of the ligand. Therefore, the HOMO -> LUMO transition would involve strong intramolecular charge transfer. Both the HOMO as well as the LUMO have local π character.

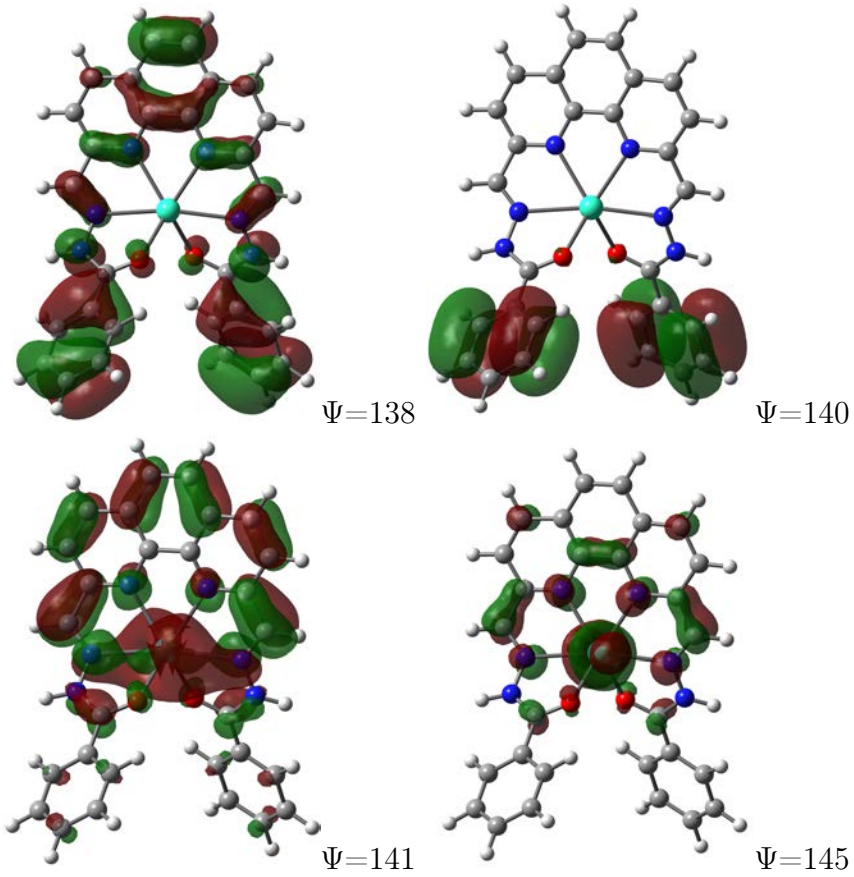

Fig. 53: *Kohn-Sham molecular orbitals Ψ of complex **4** with Tb(III), HOMO: Ψ =140, LUMO: Ψ =141.*

Like in the Y(III) complex the HOMO (Ψ =140) of complex **4** with Tb(III) has the largest coefficients at the phenyl rings, and similarly the LUMO (Ψ =141) is predominantly located at the phenanthroline part of the ligand, and both, the HOMO as well as the LUMO have local π character.

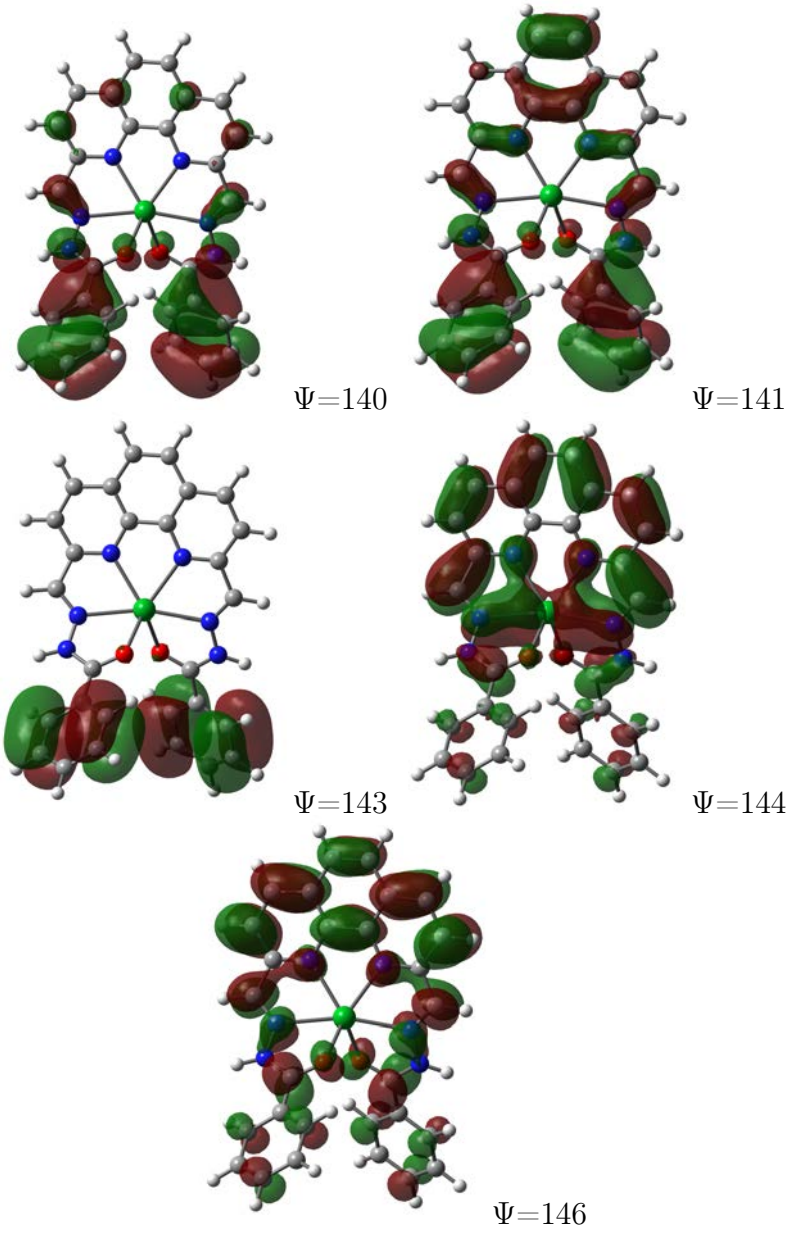

Fig. 54: *Kohn-Sham molecular orbitals* Ψ *of complex* ***4*** *with Lu(III), HOMO:* Ψ *=143, LUMO:* Ψ *=144.*

The different spectral properties of the complexes can be explained by the different ionic radii of the metal centers and the corresponding differences in the resulting structures (Figure 55). The distances between the centroids of the aromatic rings are 7.34 Å (complex with Y(III)), 7.15 Å (complex with Lu(III)), and 7.27 Å (complex with Tb(III)). A more significant difference occurs for the dihedral angles O-M-O-C and C-N-N-C which are presented in Figure 55 and 56. The dihedral angle C-N-N-C is −137.33° for Tb(III), −135.16° for Y(III), and −132.40° for Lu(III).

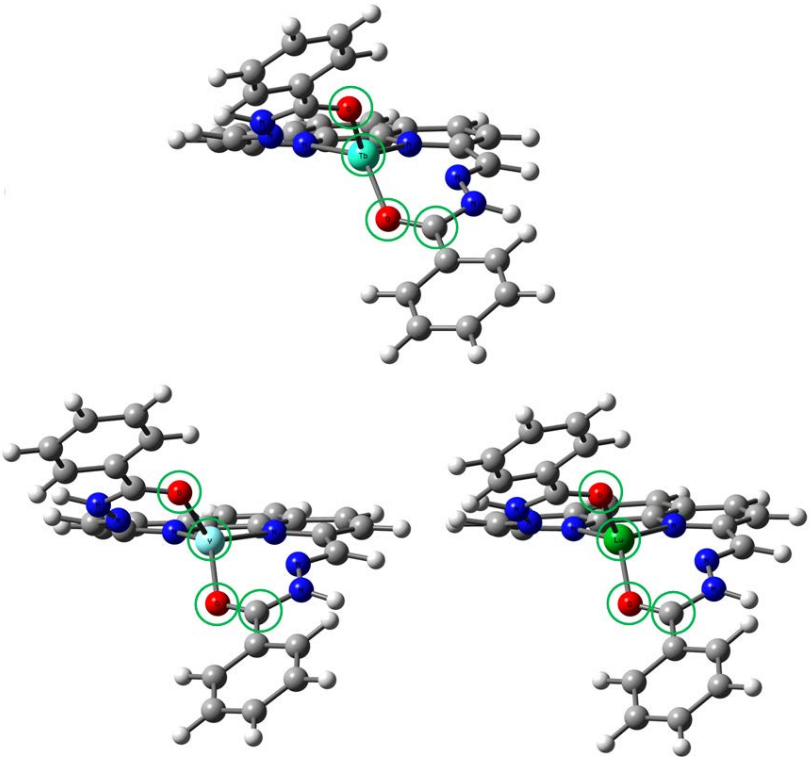

Fig. 55: *Optimized geometry of complex 4 with Tb, Y, and Lu, dihedral angle (O-M-O-C) (Tb) = −92.10°, (Y) = −90.90°, and (Lu) = −85.09°, method: PBE1PBE/TZVP.*

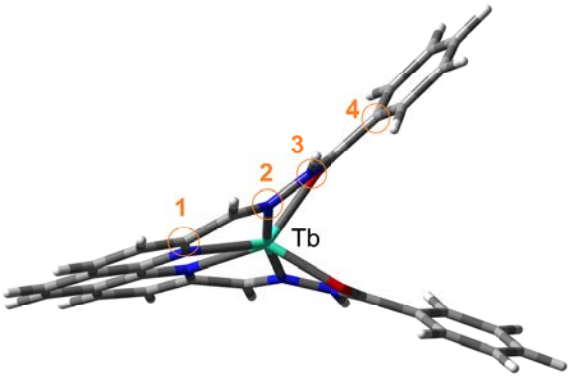

Fig. 56: *Optimized geometry of complex 4 with Tb, dihedral angle (C-N-N-C) = −137.33°, method: PBE1PBE/TZVP.*

As a conclusion, the computationally obtained results emphasize the effect of small changes at the ligand on the structure and on the spectral properties of the complex. The main difference is the "bending" of the ligand (Figure 55). This rather small change can have a significant effect on the behaviour of the molecule in catalytic reactions, as it influences the other possible coordination sides of the complex. Moreover, the influence of the metal center on the complex could be demonstrated with the help of UV/VIS and CD spectra. The varying shapes of the curves of the spectra with different metals underline the importance of the choice of the metal.

3.2 Mononuclear Complexes with Triscatecholate-Based Ligands

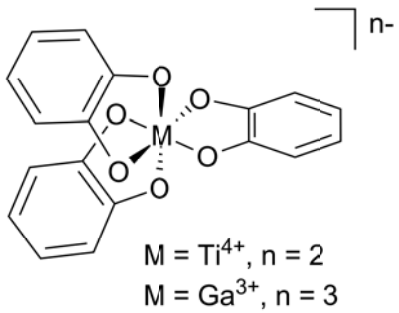

Fig. 57: *Mononuclear triscatecholate complex with titanium(IV) or gallium(III).*

Simple triscatecholate complexes with titanium(IV) (Figure 57) were studied before[81] and are still of great interest. The performed studies contribute to the elucidation of the stereochemistry of an enantiomerically pure helicate in solution with the help of DFT-calculations and CD-measurements.

First, the structure of the titanium(IV) complex was optimized with the cam-B3LYP functional, a valence triple-ζ basis set augmented by polarization functions (TZVP) and SDD/MDF10 for titanium. The resulting average Ti−O distance is 1.9685 Å. It can be compared to the measured average distance of 1.966 Å in $[Et_3NH]_2[(cat)_3Ti]$.

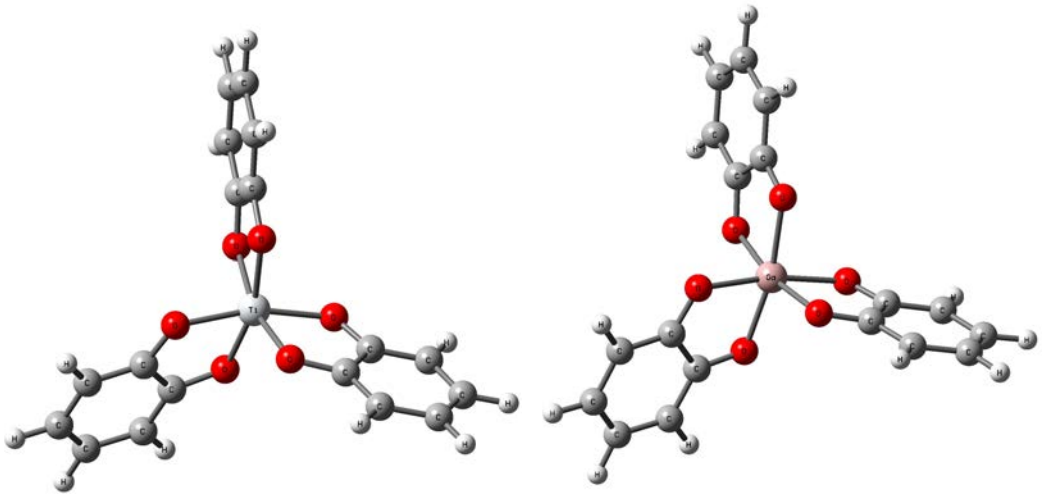

Fig. 58: *Triscatecholate complexes with Titanium(IV) (left) and Gallium(III) (right).*

As the triscatecholate complexes are relatively small (Figure 58), the results obtained with different methods and functionals and basis sets can be compared within a reasonable time. To this purpose, the structure of the complex with Ti(IV) is energetically optimized. The resulting distances of Ti(III)−O obtained with different functionals and the corresponding computation time are listed in Table 8.

functional or method	distance Ti−O in Å	deviation*	computation time
B3LYP	1.9841	0.0181	12 h 15 min
HF	1.9572	0.0088	21 h 40 min
PBE0	1.9685	0.0025	41 h 47 min
LC-wPBE	1.9597	0.0063	48 h 14 min
wB97XD	1.9692	0.0032	54 h 13 min
cam-B3LYP	1.9666	0.0006	31 h 39 min

Table 8: *optimized structures with Titanium(IV), Basis set: TZVP, ECP: MDF10, complex: Λ configuration, *deviation to the measured Ti−O distance (1.966 Å).*[81]

The structure was not only optimized at the HF level and with the most frequently used DFT functionals B3LYP and PBE1PBE but also with the help of cam-B3LYP, LC-wPBE, and wB97XD. The smallest distance between titanium(IV) and the coordinating O atoms was found at the HF level of theory with 1.9572 Å. The second smallest distance is resolved by the LC-wPBE level of theory (1.9597 Å). Nearly the same result and the smallest deviation to the measured Ti−O distance of 1.966 Å is obtained with cam-B3LYP (1.9666 Å) within less computation time. Therefore cam-B3LYP was chosen for further calculations.

The complex with Ga(III) was optimized with different methods and functionals. The results for the distance between Ga(III) and O and the computation time are presented in Table 9.

functional or method	basis set	distance Ga−O in Å	computation time
B3LYP	6-31g	2.0601	1 h 48 min
HF	TZVP	2.0039	38 h 24 min
PBE0	TZVP	2.0359	32 h 34 min
PBE0	6-311+g**	2.0443	48 h 58 min
LC-wPBE	TZVP	2.0325	48 h 14 min
cam-B3LYP	TZVP	2.0328	27 h 17 min

Table 9: *optimized structures with Gallium(III), ECP: MWB28, complex: Λ configuration.*

As anticipated, the Ti−O-distances are shorter than the Ga−O distances. The smallest distance is again obtained by HF (2.0039 Å), while the second smallest are resolved by LC-wPBE (2.0325 Å) and cam-B3LYP (2.0328 Å), which are nearly identical. Again cam-B3LYP achieves good results within a small amount of computation time.

3.2.1 CD- and UV- spectra of Mononuclear Complexes

Calculation of CD-spectra provides an excellent possibility for a better insight into the electronic as well as into the spatial structure of the complexes. Employing the TD (time dependent)- DFT method, it is possible to calculate excited states of the considered molecule. In many cases, the functional B3LYP is a good choice as it leads to reliable results, which is supported by the results given in this thesis.

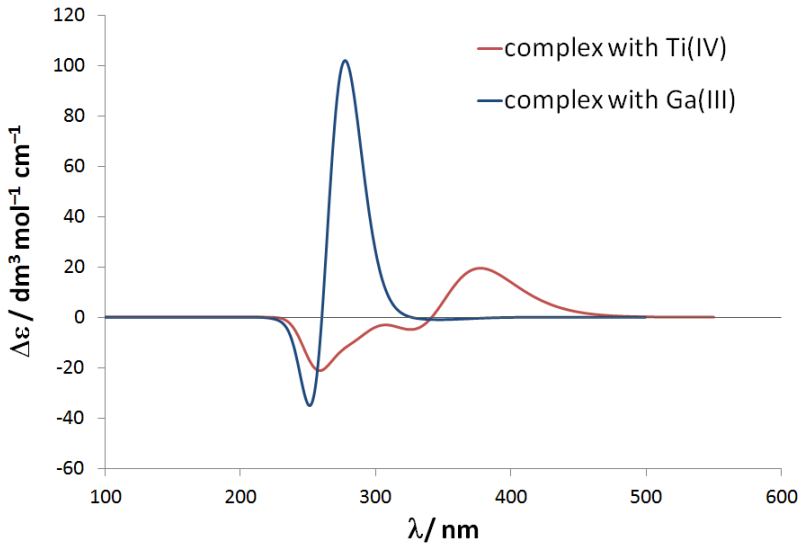

Fig. 59: *Calculated CD spectra of Triscatechol with Titanium(IV) and Gallium(III), Λ form; method: TDDFT/B3LYP/6-311g**//cam-B3LYP/TZVP.*

In order to study the CD-spectra of $[(cat)_3Ga]^{3-}$ and $[(cat)_3Ti]^{2-}$, a TD-calculation on the B3LYP level of theory with the 6-311g** basis set combined with the ECPs MWB28 (for gallium) and MDF10 (for titanium) was performed (Figure 59). The two spectra have characteristically different shapes. Thus, the spectrum of $[(cat)_3Ga]^{3-}$ has higher rotational strengths and only one positive Cotton effect, while the spectrum of $[(cat)_3Ti]^{2-}$ shows one maximum and one minimum.

wavelength	transitions	rotational strength
346.95	$87 \rightarrow 89$	-2.0356
281.36	$85 \rightarrow 92$, $86 \rightarrow 93$	58.4165
281.34	$85 \rightarrow 93$	57.8953
278.36	$87 \rightarrow 94$	-72.0082
276.36	$87 \rightarrow 95$	36.7394
276.22	$87 \rightarrow 96$	36.2124
270.77	$86 \rightarrow 94$	83.4855
270.72	$85 \rightarrow 95$, $86 \rightarrow 96$	82.3622
265.84	$85 \rightarrow 95$, $86 \rightarrow 96$	189.3881
265.84	$85 \rightarrow 96$, $86 \rightarrow 95$	190.5495
261.81	$85 \rightarrow 95$, $86 \rightarrow 96$	-475.2902

Table 10: *The 11 excited states of $[(cat)_3Ga]^{3-}$ with the highest rotational strengths, and their major components.*

Table 10 shows the most intense rotational strengths with the corresponding transition wavelengths. Figure 61 shows the local structure of the MOs of the Ga(III) complex. The HOMO ($\Psi = 87$) has local π symmetry in the aromatic part of the molecule, while the LUMO ($\Psi = 88$) is very diffuse and has significant coefficients only at the periphery of the aromatic system.

The UV spectra of the complex with Ga(III) and Ti(IV) are shown in Figure 60. The spectrum of the complex with Ga(III) has one maximum at a wavelength of 280 nm while the spectrum of the complex with Ti(IV) has two maxima: one at 272 nm and one at 349 nm.

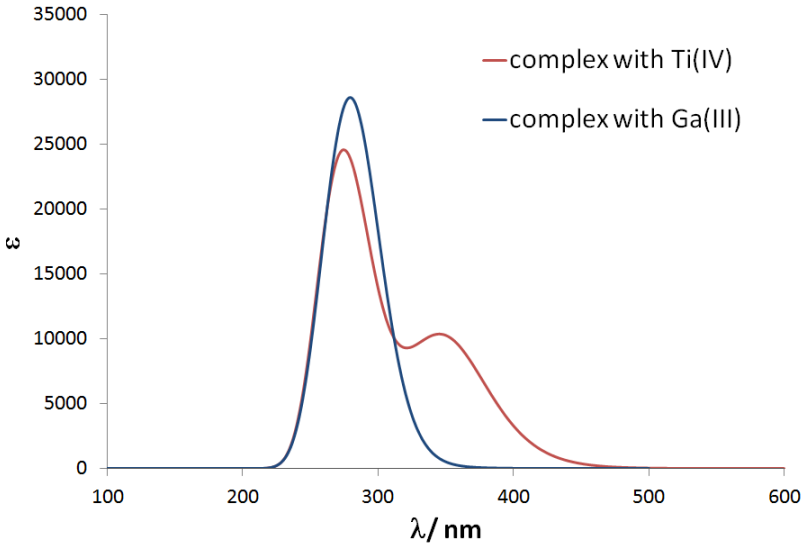

Fig. 60: *Calculated UV spectra of Triscatechol with Titanium(IV) and Gallium(III), Λ form; method: TDDFT/B3LYP/6-311g**//cam-B3LYP/TZVP.*

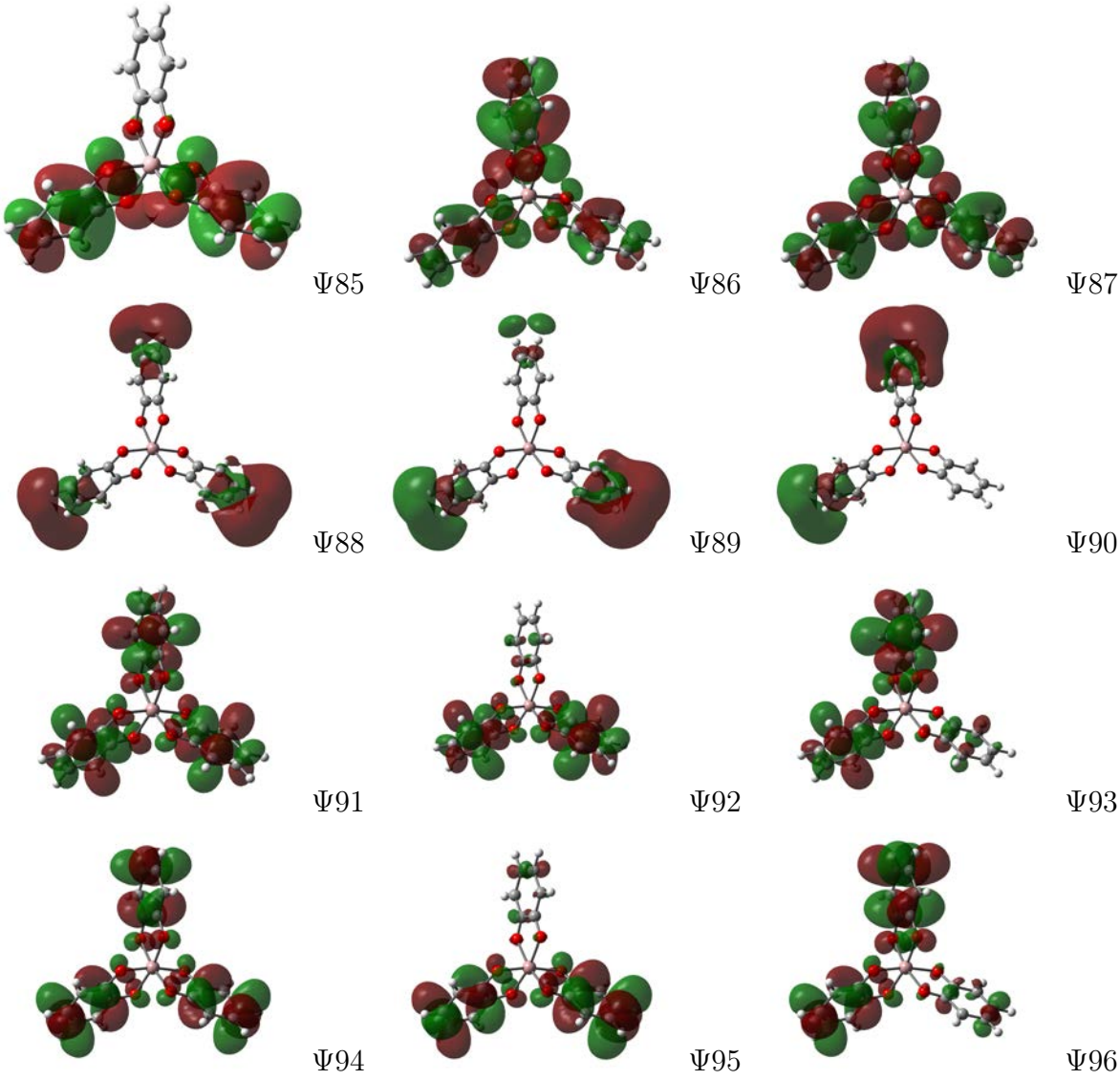

Fig. 61: *Selected Kohn-Sham orbitals of $[(cat)_3Ga]^{3-}$, HOMO: Ψ87, LUMO: Ψ88.*

Table 11 comprises the highest rotational strengths of the Ti(IV) complex with the corresponding transition wavelengths. Figure 62 shows the nodal properties of some MOs. Again the HOMO ($\Psi = 91$) has local π character in the aromatic system, the LUMO ($\Psi = 92$) is extremely diffuse and the central part of the molecule has non-vanishing coefficients only at the metal atom and aromatic carbon atoms.

wavelength	transitions	rotational strength
411.70	91 → 92	10.3959
388.43	91 → 94	13.4457
374.62	89 → 92	25.5418
367.34	90 → 94	40.8837
354.05	91 → 95	33.2670
344.52	90 → 95	−47.5803
277.37	89 → 96	−18.2626
277.37	90 → 97	−19.8182
273.17	87 → 93, 89 → 96	35.3940
269.1	88 → 95	11.4263
264.39	84 → 93	−15.4310
261.15	86 → 94	−35.8093
257.02	91 → 101	−32.5158

Table 11: *The 13 excited states of $[(cat)_3Ti]^{2-}$ with the largest rotational strength, their major components, and calculated rotational strength.*

The different modal properties of the MOs of complexes $[(cat)_3Ti]^{2-}$ and $[(cat)_3Ga]^{3-}$ reveal significant differences between their electronic structures. A transition between the HOMO and the LUMO of the complex with Ti(IV) is most likely a Rydberg state, while the longest wavelength transition of the Ga(III) complex occurs from the HOMO to the LUMO+1 but has also strong Rydberg character.

In general, the shapes of the spectral curves of the complexes with Ti and Ga (Figure 59) are very different, caused by different rotational strengths which are up to 190 for Ga but only 41 for Ti. This results from the different metal-O distances as several transitions involve strong coefficients at the O atoms and in case of Ti also coefficients at the metal.

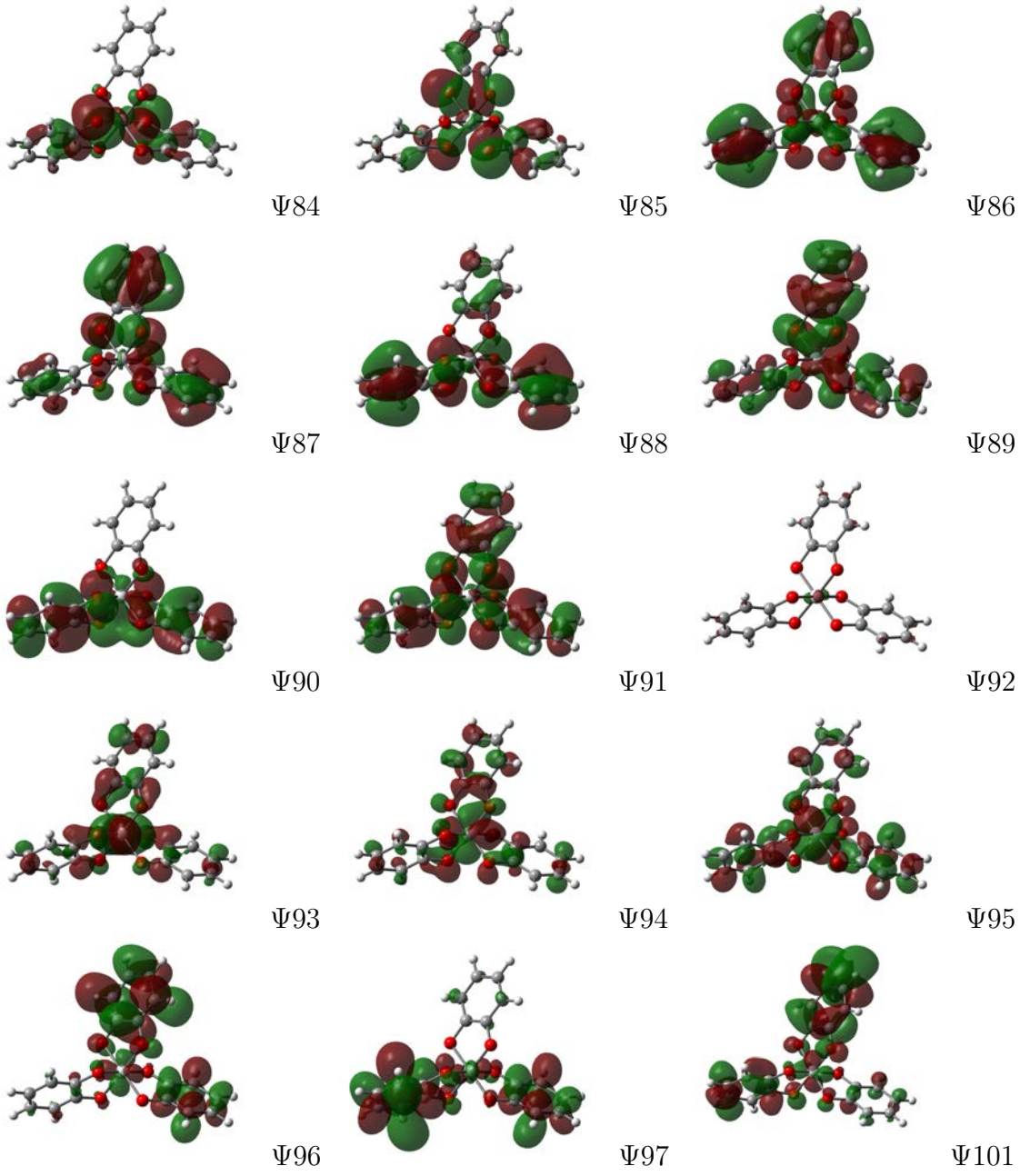

Fig. 62: *Selected Kohn-Sham orbitals of $[(cat)_3Ti]^{2-}$, HOMO: Ψ91, LUMO: Ψ92.*

3.3 Dimerization of Triscatecholate-Based Complexes

The following complexes are based on the earlier discussed mononuclear compounds $[(cat)_3Ti]^{2-}$ and $[(cat)_3Ga]^{3-}$. As ligands, (−)-β-citronellol, (*S*)-(−)-2-methyl-1-butanol, (*S*)-(−)-1-phenylethanol, (*S*)-(−)-2-phenylpropan-1-ol, cholesterol, *L*-(−)-borneol and (−)-menthol were chosen. The CD-measurements provide an insight into the dynamic behavior of the resulting complexes in MeOH and DMSO. The result of each measurement was compared to computationally obtained spectra. The complexes were energetically optimized at the PBE0 level of theory mainly with the TZVP as basis set combined with the ECPs MDF10 for titanium and MWB28 for gallium. The TD-DFT

calculations were performed with the functional B3LYP. Calculations on the model compound $[(cat)_3Ti]^{2-}$ with the catecholate dianion as ligand were done before.[81] In order to learn more about the dynamics of the complexes in solution, the molecules were energetically optimized in their monomeric form as well as in their dimeric form. Complexes with different stereogenic centers at α-, β- or γ-positions were chosen.

In the presence of lithium ions, the chosen complexes, which have aldehyde-, ketone- or ester-functions at the 3-position, show a tendency to dimerize. The equilibration of monomer and dimer can be influenced by choice of the solvent and different stereogenic centers.[82]

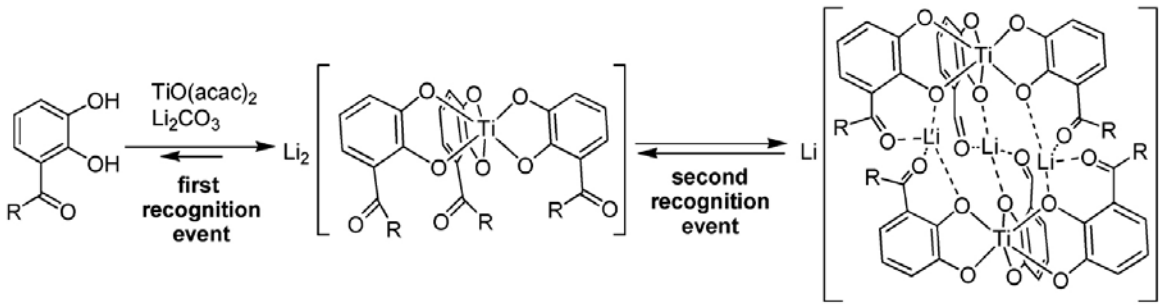

Fig. 63: *First recognition: metal center and ligands, second recognition: two monomers.*

The reaction leading to dimerization takes place in two steps: the first one is the recognition (Figure 63) between the positively charged metal center and the negatively charged ligands. The second one is the recognition between the two monomers, bridged by three lithium ions.

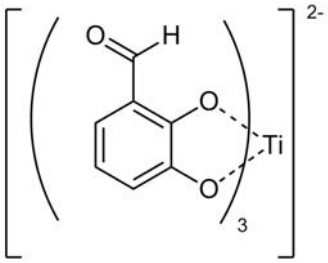

Fig. 64: *Complex* $[(\mathbf{5})_3 Ti]^{2-}$.

The structure of the complex shown in Figure 64 was calculated as a model compound on the cam-B3LYP/ TZVP level of theory to study the recognition of the two monomers. The *fac*- and *mer*-isomers of the monomeric unit are in equilibrium with each other.[83] The first isomer has a total energy energy of -1542.973034 a.u. and the second of -1542.972989 a.u. with a resulting energy difference of about 10.89 kcal/mol. Therefore, the *anti* isomer represents the more stable form (Figure 65).

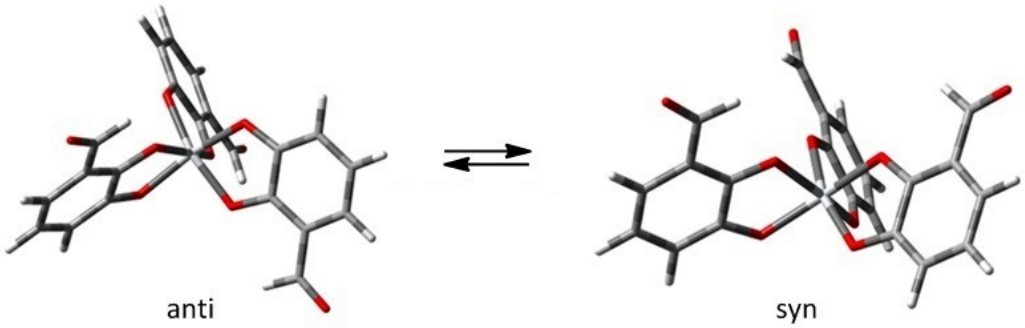

Fig. 65: *Complex $[(\mathbf{5})_3 Ti]^{2-}$, equilibrium between the anti- and syn-form of the isomers.*

The dimer of the two monomers, which is of interest, is a hierarchically assembled triple lithium bridged bistitanium(IV) complex $Li_3[(\mathbf{5})_3Ti_2]^-$. The calculations mentioned above show that the *anti* isomer is energetically favored. The dimerization takes place between two of the *syn* isomers, as the resulting dimer is sterically favored. The Ti-O distance within the optimized geometry has an average of about 1.956 Å. The energetically optimized form is shown in Figure 66. The resulting Ti−Ti distance is about 5.709 Å and the Li^+-ions are in a tetrahedral environment.

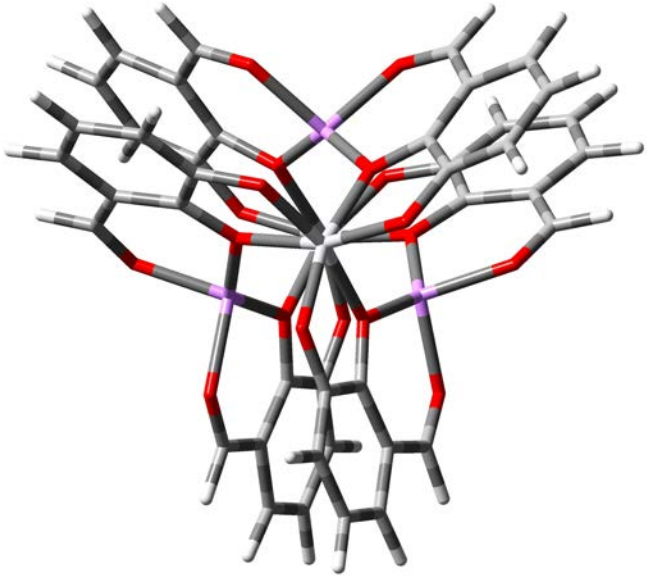

Fig. 66: *Energetically optimized complex $Li_3[(\mathbf{5})_3 Ti]_2$ in the ΔΔ form; method: cam-B3LYP/TZVP.*

Both recognition events, as mentioned earlier, were computationally reproduced. The monomer leads to the complex in its Λ or Δ form; and the second recognition event leads to the stabilized dimer in its ΛΛ or ΔΔ form with one counter ion (Figure 67).

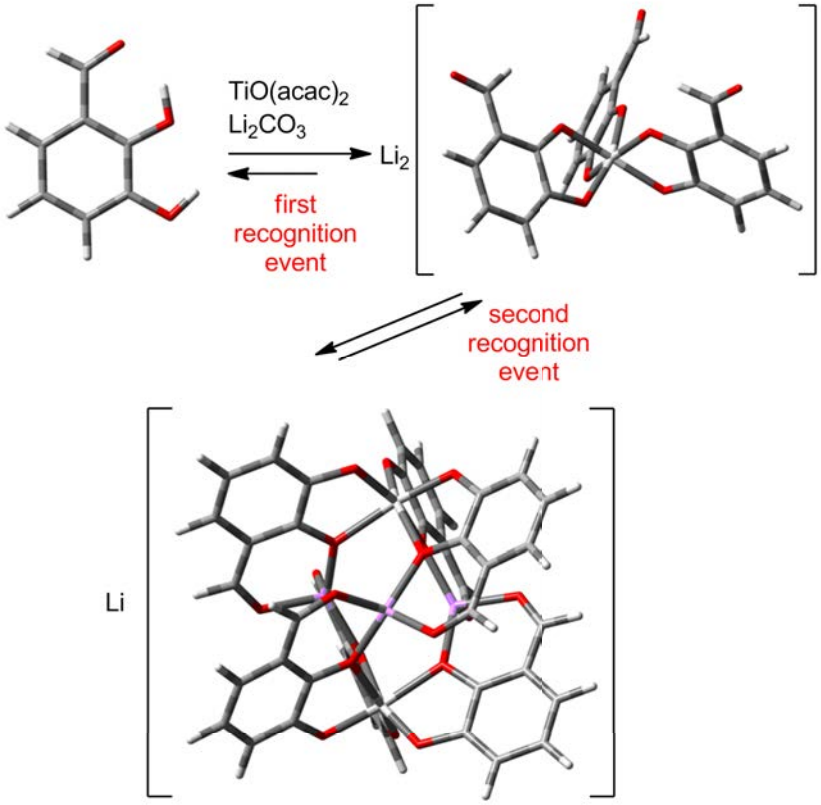

Fig. 67: *Computationally studied recognition events between the molecule and the metal ion and the complex and the Li^+ ions; method: cam-B3LYP/TZVP.*

As the second recognition event depends on the one hand on the conversion of the Λ into the Δ form of the monomer and on the other hand of the switch between the *syn* and *anti* form, the calculation of the corresponding transition states is of great importance. Figure 68 shows the resulting structures and energies. The stabilization effect of the dimerization can be calculated like this:

$$\Delta E = E(Dimer) - (2 \cdot E(Monomer) + 3 \cdot E(Li^+))$$
$$\Delta E = -3108.793189\text{a.u.} - (2 \cdot -1542.972989\text{a.u.} + 3 \cdot -7.265504\text{a.u.}) = -1.0507\text{a.u.}$$

This calculation demonstrates that the dimerization gains about 1.05 a.u. and therefore is strongly favored in the gas phase.

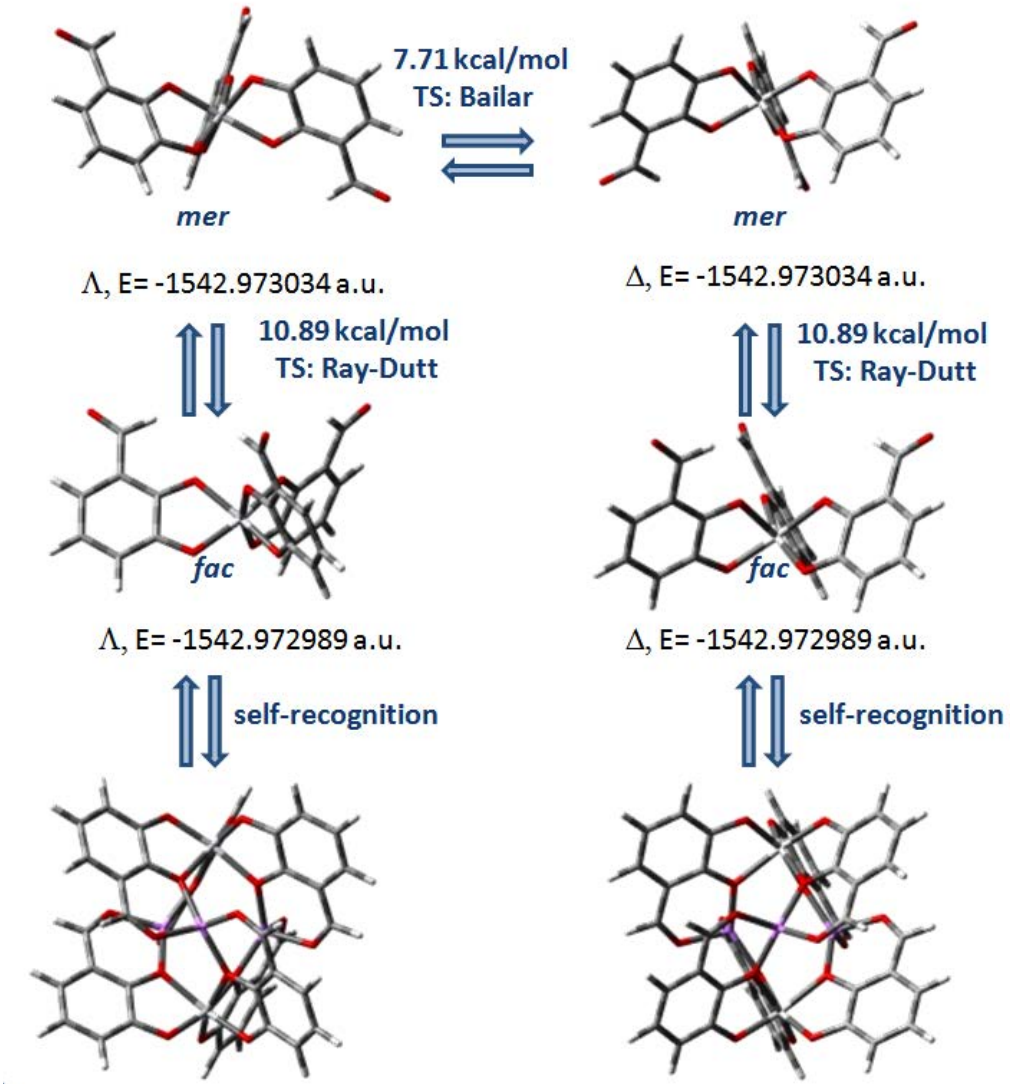

Fig. 68: *Energetically optimized structures of the different compounds involved in the dimerization of the monomer; method: cam-B3LYP/TZVP.*

Two different geometries for the transition states are possible: the "Bailar-Twist"- and the "Ray-Dutt"- transition (Figure 69). The "Ray-Dutt"- transition requires an octahedral complex with three bidentate chelating groups. The energy maximum of the corresponding reaction pathway has C_{2v} symmetry. In contrast to this, the "Bailar-Twist"- transition state involves the formation of an intermediate with a D_{3h} symmetry.

The "Bailar-Twist"- transition state is important for the conversion of the Λ into the Δ form and vice versa. The transition state is located 7.71 kcal/mol above the ground state. The transition between the *mer* and *fac* form can occur only via a "Ray-Dutt"- transition state, as one of the ligands has to turn around completely. Therefore, the transition state between the *mer* and *fac* isomer requires more energy than the conversion from the Λ into the Δ form.

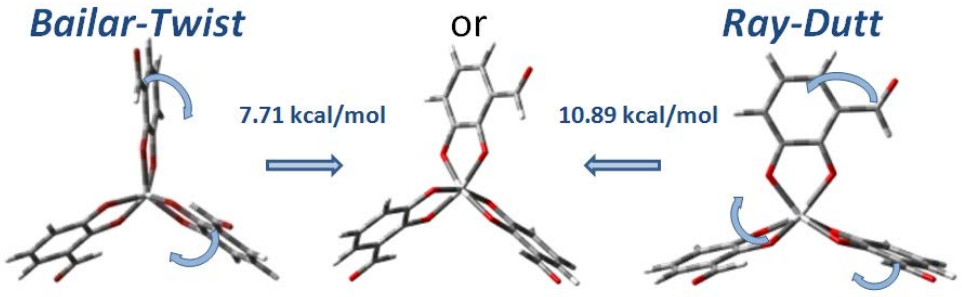

Fig. 69: *Energetically optimized structures of the two possible transition states "Bailar-Twist" and "Ray-Dutt"; method: cam-B3LYP/TZVP.*

The mechanistic study of the recognition path demonstrates, how the dimer is formed. Both transitions, Λ into Δ as well as *mer* into *fac* require energy. The energy gain of the dimerization (-1.05 a.u.) is more than sufficient to compensate this. Further studies have to be performed in order to analyze the influence of more complex ligands.

3.4 TD-DFT studies of Triscatecholate-Based Complexes

3.4.1 TD-DFT studies of the model compound

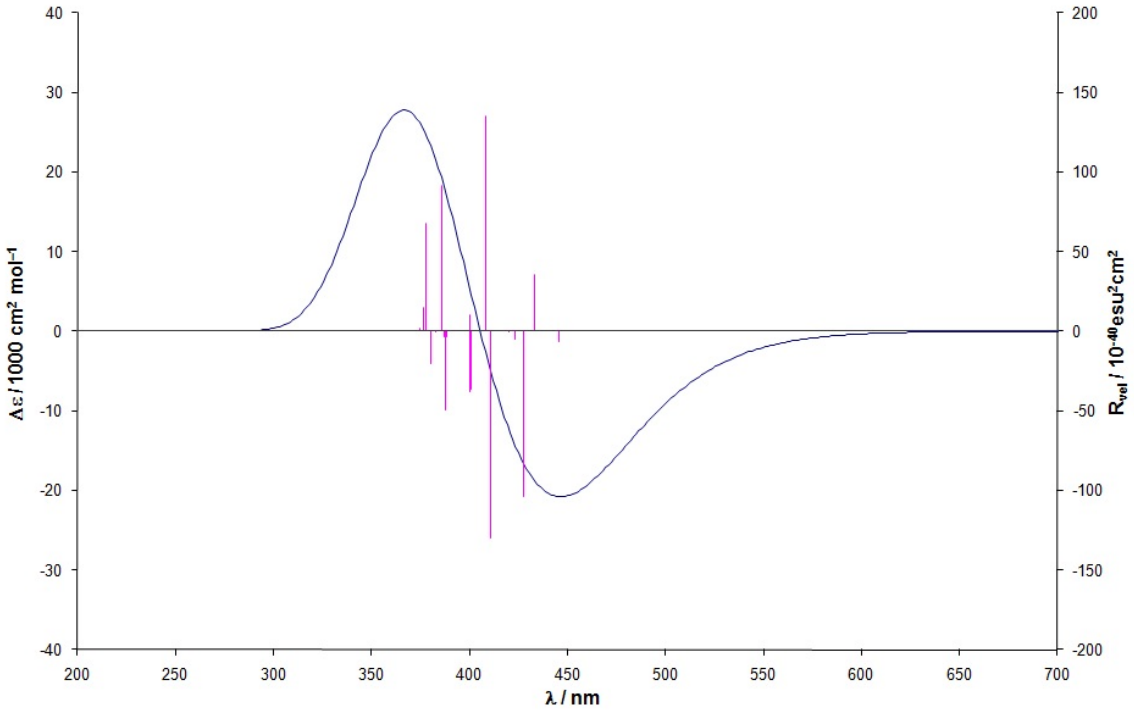

Fig. 70: *CD spectrum of complex $[(\mathbf{5})_3 Ti]^{-2}$ in the ΔΔ form with the corresponding rotational strengths; method: TDDFT/B3LYP/TZVP//cam-B3LYP/TZVP.*

The studies presented before, reveal the mechanism of the formation of the dimer. As the dimeric complexes have either a ΔΔ or a ΛΛ configuration, chiroptical methods

are employed to analyze the complex. CD spectroscopy in combination with TD-DFT calculations can reveal, which configuration is formed, because this method allows the comparison of the measured spectra with the one calculated on the basis of a certain stereochemistry.

To study the CD spectra of the model compound in more detail, TD-DFT calculations on $[(\mathbf{5})_3\mathrm{Ti}]^{2-}$ were performed on the B3LYP/TZVP level of theory. The resulting spectrum shows one maximum at 360 nm and one minimum at 450 nm (Figure 70).

Table 12 lists the most important rotational strength. The nodal properties of the MOs are visualized in Figure 71. The HOMO Ψ227 has local π-symmetry at the aromatic parts and also includes n-orbitals of the O-atoms. The LUMO Ψ228 has local $\pi*$ character at the ligands but also involves the metal center.

wavelength	transitions	rotational strength	kind
410.78	227 → 231	−128.5266	n,$\pi \rightarrow \sigma^*$
410.56	227 → 232	−129.8240	n,$\pi \rightarrow \sigma^*$,π^*
408.26	226 → 231	135.4660	n,$\pi \rightarrow \sigma^*$
408.07	226 → 232	133.3503	n,$\pi \rightarrow \sigma^*$

Table 12: *The four excited states of $[(\mathbf{5})_3 Ti]^{-2}$ with the highest rotational strength, their major components, and calculated rotational strength.*

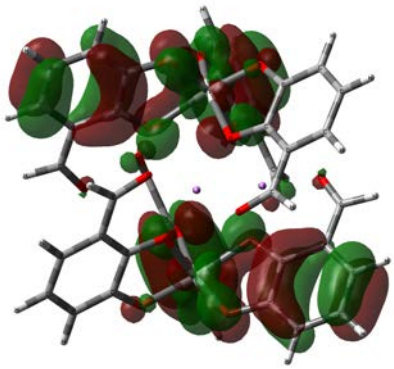

Ψ223

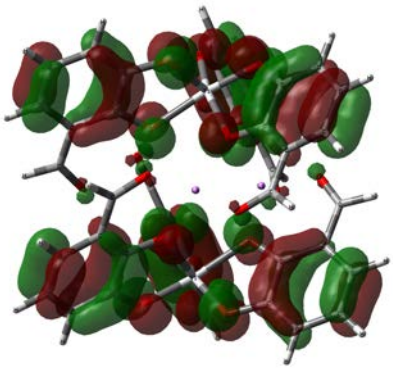

Ψ226

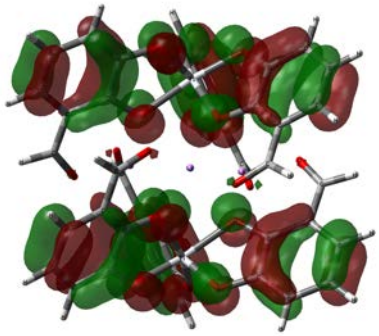

Ψ227

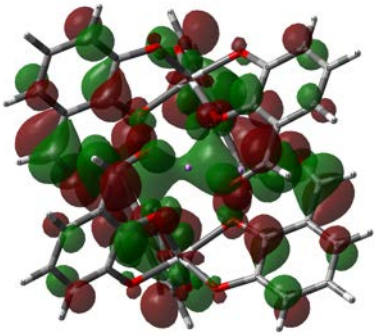

Ψ228

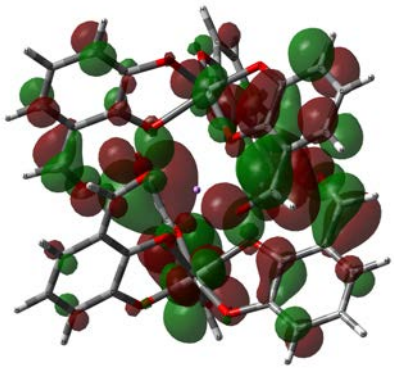

Ψ231

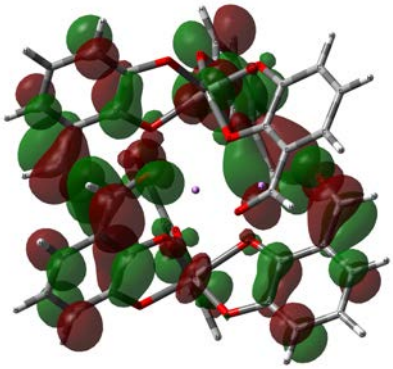

Ψ232

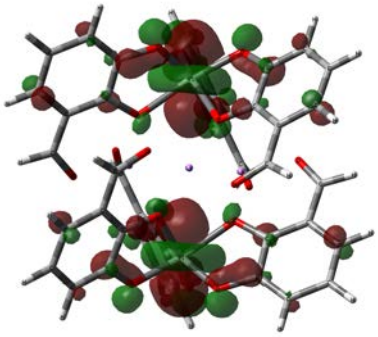

Ψ234

Fig. 71: *Selected Kohn-Sham orbitals of* $[(\mathbf{5})_3 Ti]^{-2}$*, HOMO: Ψ227, LUMO: Ψ228.*

3.4.2 Influence of Different Stereogenic Centers

In order to further elucidate the phenomenon of dimerization, complexes with spatially more demanding ligands were studied. They all have different stereogenic centers in different positions (α, β and γ) (Figure 72). The structures of the resulting complexes were energetically optimized and CD spectra were calculated. This study gives an insight into the influence of the modified rest of the ligand on the behavior of the complex.[84]

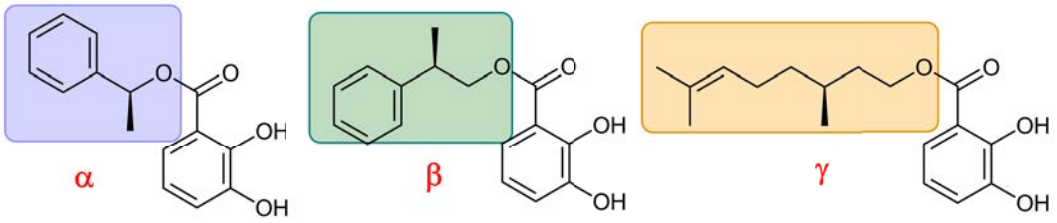

Fig. 72: *Examples for the complexes with stereogenic centers in α, β and γ position.*

The optimization of the complexes was performed at the cam-B3LYP/TZVP level of theory, where each structure was optimized in its Δ and Λ form respectively. The subsequent TD-DFT calculations were carried out with B3LYP as functional and TZVP as basis set.

- **γ-position**

The ligand with the stereogenic center in the γ-position has the largest distance of the stereo center to the metal within this study. The computational study and CD measurements can reveal, whether the stereogenic center has an influence on the rest of the complex despite of its distance from the metal center. As an example for such a complex we chose $Li_2[(\mathbf{6})_3Ti]$ with *(S)*(−)-β-citronellol (Figure 73).

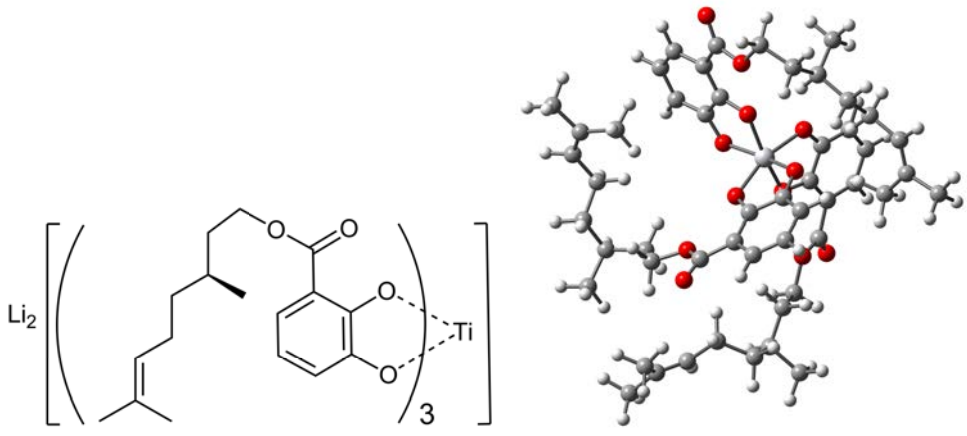

Fig. 73: *Complex $Li_2[(\mathbf{6})_3Ti]$ with (S)(−)-β-citronellol, calculated structure of $[(\mathbf{6})_3Ti]^{-2}$: Δ-form; method: cam-B3LYP/TZVP.*

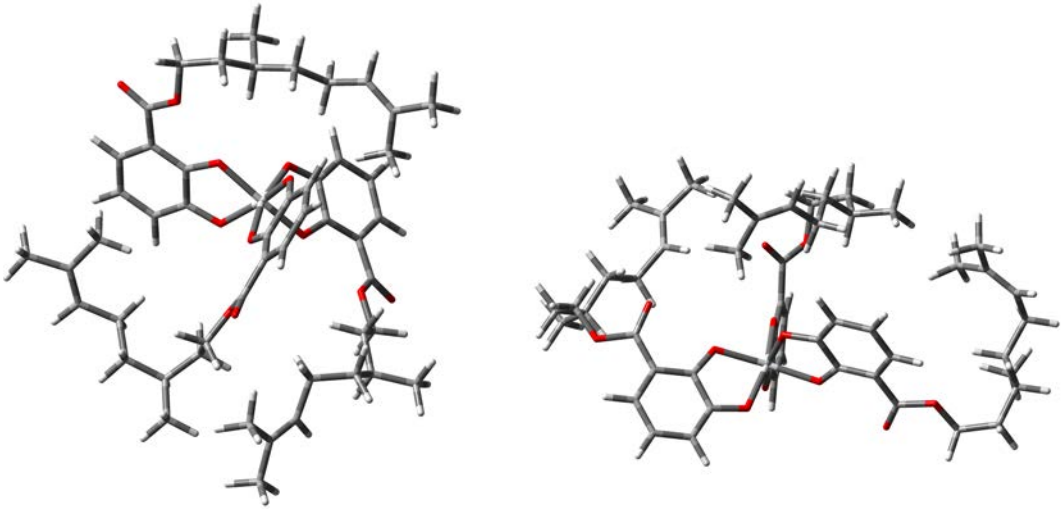

Fig. 74: *Optimized geometry of the Δ and Λ form of complex [(**6**)$_3$Ti]$^{2-}$; method: cam-B3LYP/TZVP.*

The optimized structures of the Δ and the Λ form have significantly different energies: −2944.073484 a.u. for Λ and −2944.094236 a.u. for Δ, and the energy difference is 13.02 kcal/mol in favor of the Δ form. This rather large difference is due to severe geometrical differences between the two forms (Figure 74). The Λ form is more "compact" than the Δ form causing stronger intramolecular repulsion.

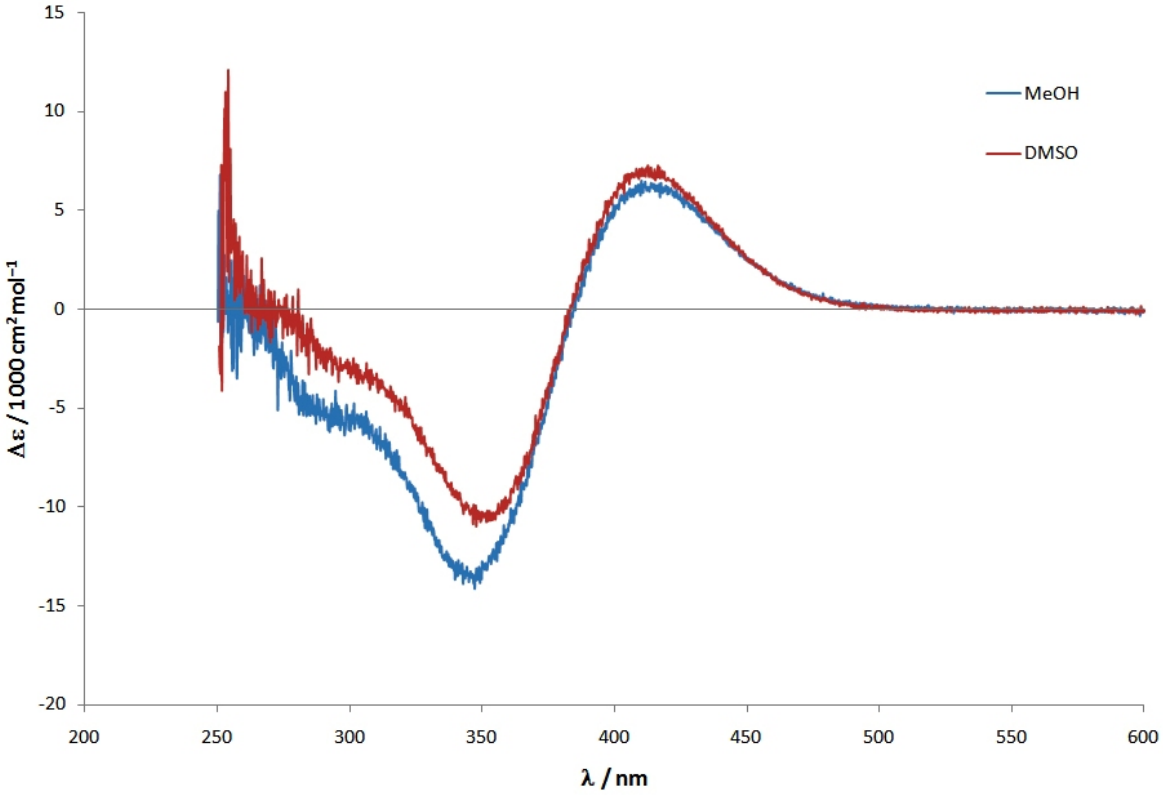

Fig. 75: *Measured CD-spectrum of Li$_2$[(**6**)$_3$Ti] in MeOH and DMSO.*

The measured CD spectrum (Figure 75) of Li$_2$[(**6**)$_3$Ti] shows one negative and one

positive Cotton effect. The maximum is found at 415 nm and the minimum at 350 nm. The difference between the spectra measured in DMSO (red) and in MeOH (blue) is very small. Only the intensity of the negative bands is significantly different for the two spectra.

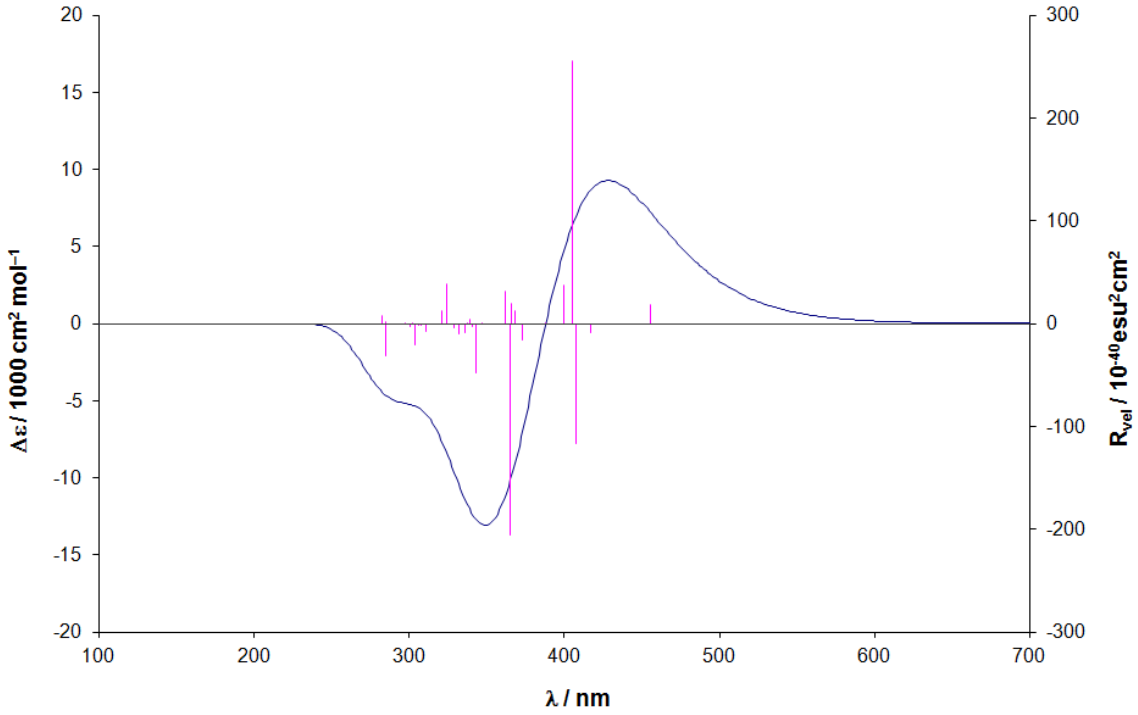

Fig. 76: *Calculated CD spectra of complex [(**6**)$_3$Ti]$^{2-}$, Λ form, red: rotational strengths; method: TDDFT/B3LYP/TZVP//cam-B3LYP/TZVP.*

The calculated CD spectrum of Λ-[(**6**)$_3$Ti]$^{2-}$ is consistent with those measured in DMSO and MeOH. The minimum of the calculated spectrum is located at 349 nm and the maximum at 430 nm. The shoulder of the curve found in the measured spectrum is reproduced in the calculated spectrum as well. The conclusion is that the molecule prefers the Λ form in the chosen solvents.

wavelength	transitions	rotational strength
407.94	240 → 245	−116.9181
405.35	241 → 244	256.1164
365.40	240 → 244	−205.9776
324.05	239 → 247	38.3266
303.73	239 → 251	−21.2295

Table 13: *The most important excited states of [(**6**)$_3$Ti]$^{2-}$ with the corresponding rotational strengths, their major components.*

The calculated rotational strengths underline the match with the measured spectra as the rotational strengths causing the shoulder can be found at 285 and 304 nm (Table 13). The corresponding MOs are presented in Figure 77 and in Figure 78. The LUMO

has the largest coefficient at the chiral part of the ligand. The MO's included in the state that cause the shoulder of the spectrum are Ψ 239 and Ψ 251. It is a transition from the catecholate part of the ligand to the external parts of the ligand.

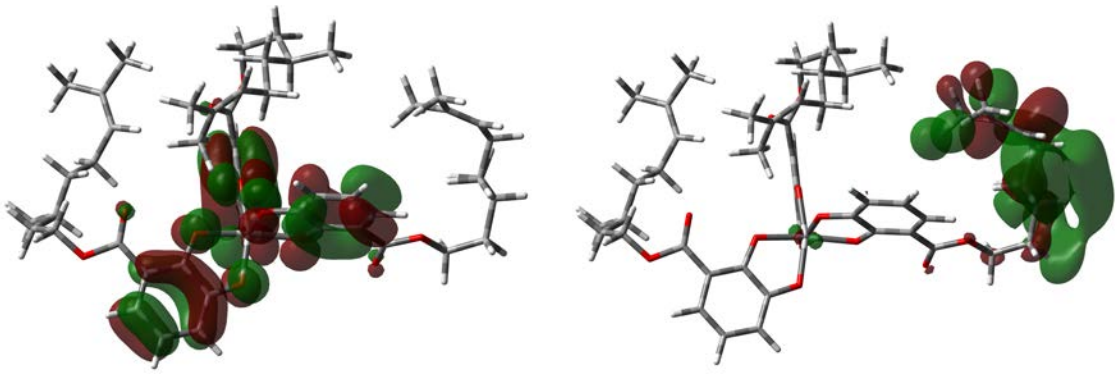

Fig. 77: *HOMO (Ψ=241) and LUMO (Ψ=242) of complex* $[(\mathbf{6})_3 Ti]^{2-}$.

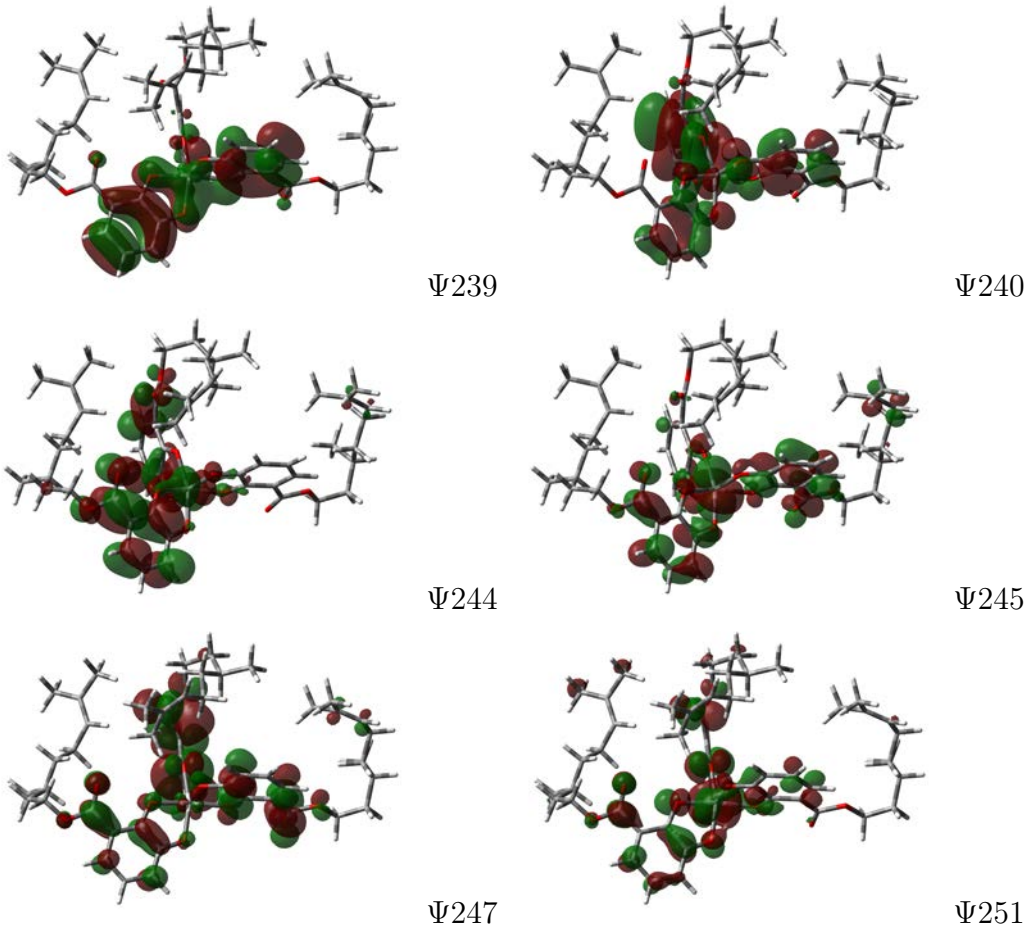

Fig. 78: *Selected Kohn-Sham orbitals of complex* $[(\mathbf{6})_3 Ti]^{2-}$.

- **β-position**

Further calculations were performed on compounds where the stereogenic center is located at the β-position instead of the γ-position. This modification might have an influence on the behaviour of the complex, as the stereogenic center is closer to the metal center. An example for such a compound is the complex $Li_2[(\mathbf{7})_3Ti]$ with *(S)*-(−)-2-methyl-1-butanol as side chain (Figure 79).

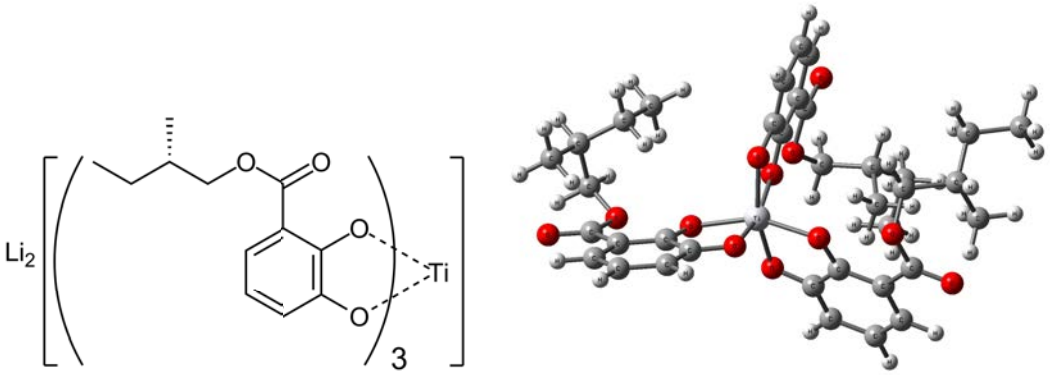

Fig. 79: *Complex $Li_2[(\mathbf{7})_3Ti]$ with (S)-(−)-2-methyl-1-butanol, calculated structure: Δ-form; method: cam-B3LYP/TZVP.*

The structures of the Δ and the Λ forms were energetically optimized. Among the monomers, the complex in its Δ form is more stable:
Total energies of −2358.242181 a.u. for Λ and −2358.243125 a.u. for Δ were obtained, resulting in a small energy difference of 0.59 kcal/mol (Figure 80).

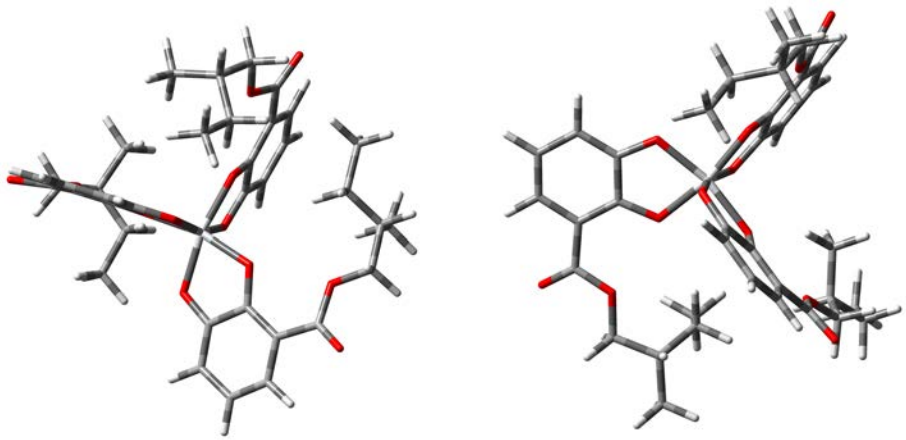

Fig. 80: *Optimized geometry of the Δ and Λ form of complex $[(\mathbf{7})_3Ti]^{2-}$; method: cam-B3LYP/TZVP.*

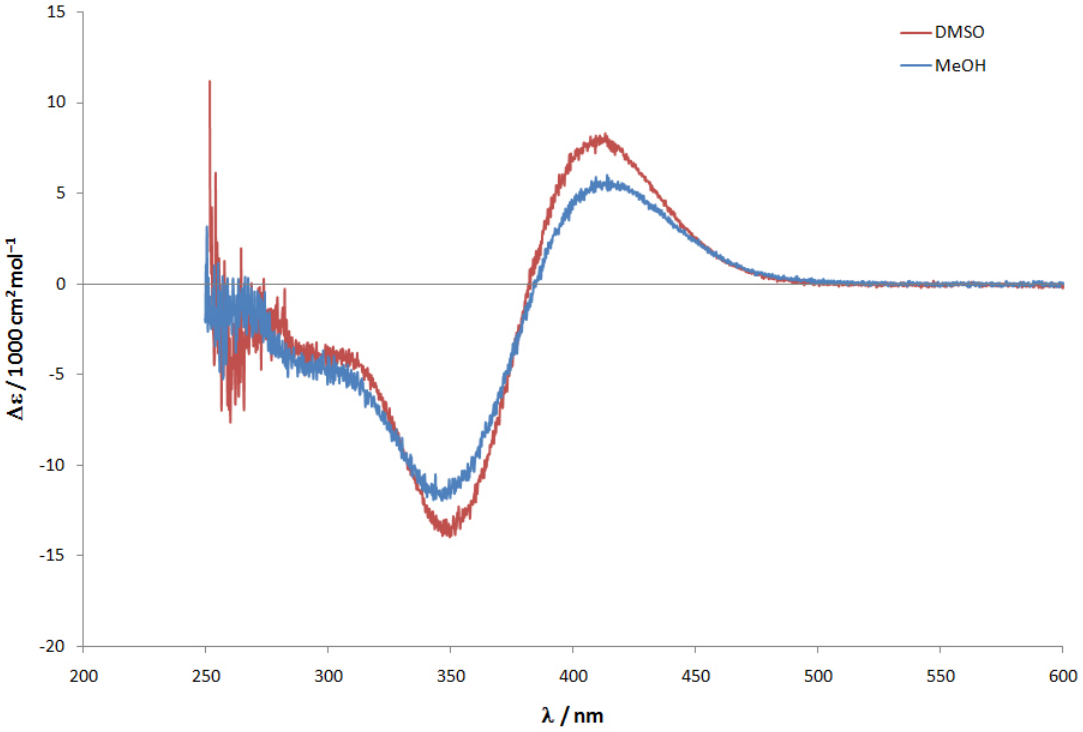

Fig. 81: *Measured CD-spectrum of $Li_2[(\mathbf{7})_3Ti]$ in MeOH and DMSO.*

The CD-spectra of $Li_2[(\mathbf{7})_3Ti]$ measured in MeOH and DMSO nearly coincide (Figure 81). In DMSO and in MeOH the minima occur at the same wavelength (352 nm). The maximum in MeOH is at 411 nm and in DMSO at 406 nm, corresponding to a red shift of 5 nm in DMSO.

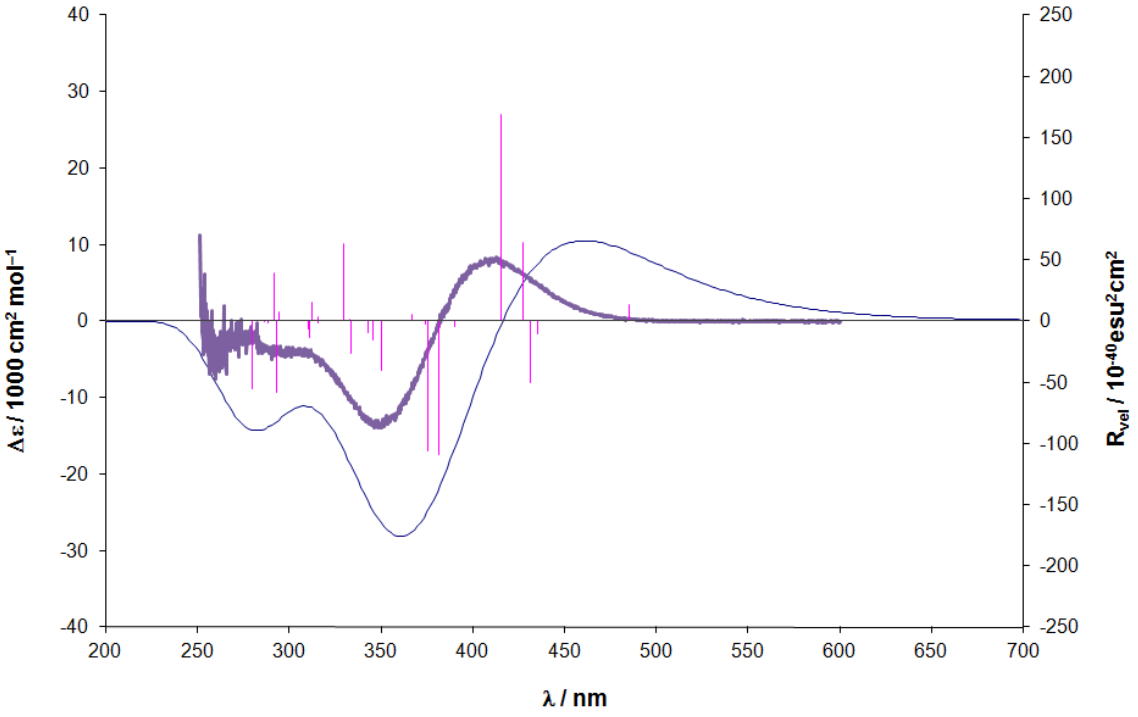

Fig. 82: *Comparison of the calculated and measured CD spectra of $Li_2[(\mathbf{7})_3Ti]$, Λ form; method: TDDFT/B3LYP/TZVP//cam-B3LYP/TZVP.*

Comparison of the calculated and measured CD spectra of complex $Li_2[(\mathbf{7})_3Ti]$ shows that the complex adopts the Λ form in MeOH as well as in DMSO.

wavelength	transitions	rotational strength
485.53	184 → 185	13.0110
415.51	184 → 187	168.7286
381.38	182 → 186	−109.0683
375.80	183 → 187	−106.1079

Table 14: *The most important excited states of $[(\mathbf{7})_3Ti]^{2-}$ with the corresponding rotational strengths, their major components.*

The transition between the HOMO and the LUMO takes place between the π-system of the ligand and the metal center. The state to which this transition contributes significantly occurs at a wavelength of 485.53 nm with a rotational strength of 13.0110. The corresponding MOs Ψ=184 and Ψ=185 are shown in Figure 83.

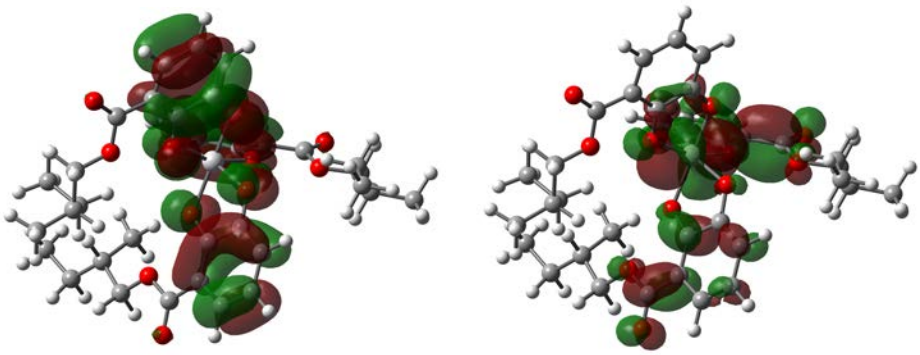

Fig. 83: *HOMO (Ψ=184) and LUMO (Ψ=185) of complex $[(\mathbf{7})_3Ti]^{2-}$.*

Another example for a compound with a stereogenic center in the β-position is $Li_2[(\mathbf{9})_3Ti]$ with the ligand containing *(S)*-(−)-2-phenylpropan-1-ol (Figure 84). The difference between the two complexes with the stereogenic center in the β-position is the size of the rest. The phenyl rest is bigger than the ethyl group, which also is more flexible. The spatially more demanding ligand might have an influence on the geometrical structure of the complex.

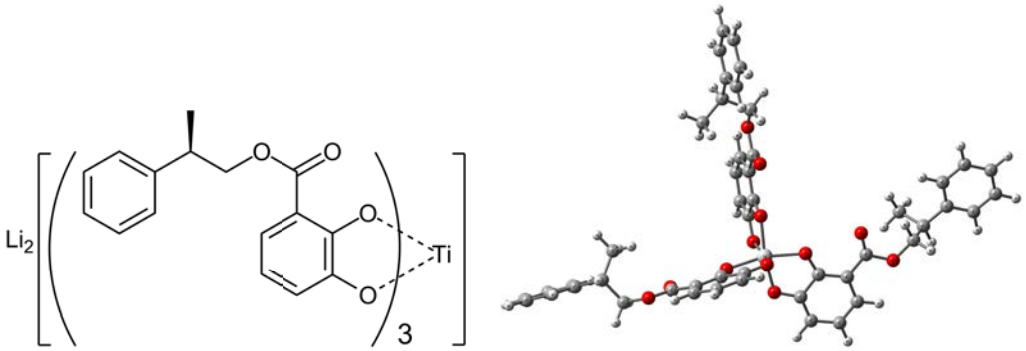

Fig. 84: *Complex $Li_2[(\mathbf{8})_3 Ti]$ with (S)-(−)-2-phenylpropan-1-ol, calculated structure: Δ-form.*

Calculations on the structures of the Δ and the Λ forms lead to the following total energies: −2815.408025 a.u. for Λ and −2815.407325 a.u. for Δ. Again, the result is a very small energy difference of 0.44 kcal/mol (Figure 85) in favor of the Λ form. This might be due to the different orientations of the phenyl groups, which are closer to the periphery within the Λ form.

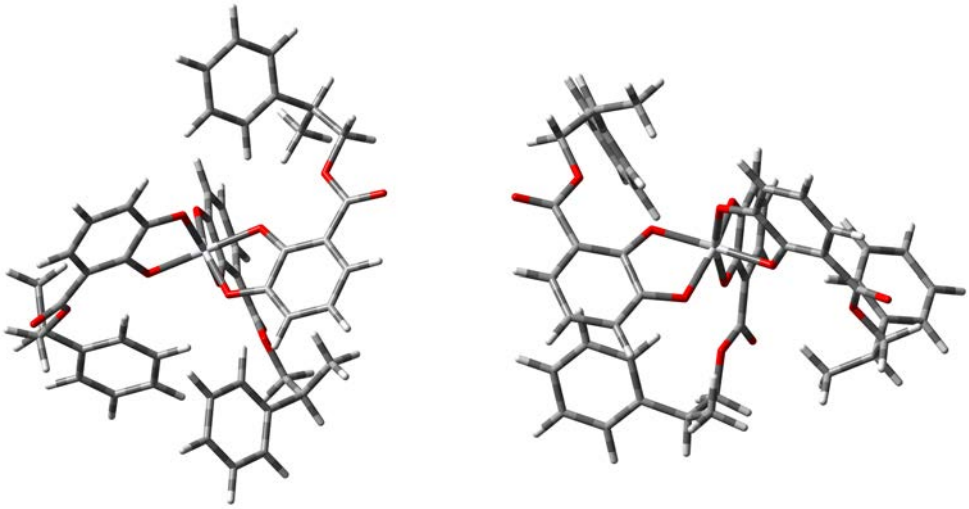

Fig. 85: *Optimized geometry of the Δ (left) and Λ (right) form of complex $[(\mathbf{8})_3 Ti]^{2-}$; method: cam-B3LYP/TZVP.*

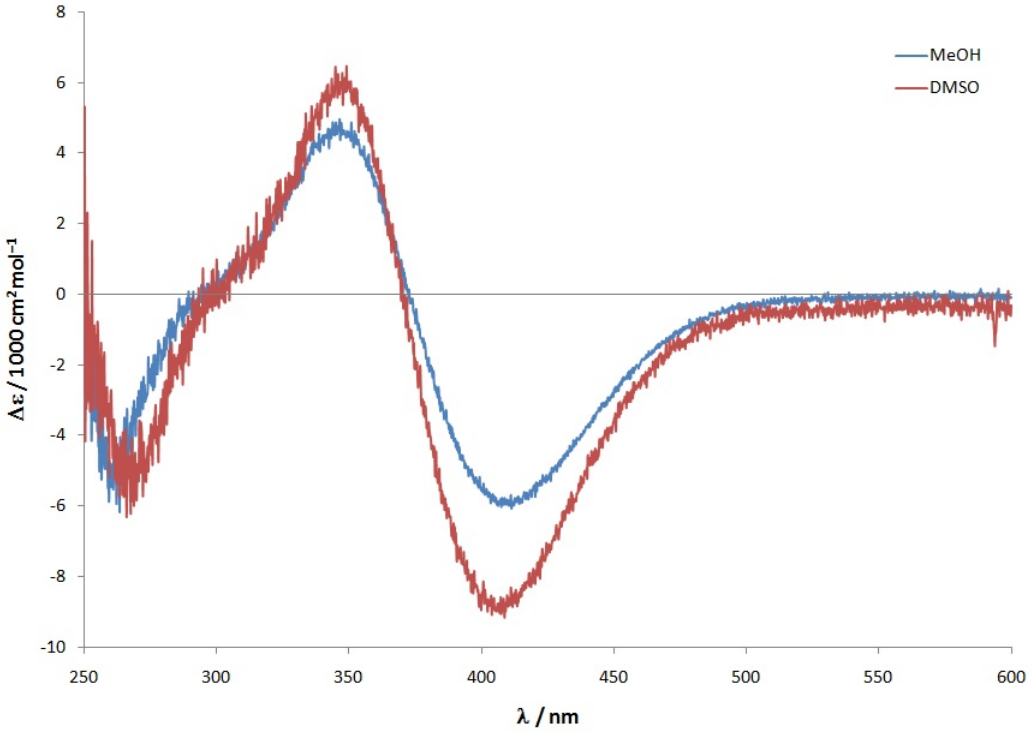

Fig. 86: *Measured CD-spectrum of $Li_2[(\mathbf{8})_3Ti]$ in MeOH and DMSO.*

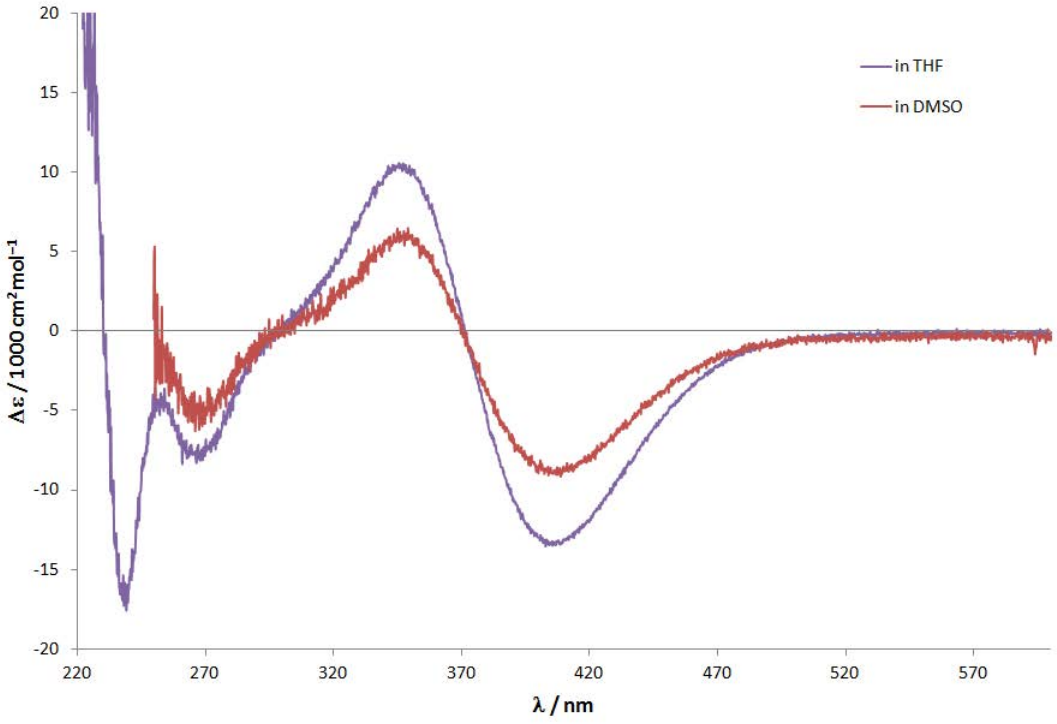

Fig. 87: *Measured CD-spectrum of $Li_2[(\mathbf{8})_3Ti]$ in THF and DMSO.*

The measured CD spectra in MeOH and DMSO show two extrema: one maximum and one minimum. The maxima of $Li_2[(\mathbf{8})Ti]$ in MeOH and DMSO occur at the same wavelength (Figure 86). The maxima are located at a wavelength of 345 nm and the

minima at 408 nm. The only difference is the intensity of the Cotton effects of both spectra, where the intensity in DMSO is somewhat higher.

The measured spectrum in THF does not differ significantly from the one in DMSO (Figure 87). This result demonstrates that the influence of the solvents DMSO, MeOH, and THF on the complex is about the same.

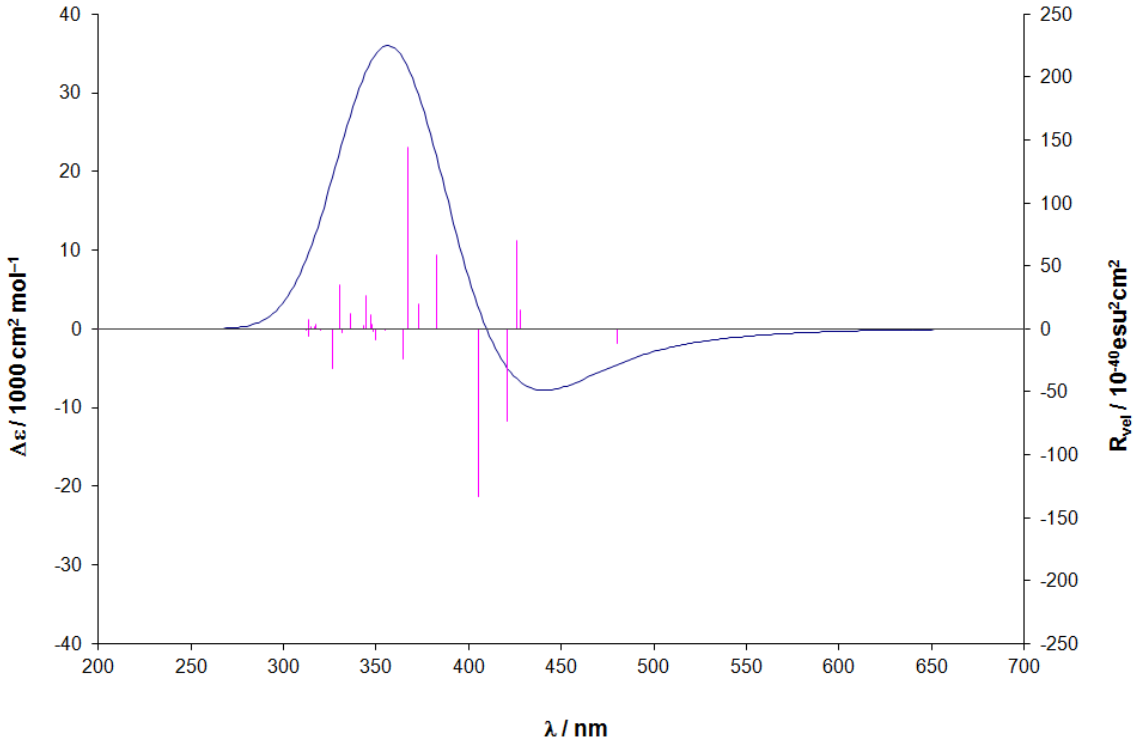

Fig. 88: *Calculated CD spectra of [(**8**)$_3$Ti]$^{2-}$, Δ form, red: rotational strengths; method: TDDFT/B3LYP/TZVP//cam-B3LYP/TZVP.*

The calculated spectrum of $[(\mathbf{8})_3\mathrm{Ti}]^{2-}$ in the Δ form has one positive and one negative Cotton effect. The maximum is found at a lower wavelength (365 nnm) than the minimum which occurs at 440 nm. This corresponds to the maximum of the measured spectrum at 345 nm and the minimum at 408 nm. Compared with the experimental result, the calculated spectrum is shifted to higher wavelengths. The dimer is supposed to be present in these solvents. Therefore, the shift of the calculated spectrum relative to the experimental one might be a result of the calculation on the monomer instead of the dimer. The comparison of calculated and measured spectra clearly shows that the Δ form is most likely present in the solvent.

wavelength	transitions	rotational strength
425.78	219 → 221	70.4923
420.93	218 → 221	−73.4485
405.56	220 → 223	−133.0100
367.34	219 → 223	144.7563

Table 15: *The most important excited states of $[(\mathbf{8})_3Ti]^{2-}$ with the corresponding rotational strengths and their major components.*

- **α-position**

The third possibility regarding the position of the stereogenic center is the closest one to the metal center. An example for a compound with such a stereogenic center in the α-position is $Li_2[(\mathbf{9})Ti]$ with (*S*)-(−)-1-phenylethanol (Figure 89). All complexes measured before have Li^+ as a counter ion. To study the influence of the cations on the complex, Na^+ and K^+ were chosen in this case. Complex $Na_2[(\mathbf{9})Ti]$ is the first one to be studied.

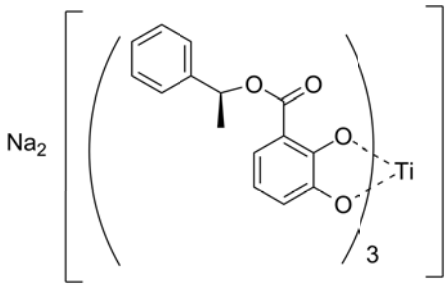

Fig. 89: *Complex $Na_2[(\mathbf{9}_3)Ti]$ with (S)-(−)-1-phenylethanol.*

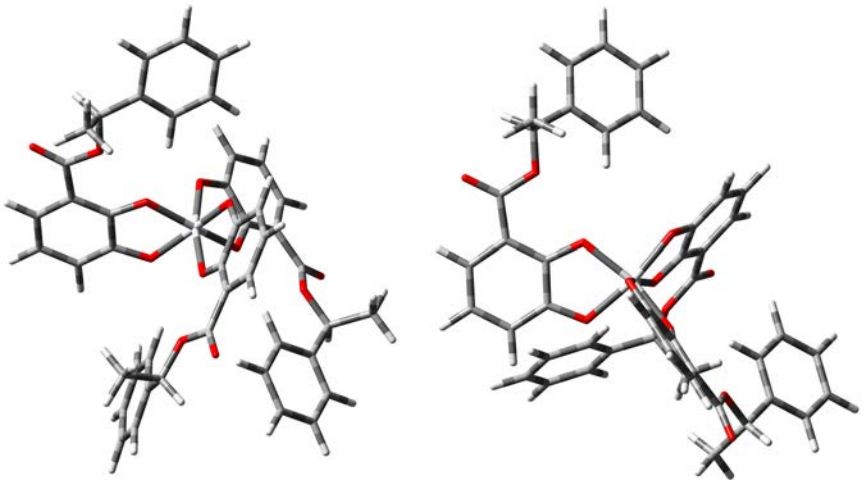

Fig. 90: *Optimized geometry of the Δ and Λ form of complex $[(\mathbf{9})_3Ti]^{2-}$; method: cam-B3LYP/TZVP.*

The structures of the Δ and the Λ form were energetically optimized. The energy for the Λ form is −2697.506206 a.u. and −2697.506284 a.u for the Δ complex, which results

in an extremely small and, therefore, insignificant energy difference of 0.05 kcal/mol (Figure 90).

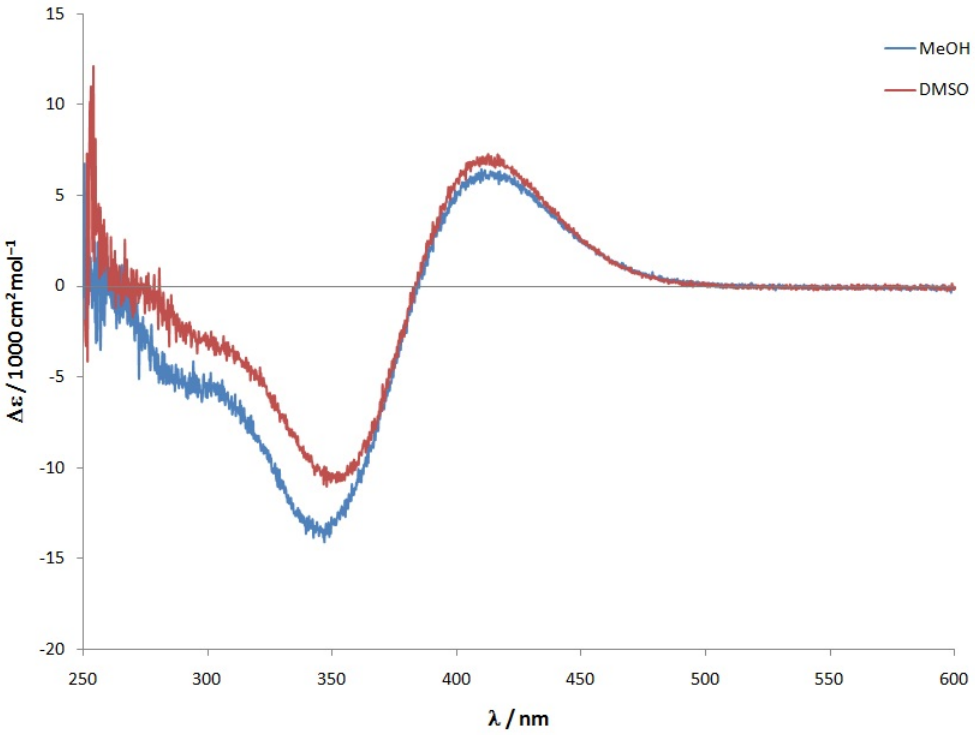

Fig. 91: *Measured CD-spectra of $Na_2[(\mathbf{9})_3Ti]$ in MeOH and DMSO.*

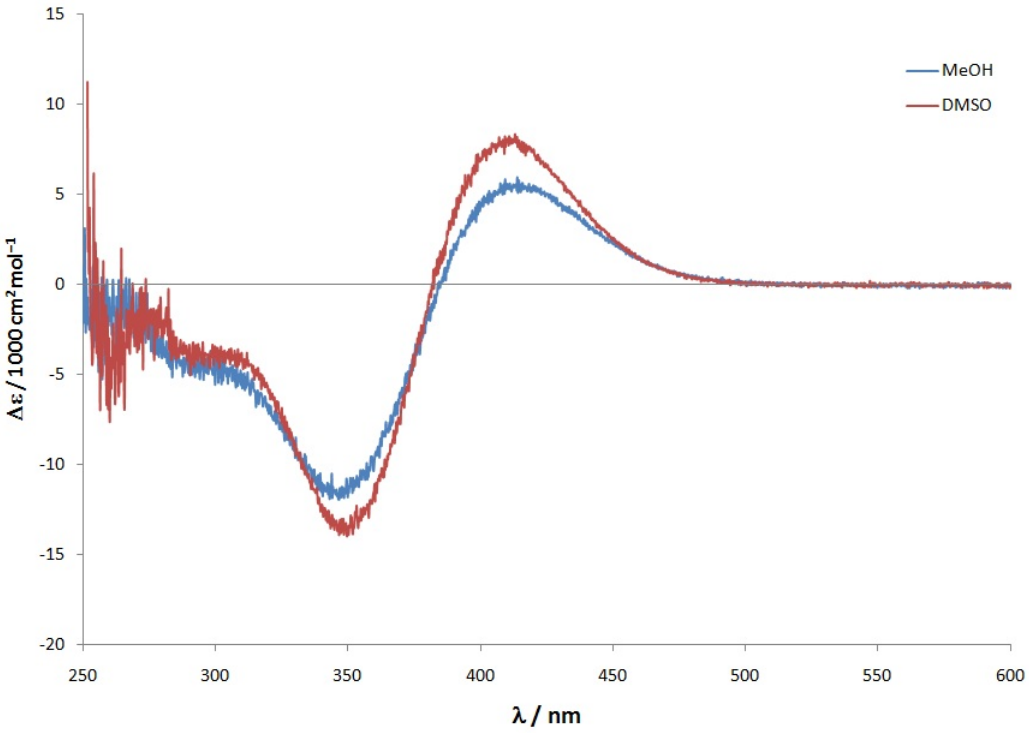

Fig. 92: *Measured CD-spectra of $[K_2(\mathbf{9})_3Ti]$ in MeOH and DMSO.*

Like in the previous cases the spectrum shows two extrema. The minima of the

measured spectrum of $Na_2[(\mathbf{9})_3Ti]$ occur at 348 nm in MeOH and at 350 nm in DMSO. The maxima were found at 414 nm in both solvents (Figure 91).

The minima of the measured spectrum of $[K_2(\mathbf{9})_3Ti]$ occur at 350 nm in both solvents, while the maximum in MeOH is at 416 nm and in DMSO at 414 nm (Figure 92). Both complexes **9** with K^+ and with Na^+ lead to qualitatively similar spectra as can be seen in the two Figures 91 and 92. However, replacement of the Na^+ by K^+ results in a reversal of the relative intensities of the CD curves measured in MeOH and DMSO at about 350 nm.

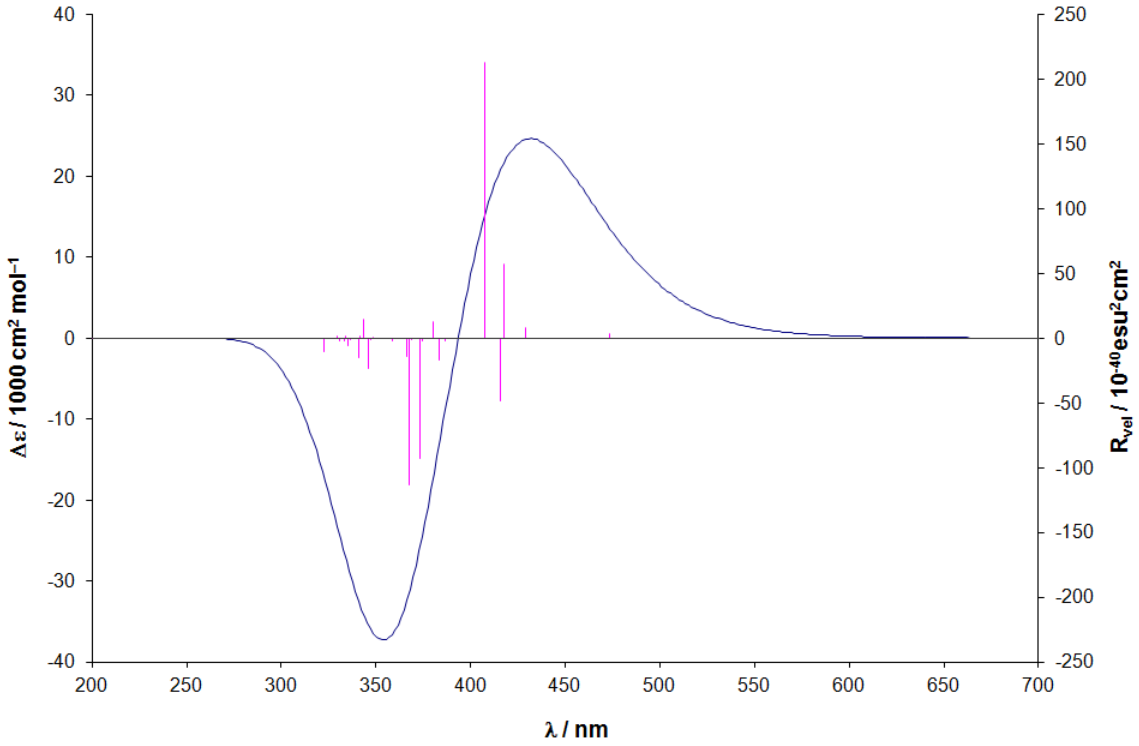

Fig. 93: *Calculated CD spectrum of $[(\mathbf{9})_3Ti]^{2-}$, Λ form, red: rotational strengths; method: TDDFT/B3LYP/TZVP//cam-B3LYP/TZVP.*

The calculated CD spectrum of $[(\mathbf{9})_3Ti]^{2-}$ in the Λ form results in Cotton effects of the same sign like the measured CD spectra with K^+ and Na^+. The minimum is located at 353 nm and the maximum at 430 nm, which corresponds to the measured minimum at 348 nm (in MeOH) and the maximum at 414 nm. Only a small shift to a higher wavelength can be noted. The optimization of the monomer indicates that the Δ form is energetically favored. As the calculation omitted the solvent effects, the monomer can adopt different conformations. Additionally, as mentioned previously the calculated energy difference is very small, which indicates that the two forms can easily switch.

wavelength	transitions	rotational strength
417.93	207 → 209	56.8748
407.36	208 → 210	212.8942
	208 → 214	
373.42	206 → 209	−92.6459
	207 → 210	
367.33	206 → 210	−113.1989

Table 16: *The most important excited states of $[(\mathbf{9})_3Ti]^{2-}$ with the corresponding rotational strengths and their major components.*

In an additional study the CD spectrum of the complex with Li^+ as a counter ion was measured. The CD spectra with K^+ and Na^+ show no dependence on the solvent. The comparison with the calculated CD spectrum reveals that the Λ form is preferred with these counter ions. Li^+ is supposed to form a dimer as it is much smaller than the other ions.

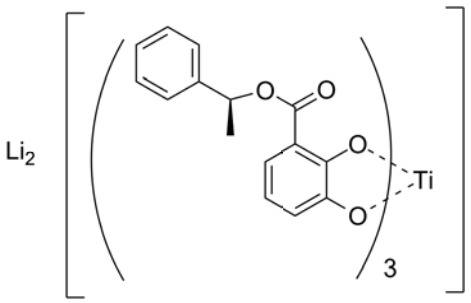

Fig. 94: *Complex $Li_2[(\mathbf{9})_3Ti]$ with (S)-(−)-1-phenylethanol.*

With lithium instead of potassium or sodium, the complex $M_2[(\mathbf{9})_3Ti]$ shows a configurational reversal at the metal center depending on the solvent.

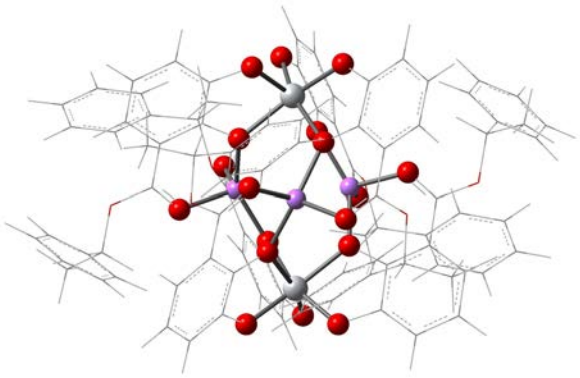

Fig. 95: *Layer view of the optimized geometry of $Li_3[(\mathbf{9})_3Ti]_2$ in dimer form, red: O, white: Ti, purple: Li; method: cam-B3LYP/TZVP.*

Figure 95 shows the octahedral coordination of the Ti(IV) atoms and the tetrahedral coordination of Li^+.

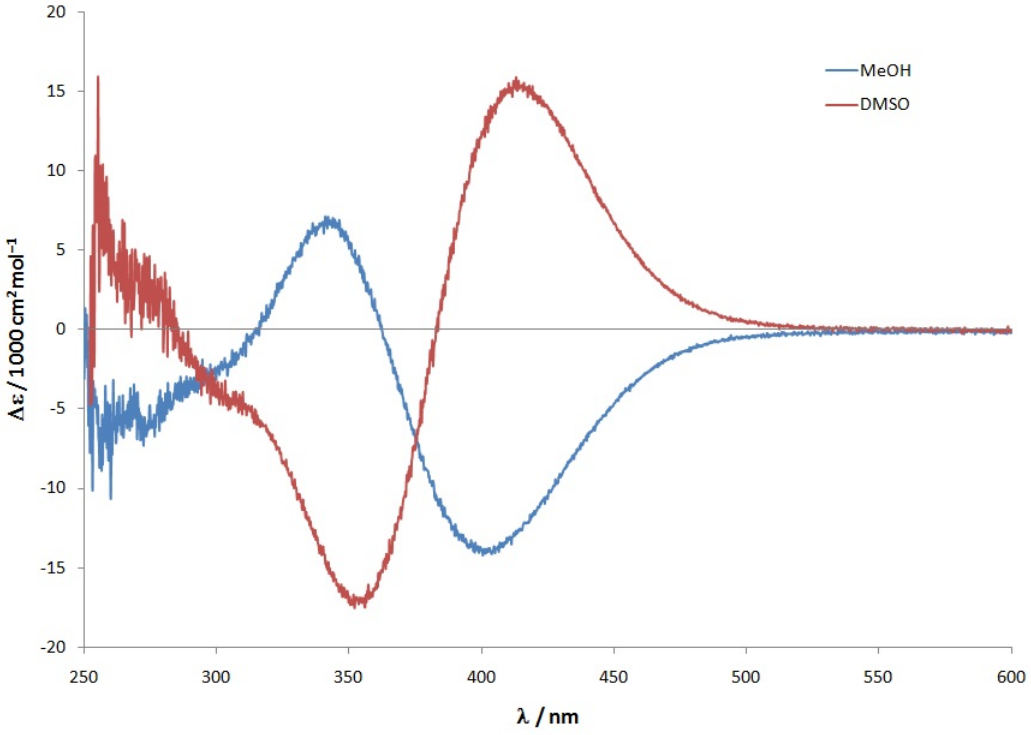

Fig. 96: *Measured CD-spectrum of $Li_2[(\mathbf{9})_3Ti]$ in MeOH and DMSO.*

The different configurations at the metal complexes within the monomer and the dimer are due to different sterical aspects. As mentioned before, the energetically optimized Δ and Λ forms of the monomer result in different energies, but the energy difference is very small (0.05 kcal/mol). Figure 97 shows the different sterical demands of the phenyl rings within both forms.

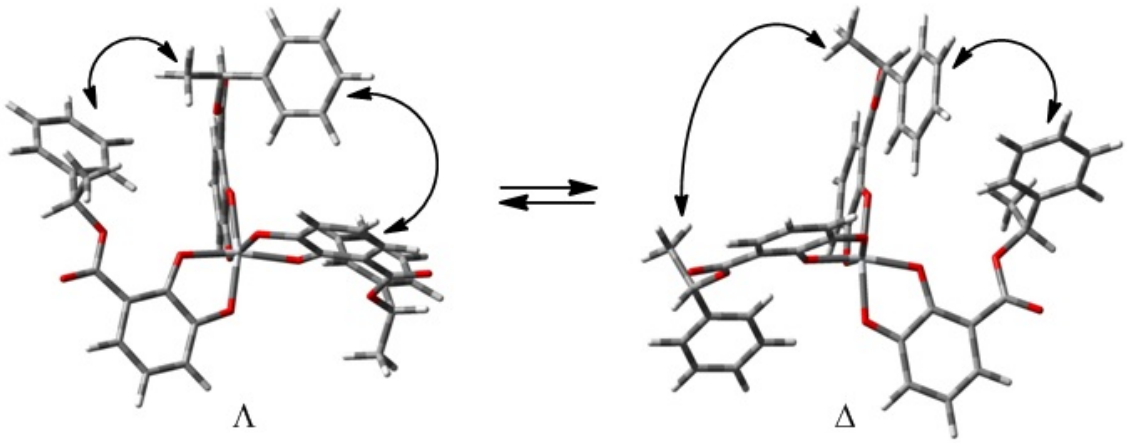

Fig. 97: *Complex $Li_2[(\mathbf{9})_3Ti]$, equilibrium of the isomers.*

The phenyl groups of the Δ form are 4.284 Å apart (smallest C-C distance), which is a quite large distance for π-π stacking. Moreover, the relative orientation of the aromatic systems is not ideal for an interaction of this type. However, since the closer distance between the phenyl groups in the Δ form does not significantly destabilize

the Δ relative to the Λ form, it is concluded that the relative orientation of the phenyl groups in the Δ complex is electronically favorable. The Λ form does not have very close distances between the ligands either. The smallest distance occurs between a phenyl group and a catecholate part (3.74 Å). The average Ti−O distance is about 1.950 and 1.994 Å, respectively. The distances are presented in Figure 98.

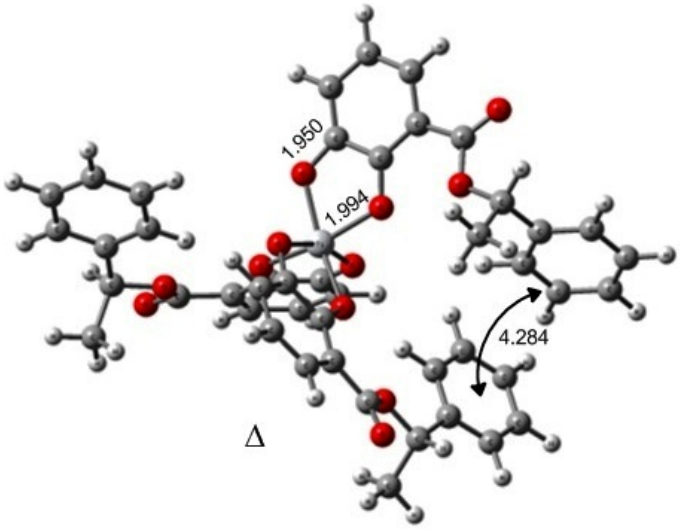

Fig. 98: *Complex Li₂[(9)₃Ti], Δ configuration.*

The optimized geometry of complex $Li_3[(\mathbf{9})_3Ti]_2^-$ results in an approximately C_3-symmetrical structure with only closely packed phenyl groups (Figure 99).

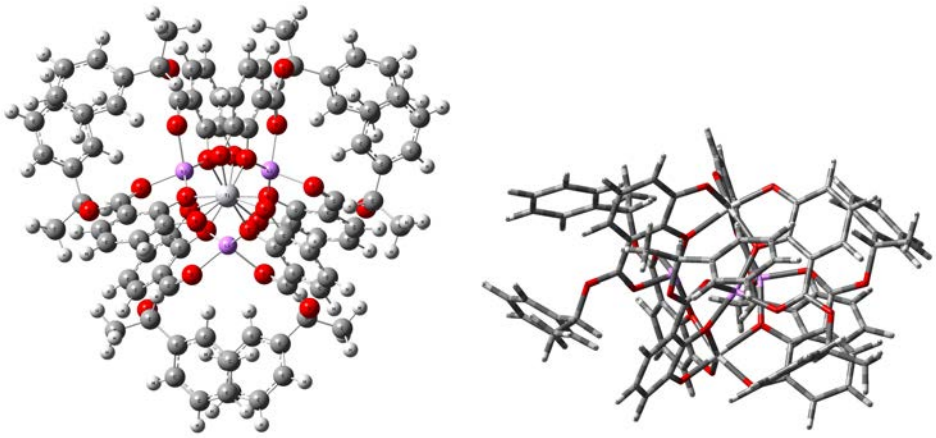

Fig. 99: *Left: optimized geometry of complex $Li_3[(\mathbf{9})_3Ti]_2^-$, right: "tube" form.*

The optimized geometries show that the ester groups are oriented differently in the monomer and the dimer (Figure 100). The coordinated Li^+ ion within the dimer leads to a repulsion between the sterically demanding groups of the ligand. This "switch" of the ester group lead to the difference of the favored form within the monomer (Λ) and the dimer (Δ).

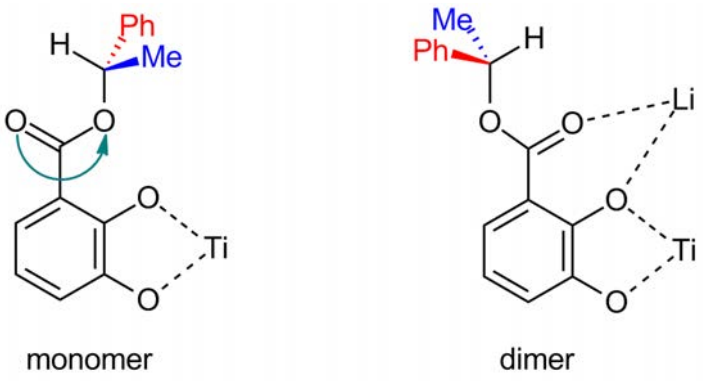

Fig. 100: *Illustration of the "switch" of the ester group within the monomer and the dimer.*

The TD calculation of the CD curve of the monomer ($[(\mathbf{9})_3\mathrm{Ti}]^{2-}$) leads to results close to the spectra measured for $\mathrm{Li}_2[(\mathbf{9})_3\mathrm{Ti}]$. If solvent effects are considered, the curve of the spectrum does not change significantly (Figures 101 and 102).

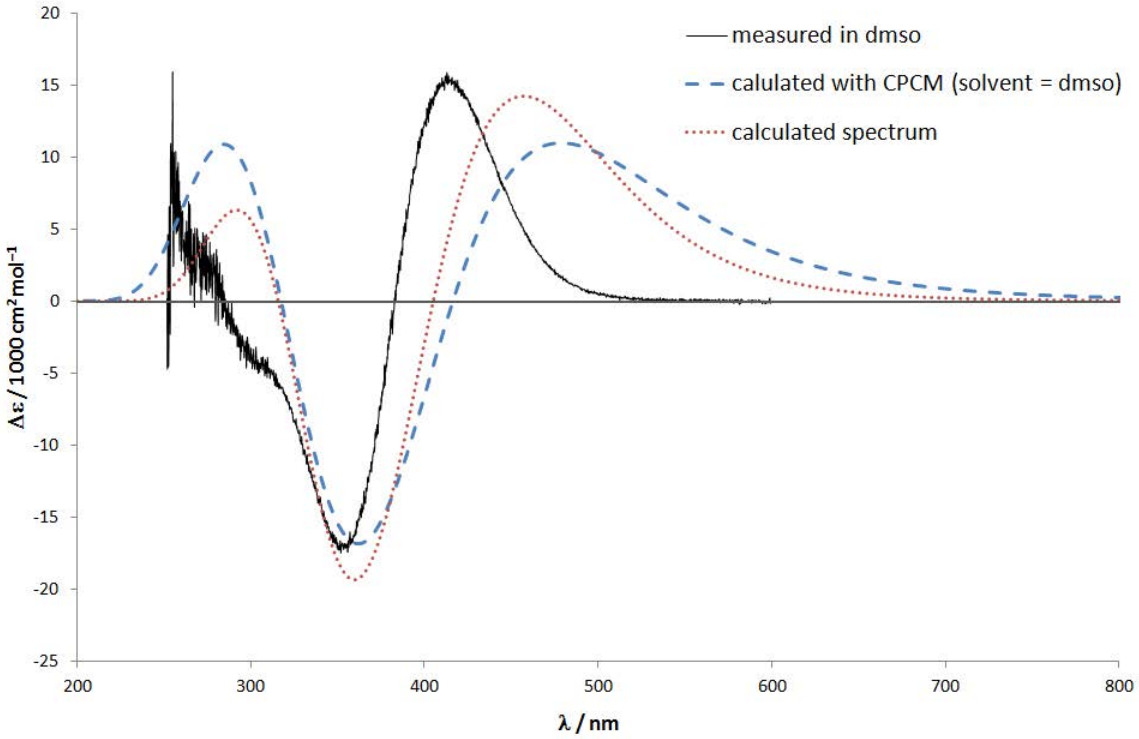

Fig. 101: *Measured spectrum of complex $Li_2[(\mathbf{9})_3Ti]$ in DMSO, the spectra of $[(\mathbf{9})_3Ti]^{-2}$ were calculated with and without the CPCM solvation model, blue: calculation with CPCM, red: calculation in the gas phase; method: TDDFT/B3LYP/TZVP//cam-B3LYP/TZVP.*

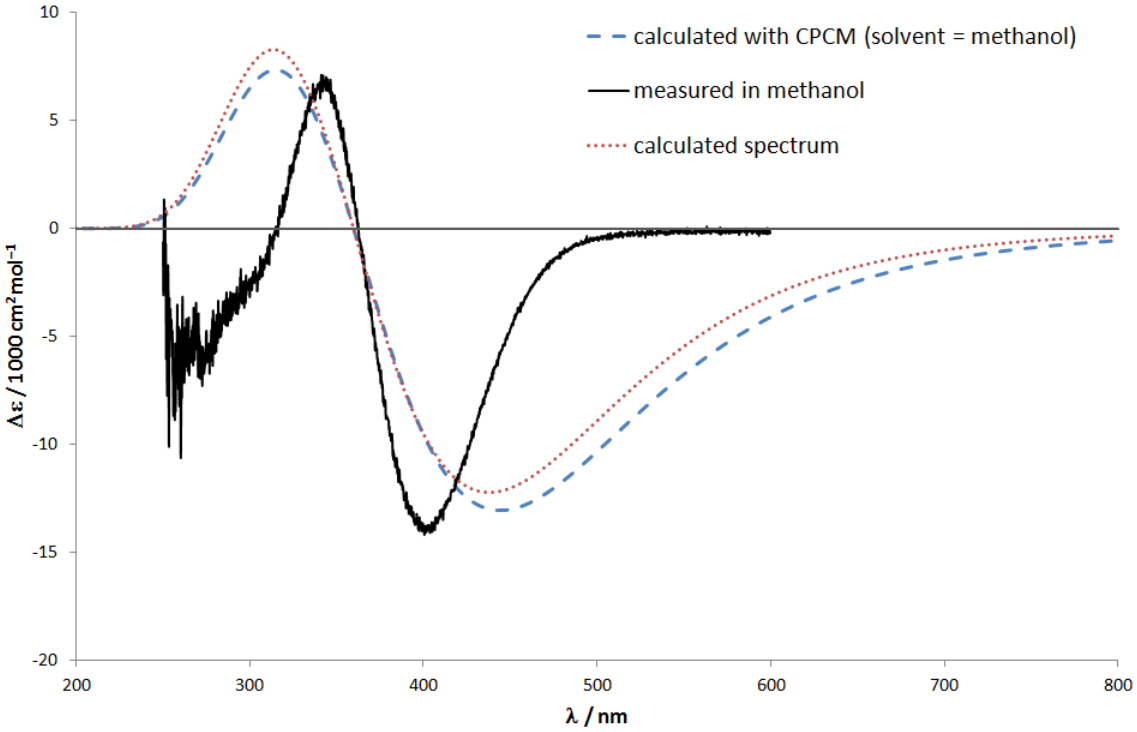

Fig. 102: *Measured spectrum of complex $Li_2[(\mathbf{9})_3Ti]$ in methanol, the spectra of $[(\mathbf{9})_3Ti]^{-2}$ were calculated with and without the CPCM solvation model, blue: calculation with CPCM, red: calculation in the gas phase; method: TDDFT/B3LYP/TZVP//cam-B3LYP/TZVP.*

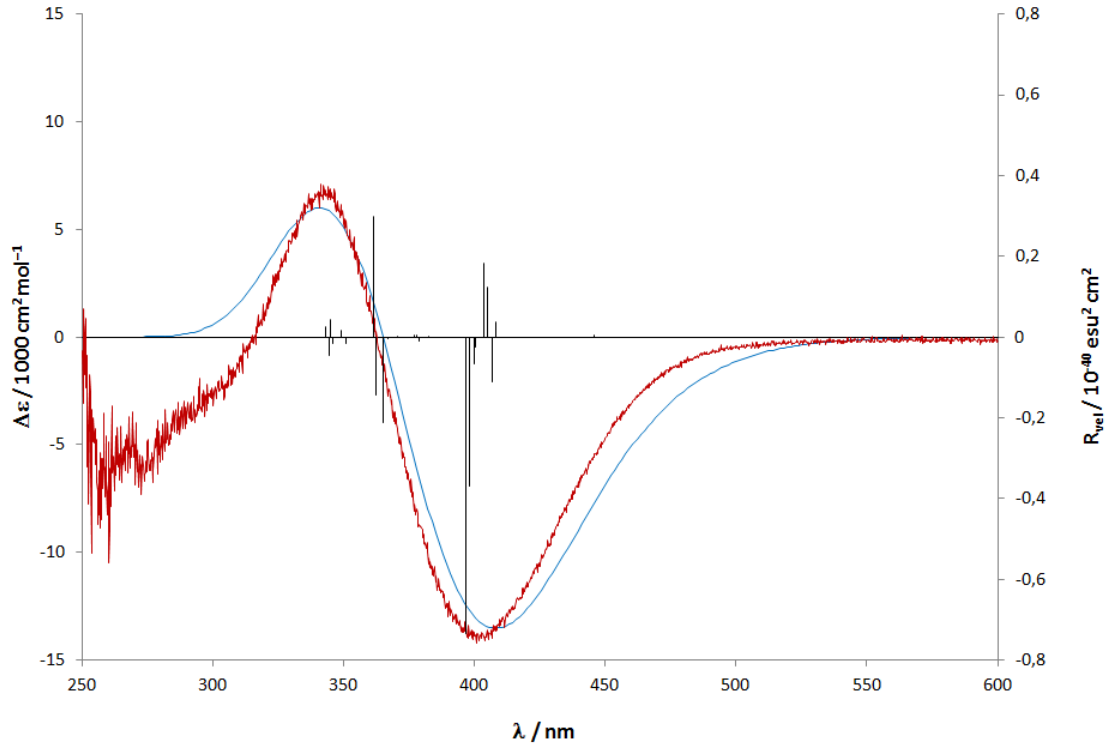

Fig. 103: *Measured spectrum of complex $Li_2[(\mathbf{9})_3Ti]$ in methanol and calculated spectrum of the dimer form ($\Delta\Delta$) of complex $Li_2[(\mathbf{9})_3Ti]$; method: TDDFT/B3LYP/TZVP//B3LYP/TZVP.*

The TD-DFT calculation of the dimeric form of complex $Li_2[(\mathbf{9})_3Ti]$ results in the best match with the measured spectrum (Figure 103). The minima and maxima of both spectra nearly coincide and the shift of the calculated spectrum relative to its experimental counterpart is very small.

As the stereochemistry of the complex shows a profound dependence on the solvents DMSO and MeOH, the next step was the measurement in a third solvent. The curvature of the resulting spectrum in THF shows a completely different shape. It might be that the solvent molecules interact with the complex in a different way than DMSO and MeOH causing the shape of the spectrum to be different. Attempts to computationally reproduce this spectrum met with failure.

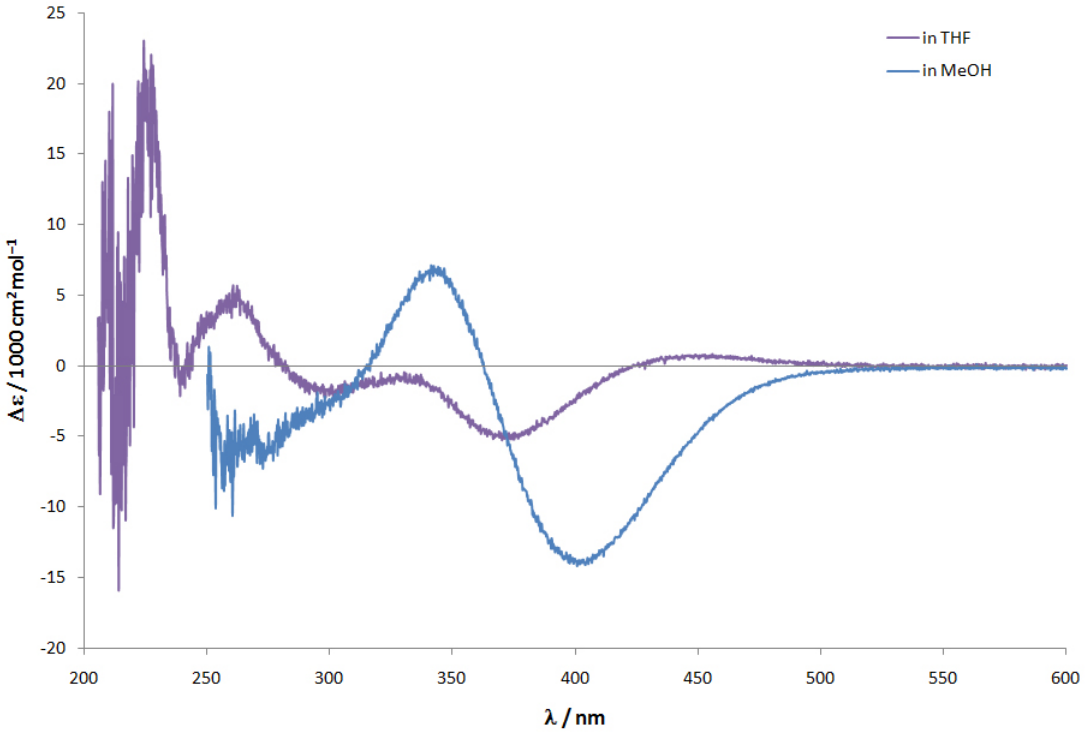

Fig. 104: *Measured CD-spectrum of $Li_2[(\mathbf{9})_3Ti]$ in MeOH and THF.*

A third example for a compound with a stereogenic center at the α position is the complex with naphthalene in the ligand presented in Figure 105. In contrast to complex $Li_2[(\mathbf{10})_3Ti]$, the rest of the ligand is much bigger and, therefore, its sterical demanding part is expected to have an influence on the structure of the complex.

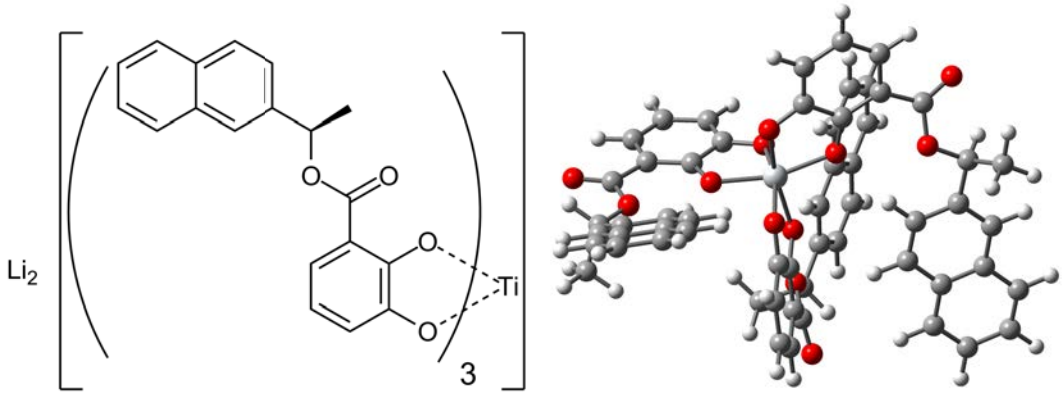

Fig. 105: *Complex $Li_2[(\mathbf{10})_3Ti]$ with (S)-1-(naphthalene-2-yl)ethanol, calculated structure: Δ-form; method: cam-B3LYP/TZVP.*

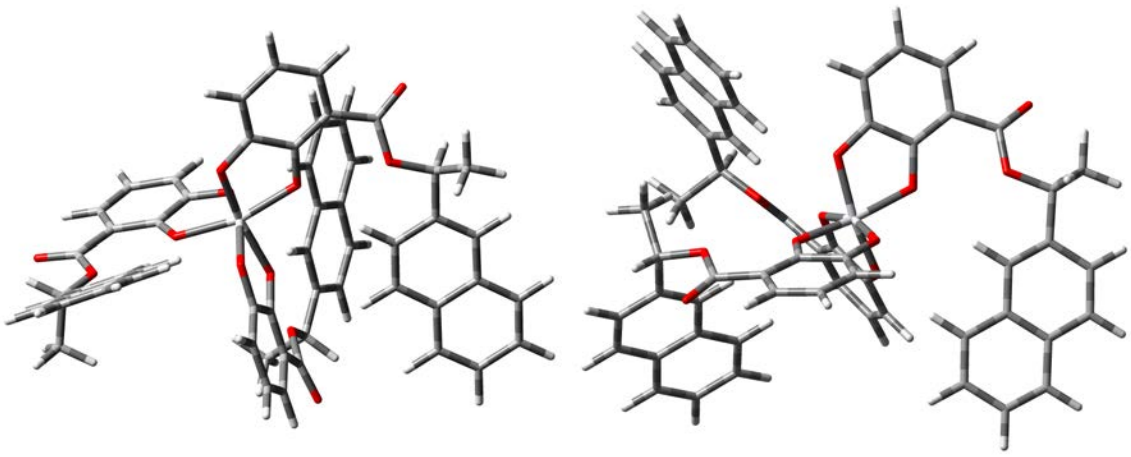

Fig. 106: *Optimized geometry of the Δ and Λ form of complex $[(\mathbf{10})_3Ti]^{2-}$; method: cam-B3LYP/TZVP.*

The energy of the Λ form is -3158.316623 a.u. and for Δ -3158.315383 a.u., which results in an energy difference of 0.78 kcal/mol (Figure 106). This result is somewhat larger than the differences calculated before for the Δ and Λ form of complex $[(\mathbf{10})_3\mathrm{Ti}]^{2-}$. Although this might indicate that the Λ form of the monomer is energetically favored this difference is still quite small and a similar solvent effect as before can be anticipated.

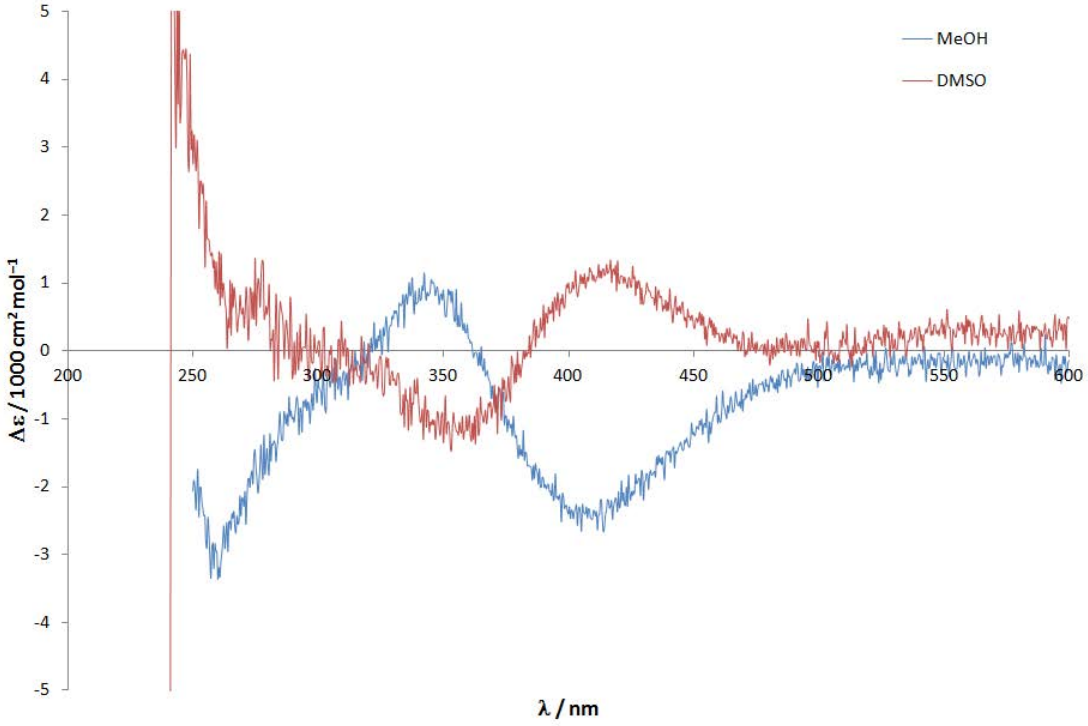

Fig. 107: *Measured CD-spectrum of $Li_2[(\mathbf{10})_3Ti]$ in MeOH and DMSO.*

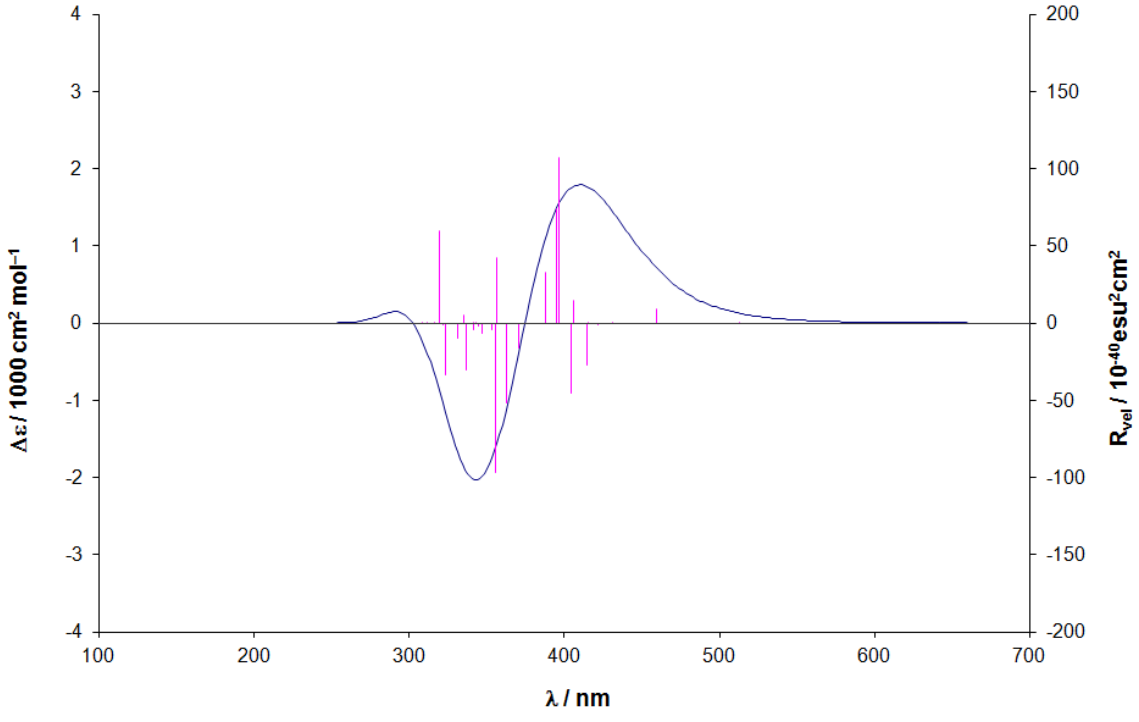

Fig. 108: *Calculated CD spectrum of $[(\mathbf{10})_3Ti]^{2-}$, Λ form, green: rotational strengths; method: TDDFT/cam-B3LYP/TZVP//cam-B3LYP/TZVP.*

Indeed the measured spectrum reveals a "switch" between the monomer- and the dimer-form of the complex (Figure 107) upon change of the solvent. Like complex $Li_2[(\mathbf{9})_3Ti]$, the complex adopts its monomer-form in DMSO and its dimer-form in

MeOH. The bigger group does not seem to have an influence on the dynamics of the complex regarding the shape of the CD curve.

wavelength	transitions	rotational strength
396.54	247 → 251	107.37
394.72	247 → 251	74.2534
362.58	246 → 255	−51.6332
355.52	246 → 256	−96.7336
319.61	245 → 257	59.7596

Table 17: *The most important excited states of [(**10**)$_3$Ti]$^{2-}$ with the corresponding rotational strengths and their major components.*

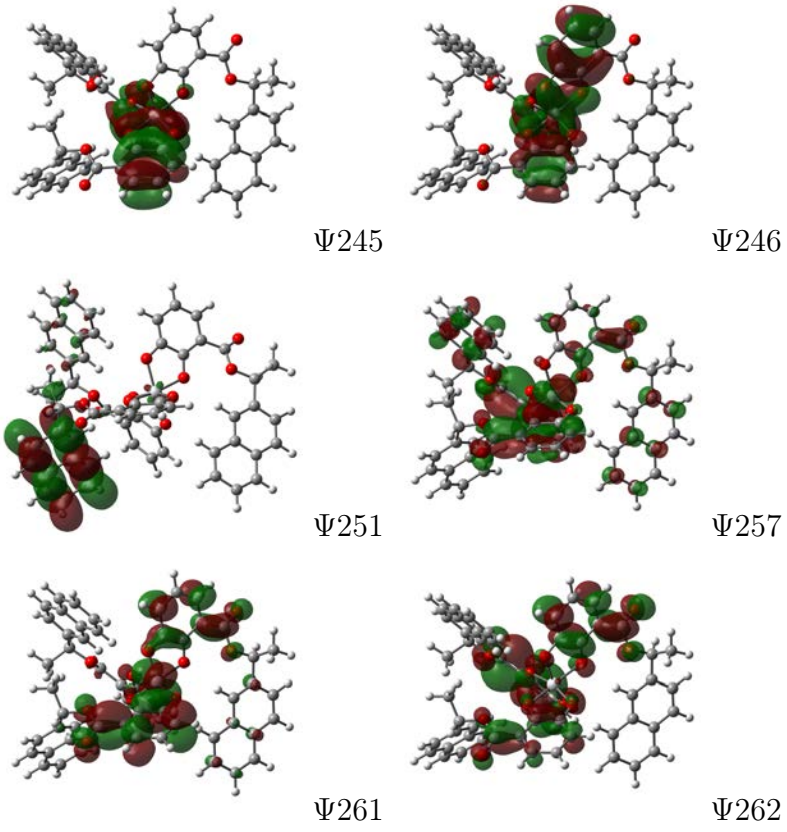

Fig. 109: *Selected Kohn-Sham orbitals of complex [(**10**)$_3$Ti]$^{2-}$.*

Figure 109 shows the Kohn-Sham MOs, which take part in the main transitions (Table 17).

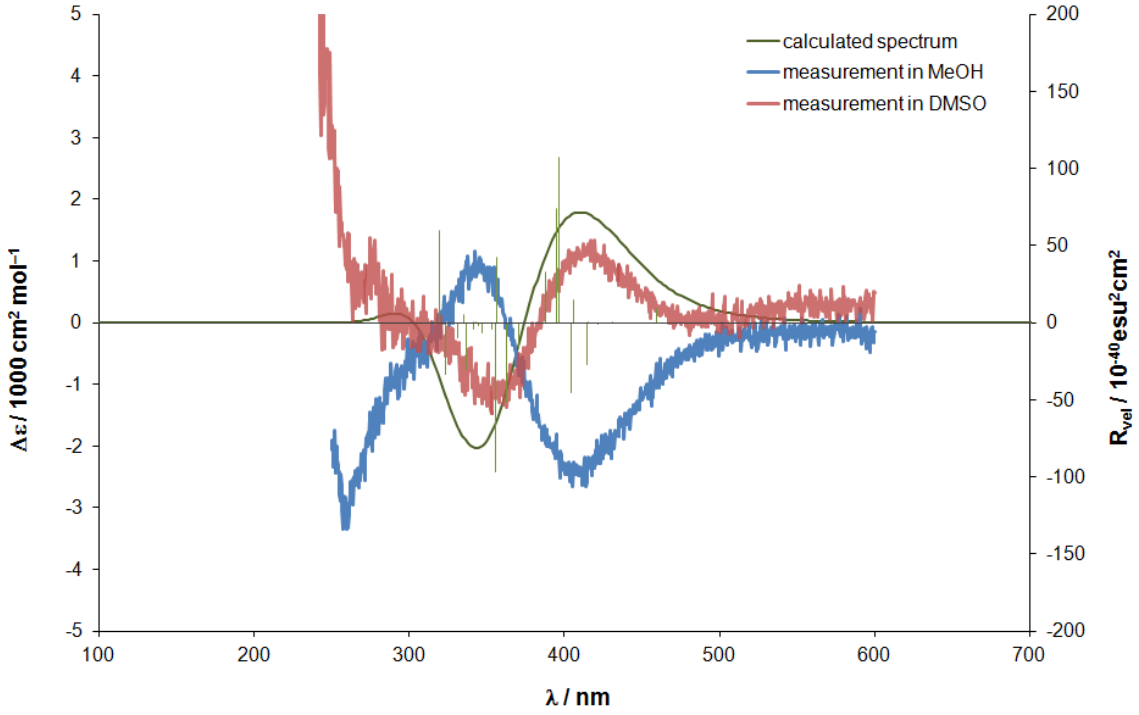

Fig. 110: *Calculated CD spectrum of [(**10**)$_3$Ti]$^{2-}$, Λ form, red: rotational strengths; method: TDDFT/cam-B3LYP/TZVP//cam-B3LYP/TZVP.*

The comparison of the calculated spectrum (Figure 110) with the two measured CD curves reveals a good agreement with the one measured in DMSO. The minimum of the calculated spectrum was found at 341 nm and the maximum at 410 nm, while the measured spectrum has its extrema at 350 nm and 414 nm. A small shift of the calculated spectrum to lower wavelengths was observed. As a result, the calculation shows that the complex adopts the Λ form in DMSO and the Δ form in MeOH.

As a bigger rest like naphthalene does not seem to have a profound influence on the behaviour of the complex, the rest was further modified. Halogenation of the phenyl group is another possibility to extend the size of the rest. In the current case, the *ortho*-position of the phenyl group was substituted by bromine.

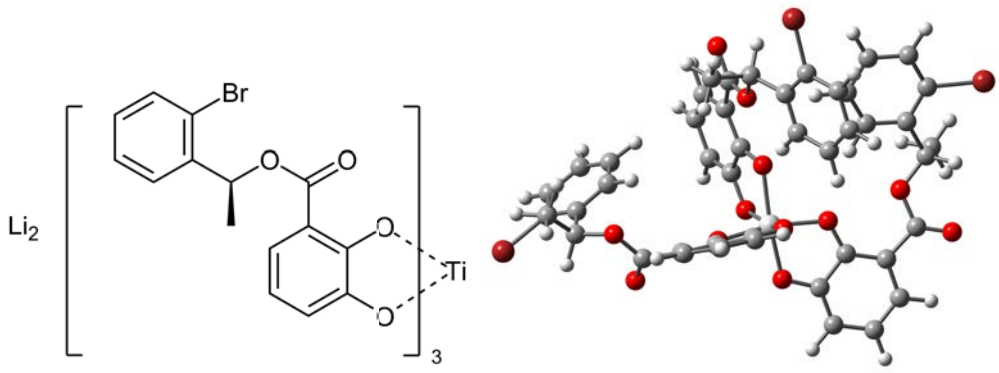

Fig. 111: *Complex Li$_2$[(**11**)$_3$Ti] with (S)-2-bromo-α-methylbenzyl-alcohol, calculated structure: Δ form; method: cam-B3LYP/TZVP.*

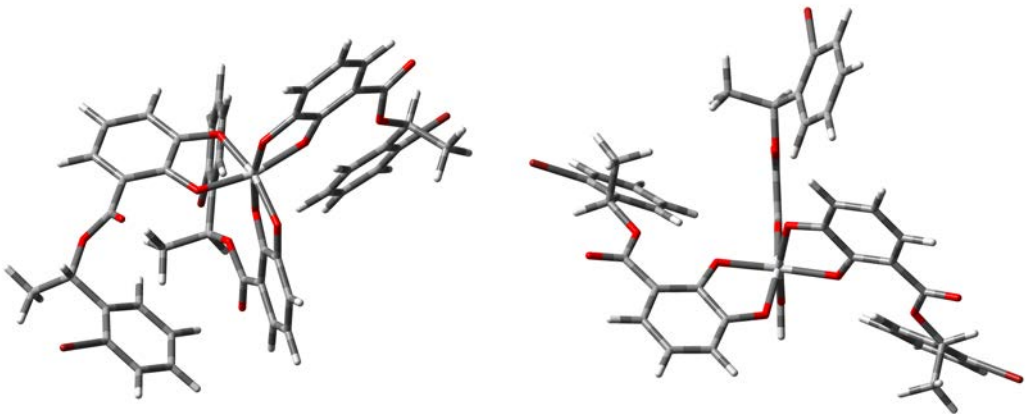

Fig. 112: *Optimized geometry of the Δ and Λ form of complex [(**11**)$_3$Ti]$^{2-}$; method: cam-B3LYP/TZVP.*

The total energy for the Λ form is −10418.547707 a.u. and for Δ −10418.534940 a.u., which results in a significant energy difference of 8.01 kcal/mol (Figure 112). This is one of the largest energy differences between the Λ and the Δ form encountered so far.

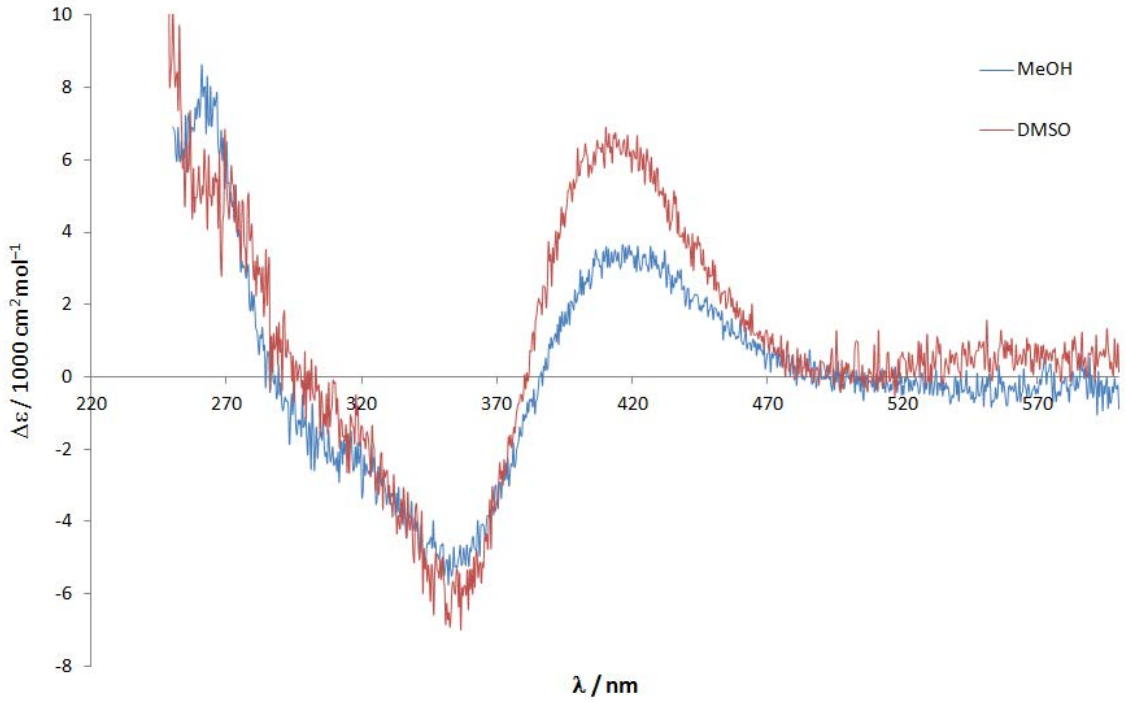

Fig. 113: *Measured CD-spectrum of Li$_2$[(**11**)$_3$Ti] in MeOH and DMSO.*

As a consequence the solvent dependence of the spectra is low and no "switch" occurs if the solvent is changed from MeOH to DMSO. The minima of the spectra are found at 354 nm and the maxima at 418 nm. The measured spectrum in DMSO has a more intense maximum than the one measured in MeOH (Figure 113). The result that no "switch" was observed upon change of the solvent might also be due to the low concentration for the CD measurement of 0.001 mol/l. The dimerization constant has to be considered to investigate the behavior of the complex further.

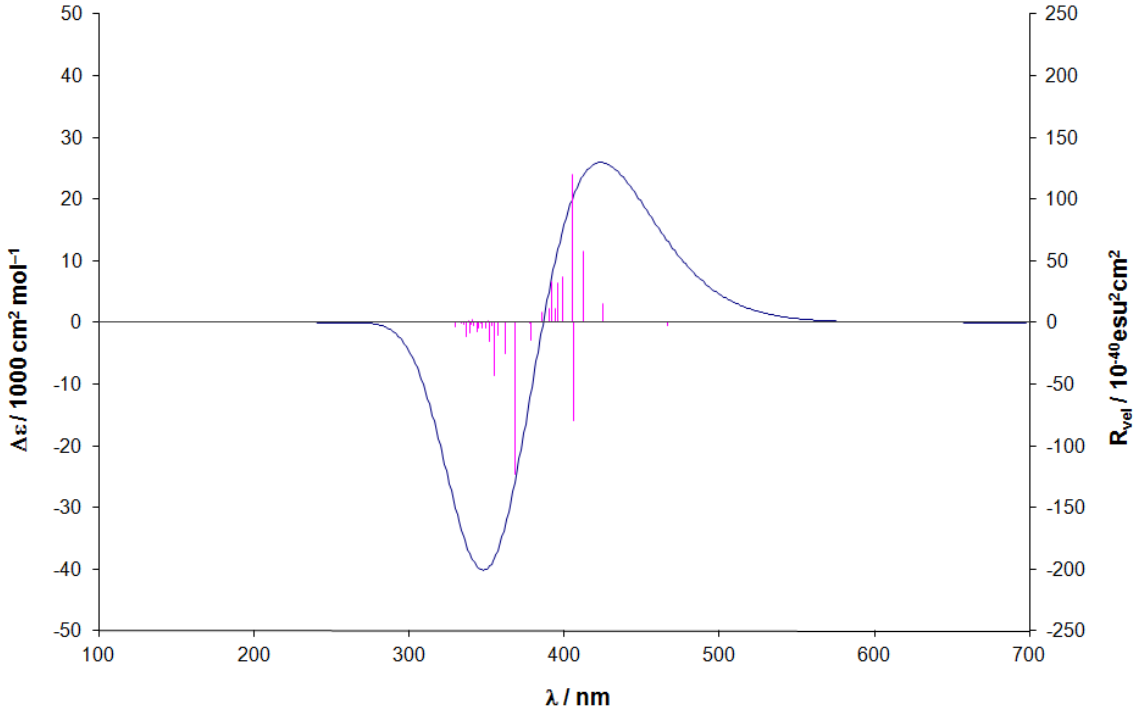

Fig. 114: *Calculated CD spectrum of $[(\mathbf{11})_3Ti]^{2-}$, Λ form, red: rotational strengths; method: TDDFT/B3LYP/TZVP//cam-B3LYP/TZVP.*

wavelength	transitions	rotational strength
412.62	258 → 260	57.7895
405.89	257 → 265	−79.1238
405.17	259 → 261	119.76
368.06	257 → 260	−122.5644
355.26	261 → 210	−42.8599

Table 18: *The most important excited states of $[(\mathbf{11})_3Ti]^{2-}$ with the corresponding rotational strengths and their major components.*

The comparison of the calculated CD spectrum of $[(\mathbf{11})_3\mathrm{Ti}]^{2-}$ (Figure 114) reveals that the complex adopts the Λ form in both DMSO and MeOH. The minimum of the calculated spectrum is found at 348 nm and the maximum at 422 nm, which is a good match with the measured CD curve. Only the shape of the measured spectrum below 300 nm could not be reproduced. Therefore, cam-B3LYP was used for another TD-DFT calculation.

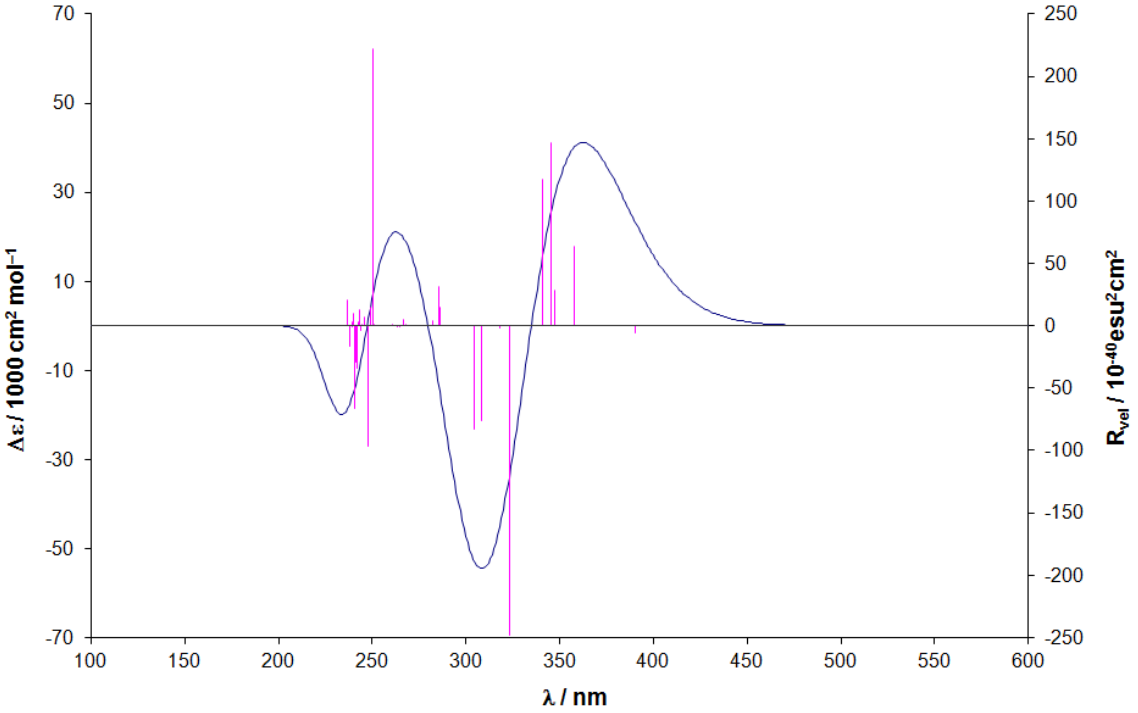

Fig. 115: *Calculated CD spectrum of* $[(\mathbf{11})_3 Ti]^{2-}$, Λ *form, red: rotational strengths; method: TDDFT/cam-B3LYP/TZVP//cam-B3LYP/TZVP.*

The spectra calculated with cam-B3LYP and the one with B3LYP are compared to the spectra measured in MeOH and DMSO in Figure 116. The spectrum obtained with cam-B3LYP shows an additional pair of bands below about 275 nm consisting of a minimum at 240 nm and a maximum at 263 nm. The next minimum occurs at 307 nm and the next maximum at 363 nm. These numbers show that the calculation with cam-B3LYP results in a larger blue shift of the spectrum than the calculation with B3LYP. The measured Cotton effect at about 287 nm could be reproduced with the cam-B3LYP functional while this band is missing in the CD curve calculated with the B3LYP hybrid functional.

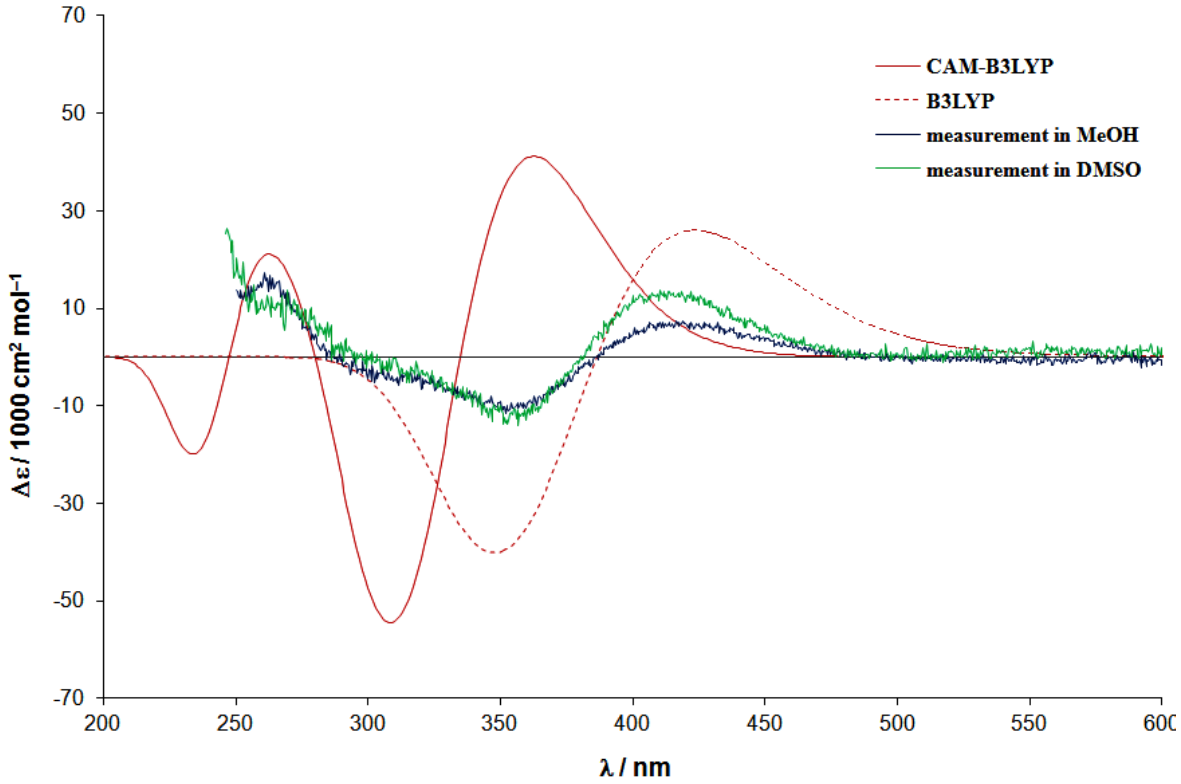

Fig. 116: *Comparison of the CD spectra calculated with cam-B3LYP/TZVP and B3LYP/TZVP of $[(\mathbf{11})_3 Ti]^{2-}$ with the measured spectra in MeOH and DMSO.*

wavelength	transitions	rotational strength
358.00	259 → 261	64.1733
345.71	259 → 272	146.7995
323.52	257 → 261	−248.1956
308.61	259 → 273	−76.0558
304.17	257 → 272	−82.6182
250.48	254 → 261	222.3564
	255 → 265*	
247.69	254 → 261	−96.225
	257 → 262**	

Table 19: *The most important excited states of $[(\mathbf{11})_3 Ti]^{2-}$ with the corresponding rotational strengths and their major components; *coefficients: (254 → 261) -0.21521, (255 → 265) -0.20934; **coefficients: (254 → 261) 0.26920, (257 → 262) -0.25720; method: cam-B3LYP.*

Figure 117 shows the Kohn-Sham orbitals Ψ254, Ψ255, Ψ261, and Ψ265 which participate in the transition at the wavelength of 250 nm. The rotational strength at this wavelength is caused by a state involving a transition between the aromatic part of the ligand and the metal center (Ψ254->Ψ261 and Ψ255->Ψ265). The MO Ψ262 (Figure 117) has a strong coefficient at the *ortho*-Br. It takes part in the transition between the MO Ψ257 to the MO Ψ262, which contributes to the strongly negative rotational strength at 248 nm.

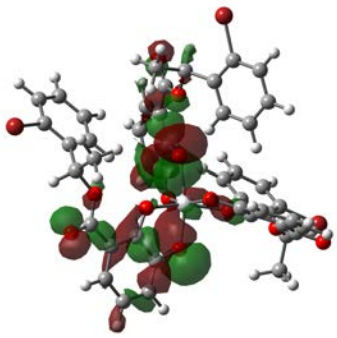

Ψ252

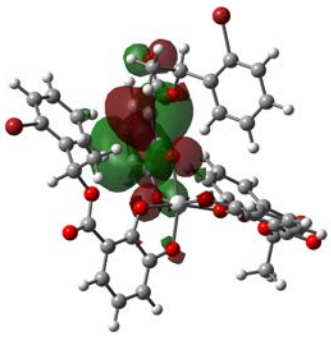

Ψ254

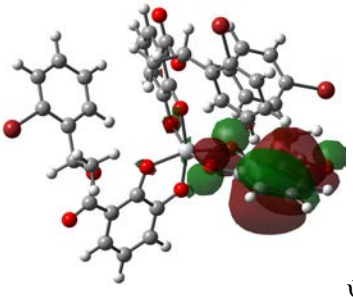

Ψ255

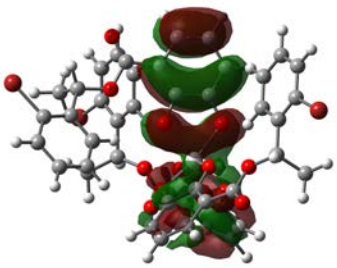

Ψ257

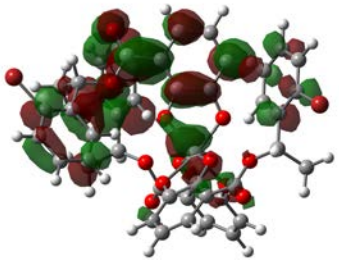

Ψ261

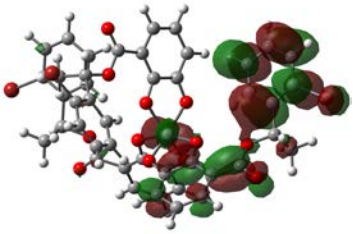

Ψ262

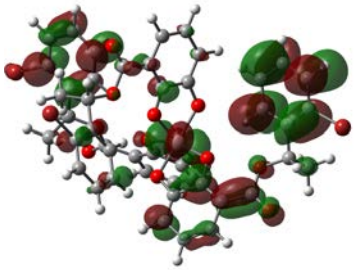

Ψ265

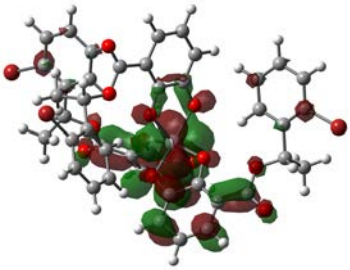

Ψ272

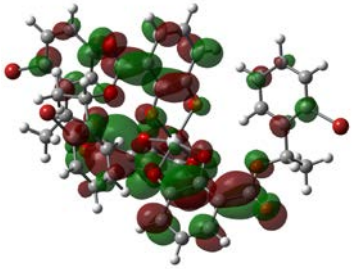

Ψ273

Fig. 117: *Selected Kohn-Sham orbitals of complex* $[(\mathbf{11})_3 Ti]^{2-}$*, method: cam-B3LYP/TZVP.*

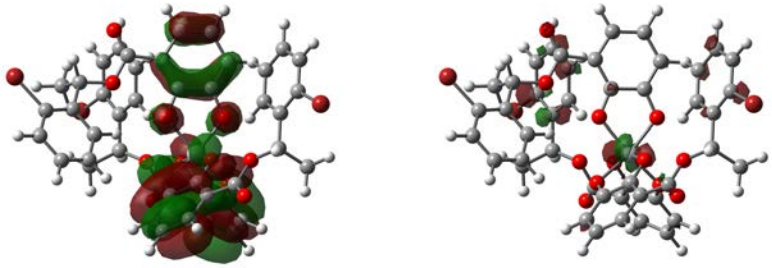

Ψ259 Ψ260

Fig. 118: *HOMO (Ψ=259) and LUMO (Ψ=260) of complex [(**11**)$_3$Ti]$^{2-}$, method: cam-B3LYP/TZVP.*

The excitation from the HOMO to the LUMO (Figure 118) is a transition between the ligand and the metal center being the major contribution to a state at 390.19 nm with a rotational strength of -6.1920. This corresponds to the calculation with B3LYP. One difference to the cam-B3LYP result is the distribution of the coefficients at the ligand within MO Ψ260. The calculation with cam-B3LYP results in no significant coefficient at the ligand while the calculation with B3LYP gives large coefficients also at the aromatic part. In Figure 119 the MOs Ψ261 and Ψ262 are shown. As they participate in the transitions at low wavelengths the differences in the distribution of their coefficients are important. The MOs Ψ261* and Ψ262* which were calculated with B3LYP show smaller coefficients than the MOs derived from the cam-B3LYP calculations.

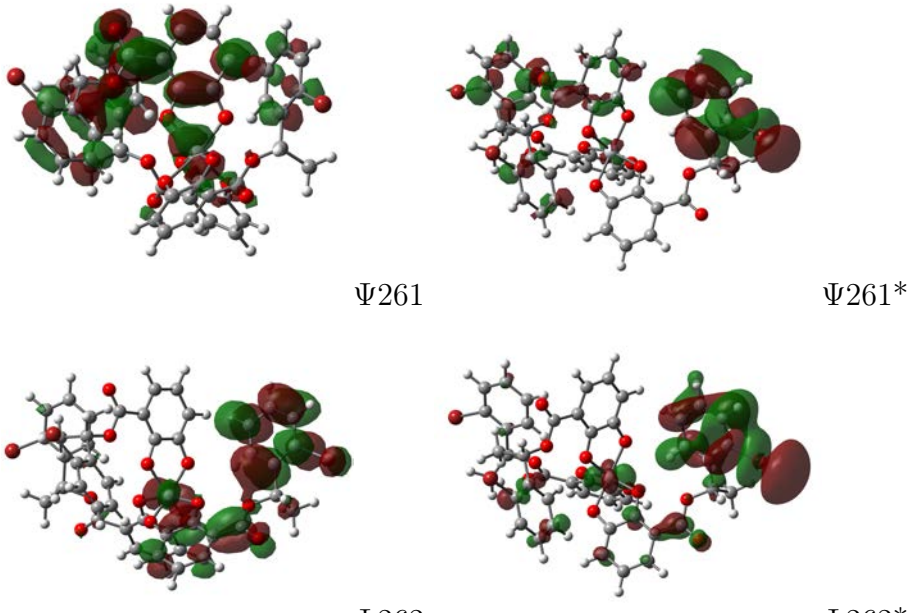

Ψ261 Ψ261*

Ψ262 Ψ262*

Fig. 119: *Comparison of selected Kohn-Sham orbitals of complex [(**11**)$_3$Ti]$^{2-}$, methods: cam-B3LYP, *B3LYP.*

The comparison of the two CD spectra obtained from the two calculations with the

functionals B3LYP and cam-B3LYP shows that cam-B3LYP gives a result that agrees better with the calculated CD curves because it reproduces the experimentally observed maximum at 263 nm. Therefore, the cam-B3LYP result was used as the reference.

In order to find out, why the ΛΛ form is preferred in DMSO as well as in MeOH, the ΔΔ form of the dimer was energetically optimized at the LSDA/TZVP level of theory (Figure 120). The energetically optimized ΔΔ form has a small distance between the two phenyl rings of 3.31 Å (Figure 121). In the solid state, the closest distance of the phenyl rings of the ΛΛ form is 4.30 Å and, therefore, much larger (Figure 122). This offers a possible explanation why the ΛΛ form is energetically favored.

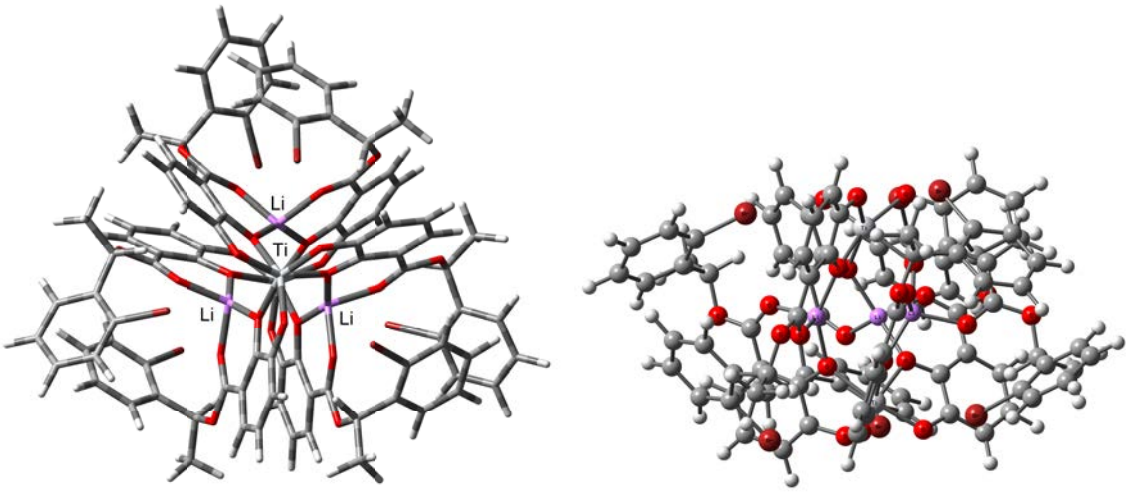

Fig. 120: *With LSDA/TZVP optimized geometry of the ΔΔ form of the dimer of complex [(**11**)$_3$Ti]$^{2-}$ with Li$^+$ as counter ions; white: Ti, purple: Li, dark red: Br, red: O.*

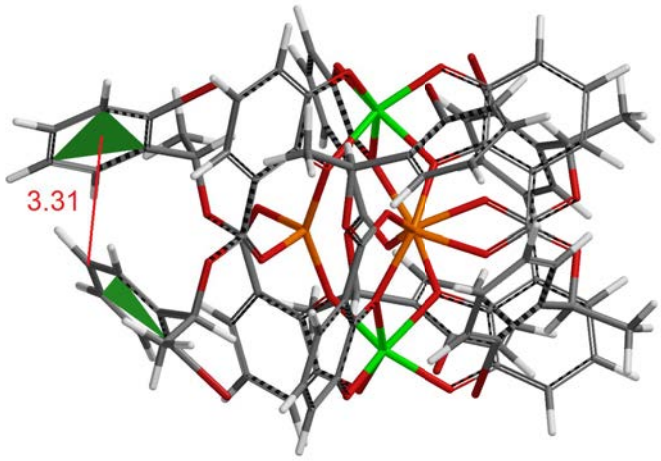

Fig. 121: *With LSDA/TZVP optimized geometry of the ΔΔ form of the dimer of complex [(**11**)$_3$Ti]$^{2-}$ with Li$^+$ as counter ions, distance of the two phenyl groups in red; green: Ti, orange: Li, red: O.*

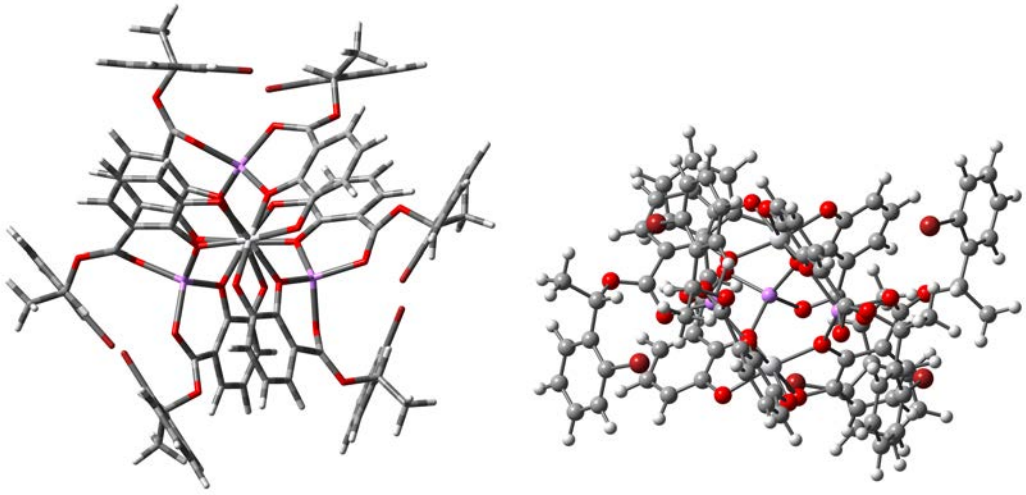

Fig. 122: *The solid state structure of the ΛΛ form of the dimer of complex [(**11**)$_3$Ti]$^{2-}$ with Li$^+$ as counter ions.*

- **Two or more stereogenic centers**

The most significant dependence of the structure on the solvent was found for ligands with a stereogenic center at the α position. As this position is very close to the metal center, it is of great interest to analyze which influence other sterically demanding substituents in this position might have on the stereochemistry of the complex. An example for a complex with several stereogenic centers is Li_2[(**12**)Ti] with cholesterol derived substituent (Figure 123).

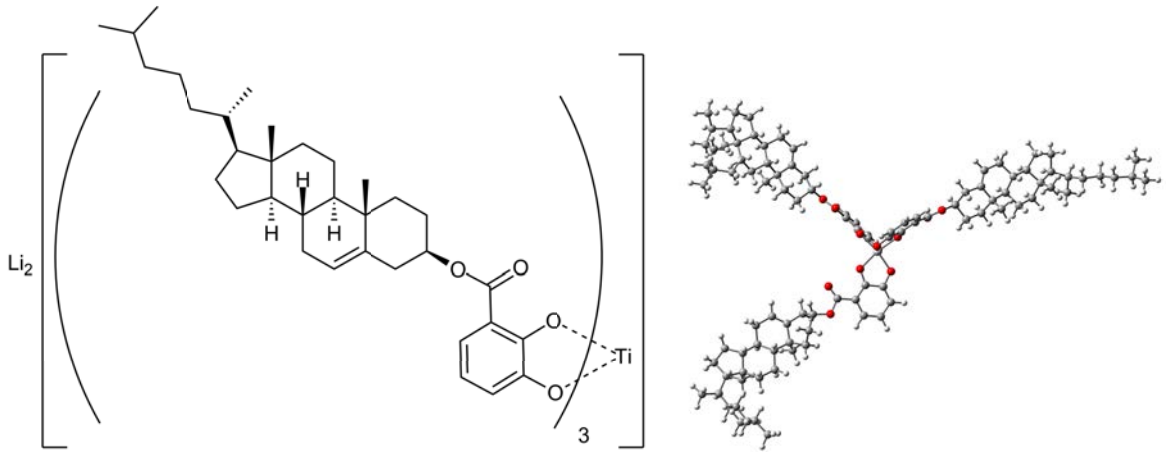

Fig. 123: *Complex Li$_2$[(**12**)$_3$Ti] with cholesterol, below: optimized geometry of the complex in its Λ form; method: cam-B3LYP/TZVP.*

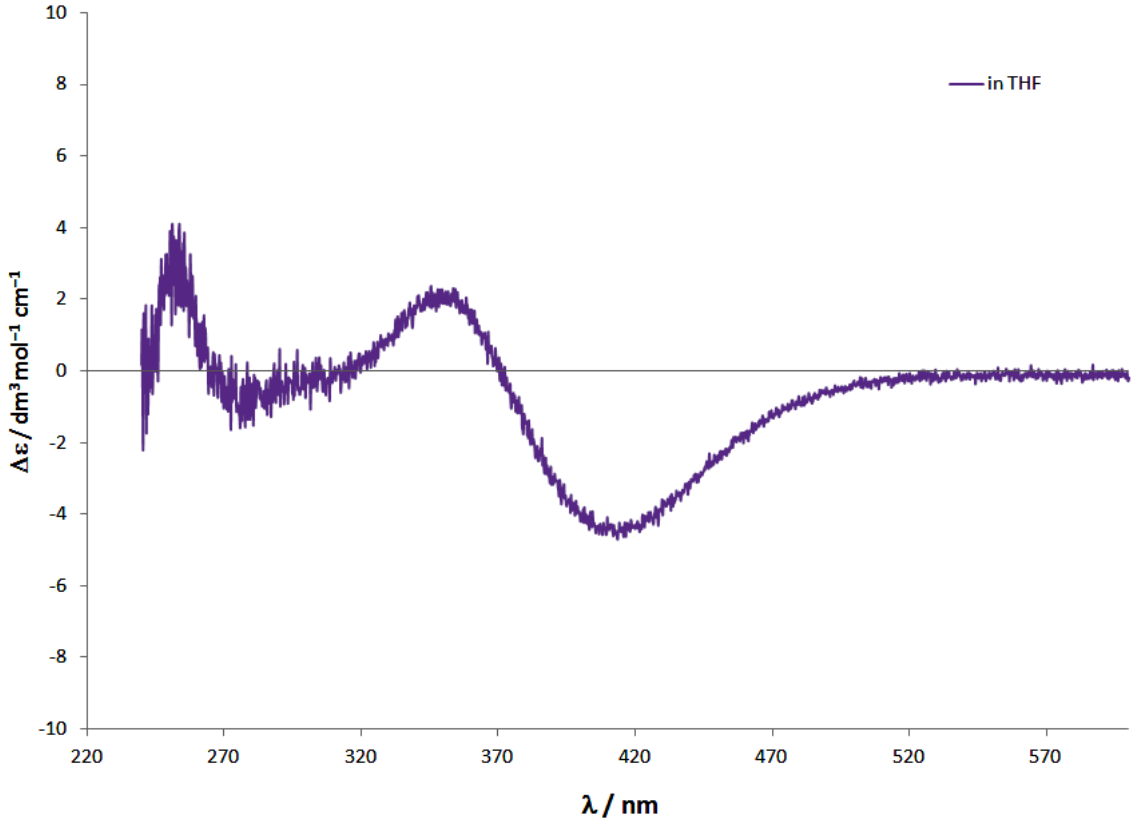

Fig. 124: *Measured CD-spectrum of Li_2[(**12**)Ti] in THF.*

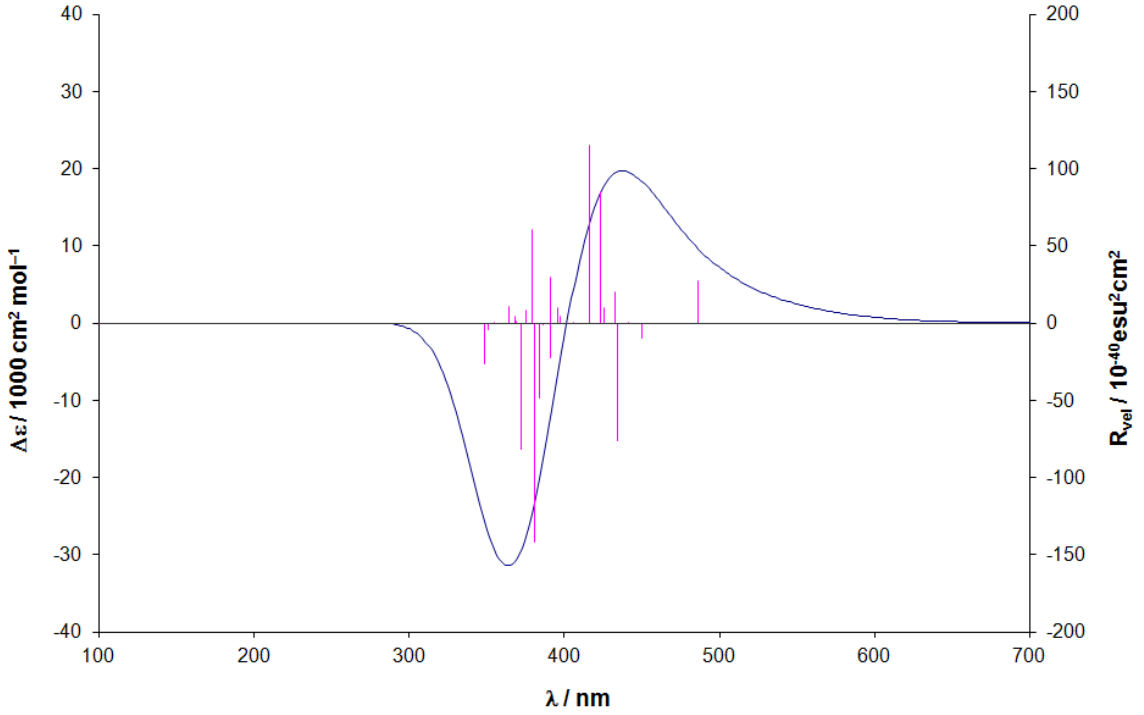

Fig. 125: *Calculated CD spectrum of $[(\mathbf{12})_3Ti]^{2-}$, Λ form, red: rotational strengths; method: TDDFT/B3LYP//cam-B3LYP/TZVP.*

Complex Li_2[(**12**)Ti] is only soluble in THF and not in DMSO or MeOH. For this

reason, the complex could only be measured in one solvent (Figure 124). The experimental spectrum has two local maxima (253 and 350 nm) and two local minima (278 and 411 nm). This is different from the CD spectra of the complexes with only one stereogenic center, which have only one maximum and one minimum. An exception is the complex with bromine (Figure 113).

wavelength	transitions	rotational strength
449.91	433 → 434	−9.5103
433.98	432 → 441	−75.8318
423.33	431 → 441	84.8444
	431 → 437	
416.43	433 → 444	115.3109
380.74	431 → 434	−142.0321
	432 → 443	
372.04	431 → 437	−82.0948
	432 → 437	

Table 20: *The most important excited states of $[(\mathbf{12})_3Ti]^{2-}$ with the corresponding rotational strengths and their major components.*

The calculated spectrum of $[(\mathbf{12})_3\mathrm{Ti}]^{2-}$ in its Λ form (Figure 125) is the mirror image of the measured spectrum in THF. This comparison indicates that the complex adopts the Δ form in the chosen solvent. The calculated minimum is located at 363 nm and the maximum at 437 nnm, which corresponds to the measured maximum at 350 nm and the minimum at 411 nm. The calculated spectrum has only two Cotton effects, while the measured one displays two more signals in the short wavelengths region. Despite this difference, the agreement in the more important long wavelengths region is good and, therefore, the calculated spectrum leads to the conclusion that most likely the Δ form is adopted in this solvent.

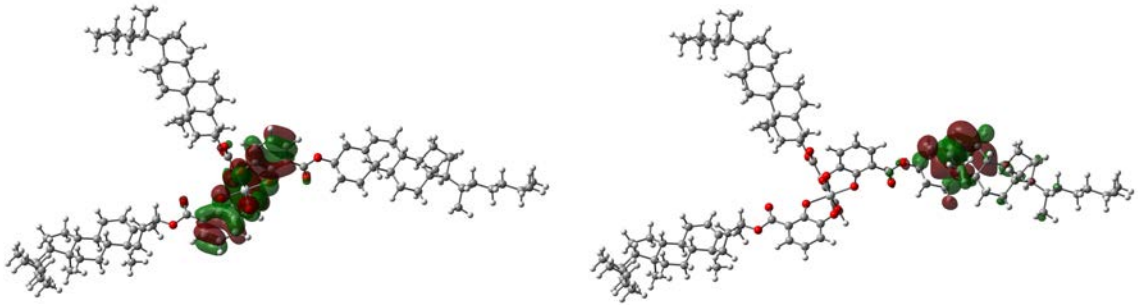

Fig. 126: *HOMO (Ψ=433) and LUMO (Ψ=434) of complex $[(\mathbf{12})_3Ti]^{2-}$.*

The transition between the HOMO (Ψ=433) and the LUMO (Ψ=434) takes place between the triscatecholate and the cholesterol part of the ligand (Figure 126) and occurs at a wavelength of 449.91 nm with a rotational strength of -9.5103.

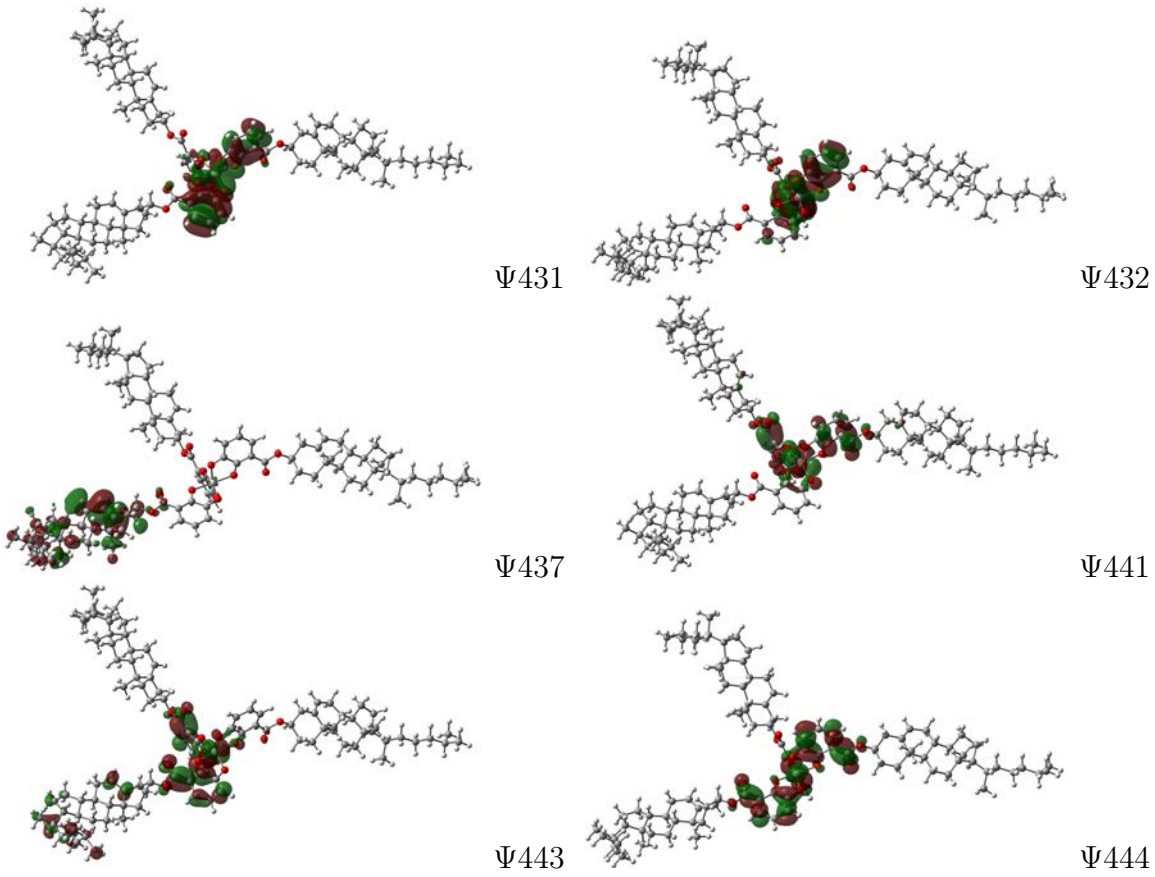

Fig. 127: *Selected Kohn-Sham orbitals of complex [(**12**)$_3$Ti]$^{2-}$.*

Figure 127 shows the MOs taking part in the most important transitions. As the higher MOs like Ψ441 (LUMO+7), Ψ443 (LUMO+9) and Ψ444 (LUMO+10) have large coefficients at the metal center, several transitions take place from the ligand to the metal center.

The second example for a complex with more than one stereogenic center is $Li_2[(\mathbf{13})_3Ti]$ with (−)-menthol (Figure 128). The resulting ligand has three stereogenic centers and is sterically very demanding.

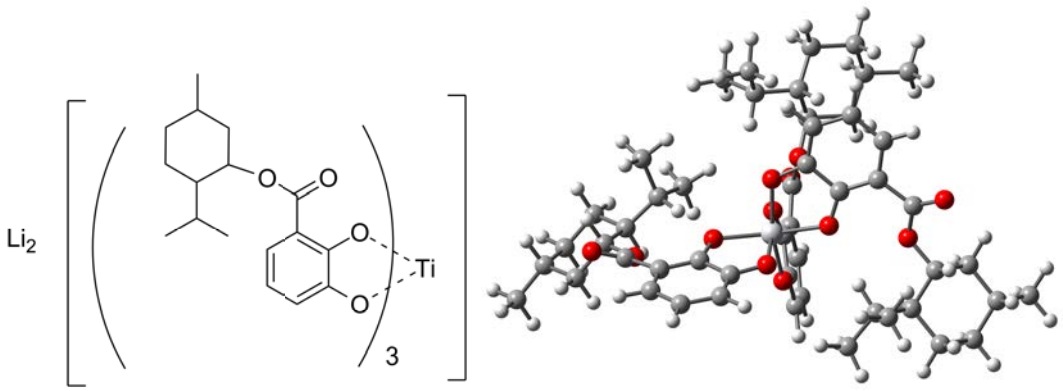

Fig. 128: *Complex Li$_2$[(**13**)$_3$Ti] with (−)-menthol, right: optimized geometry of the complex in its Λ form; method: cam-B3LYP/TZVP.*

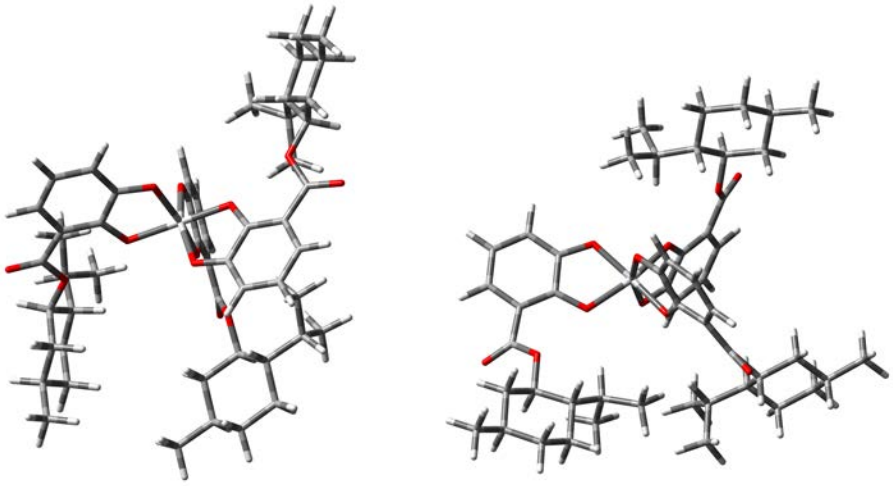

Fig. 129: *Optimized geometry of the* Δ *(left) and* Λ *(right) form of complex* $[(\mathbf{13})_3 Ti]^{2-}$*; method: cam-B3LYP/TZVP.*

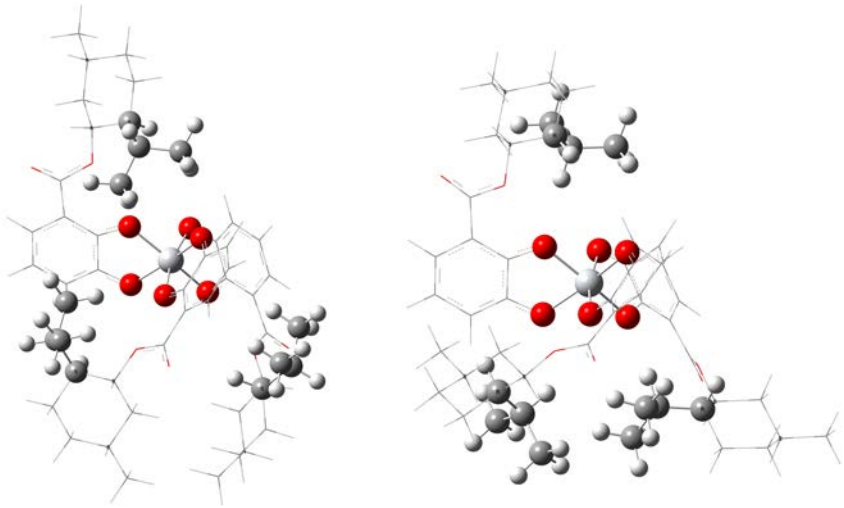

Fig. 130: *Structure of the* Δ *form of complex* $[(\mathbf{13})_3 Ti]^{2-}$*: (−)-menthol (left) and mirror image of the* Λ *form (right).*

The total energy for the Λ form is -2944.185445 a.u. and -2944.174584 a.u. for Δ resulting in an energy difference of 6.81 kcal/mol (Figure 129) in favor of the Λ species. Within the Δ form, the menthol rest points outwards, while the Λ form leads to a more compact structure. Figure 130 shows the structure of the mirror image of the Λ form on the left side.

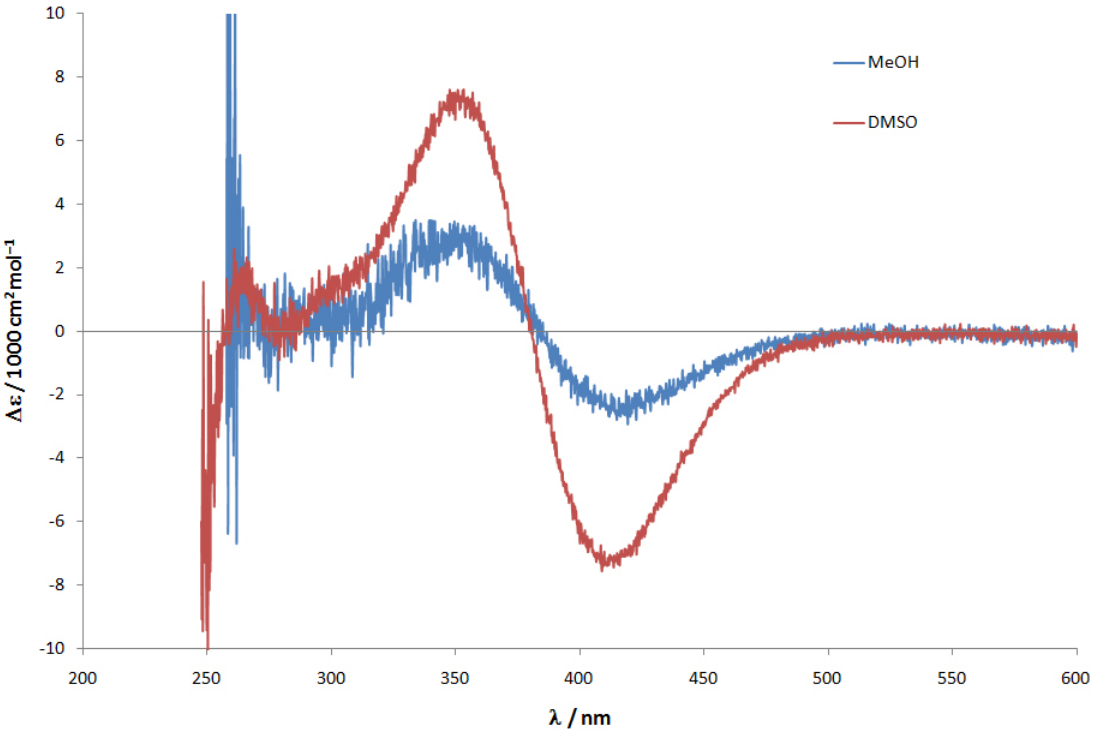

Fig. 131: *Measured CD-spectrum of $Li_2[(\mathbf{13})_3Ti]$ in MeOH and DMSO.*

The maxima of the CD-spectra measured in MeOH and DMSO are at 353 nm and the minima at 420 nm (MeOH) and 415 nm (DMSO) (Figure 131). Only the intensity of the curves of the two spectra is different. A large difference results, if the sample is measured in THF (Figure 132).

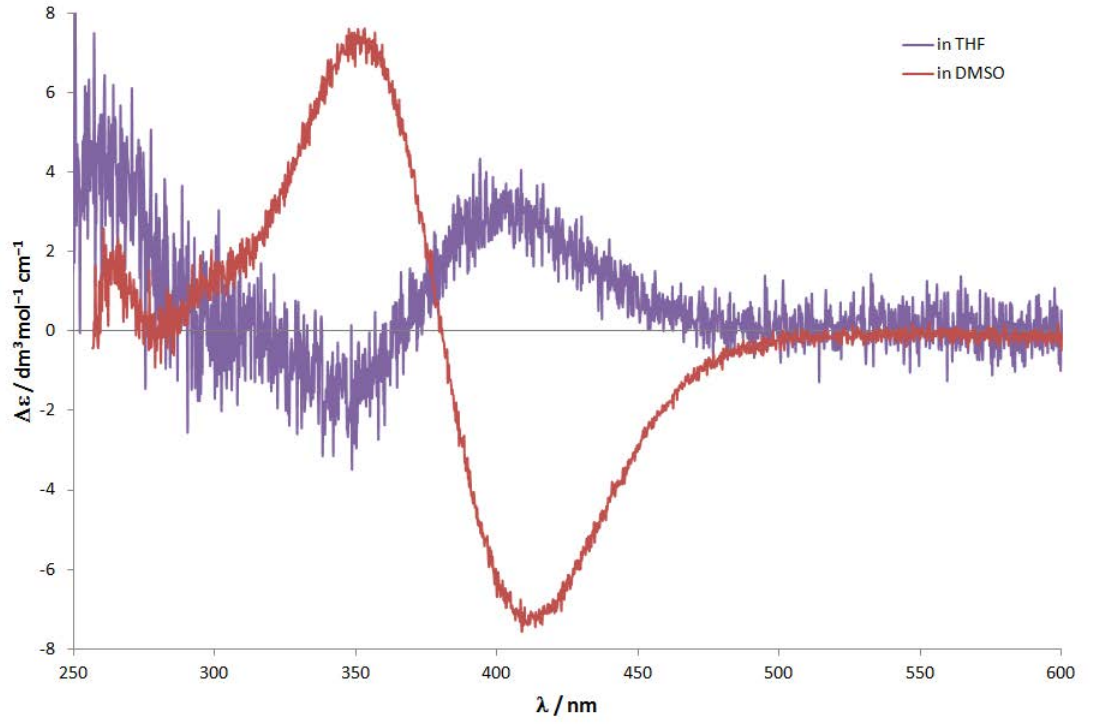

Fig. 132: *Measured CD-spectrum of $Li_2[(\mathbf{13})_3Ti]$ in THF and DMSO.*

The complex Li_2[(**13**)Ti] shows a configurational reversal at the metal center in the experimental spectrum in THF relative to the spectrum recorded in DMSO. THF has the lowest dipole moment of the three chosen solvents. The dipole moment of THF (20°C) is 1.75 D, the one of DMSO is 4.1 D and the one of MeOH is 2.87 D.[85] This might imply that the molecule needs a less polar solvent to adopt the Λ form. This behavior of the complex might indicate that the more stable Λ form is less polar than the energetically less favorable Δ species. Consequently, the Δ form will be stabilized more effectively in a polar medium and, therefore, be formed in polar DMSO although it is less stable in the gas phase or in solvents of lower polarity.

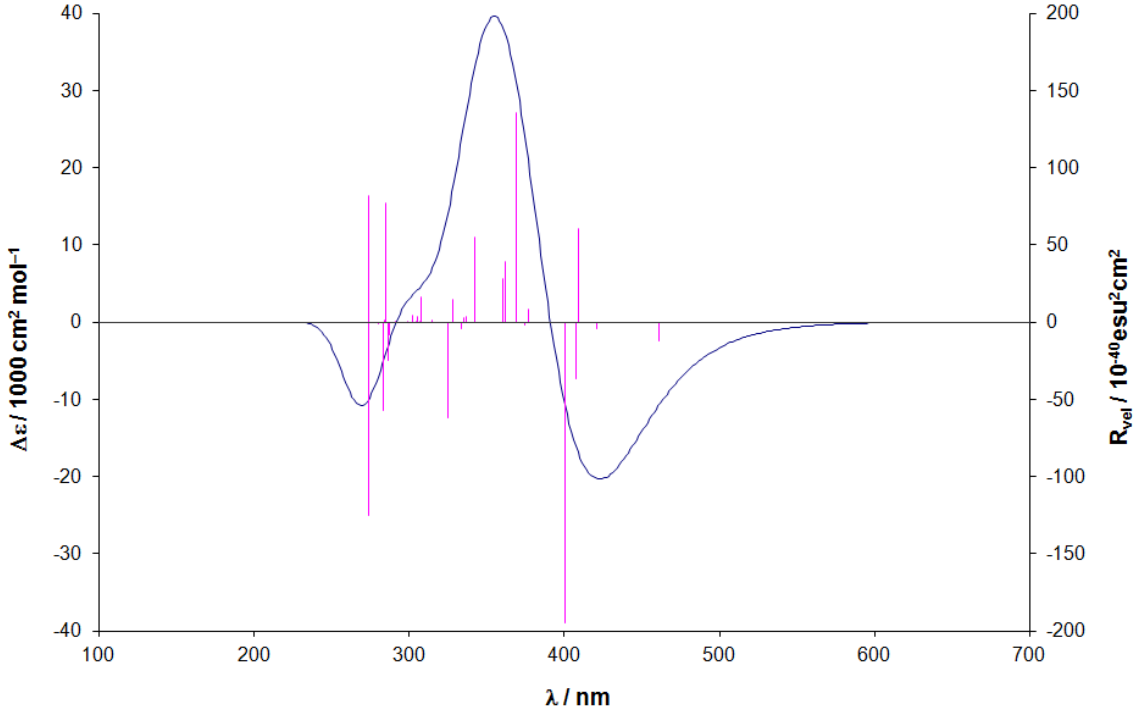

Fig. 133: *Calculated CD spectrum of [(**13**)$_3$Ti]$^{2-}$, Λ form, red: rotational strengths; method: TDDFT/B3LYP//cam-B3LYP/TZVP.*

The first minimum of the calculated CD spectrum is located at 270 nm, the second one at 421 nm and the maximum at 354 nm. These extrema can be correlated with those measured (solvent = DMSO) at 280, 316 and 415 nm.

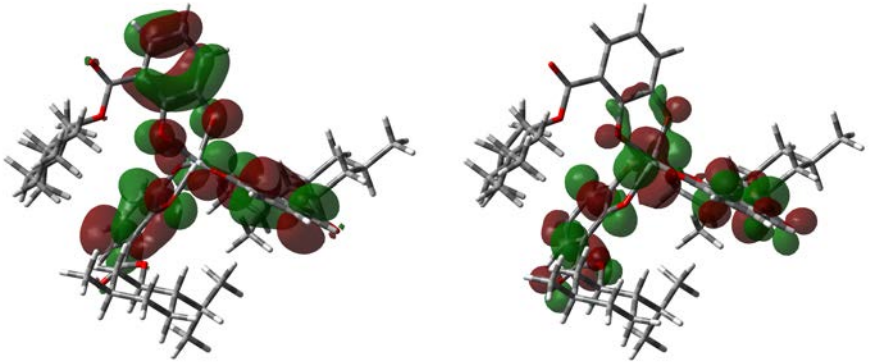

Fig. 134: *HOMO (Ψ=241) and LUMO (Ψ=242) of complex [(**13**)$_3$Ti]$^{2-}$.*

The third example for a complex with several stereogenic centers is $Li_2[(\mathbf{14})_3Ti]$ with *L*-(−)-borneol (Figure 135).

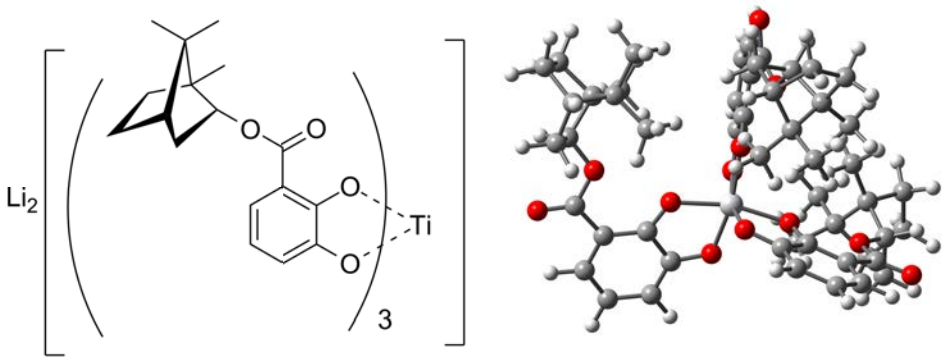

Fig. 135: *Complex Li$_2$[(**14**)$_3$Ti] with L-(−)-borneol, right: optimized geometry of the complex in its Λ form; method: cam-B3LYP/TZVP.*

The total energy of the Λ form is −2940.519372 a.u. and of the Δ form −2940.520495 a.u., and the energy difference is about 0.70 kcal/mol (Figure 129), which is very low compared to the difference found with (−)-menthol. Figure 136 shows the two possible structures.

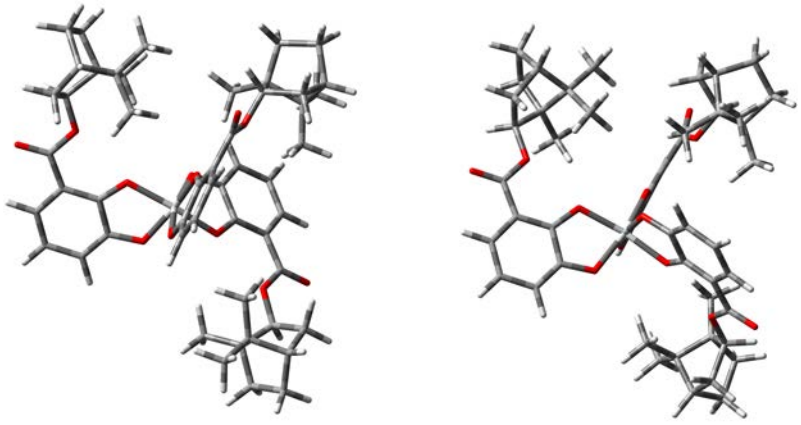

Fig. 136: *Optimized geometries of the Δ and Λ form of complex [(**14**)$_3$Ti]$^{2-}$; method: cam-B3LYP/TZVP.*

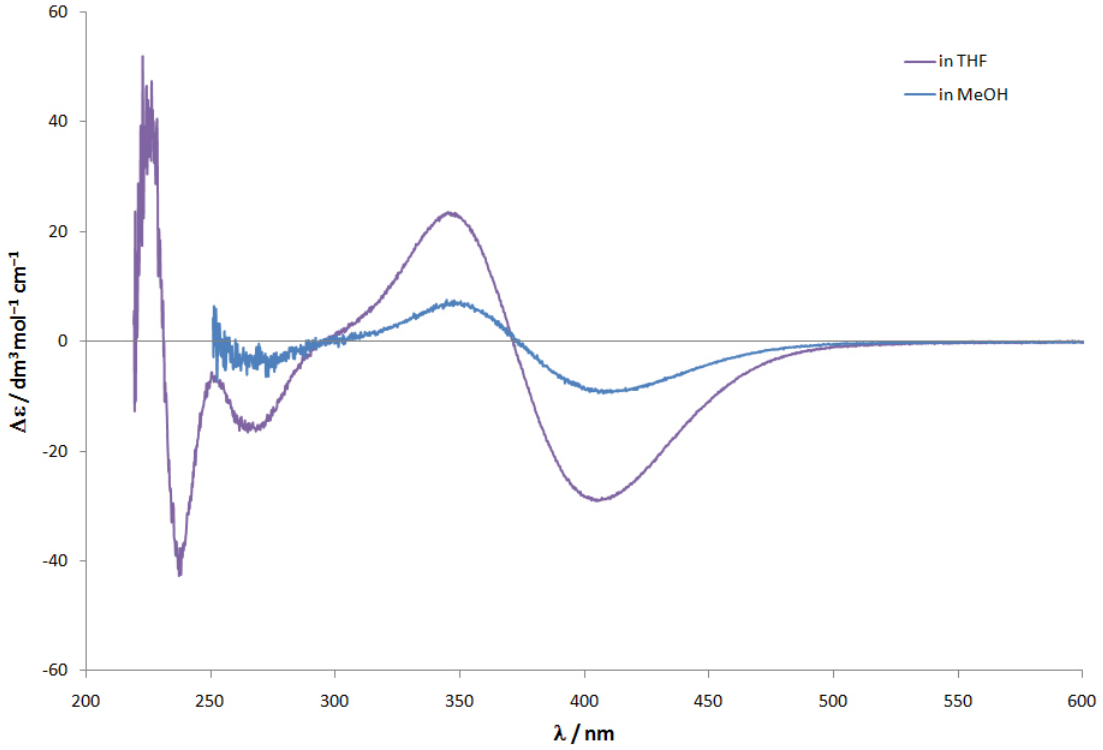

Fig. 137: *Measured CD-spectrum of $Li_2[(\mathbf{14})_3Ti]$ in THF and DMSO.*

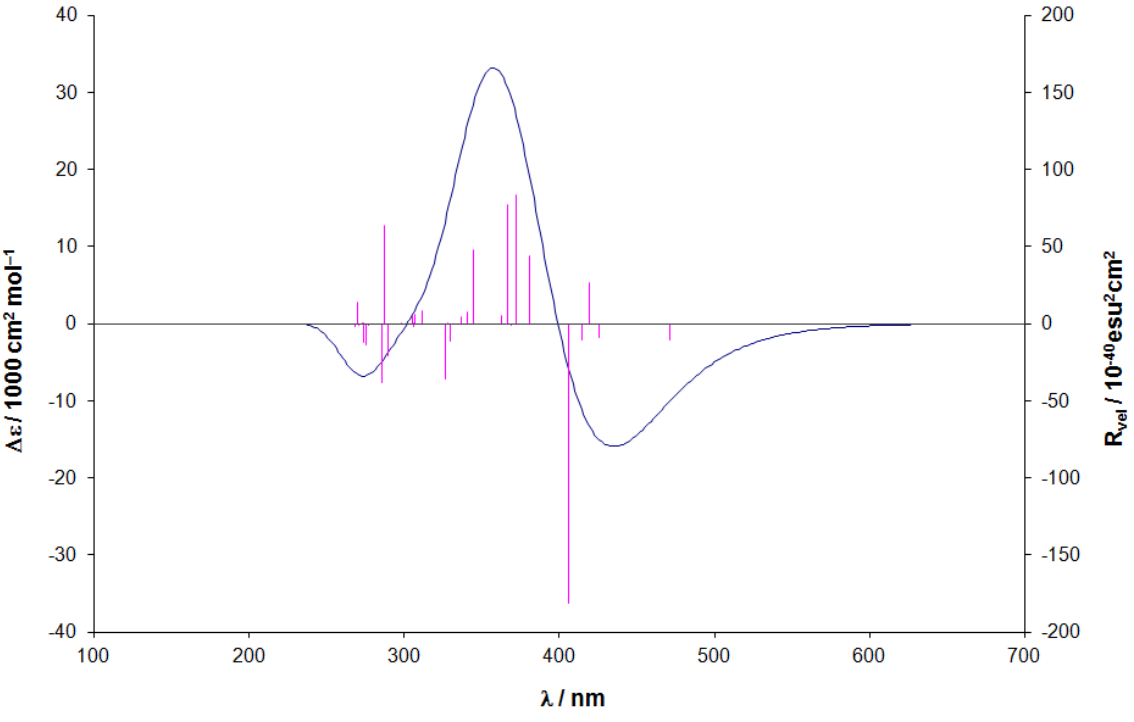

Fig. 138: *Calculated CD spectrum of $[(\mathbf{14})_3Ti]^{2-}$, Δ form, red: rotational strengths; method: TDDFT/B3LYP//cam-B3LYP/TZVP.*

The calculated spectrum of complex $[(\mathbf{14})_3\mathrm{Ti}]^{2-}$ shows one positive and two negative Cotton effects with minima at 273 and 431 nm. The maximum is found at 357 nm. The corresponding extrema of the measured spectrum in THF are: 266 nm (minimum), 345

nm (maximum) and 405 nm (minimum). The calculated spectrum is slightly shifted to the red. Figure 139 illustrates that the shape of the calculated spectrum matches the spectrum measured in THF. As a result, the complex most likely adopts the Δ form within the chosen solvent.

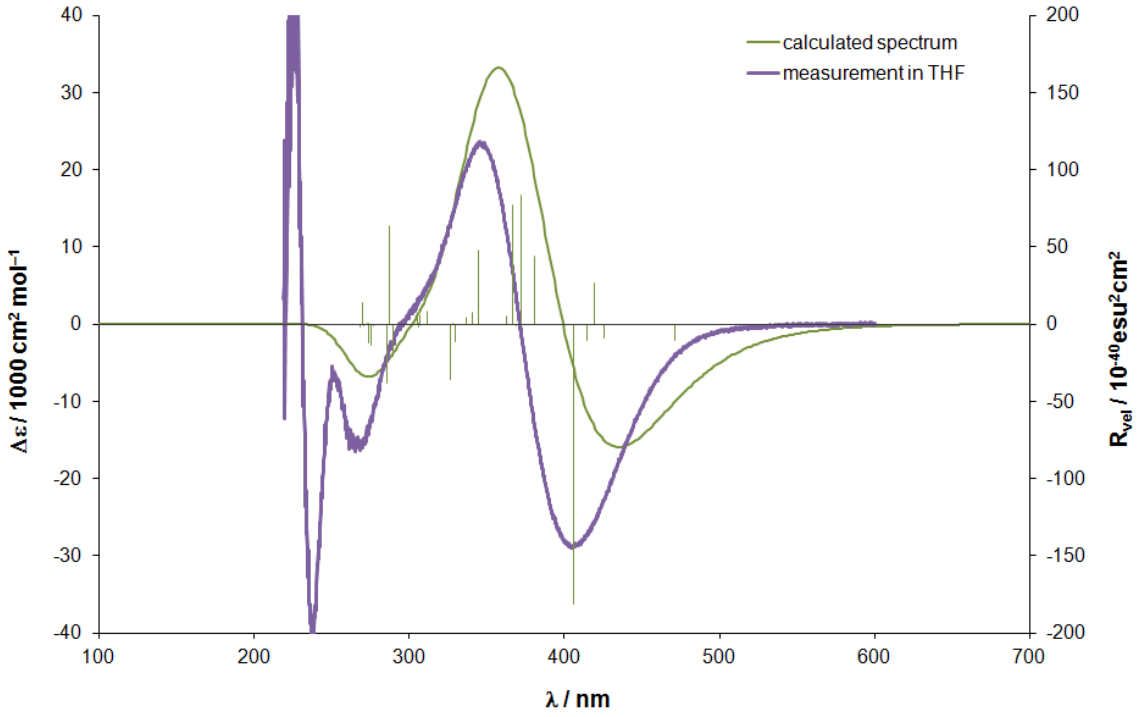

Fig. 139: *Comparison of the calculated and the measured CD spectrum of* $[(\mathbf{14})_3Ti]^{2-}$, Δ *form.*

wavelength	transitions	rotational strength
405.78	238 → 241	−181.4486
381.05	236 → 240	44.1301
372.21	236 → 240	83.5613
	237 → 240	
366.65	237 → 241	76.8749
326.46	236 → 243	−35.8740
287.44	234 → 239	63.9360

Table 21: *The most important excited states of* $[(\mathbf{14})_3Ti]^{2-}$ *with the corresponding rotational strengths and their major components.*

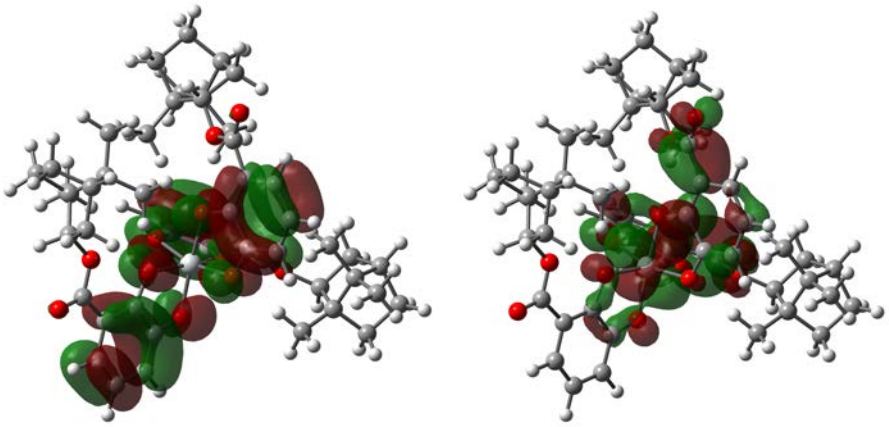

Fig. 140: *HOMO (Ψ=238) and LUMO (Ψ=239) of complex [(**14**)$_3$Ti]$^{2-}$.*

The transition between HOMO (Ψ=238) and LUMO (Ψ=239) of complex [(**14**)$_3$Ti]$^{2-}$ is one from the ligand to the metal center and is involved in a state that occurs at a wavelength of 471.55 nm with a rotational strength of -10.4417. The transitions at the lower wavelength causing the Cotton effect take place from Ψ=236 to Ψ=243 and from Ψ=234 to Ψ=239. The respective MOs are presented in Figure 141.

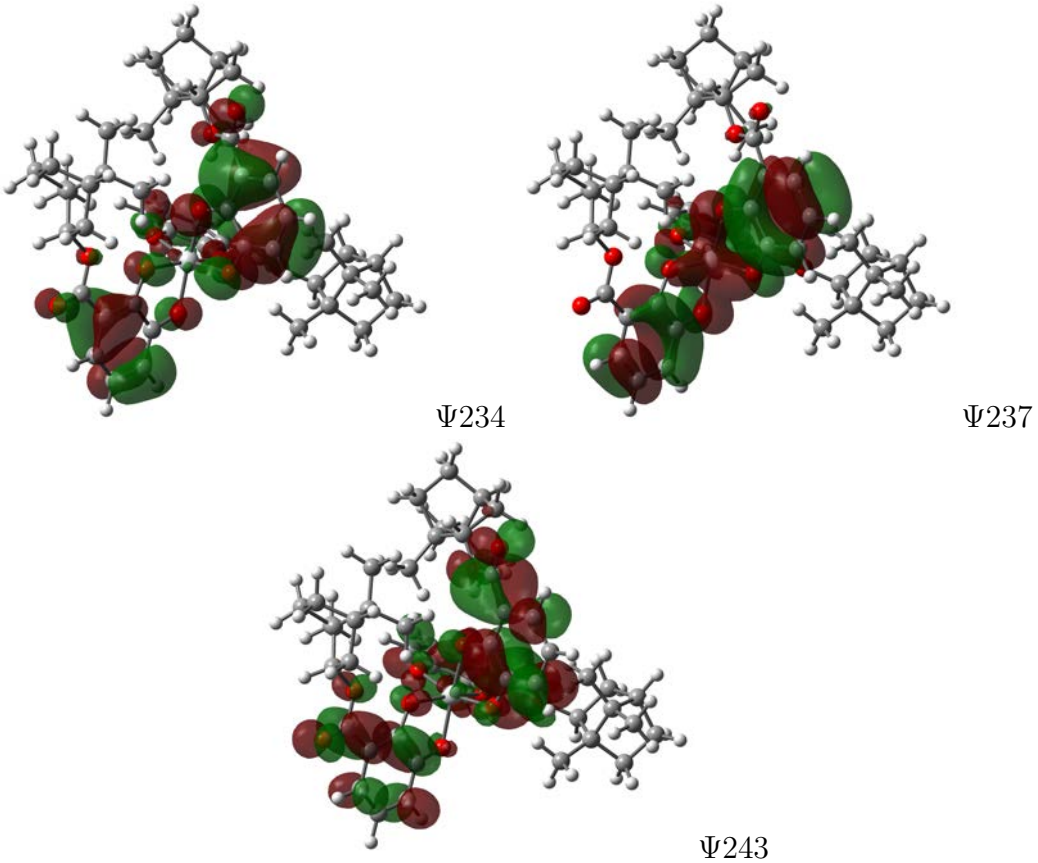

Fig. 141: *Selected Kohn-Sham orbitals of complex [(**14**)$_3$Ti]$^{2-}$.*

The final example for a complex with a ligand with more than one steroegenic center is (1*R*)-(−)-myrthenol. The resulting complex Li_2[(**15**)$_3$Ti] is presented in Figure 142.

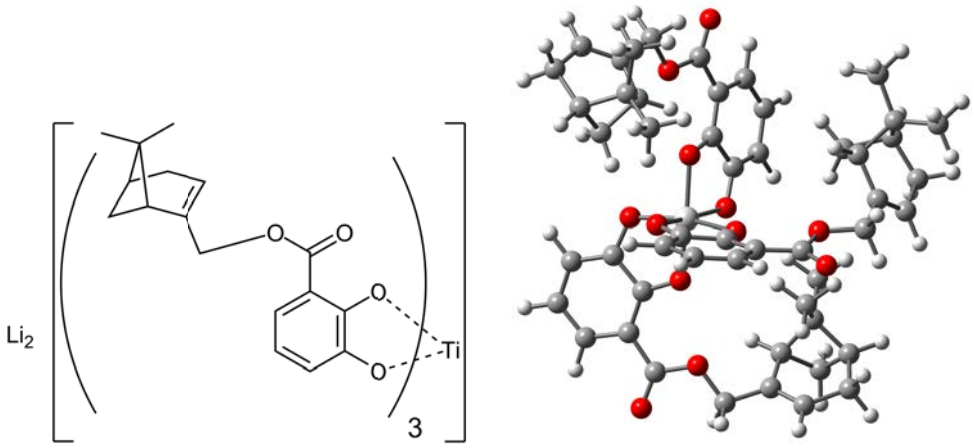

Fig. 142: *Complex $Li_2[(\mathbf{15})_3 Ti]$ with myrthenol, right: optimized geometry of the complex in its Λ form; method: cam-B3LYP/TZVP.*

The total energy of the Λ form is -2936.759242 a.u. while the Δ has an energy of -2936.764205 a.u., and the energy difference is about 3.11 kcal/mol (Figure 143).

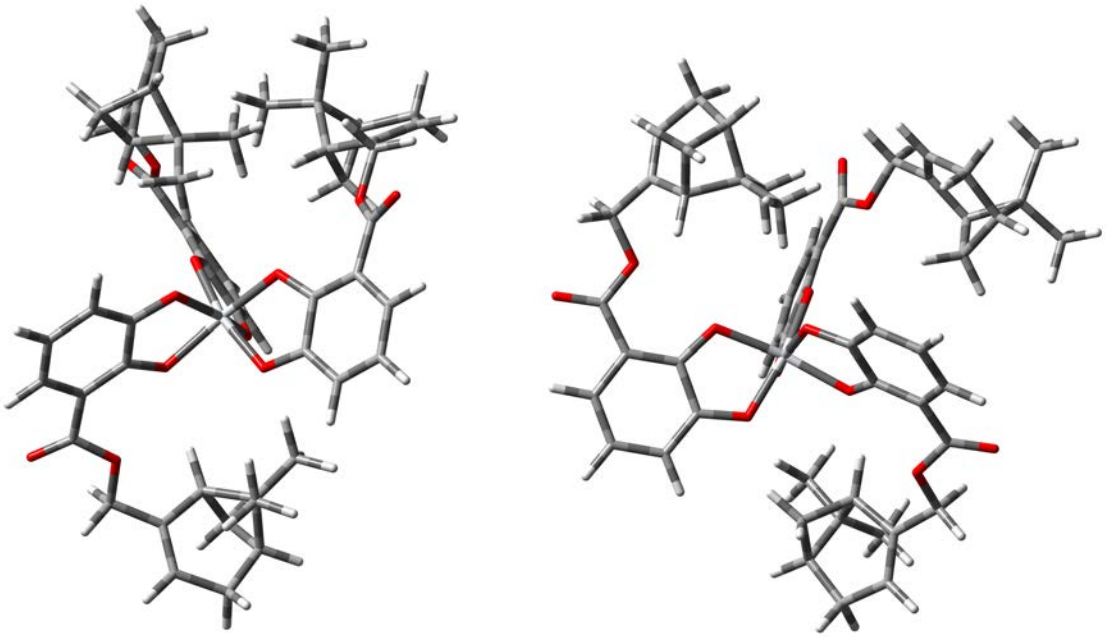

Fig. 143: *Optimized geometry of the Δ and Λ form of complex $[(\mathbf{15})_3 Ti]^{2-}$; method: cam-B3LYP/TZVP.*

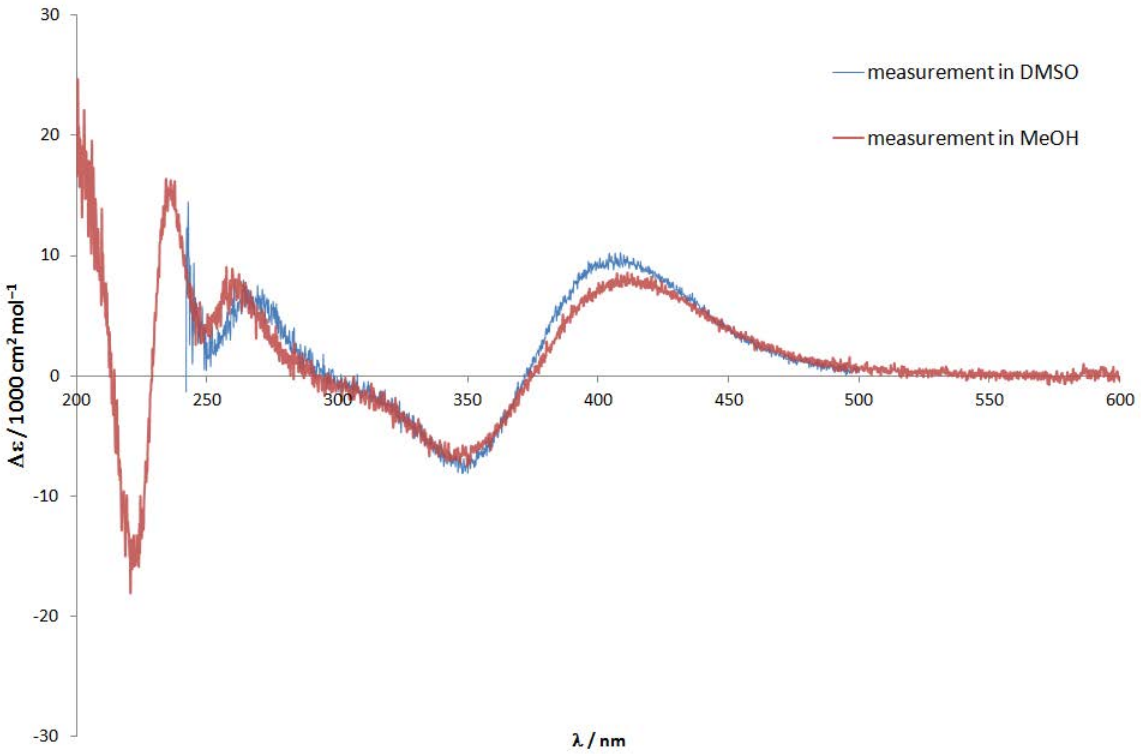

Fig. 144: *Measured CD-spectra of $Li_2[(\mathbf{15})_3Ti]$ in THF and DMSO.*

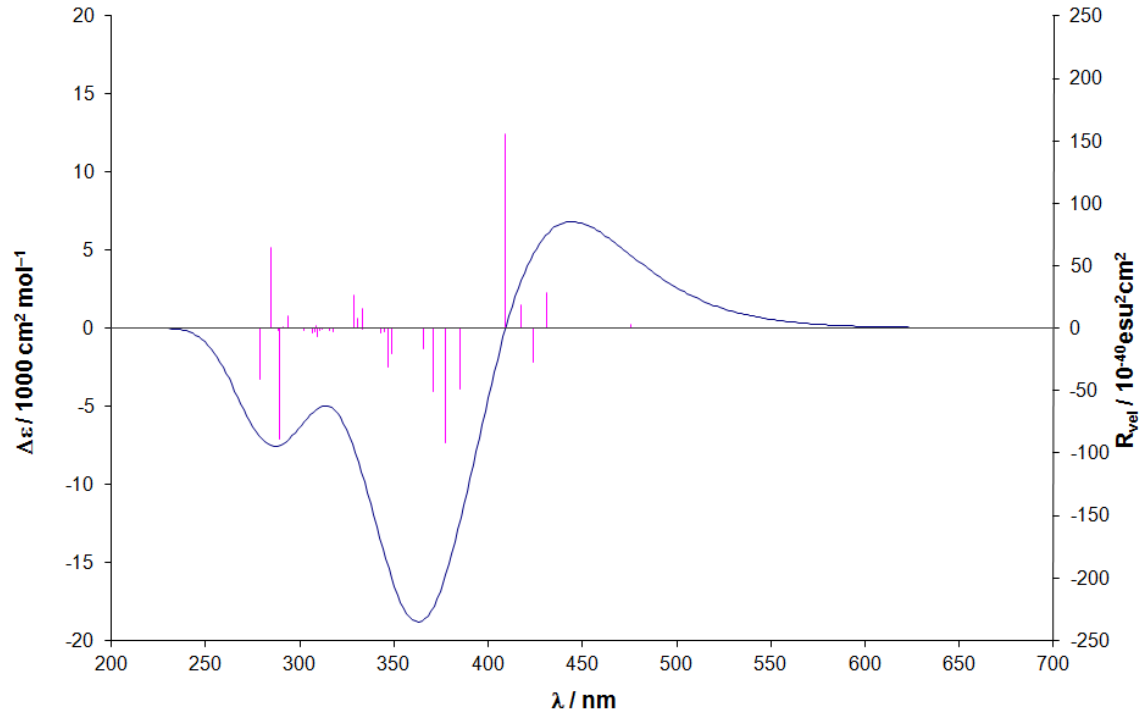

Fig. 145: *Calculated CD spectrum of $[(\mathbf{15})_3Ti]^{2-}$, Λ form, red: rotational strengths; method: TDDFT/B3LYP/TZVP//cam-B3LYP/TZVP.*

The spectra measured in MeOH and in DMSO possess nearly the same shape (Figure 144). As the spectrum in DMSO can be recorded at smaller wavelength, two additional Cotton effects were found in this solvent. The first minimum is located at 220 nm, the

next at 247 nm and the last one at 346 nnm. The maxima are observed at wavelengths of 235, 260 and 408 nm.

wavelength	transitions	rotational strength
408.97	235 → 238	−155.4078
377.6	234 → 237	−91.3243
289.03	231 → 236	−89.1565
284.70	230 → 236	65.042
278.66	232 → 237	−41.3302

Table 22: *The most important excited states of $[(\mathbf{15})_3 Ti]^{2-}$ with the corresponding rotational strengths and their major components.*

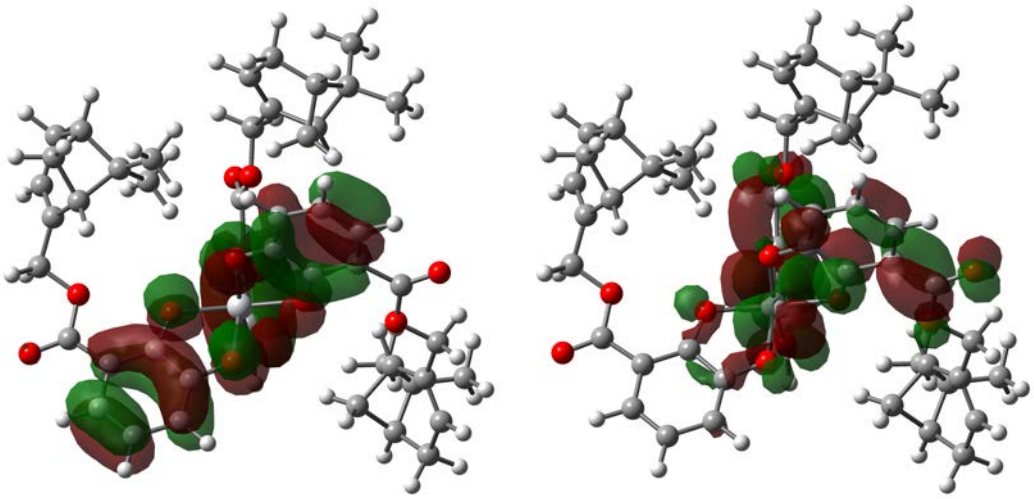

Fig. 146: *HOMO (Ψ=235) and LUMO (Ψ=236) of complex $[(\mathbf{15})_3 Ti]^{2-}$.*

The excitation from HOMO(Ψ=235) to LUMO (Ψ=236) of complex $[(\mathbf{15})_3\mathrm{Ti}]^{2-}$ corresponds as in most of the previously discussed cases to a transition between ligand and the metal center (Figure 146). It contributes significantly to a state that occurs at a wavelength of 431.23 nm with a rotational strength of 28.9991. The calculated CD spectrum (Figure 145) has two minima (268 and 363 nm) and two maxima (314 and 442 nm). Only the Cotton effects at 442 nm and 363 nm can be assigned to CD bands in the experimental spectrum. The measured minimum at 220 in MeOH could not be computationally reproduced. Nevertheless, the comparison of the calculated and the measured spectra shows that the complex most likely adopts the Λ form in both MeOH and DMSO.

Since in a previous case the TD calculation with B3LYP could not explain the Cotton effects of the measured spectrum at smaller wavelengths, the TD calculation was repeated with the cam-B3LYP functional. The result is a spectrum with three maxima (226, 269 and 377 nm) and two minima (251 and 315 nm). They correspond to the

measured extrema at 235 nm (maximum), 247 nm (minimum), 260 nm (maximum), 346 nnm (minimum) and 408 nm (maximum). Again, the blue shift of the calculated spectrum is stronger with cam-B3LYP than with B3LYP, but the low wavelengths region of the spectrum could be reproduced much better at this level of theory.

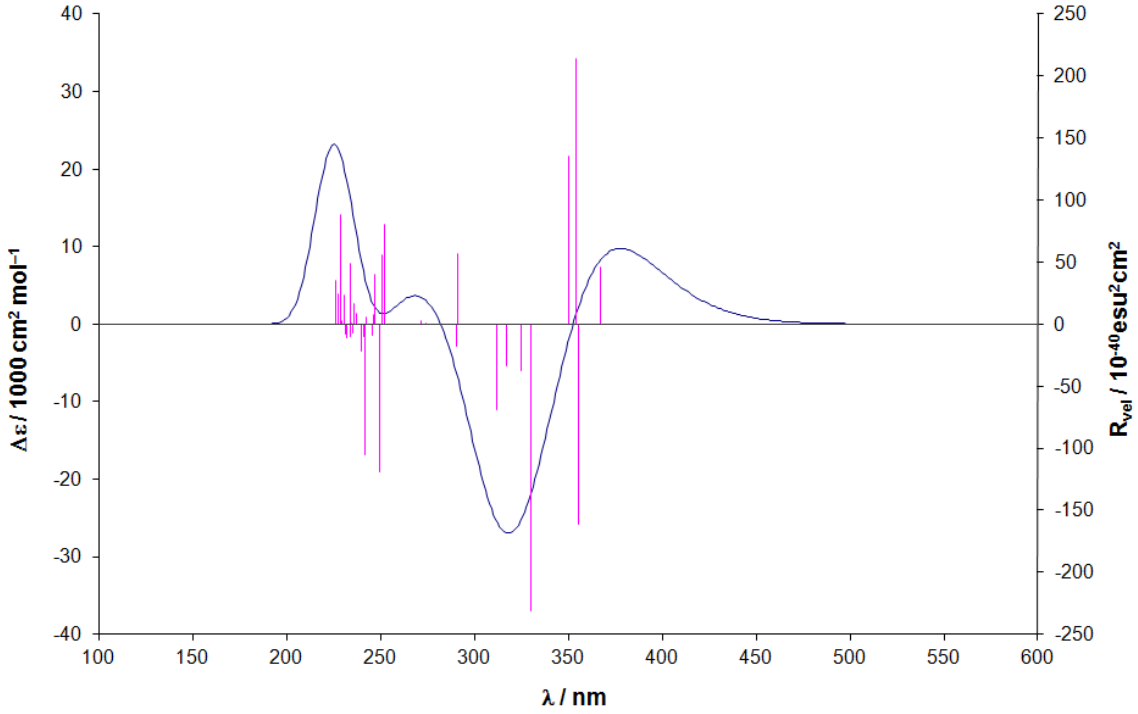

Fig. 147: *Calculated CD spectrum of $[(\mathbf{15})_3 Ti]^{2-}$, Λ form, red: rotational strengths; method: TDDFT/cam-B3LYP/TZVP//cam-B3LYP/TZVP.*

wavelength	transitions	rotational strength
355.73	234 → 239	−161.5931
353.79	235 → 238	214.4111
350.19	233 → 239	135.8975
330.28	234 → 237	−230.9193
251.88	230 → 237	80.1908
249.43	232 → 238	−118.7226
241.68	225 → 239	−104.9468
233.68	230 → 239	49.0931
	226 → 239	
228.59	225 → 237	88.129
	226 → 237	

Table 23: *The most important excited states of $[(\mathbf{15})_3 Ti]^{2-}$ with the corresponding rotational strengths and their major components; method: cam-B3LYP.*

One of the main differences between the transitions calculated with B3LYP and cam-B3LYP is that the low lying occupied MOs like Ψ 225 are not involved in the

TD calculation with B3LYP. The additional Cotton effects observed in the short wavelengths range of the measured spectrum can only be reproduced computationally, if the energetically high transition from these MOs are included into the calculation of the CD spectra.

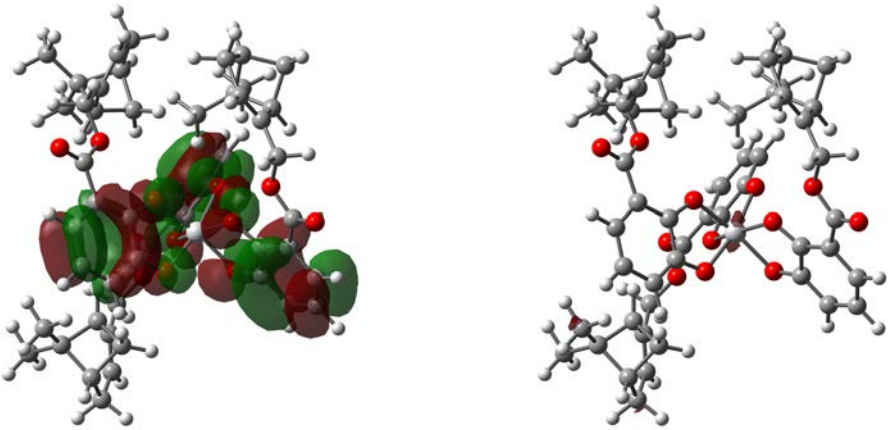

Fig. 148: *HOMO (Ψ=235) and LUMO (Ψ=236) of complex [(**15**)$_3$Ti]$^{2-}$; method: cam-B3LYP.*

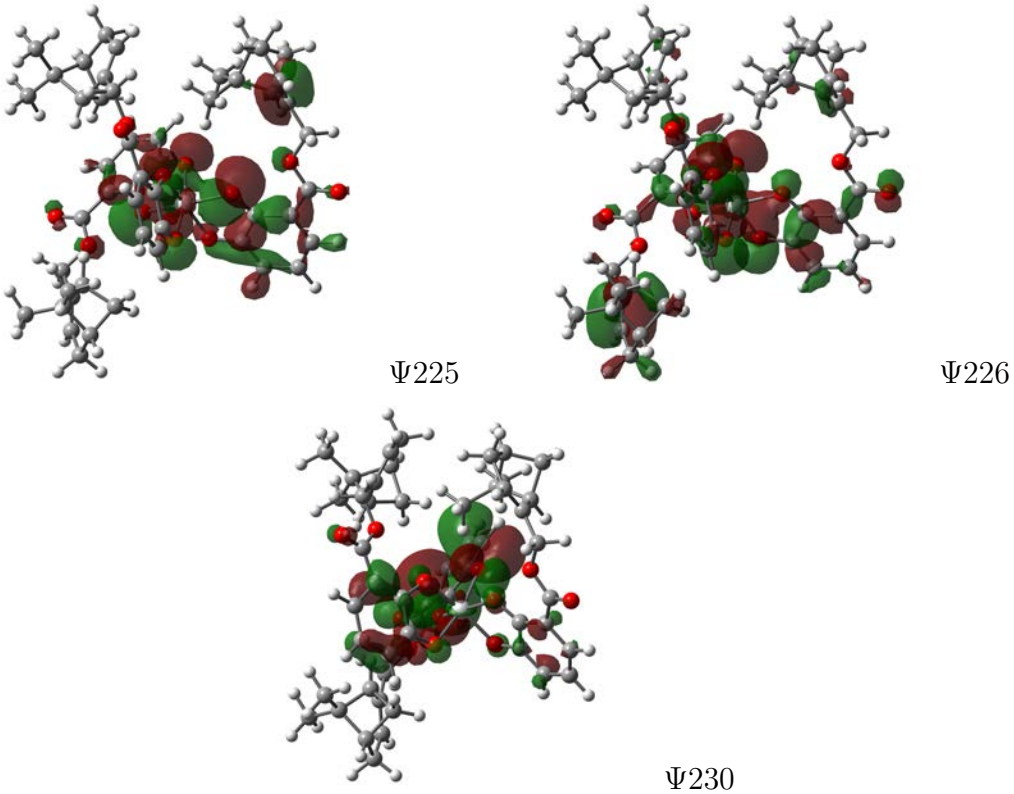

Fig. 149: *Selected Kohn-Sham orbitals of complex [(**15**)$_3$Ti]$^{2-}$; method: cam-B3LYP.*

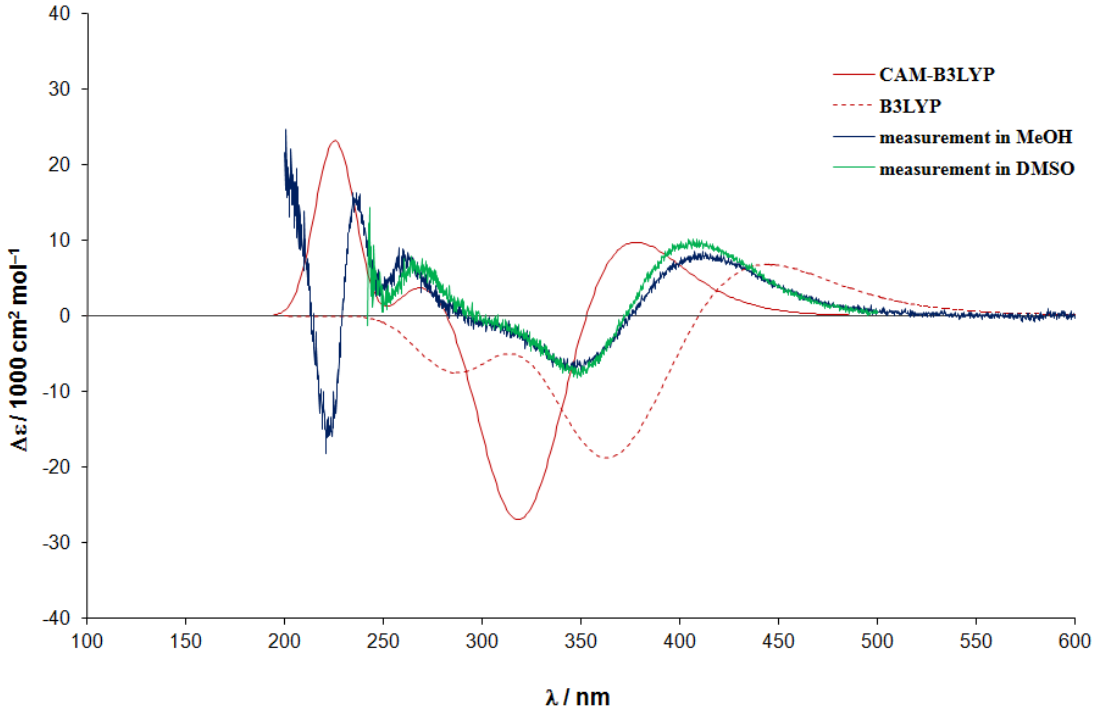

Fig. 150: *Comparison of the measured CD-spectrum of $Li_2[(\mathbf{15})_3Ti]$ with myrthenol in MeOH and DMSO and the calculated spectra (cam-B3LYP and B3LYP).*

The direct comparison between the results obtained with the functional cam-B3LYP and B3LYP (Figure 150) emphasizes that it is important to use cam-B3LYP any time the spectrum shows extrema at low wavelengths, while the match between calculated and measured Cotton effects at longer wavelengths is often better with B3LYP.

In summary, the stereogenic center in the γ position leads to the largest energy difference between the Λ and Δ form of the complex. The most stable monomer is the Λ form. With the stereogenic center in the β position, the energy differences are very small (0.44 and 0.59 kcal/mol). Therefore, the monomer can occur in its Λ or Δ form. This effect is reflected by the measured spectrum as well. Depending on the dipole moment of the solvent and the polarity of the solute one complex adopts the Λ form and the other one the Δ form. Only the complexes with the stereogenic center in the α position always adopt the Λ form in relatively polar DMSO. In less polar MeOH, the complex can switch to the Δ form. With bromine added to the ligand, the switch between the two forms is prohibited as the energy difference of the two monomer forms is much higher (8.01 kcal/mol).

With more than one stereogenic center, the shape of the curve changes and additional Cotton effects occur. To further analyze the effect of changes of the ligands, calculations on slightly changed ligands were performed.

3.4.2.1 Dependence of the CD spectra on small structural changes of the ligand

The influence of different ligands was discussed in the previous chapter. The next step is the analysis of the influence of smaller changes to complex $Li_2[(\mathbf{9})_3Ti]$, as the structure of this complex has shown the strongest dependence on the solvent so far. With bromine at the *ortho* position, the complex does not show this. Therefore, the position of the substituent was changed to the *para* position and bromine was replaced by fluorine, chlorine and iodine (Figure 151).

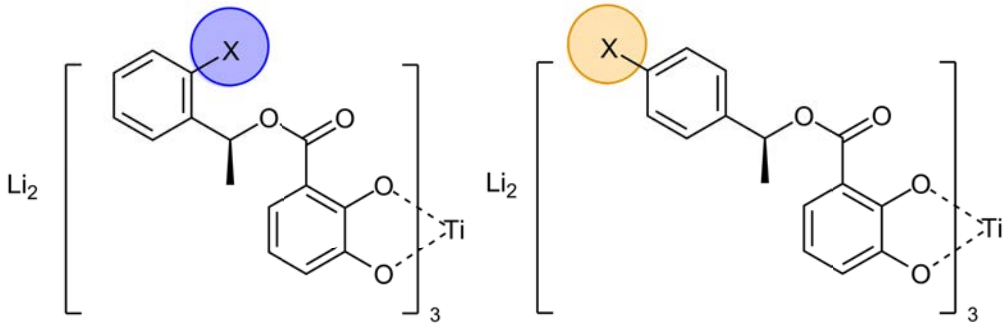

Fig. 151: *Complex $Li_2[(\mathbf{9})_3Ti]$ with X=F, Cl, Br, or I in ortho (blue) or para position (yellow).*

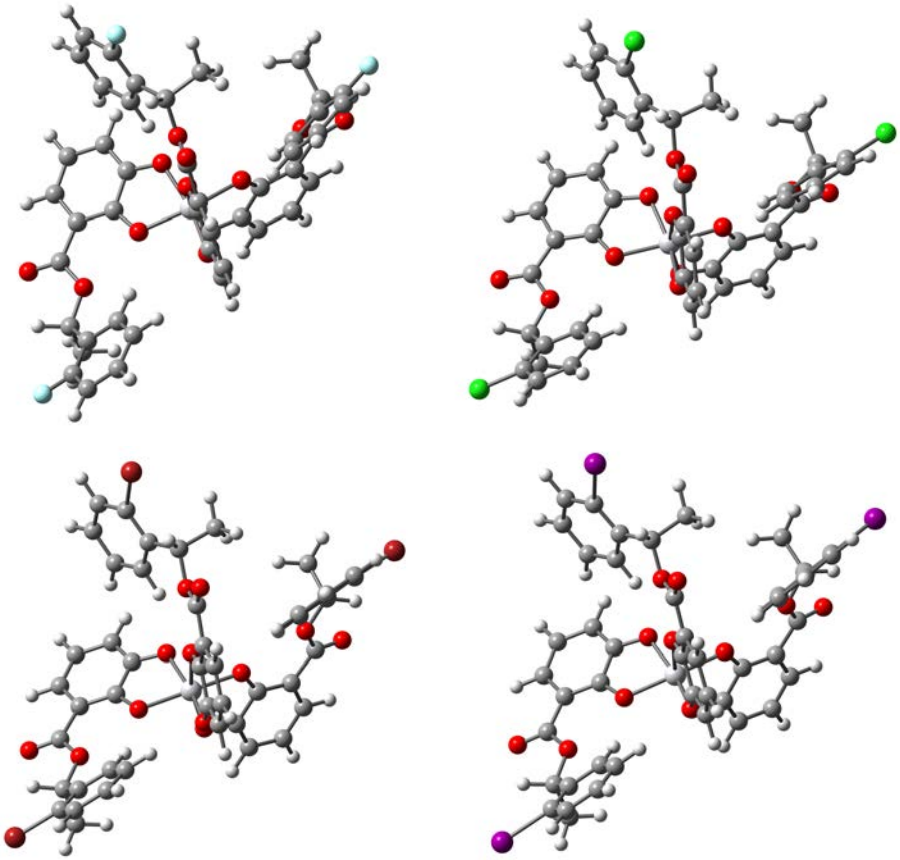

Fig. 152: *With cam-B3LYP/TZVP energetically optimized complex $Li_2[(\mathbf{9})_3Ti]$ with F (blue), Cl (green), Br (red), and I (purple).*

The complexes with X= F, Cl, Br, or I were geometrically optimized with the halogen in their *ortho* and *para* position. The resulting energies of the Λ and Δ form are presented in Tables 24 and 25. The energy of the halogens was subtracted to obtain a "reduced" energy of the different complexes, which reflects merely the influence of the halogen on the rest of the complex and, therefore, allows the comparison of their energies.

halogen	form	energy in a.u.*	energy difference in kcal/mol
F	Λ	−2696.062872	−7.800
F	Δ	−2696.050442	
Cl	Λ	−2695.892451	−7.964
Cl	Δ	−2695.879760	
Br	Λ	−2695.835303	−8.011
Br	Δ	−2695.822536	
I	Λ	−2695.753943	−8.052
I	Δ	−2695.741112	

Table 24: *Energies of the optimized complexes $Li_2[(\mathbf{9})_3Ti]$ with the different halogens in the ortho position, *the energy of the halogens was subtracted.*

The differences of the energies of the Λ and Δ form (Table 24) show a clear tendency to increase in the order F, Cl, Br, and I; the energy of the complexes increase in the same order. As iodine has the largest radius, the effect on the complex is the most significant one. The resulting difference between the Λ and Δ form is significant.

halogen	form	energy in a.u.*	energy difference in kcal/mol
F	Λ	−2696.062019	−9.024
F	Δ	−2696.047637	
Cl	Λ	−2695.895084	−7.624
Cl	Δ	−2695.882934	
Br	Λ	−2695.839403	−7.732
Br	Δ	−2695.827081	
I	Λ	−2695.759979	−7.880
I	Δ	−2695.747422	

Table 25: *Energies of the optimized complexes $Li_2[(\mathbf{9})_3Ti]$ with the different halogens in the para position, *the energy of the halogens was subtracted.*

The energy difference of the complexes with the halogen at the *para* position (Table 25) does not show a clear tendency. The *para* position seems to have a less significant influence on the structure of the complex. The complex with the smallest halogen fluorine results in the largest energy difference of 9.024 kcal/mol, where the Λ form has a lower energy. Its methyl groups (blue) (Figure 153) point towards the opposite phenyl group (yellow) of the bordering ligand. Within the Δ form, the two phenyl

groups point towards each other. The smallest C-C distance between the phenyl rings of the complex with fluorine is 3.689 Å.

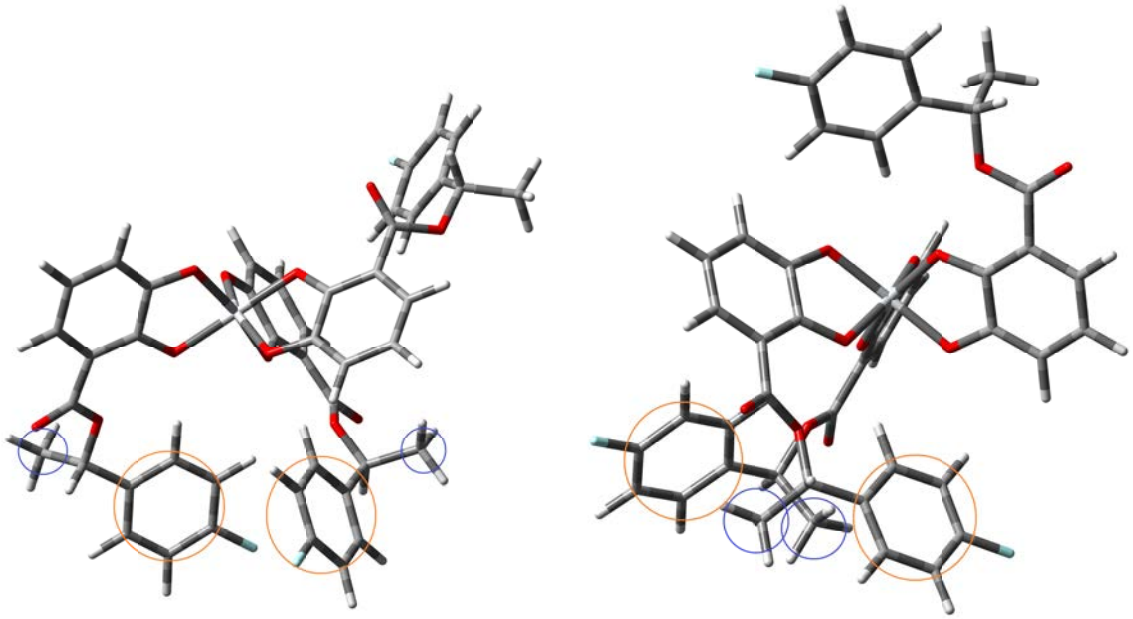

Fig. 153: *Calculated* Δ *(left) and* Λ *(right) form of complex* $[(\mathbf{9})_3 Ti]^{2-}$ *with fluorine; method: cam-B3LYP/TZVP.*

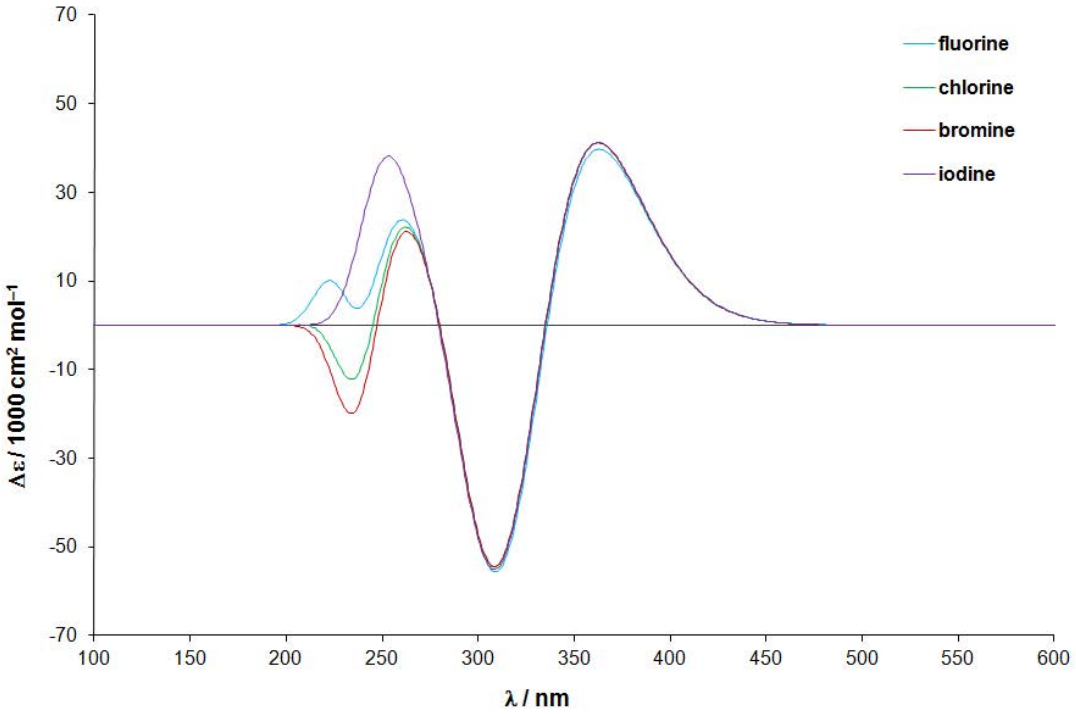

Fig. 154: *Calculated CD spectrum of complex* $[(\mathbf{9})_3 Ti]^{2-}$ *with the halogens F, Cl, Br, and I in the ortho position; method: TDDFT/cam-B3LYP/TZVP//cam-B3LYP/TZVP.*

halogen	wavelength	transitions	rotational strength
F	230.86	215 → 227	42.85
	249.99	215 → 222	216.02
	323.30	218 → 222	−255.42
	341.39	218 → 223	128.48
Cl	247.72	227 → 234	−131.73
	249.85	227 → 234	161.92
		230 → 235	
	323.27	230 → 234	−249.08
	345.60	232 → 242	141.98
Br	247.69	254 → 261	−96.23
	250.48	255 → 262	222.36
	323.52	257 → 261	−248.20
	345.71	259 → 272	141.98
I	247.72	213 → 225	209.75
	249.85	215 → 222	−249.05
	323.27	217 → 233	149.59

Table 26: *The most important excited states of $[(\mathbf{9})_3Ti]^{2-}$ with the corresponding rotational strengths and their major components, halogens in the ortho position, HOMO: Ψ=220 (for F), Ψ=232 (for Cl), Ψ=259 (for Br) and Ψ=217 (for I).*

The most important excited states of $[(\mathbf{9})_3\mathrm{Ti}]^{2-}$ with the different halogens are presented in Table 26. The largest difference between the rotational strengths are found at the smallest wavelengths. The spectra of the complexes with chlorine and bromine differ from those obtained for iodine and fluorine compounds in that they are negative below 250 nm while the curves of the complexes with F- and I-substituted ligands have only positive Cotton effects in this region.

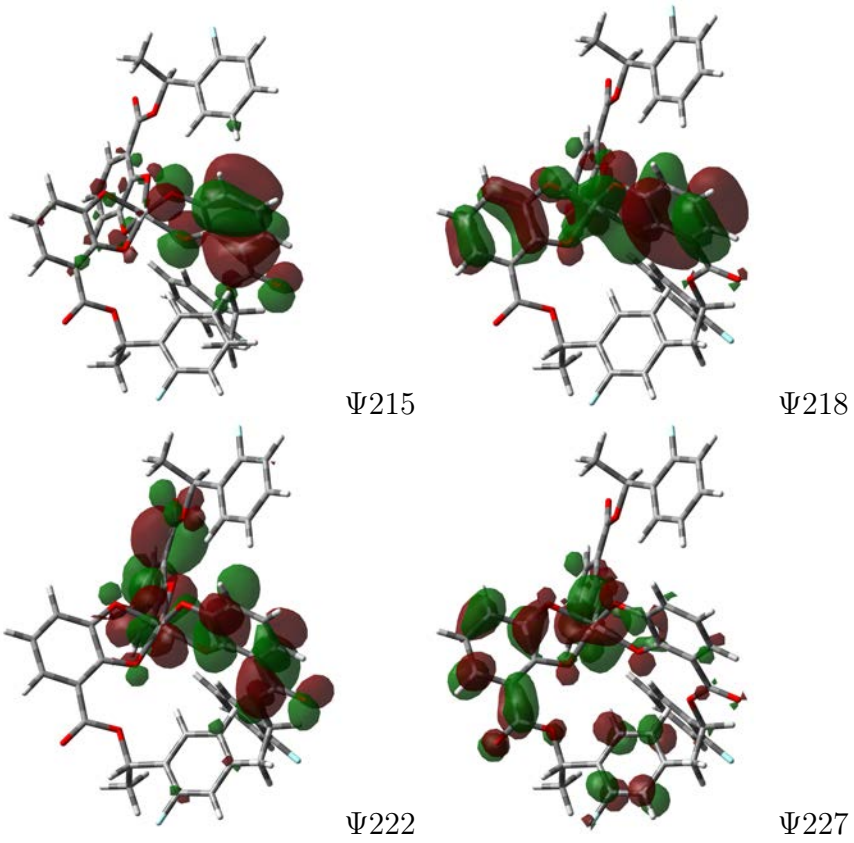

Fig. 155: *Selected Kohn-Sham orbitals of complex $[(\mathbf{9})_3 Ti]^{2-}$ with fluorine in the ortho position; HOMO: Ψ=220, method: cam-B3LYP.*

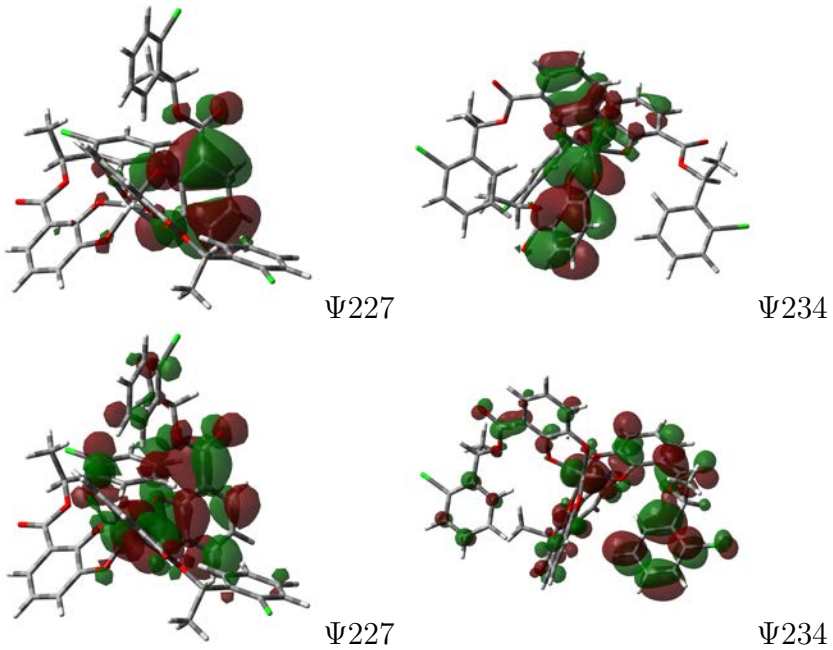

Fig. 156: *Selected Kohn-Sham orbitals of complex $[(\mathbf{9})_3 Ti]^{2-}$ with chlorine in the ortho position; HOMO: Ψ=232, method: cam-B3LYP.*

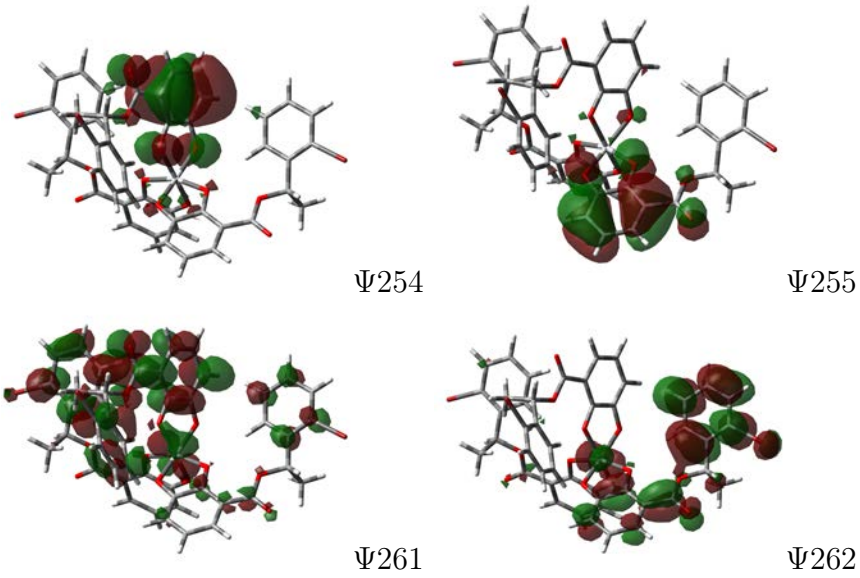

Fig. 157: *Selected Kohn-Sham orbitals of complex $[(\mathbf{9})_3 Ti]^{2-}$ with bromine in the ortho position; HOMO: Ψ=259, method: cam-B3LYP.*

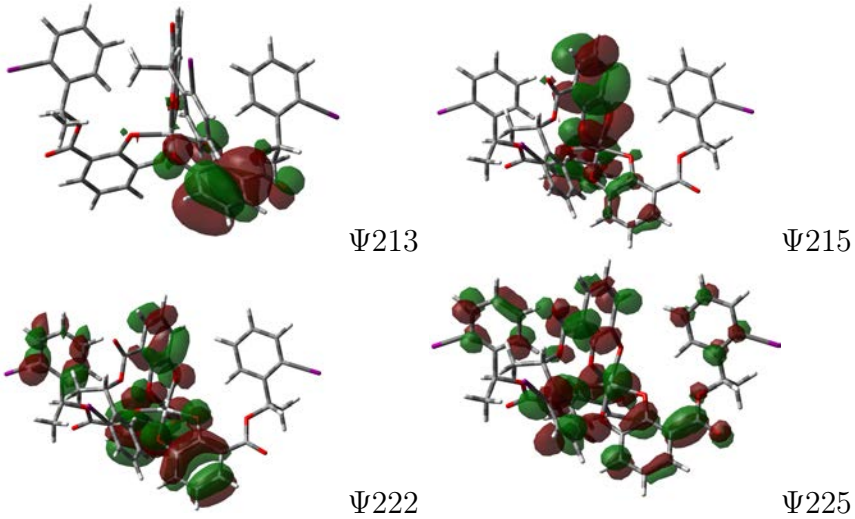

Fig. 158: *Selected Kohn-Sham orbitals of complex $[(\mathbf{9})_3 Ti]^{2-}$ with iodine in the ortho position; HOMO: Ψ=217, method: cam-B3LYP with ECP for I (MWB46).*

Figures 155, 156, 157 and 158 reveal that the most important states at lower wavelengths include transitions between the ligand and the metal center. The corresponding transitions of the complexes with bromine and chlorine also involve the halogen. Both give CD curves of similar shapes.

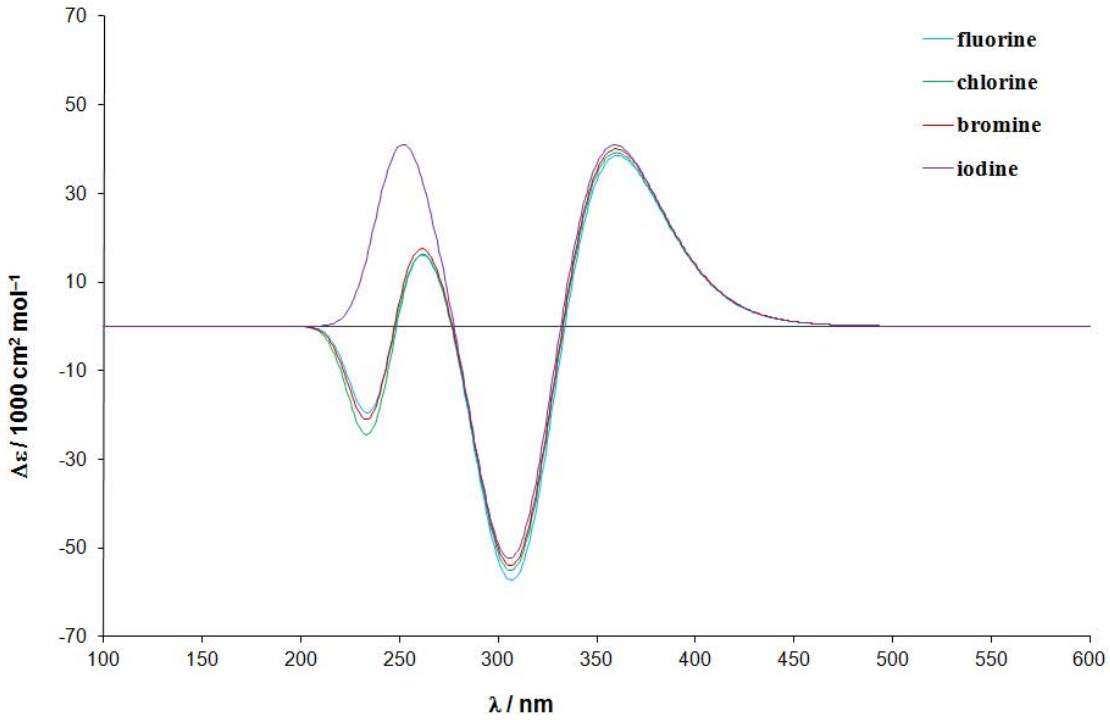

Fig. 159: *Calculated CD spectrum of complex $[(\mathbf{9})_3Ti]^{2-}$ with the halogens F, Cl, Br, and I in the para position; method: TDDFT/cam-B3LYP/TZVP//cam-B3LYP/TZVP.*

The shape of the spectra of complex $[(\mathbf{9})_3\mathrm{Ti}]^{2-}$ with the halogens in the *para* position (Figure 159) is similar to the shape of the spectra of the complex with the *ortho*-halogenated ligands. However, there are some minor differences. In the last one, only the CD spectrum of complex containing iodine differs from the spectra of the complexes containing the other halogens, which are quite similar. This underlines that the influence of the halogen in the *para* position is apparently less significant.

All in all the influence of the change of the halogen position (*ortho* or *para*) on the CD spectrum depends on the halogen size. Therefore iodine has the largest influence on the spectrum in the *ortho* position (Table 26). The energies of the complexes with the halogen in *para* position indicate that fluorine should have the most significant effect (Table 27) and, therefore, the corresponding spectrum should differ significantly from those with the other halogens. However, this is not the case: Iodine is the exception as the spectrum looks different for this halogen.

halogen	wavelength	transitions	rotational strength
F	246.84	215 → 227	−127.99
	249.24	215 → 222	122.89
	319.52	218 → 222	−241.07
	344.71	218 → 223	138.02
Cl	246.93	227 → 234	−153.89
	248.15	227 → 234	156.71
	319.65	230 → 234	−231.07
	340.73	232 → 242	155.68
Br	240.89	254 → 261	−109.63
	250.03	255 → 262	123.37
	319.66	257 → 261	−233.16
	340.66	259 → 272	144.63
I	248.33	213 → 225	187.52
	320.67	215 → 222	−177.05
	340.61	217 → 233	151.56

Table 27: *The most important excited states of $[(\mathbf{9})_3 Ti]^{2-}$ with the corresponding rotational strengths and their major components, halogens in the para position, HOMO: Ψ=220 (for F), Ψ=232 (for Cl), Ψ=259 (for Br) and Ψ=217 (for I).*

- **Dependence of the number of stereogenic centers on the CD spectra**

To understand the influence of the stereogenic centers on the CD spectra, the three possible positions of such a center within one complex were stepwise eliminated (Figure 160). The resulting structures were energetically optimized at the cam-B3LYP level of theory and TD-DFT calculations were performed afterwards.

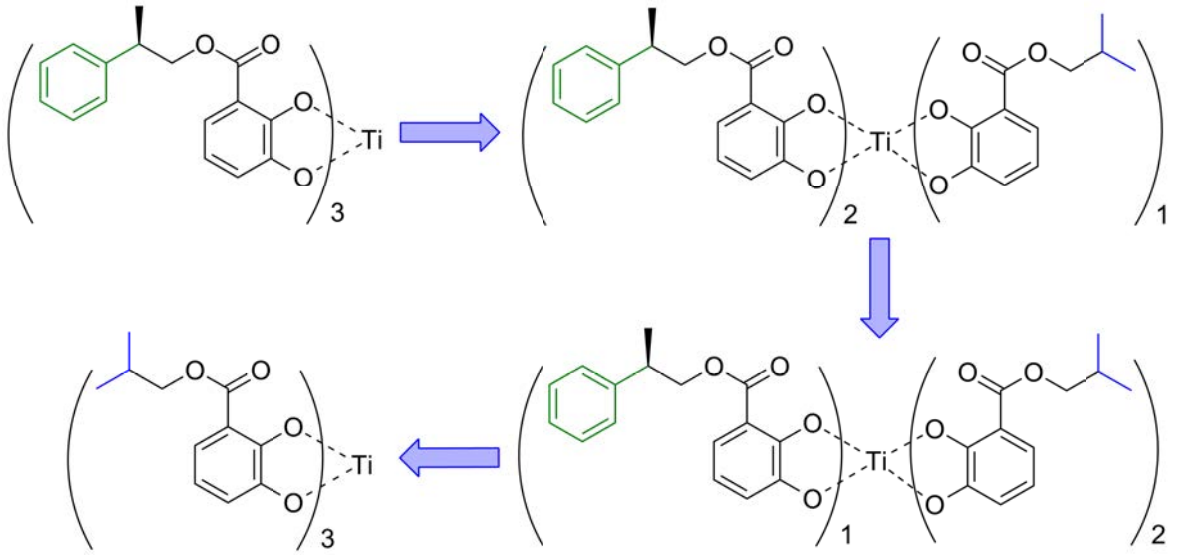

Fig. 160: *Stepwise elimination of the stereogenic centers by replacing the phenyl substituents with methyl-groups; method: cam-B3LYP/TZVP.*

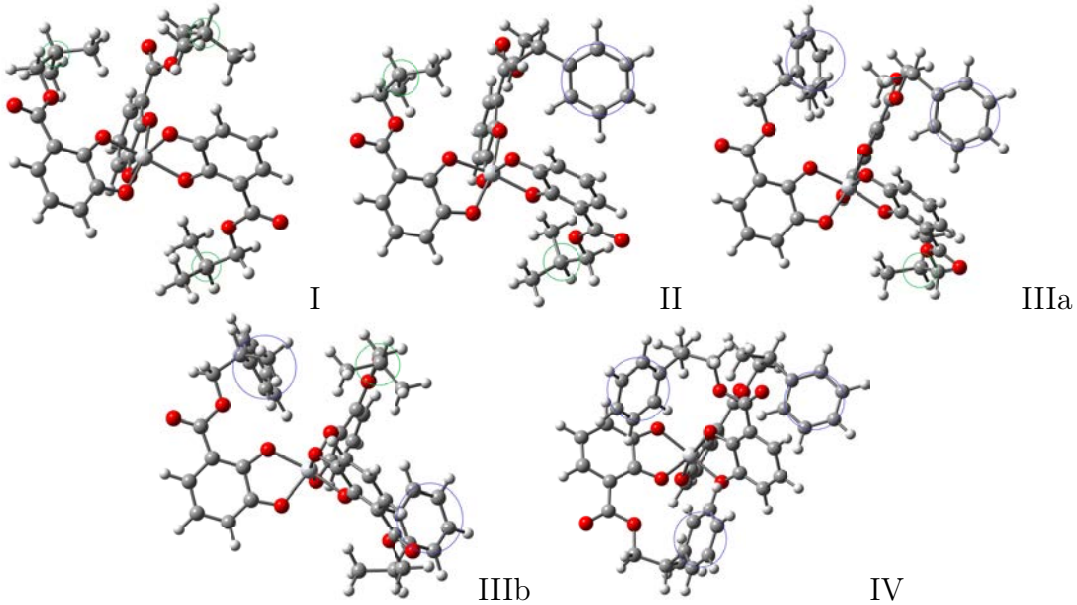

Fig. 161: *Calculated structures of complex [(**9**)$_3$Ti]$^{2-}$ (Λ form) with different numbers of stereogenic centers; blue: phenyl groups, green: methyl-groups.*

form	stereogenic centers	energy in a.u.	energy difference in kcal/mol
Λ	0	−2240.339635	0.00
Δ	0	−2240.339635	
Λ	1	−2432.029671	0.54
Δ	1	−2432.030524	
Λ	2*	−2623.718720	−0.14
Δ	2*	−2623.718492	
Λ	2	−2623.718012	−2.19
Δ	2	−2623.714996	
Λ	3	−2815.408025	−0.44
Δ	3	−2815.407325	

Table 28: *method: B3LYP, *with stereogenic center pointing in different directions.*

In Figure 161 the geometrically optimized structures of complex [(**9**)$_3$Ti]$^{2-}$ with different numbers of stereogenic centers are presented (complex **9- I, II, IIIa, IIIb, and IV**). The resulting energies (Table 28) show no difference between the Δ and Λ form without a stereogenic center (complex **9-I**). This value increases if more stereogenic centers are involved. They have a big influence on the geometry of the complex. The largest energy difference (−2.19 kcal/mol) is obtained with two stereogenic centers pointing in the same direction (complex **9-IIIa**). If the stereogenic centers are oriented like this, they have the smallest possible distance to each other. Pointing in different directions (complex **9-IIIb**), the complex with two stereogenic centers has a very small energy difference (0.014 kcal/mol). The complex with three different stereogenic centers does not have the largest energy difference, as the big rests of the ligand have

strong repulsive interactions in the Δ and in the Λ form.

Table 29 compares the energies resulting from the cam-B3LYP calculations. The tendency is the same as in the previous Table with the results of the B3LYP calculations. The only difference is a smaller difference between the two possible conformations of the complexes with two stereogenic centers (Figure160 **IIIa**, **IIIb**).

form	stereogenic centers	energy in a.u.	energy difference in kcal/mol
Λ	0	−2122.434713	0.00
Δ	0	−2122.434713	
Λ	1	−2314.125622	0.65
Δ	1	−2314.124580	
Λ	2*	−2505.815609	0.64
Δ	2*	−2505.814590	
Λ	2	−2505.815510	0.71
Δ	2	−2505.816649	
Λ	3	−2697.506206	0.05
Δ	3	−2697.506284	

Table 29: *method: cam-B3LYP, *with stereogenic center pointing in different directions.*

In the next step, the CD spectra of each complex were calculated. The results for the TD-DFT calculations with B3LYP are shown in Figure 162 and for the calculations with cam-B3LYP in Figure 163.

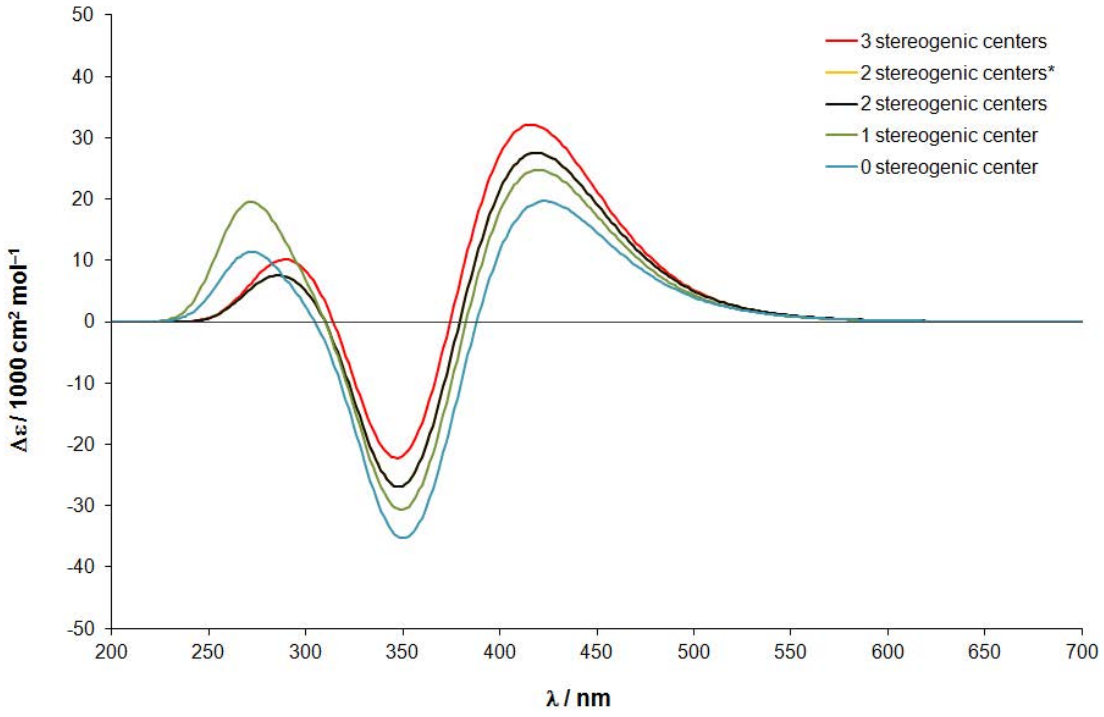

Fig. 162: *Calculated CD spectrum of complex $[(\mathbf{9})_3 Ti]^{2-}$ with different numbers of stereogenic centers, method: B3LYP, *with stereogenic center pointing in different directions.*

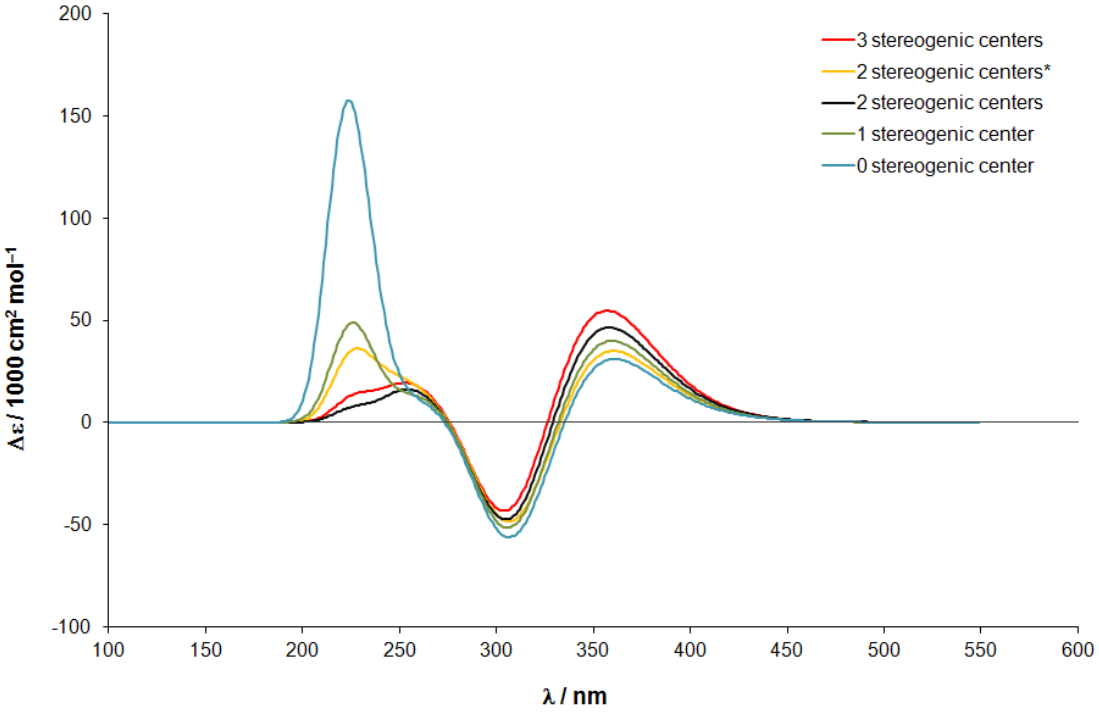

Fig. 163: *Calculated CD spectrum of complex $[(\mathbf{9})_3 Ti]^{2-}$ with different numbers of stereogenic centers, method: cam-B3LYP, *with stereogenic center pointing in different directions.*

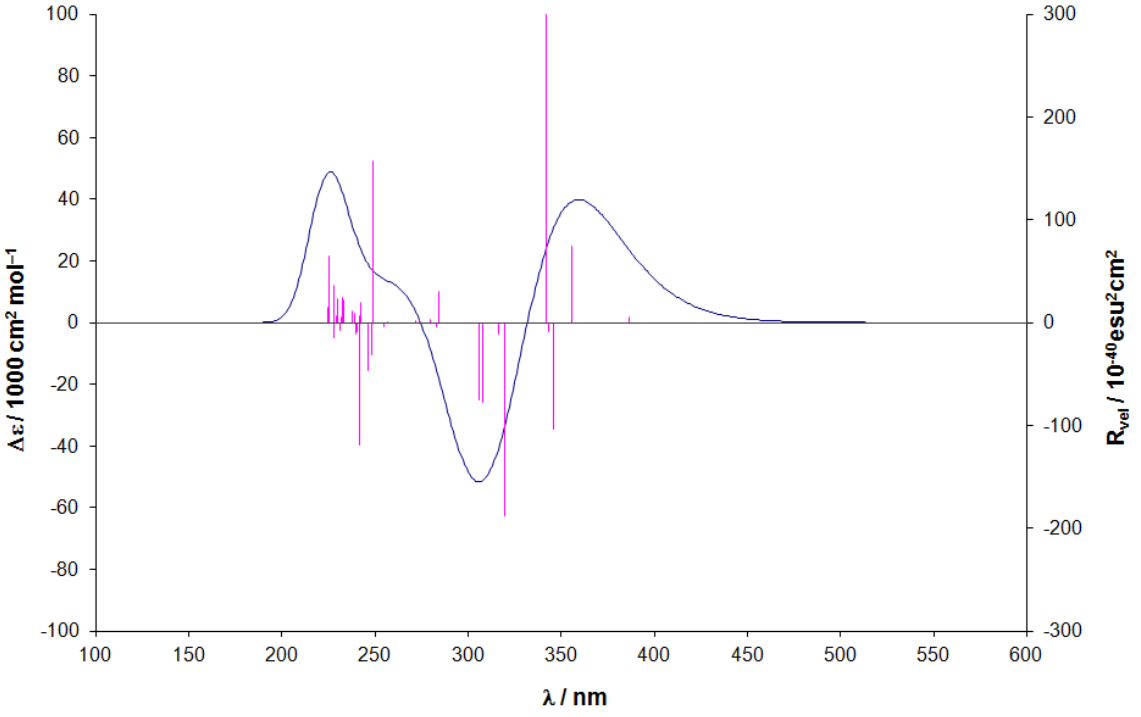

Fig. 164: *Calculated CD spectrum with rotational strength of complex $[(\mathbf{9})_3 Ti]^{2-}$ without stereogenic centers; method: TDDFT/cam-B3LYP/TZVP//cam-B3LYP/TZVP.*

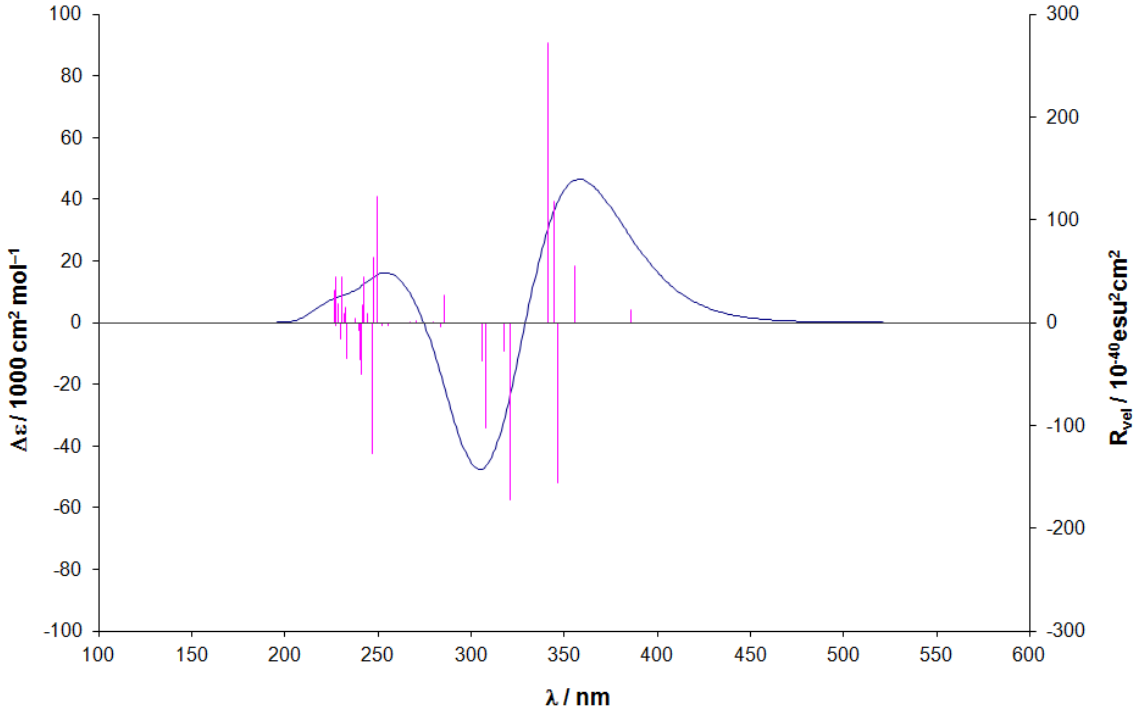

Fig. 165: *Calculated CD spectrum with rotational strength of complex [(**9**)$_3$Ti]$^{2-}$ with two stereogenic centers pointing in the same direction (complex **9-IIIa**); method: TDDFT/cam-B3LYP/TZVP//cam-B3LYP/TZVP.*

The calculated spectra obtained with the B3LYP functional do not show differences in the shapes of the curves. Only with the cam-B3LYP functional, differences at the smaller wavelength become obvious. The most significant difference was obtained between the spectra of the complex without stereogenic centers and the complex with two stereogenic centers pointing in the same direction (complex **9-IIIa**). Therefore the two spectra of the most stable conformers including the underlying rotational strengths are presented in the Figures 164 and 165.

Table 30 lists the most important excited states of [(**9**)$_3$Ti]$^{2-}$ with the corresponding rotational strengths and their major components obtained with the cam-B3LYP functional.

The different spectra of the complex without a stereogenic center and with one stereogenic center can be explained by means of the rotational strengths listed in Table 30. At lower wavelengths, both spectra have strong rotational strength. Without a stereogenic center, the spectrum has strong rotational strengths at wavelengths of 224 nm and at 222 nm. With one stereogenic center, the strong effects can be noticed at a wavelengths of 228 nm and 225 nm. With more stereogenic centers, the rotational strengths at lower wavelengths are much smaller. The magnetic transition dipole moments for the transition at the lower wavelengths increase if less stereogenic centers are present (Table 31) while the electronic dipole moment increases (exception: one stereogenic center) with an increasing number of stereogenic centers (Figure 32).

stereogenic centers	wavelength/ nm	transitions	rotational strength
0	345.22	171 → 176	−99.2237
	342.10	171 → 176	306.1687
	317.97	170 → 174	−119.5649
	316.81	171 → 174	−100.556
	248.58	169 → 174	134.9517
	225.29	164 → 174	151.9402
	223.62	166 → 175	134.9517
	222.39	169 → 173	147.8123
1	345.71	187 → 192	−104.1893
	341.72	188 → 191	352.4056
	319.56	186 → 190	−187.687
	248.69	183 → 190	156.6591
	241.32	182 → 192	−118.5431
	227.53	185 → 190	35.7954
	225.18	179 → 190	65.1275
2*	346.64	203 → 208	−155.2282
	344.43	202 → 208	118.0582
	341.54	204 → 207	272.7771
	320.94	203 → 206	−173.0085
	307.95	202 → 207	−101.9329
	249.16	199 → 206	122.3023
	246.55	201 → 207	−126.9166
	226.97	194 → 206	44.9041
	226.76	195 → 206	31.6536
2	344.58	203 → 208	−88.8918
	341.60	202 → 208	370.2818
	319.04	202 → 206	−163.2441
	248.38	200 → 206	98.7388
	247.31	201 → 207	121.2646
	245.88	199 → 206	−167.8967
	230.68	203 → 211	24.0064
	228.12	202 → 212	18.2874
3	356.12	220 → 222	106.7144
	341.35	218 → 224	372.0257
	320.36	218 → 222	−171.5036
	247.34	215 → 223	179.1379
	246.01	217 → 223	−146.4981
	240.20	217 → 224	−130.4897
	228.57	218 → 230	9.2993

Table 30: *The most important excited states of $[(\mathbf{9})_3Ti]^{2-}$ with the corresponding rotational strengths and their major components, method: cam-B3LYP, *with the stereogenic center pointing in different directions.*

stereogenic centers	wavelength / nm	dipole moments [a]			$\sqrt{X^2+Y^2+Z^2}$
		X	Y	Z	
0	222.39	-0.9246	1.2310	-0.1379	1.55
1	225.18	-0.1160	0.2975	-0.6809	0.75
2*	226.76	-0.1004	-0.0167	0.6149	0.62
2	228.12	0.1040	-0.2074	-0.3834	0.45
3	228.57	-0.1782	-0.2241	0.2399	0.37

Table 31: *Magnetic transition dipole moments $[(\mathbf{9})_3Ti]^{2-}$, method: cam-B3LYP/TZVP, *with the stereogenic center pointing in different directions, [a] ground to excited state transition magnetic dipole moments in Au.*

stereogenic centers	wavelength / nm	dipole moments [a]			$\sqrt{X^2+Y^2+Z^2}$
		X	Y	Z	
0	222.39	0.1263	-0.2429	-0.0146	0.27
1	225.18	0.2770	0.1817	0.3963	0.52
2*	226.76	-0.1296	0.0005	-0.1795	0.22
2	228.12	0.2648	0.2661	0.1606	0.41
3	228.57	-0.3471	0.3345	-0.0970	0.49

Table 32: *Electric transition dipole moments $[(\mathbf{9})_3Ti]^{2-}$, method: cam-B3LYP/TZVP, *with the stereogenic center pointing in different directions, [a] ground to excited state transition electric dipole moments in Au.*

The following Figures show the corresponding Kohn-Sham orbitals which participate in the main transition of the different spectra of complex $[(\mathbf{9})_3Ti]^{2-}$.

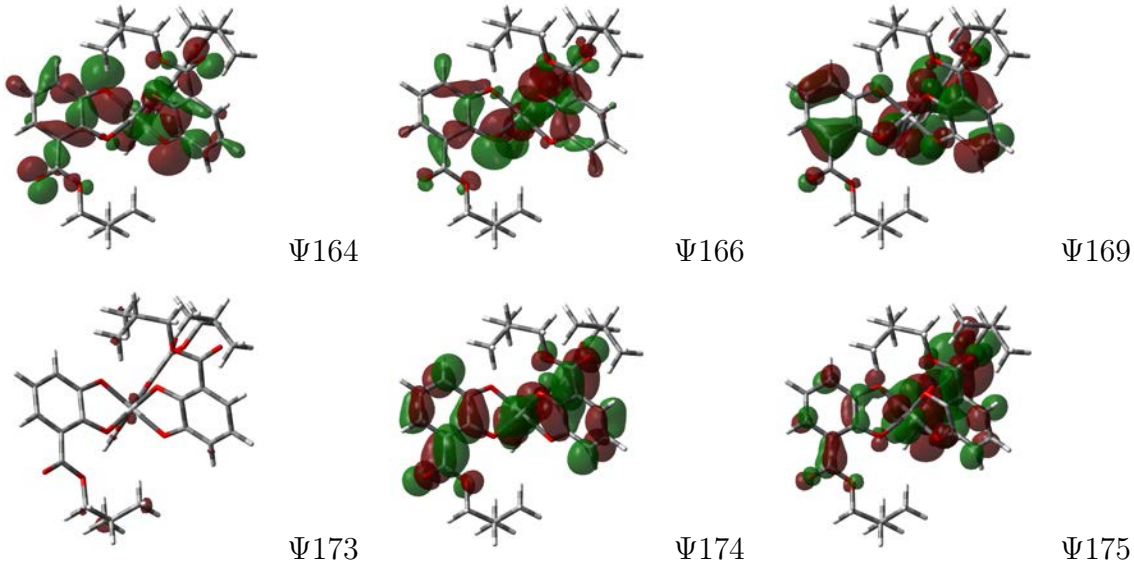

Fig. 166: *Selected Kohn-Sham orbitals of complex $[(\mathbf{9})_3Ti]^{2-}$ without stereogenic centers; HOMO: Ψ=172, method: cam-B3LYP.*

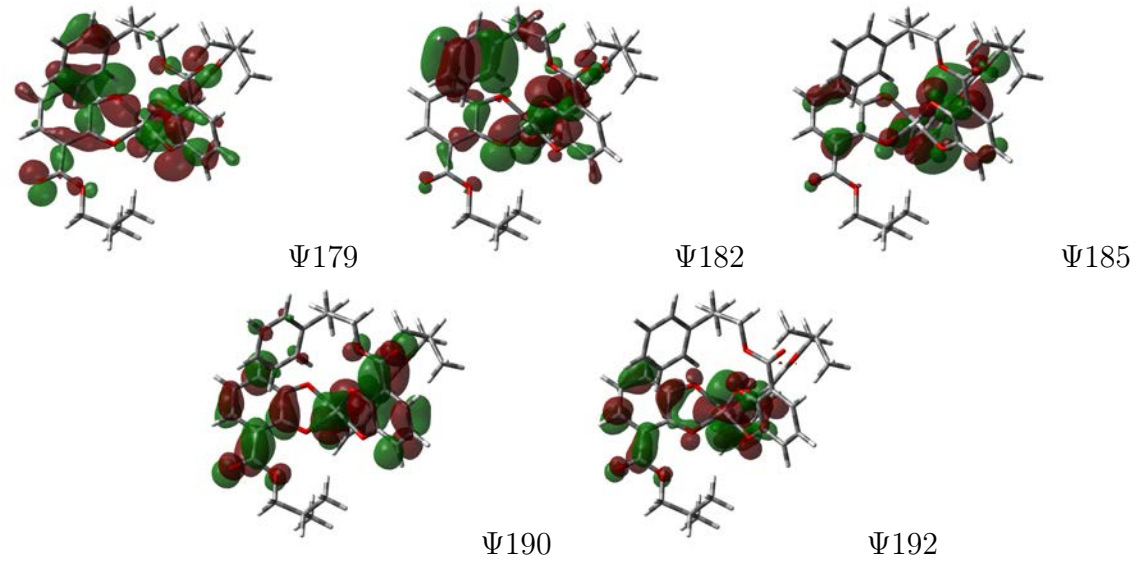

Fig. 167: *Selected Kohn-Sham orbitals of complex* $[(\mathbf{9})_3 Ti]^{2-}$ *without stereogenic centers; HOMO:* Ψ*=188, method: cam-B3LYP.*

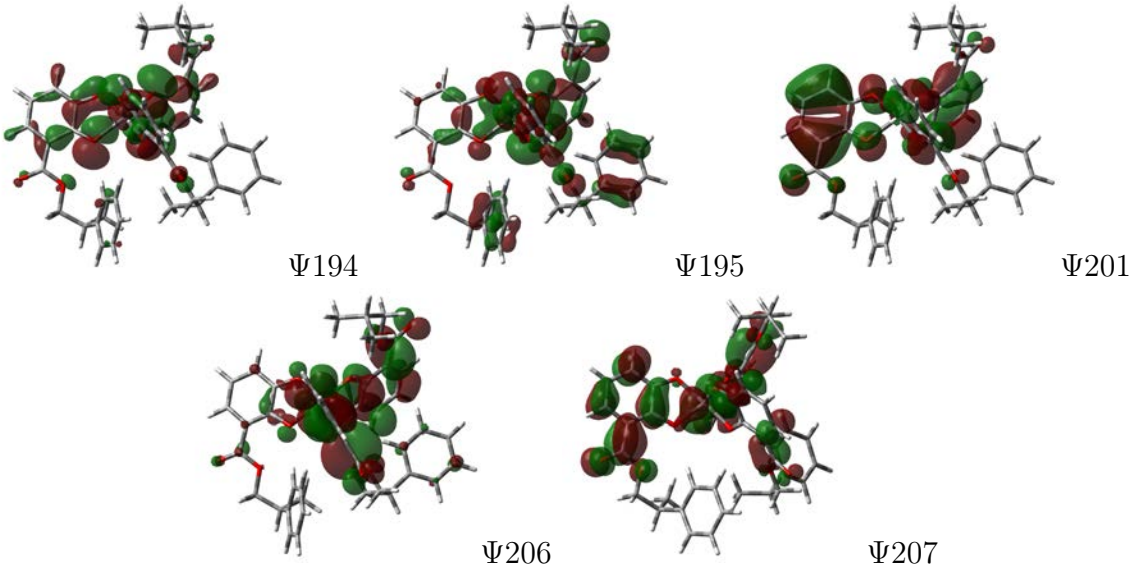

Fig. 168: *Selected Kohn-Sham orbitals of complex* $[(\mathbf{9})_3 Ti]^{2-}$ *with two stereogenic centers pointing in different directions; HOMO:* Ψ*=204, method: cam-B3LYP.*

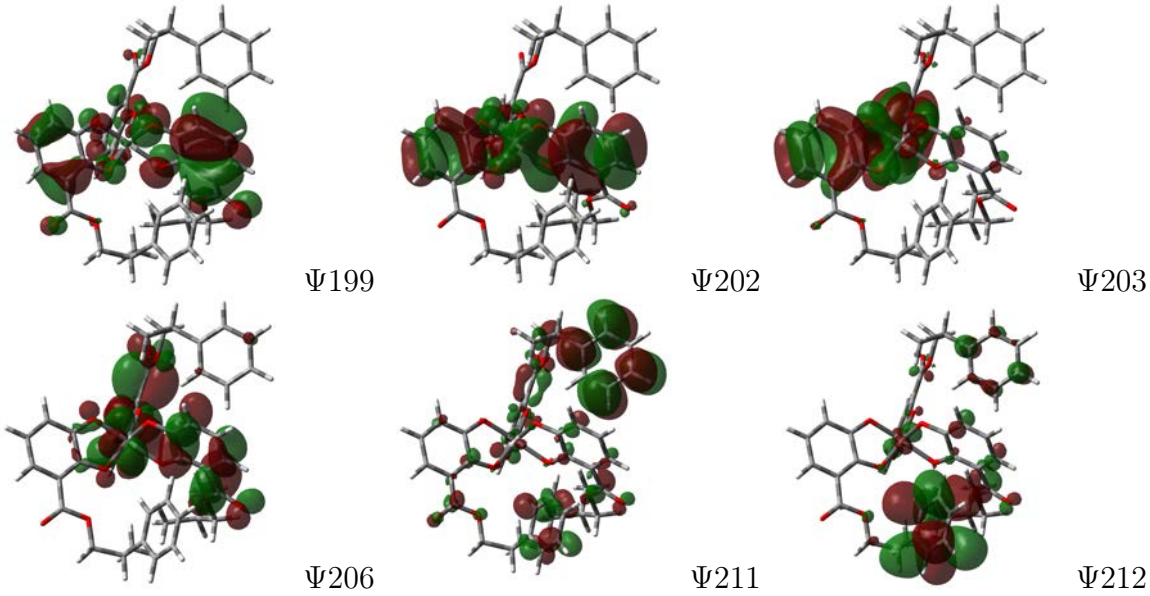

Fig. 169: *Selected Kohn-Sham orbitals of complex $[(\mathbf{9})_3 Ti]^{2-}$ with two stereogenic centers; HOMO: Ψ=204, method: cam-B3LYP.*

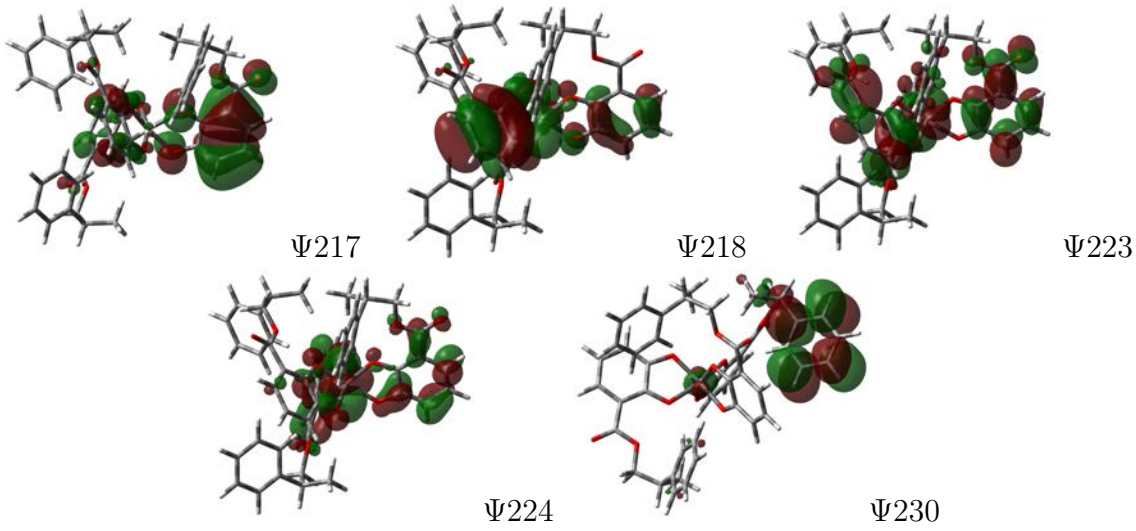

Fig. 170: *Selected Kohn-Sham orbitals of complex $[(\mathbf{9})_3 Ti]^{2-}$ with three stereogenic centers; HOMO: Ψ=220, method: cam-B3LYP.*

The study of the dependence of the CD spectra on the stereogenic center has shown that the shape of the main part of the curve is widely independent on the number of stereogenic centers. The most significant effect on the shape of the spectral curves of the complexes is observed at smaller wavelengths, where a more intense Cotton effect is obtained for the complexes with one and no stereogenic center. The underlying states in this part of the spectrum involve significant ligand to metal transitions, which cause stronger rotational strengths if less stereogenic centers are present.

- **Complexes with Ga(III)**

To analyze the effect of the metal center on the Circular Dichroism, complexes with Ga(III) instead of Ti(IV) were chosen as an alternative. The studies with the model complex $[(5)_3Ga]^{3-}$ indicate that the change of the anticipated spectra compared to those of the complexes with Ti(IV) will be significant.

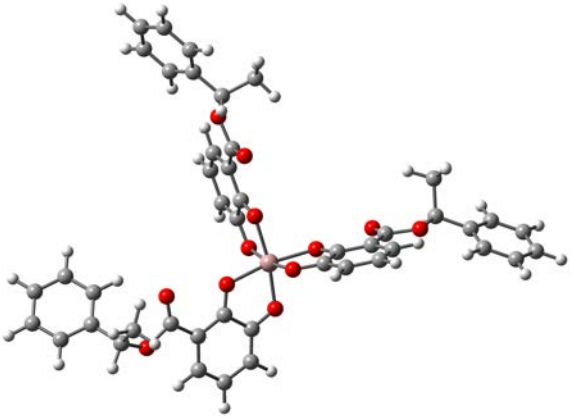

Fig. 171: *Optimized geometry of the Δ form of complex [(**9a**)$_3$Ga]$^{3-}$; method: cam-B3LYP/TZVP.*

One of these complexes is based on complex **9** where Ga(III) is the metal instead of Ti(IV) and the stereogenic center is in the α position. The CD spectrum of the resulting complex was measured. The experimental spectra in MeOH and DMSO include a configurational reversal upon change of the solvent as was already detected with $Li_2[(\mathbf{9})_3Ti]$ (Figure 102). In DMSO, the minima appear at 270 and 410 nm, while a maximum is found at 351 nm (Figure172). In MeOH, two maxima are found at 246 and 381 nm, and a minimum is detected at 344 nm.

The calculated CD spectrum of the Λ form shows one minimum at 354 nm and two maxima at 326 and 386 nm. The measured spectrum in MeOH has the same number of Cotton effects and extrema. The first maximum is located at 246 nm instead of 326 nm. Thus compared with the CD curve recorded in MeOH, the calculated spectrum is strongly shifted to the red in this part of the spectrum. As anticipated, the extrema at the higher wavelengths fit better: the minimum of the calculated spectrum is located at 354 nm and the maximum at 386 nm. These bands correspond to the extrema at 344 nm and 381 nm in the measured spectrum. As a conclusion, the calculation reveals that the molecule most likely adopts the Λ form in MeOH. The experimental spectrum in DMSO differs significantly from the spectrum in MeOH. This spectrum could not be reproduced computationally.

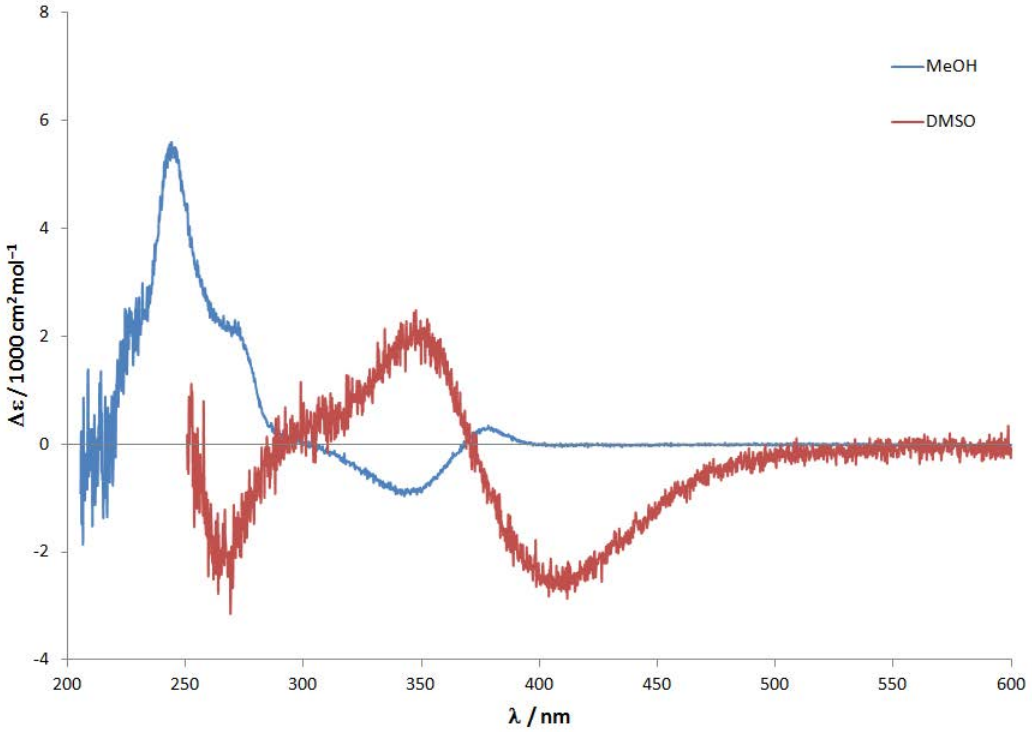

Fig. 172: *Measured CD-spectrum of Li$_3$[(**9a**)$_3$Ga] in MeOH and DMSO.*

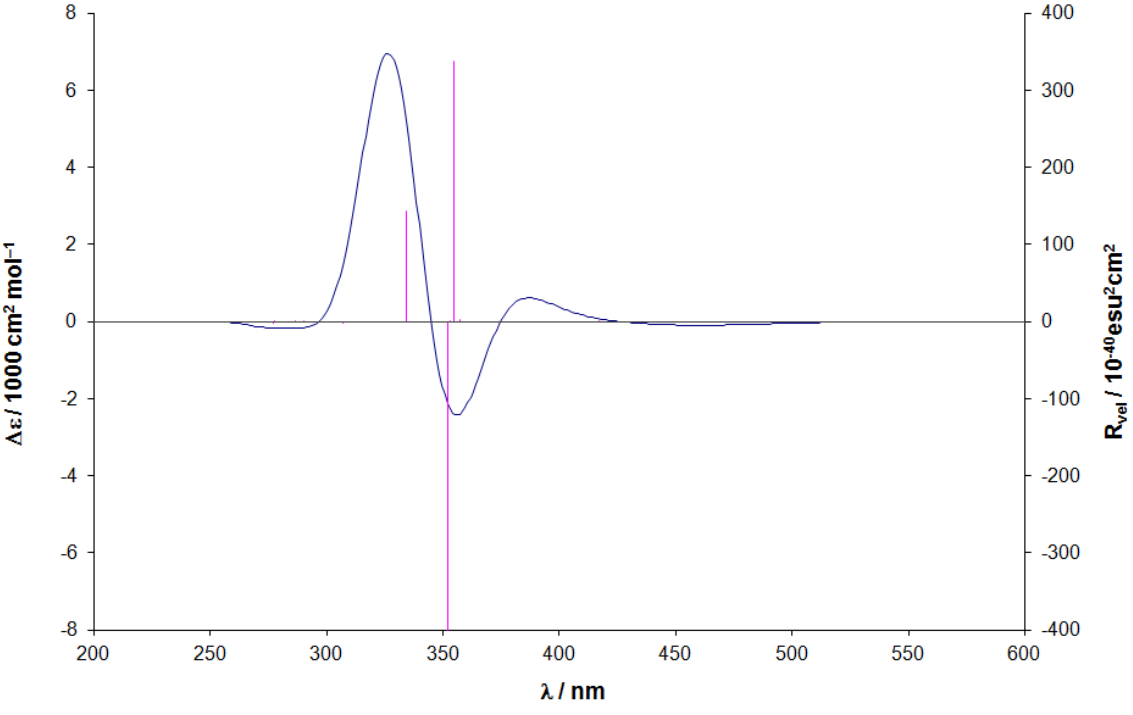

Fig. 173: *Calculated CD spectrum of [(**9a**)$_3$Ga]$^{3-}$, Λ form, red: rotational strengths; method: TDDFT/cam-B3LYP/TZVP//cam-B3LYP/TZVP.*

Complex Li$_2$[(**7a**)$_3$Ga] with a stereogenic center in the β-position, which is similar to Li$_2$[(**7**)$_3$Ti] except that Ti(IV) was replayed by Ga(III), was also measured in DMSO and in MeOH. The optimized structure of complex [(**7a**)$_3$Ga]$^{3-}$ is shown in Figure 174.

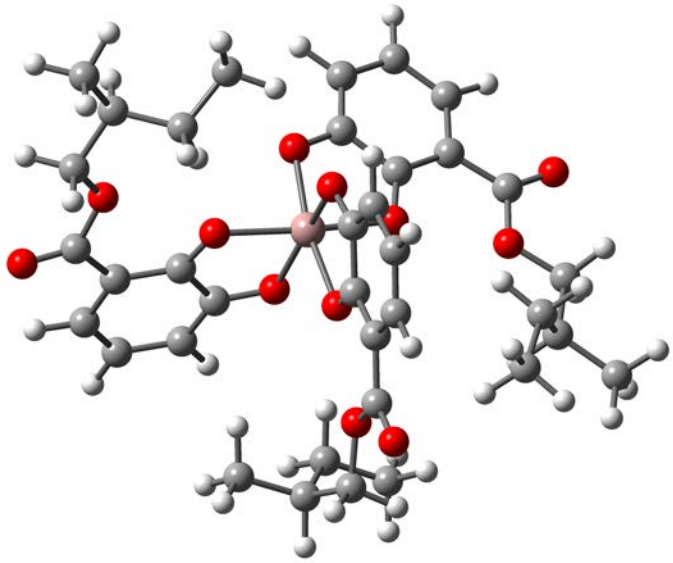

Fig. 174: *Optimized geometry of the Δ form of complex [(**7a**)$_3$Ga]$^{3-}$; method: cam-B3LYP/TZVP.*

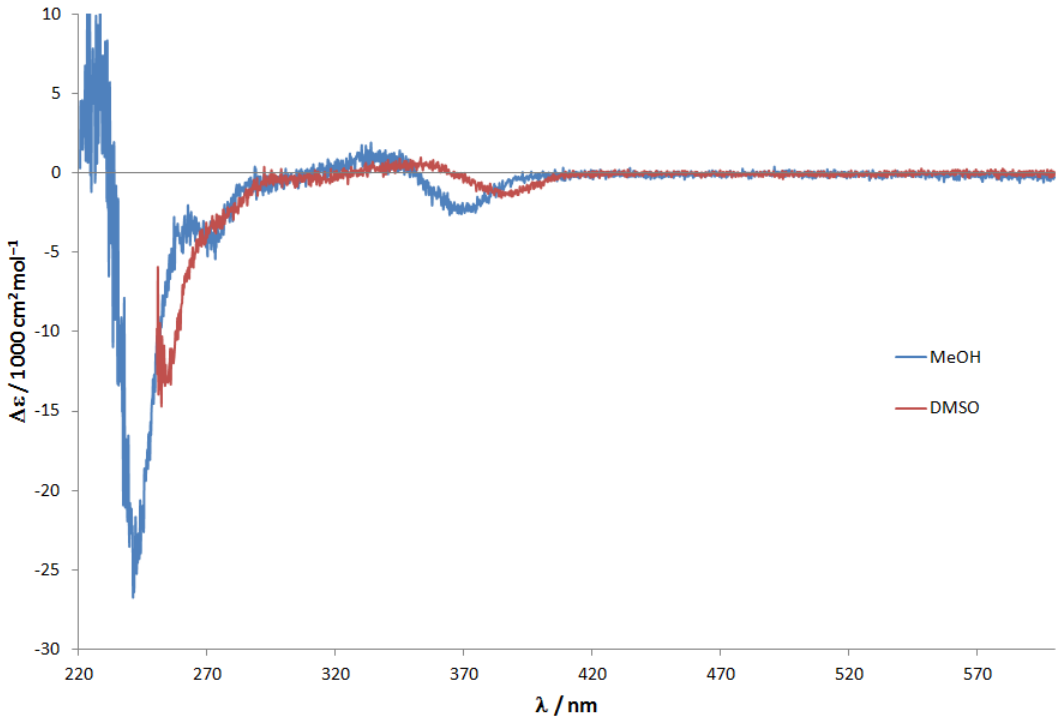

Fig. 175: *Measured CD-spectrum of Li$_2$[(**7a**)$_3$Ga] in MeOH and DMSO.*

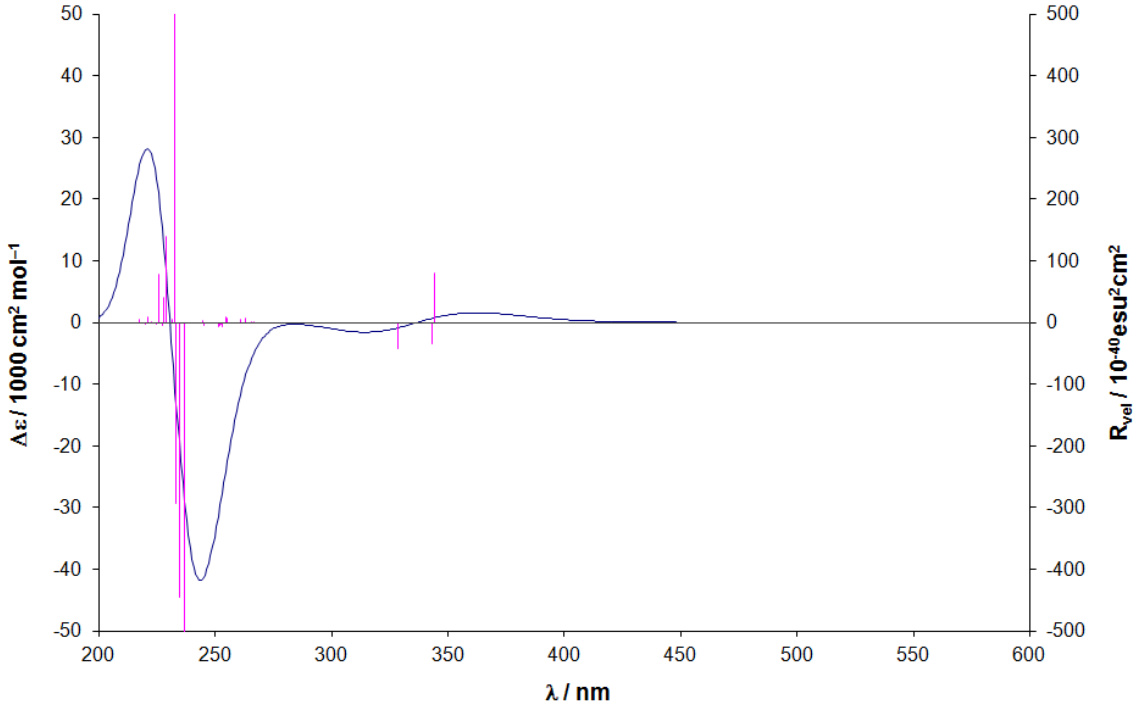

Fig. 176: *Calculated CD spectrum of [(**7a**)$_3$Ga]$^{3-}$, Δ form, red: rotational strengths; method: TDDFT/cam-B3LYP/TZVP//cam-B3LYP/TZVP.*

The comparison of the calculated and the measured spectrum (solvent = MeOH) reveals a good match in the short-wavelength region: the maximum of the calculated spectrum is located at 221 nm and the minimum at 244 nm and the extrema of the measured spectrum are found at 225 and 242 nm. A negative Cotton effect in the measured spectrum at 375 nm (MeOH) and 390 nm (DMSO) could be reproduced as well, however with a significant blue shift. The calculated spectrum shows an additional positive Cotton effect at 355 nm which has no counterpart in the experimental CD curve. This positive Cotton effect, appears to be an arte fact caused by the overestimation of the rotational strength of the state at 344 nm, which is too strong to be canceled out by the negative rotational strengths of the state at 328 and 343 nm.

The measured spectra of the complex with Ga(III) instead of Ti(IV) show stronger Cotton effects at lower wavelengths in the chosen solvents MeOH and DMSO. As the calculations with the model compound $[(cat)_3Ga]^{3-}$ indicated (Figure 59) the spectra with Ga(III) also have more extrema than the spectra with Ti(IV). While the effect of the "switch" between the Λ and Δ form can be analyzed CD spectroscopically more easily with Ti(IV) as a metal center (Figure 101 and 102).

• **Complexes with Zn(II)**

Complexes with Zn(II) instead of Ti(IV) or Ga(III) were treated computationally at the PBE1PBE/TZVP level of theory. Comparison of the calculated and measured spectrum should provide an analysis of the geometrical structure of the complex, as it is so far undecided whether the complex contains two or three ligands per metal. Therefore, the TD-DT calculations are performed for $[(\mathbf{16})_3\mathrm{Zn}]^{1-}$ and $[(\mathbf{16})_2\mathrm{Zn}]$.

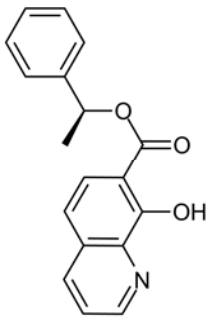

Fig. 177: *Ligand (S)-2-phenylpropyl-8-hydroxyquinoline-7-carboxylate of complex **16**.*

The geometries of the energetically optimized complex $[(\mathbf{16})_3\mathrm{Zn}]^{1-}$ and $[(\mathbf{16})_2\mathrm{Zn}]$ are presented in Figure 178.

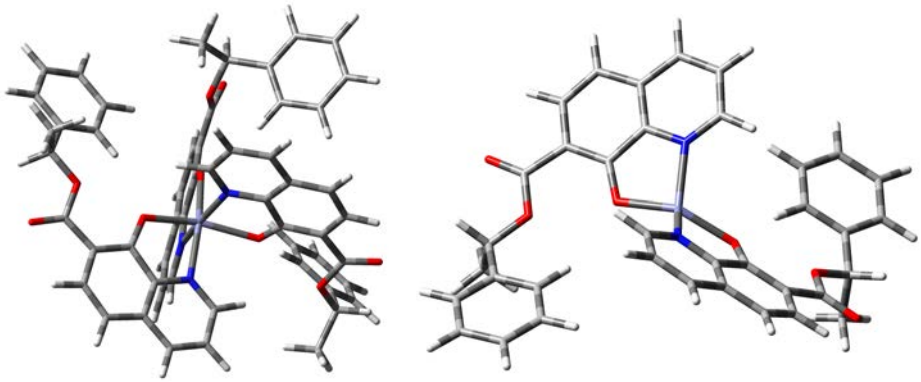

Fig. 178: *Optimized geometry of complex $[(\mathbf{16})_3Zn]^{1-}$ and $[(\mathbf{16})_2Zn]$, light blue: Zn, blue: N, red: O; method: PBE1PBE/TZVP.*

The energy of the ligands plus the metal is given by:

$E_1 = E(Zn^{2+}) + 2\ E(\text{ligand})$

$= -1.778.14792\ \text{a.u.} + 2 \cdot -974.047713\ \text{a.u.} = -3726.243345\ \text{a.u.}$

$E_2 = E(Zn^{2+}) + 3\ E(\text{ligand})$

$= -1.778.14792\ \text{a.u.} + 3 \cdot -974.047713\ \text{a.u.} = -4700.291058\ \text{a.u.}$

The energy difference to the optimized structures is:

$\Delta\ E_1 = -3726.243345\ \text{a.u.} - (-3727.240329\ \text{a.u.}) = 0.997\ \text{a.u.}$

$\Delta\ E_2 = -4700.291058\ \text{a.u.} - (-4701.360644\ \text{a.u.}) = 1.070\ \text{a.u.}$

The results for Δ E_1 and Δ E_2 of the two possibilities $[(\mathbf{16})_3Zn]^{1-}$ and $[(\mathbf{16})_2Zn]$ differ significantly. To decide, which complex is formed in the solvent, CD analyses have to be performed as solvent effects might play an important role in the formation of either $[(\mathbf{16})_3Zn]^{1-}$ or $[(\mathbf{16})_2Zn]$.

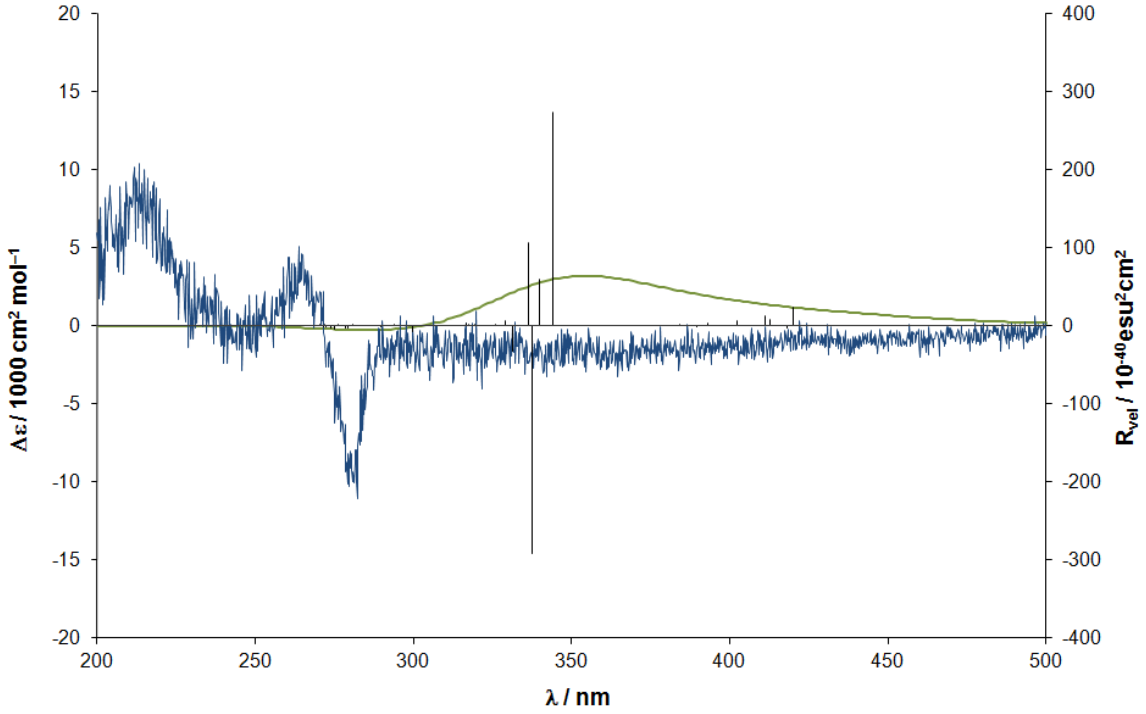

Fig. 179: *Measured (solvent: MeOH) and calculated CD spectrum of $[(\mathbf{16})_3Zn]^{1-}$, Λ form with three ligands; method: TDDFT/B3LYP/TZVP//Pbe1PBE/TZVP.*

The better agreement between the measured and the two calculated spectra of the complex are obtained for the one with two ligands (Figure 179 and 180). The calculated maximum is located at 247 nm and the minimum at 266 nm. The second smaller maximum is located at 293 nm. These extrema can be correlated with the measured ones at 264 nm and 280 nm. The small shoulder at 293 nm is reproduced by the smaller calculated maximum. This good match shows that most likely complex $[(\mathbf{16})_2Zn]$ is formed. This spectroscopic result contradicts the outcome of the energetic considerations which gave an energetic preference of -45.8 kcal/mol for the formation of the complex with three ligands. As the energetics were obtained in the gas phase the energetic preference of $(\mathbf{16})_3Zn]^-$ might be misleading. Solvent effects might play an important role in the measured spectrum and therefore, the complex with only two ligands is preferred in solution.

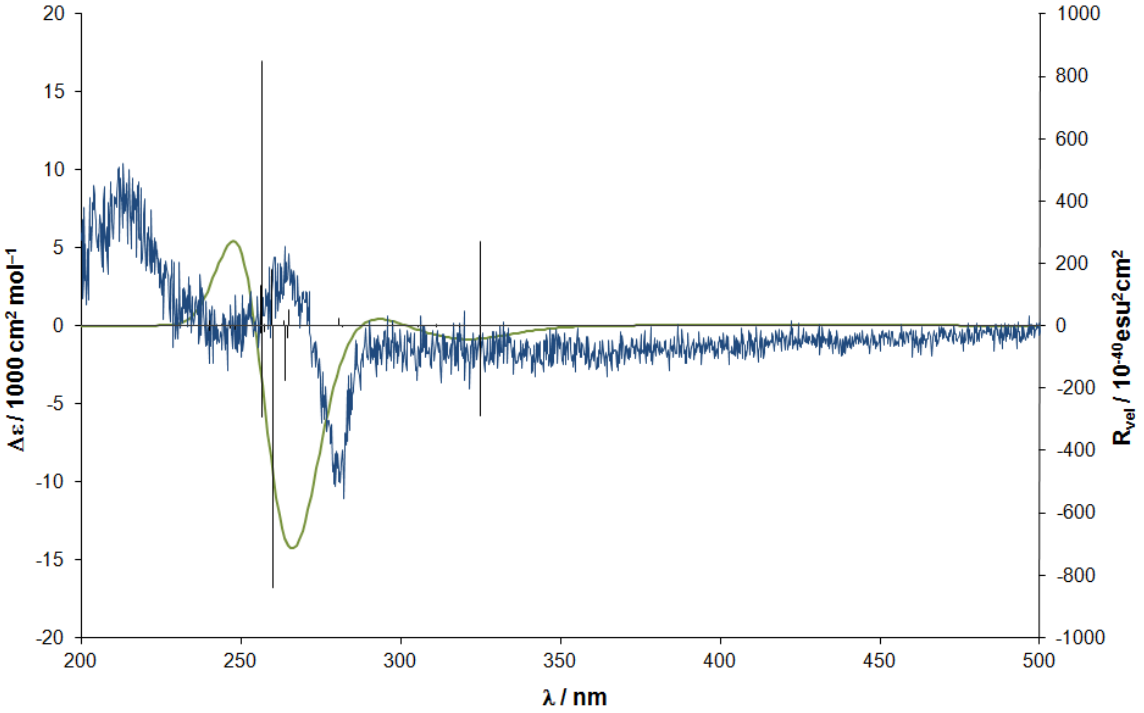

Fig. 180: *Measured (solvent: MeOH) and calculated CD spectrum of [(**16**)$_2$Zn], Λ form with two ligands method: TDDFT/B3LYP/TZVP//PBE1PBE/TZVP.*

This example shows that the comparison of calculated and measured CD spectra not only provides information about the configuration of the complex, but also reveals more aspects of the structure of the treated molecule. Thus, the problems of how many ligands are bound to the metal center could be solved.

Within this part of the thesis three different positions were defined for the stereogenic center: α, β and γ. Only with the stereogenic center in the α position, a "switch" of the Δ into the Λ form depending on the choice of the solvent was observed. The Λ form is adopted in DMSO and changing the solvent to MeOH, the complex switches to the Δ form. However, if changes are applied to the ligand even in a large distance from the metal center, like for example the substitution of one H atom of the aromatic system for bromine, this switch of configuration becomes impossible.

Replacement of Ti(IV) by Ga(III) results in more complex spectra. The most intense Cotton effects occur at very low wavelengths (i.e. high energies), making it difficult to reproduce the measured spectra since the corresponding transition energies are quite above Koopmans' ionization potential and, therefore, the calculated transitions are not very reliable. An interesting choice for the center is Zn(II), as this metal ion tends to build complexes with two ligands instead of three. All in all, the presented calculation show that the comparison of the measured with the calculated spectra of the complex can give an insight into the behavior of the complex in the chosen solvent.

4 Binuclear Complexes

4.1 Homodinuclear Complexes with Alkyl-Bridged Dicatecholate-Ligands

As metal-controlled self-assembly of complexes is of high interest in the field of Supramolecular Chemistry, binuclear complexes with different spacers were synthesized and the influence of the chain length on their relative energy was studied. In our investigations, titanium(IV) (Figure 181) or gallium(III) were used as metal center leading to either tetra-anionic or hexa-anionic complexes. As the common functionals like PBE0 do not describe long-range interactions properly, we chose the coulomb-attenuating method cam-B3LYP which corrects the exchange interaction at long range. The quality of the basis set has to be chosen carefully, as the systems in our calculations are sometimes highly polar. Accordingly, the target is to achieve good results at least with 6-311g* or higher basis sets.

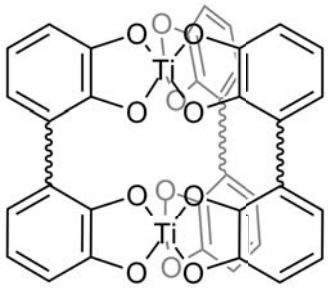

Fig. 181: *General structure of the complexes with titanium(IV).*

Initially, the methylene-, ethylene-, and propylene-bridged complexes with titanium(IV) in their ΔΔ-form have been optimized at the PBEO and B3LYP level of theory with the basis set 6-311g** and MDF10 as ECP (Figure 182 and Table 33).

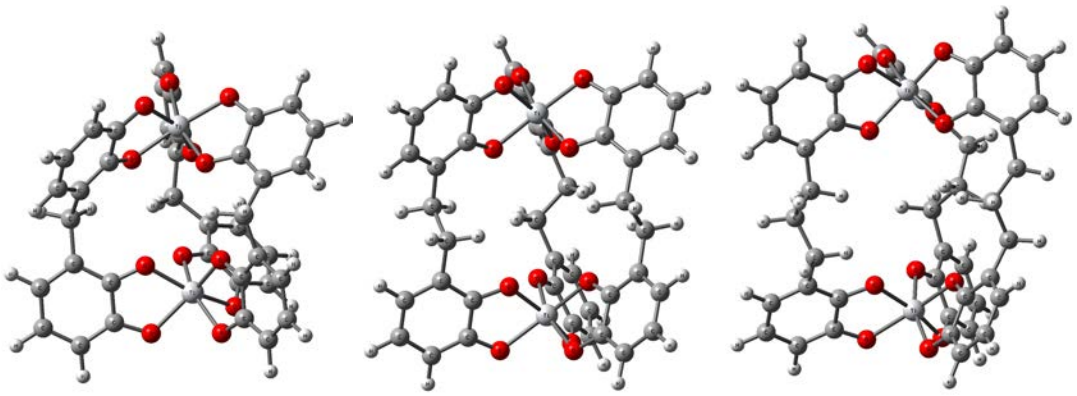

Fig. 182: *With PBE0, 6-311g**/MDF10 optimized complexes with titanium(IV), a) methylene-bridged, b) ethylene-bridged, c) propylene-bridged, ΔΔ-form.*

functional	bridge	distance Ti−Ti in Å	energy in a.u.
PBE0	methylene	5.6628	−2520.906048
B3LYP	methylene	5.6440	−2518.108388
PBE0	ethylene	6.8860	−2636.012934
B3LYP	ethylene	6.9146	−2638.956224
PBE0	propylene	7.6606	−2756.929084
B3LYP	propylene	7.7065	−2653.833513

Table 33: *optimized structures with titanium(IV), ΔΔ-form, basis set: 6-311g**, ECP: MDF10.*

Further calculations with the functional cam-B3LYP in combination with the TZVP basis set show that the complex with Ti(IV) forms a *meso*-helicate (ΔΛ) if the bridge has an odd number of methylene units. An even number leads to a helicate (ΔΔ or ΛΛ) (Figure 183).

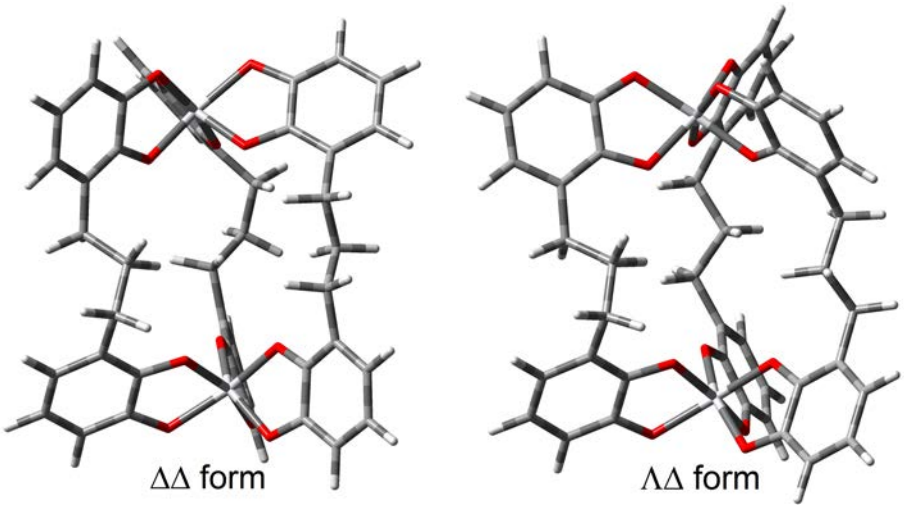

Fig. 183: *ΔΔ and ΔΛ form of the complex with a propylene spacer; method: cam-B3LYP/TZVP.*

bridge	form	distance Ti−Ti in Å	energy in a.u.	energy difference in kcal/mol
1	ΔΔ	5.6242	−2519.676508	20.354
1	ΔΛ	5.8597	−2519.708944	
2	ΔΔ	6.8813	−2637.656716	−12.027
2	ΔΛ	6.8404	−2637.637550	
3	ΔΔ	7.6483	−2755.551314	12.149
3	ΔΛ	7.6586	−2755.570675	
4	ΔΔ	8.9163	−2873.727971	−9.994
4	ΔΛ	9.0066	−2873.712045	
5	ΔΔ	10.0410	−2991.635849	10.124
5	ΔΛ	10.0677	−2991.651982	
6	ΔΔ	11.3078	−3109.578426	−7.660
6	ΔΛ	11.3625	−3109.566219	
7	ΔΔ	12.3609	−3227.479249	16.160
7	ΔΛ	12.8116	−3227.505002	
8	ΔΔ	12.8960	−3345.414708	−11.842
8	ΔΛ	13.0148	−3345.395836	
9	ΔΔ	14.0844	−3463.313584	4.409
9	ΔΛ	14.1981	−3463.320610	
10	ΔΔ	15.8716	−3581.243344	−5.676
10	ΔΛ	16.1874	−3581.237298	

Table 34: *Total and relative energies of the optimized structures with Ti(IV), functional: cam-B3LYP, basis set: TZVP, ECP: MDF10.*

The numbers in table 34 clearly show that the complex with Ti(IV) forms a *meso*-helicate (ΔΛ) if the bridge has an odd number of methylene units and helicate (ΔΔ) if the bridge has an even number of methylene units. The energy difference between those two forms tends to get smaller, if the chain length is bigger.

The only exception is the higher value of ΔE with seven or eight methylene units. With seven methylene units, a structure of approximate C_3 symmetry results for the *meso*-helicate (Figure 184). In contrast to this, the optimized structure of the helicate form has a more twisted structure and a relatively high energy (−3227.505002 a.u.). This leads to a larger energy difference compared to the energy difference of the structure with five methylene units. Eight methylene units lead to an unstable ΔΔ form as the spacer adopts a winding structure (Figure 185). The ΔΛ has an even higher energy, as even more of the ligands have a winding structure. This result also leads to a high energy difference. The higher energy difference between the ΔΔ and ΔΛ forms might also be caused by the energetically optimized structures as there might be energetically more favored ones, which could not be found so far.

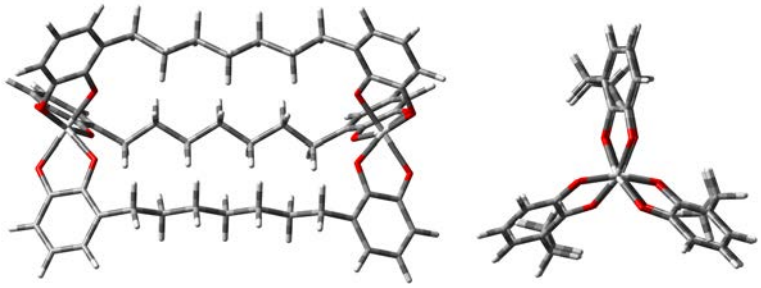

Fig. 184: *Structurally optimized ΔΛ form of the complex with seven methylene units, view from the side and the top of the molecule.*

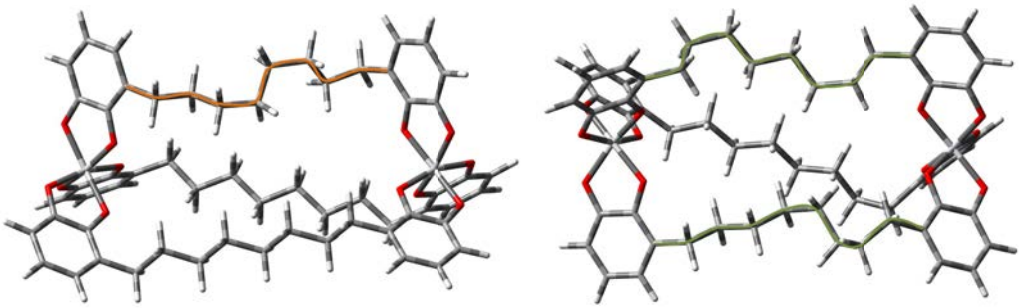

Fig. 185: *Structurally optimized ΔΔ and ΔΛ form of the complex with eight methylene units, view from the side of the molecule, structure of the ligand marked in orange (ΔΔ) and in green (ΔΛ).*

bridge	form	distance Ga−Ga in Å	energy in a.u.	energy difference in kcal/mol
1	ΔΔ	6.1899	−2406.559173	21.131
1	ΔΛ	5.9420	−2406.592847	
2	ΔΔ	7.0978	−2524.588634	
2	ΔΛ	-	-	
3	ΔΔ	7.9853	−2642.519580	12.403
3	ΔΛ	7.9056	−2642.539345	
4	ΔΔ	9.0157	−2760.491726	−7.516
4	ΔΛ	9.2239	−2760.479749	
5	ΔΔ	10.1413	−2878.416953	15.312
5	ΔΛ	10.1000	−2878.441355	
6	ΔΔ	11.4477	−2996.402119	−13.291
6	ΔΛ	11.4979	−2996.380938	
7	ΔΔ	12.3927	−3114.311338	8.366
7	ΔΛ	12.2418	−3114.324670	
8	ΔΔ	13.6935	−3232.272713	−16.408
8	ΔΛ	13.3331	−3232.246565	
9	ΔΔ	15.0561	−3350.177143	1.515
9	ΔΛ	14.2238	−3350.179556	
10	ΔΔ	16.1467	−3468.135279	−20.181
10	ΔΛ	15.5333	−3468.103183	

Table 35: *Total and relative energies of the optimized structures with Ga(III), functional: cam-B3LYP, basis set: TZVP, ECP: MWB28.*

With Ga(III) instead of Ti(IV) and with exception of n = 5, the energy difference between the ΔΔ and the ΔΛ forms of the complexes with an odd number of methylene units has the tendency to get smaller with an increasing size of the spacer. An optimized structure for the complex with two methylene units for the ΔΛ form could not be obtained, because the optimization did not lead to an energetical minimum.

Compared to the result with Ti(IV) as metal center the trend of the energy differences of the two forms of the complexes with an even number of methylene units is the opposite. Here, the largest energy difference is found with the biggest spacer. This result was not expected as the energy differences are supposed to get smaller as the spacer gets bigger, because the longer chain length provides a more "flexible" structure. The reason for the result might be that the ΔΔ form gets more and more energetically favored as the chain length grows, but the energy of the ΔΛ form does not change equally.

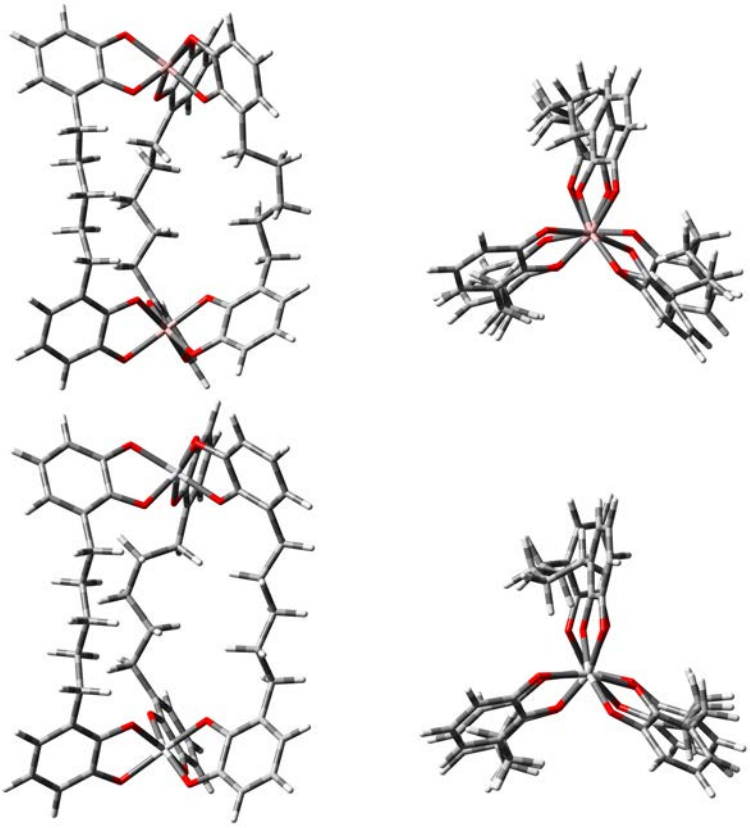

Fig. 186: *Structurally optimized ΔΛ form of the complexes with Ga(III) or Ti(IV) and a pentane spacer, green: meta-metal distance.*

With a pentyl spacer and a ΔΛ form, the Ti−O distance is about 1.967 Å and the Ga−O Å distance is larger with 2.204 Å. The metal-metal distances differ only slightly: the Ti-Ti distance is about 10.068 Å and the Ga-Ga distance is bigger with 10.100 Å. Therefore, complexes with either Ga(III) or Ti(IV) will form similar structures.

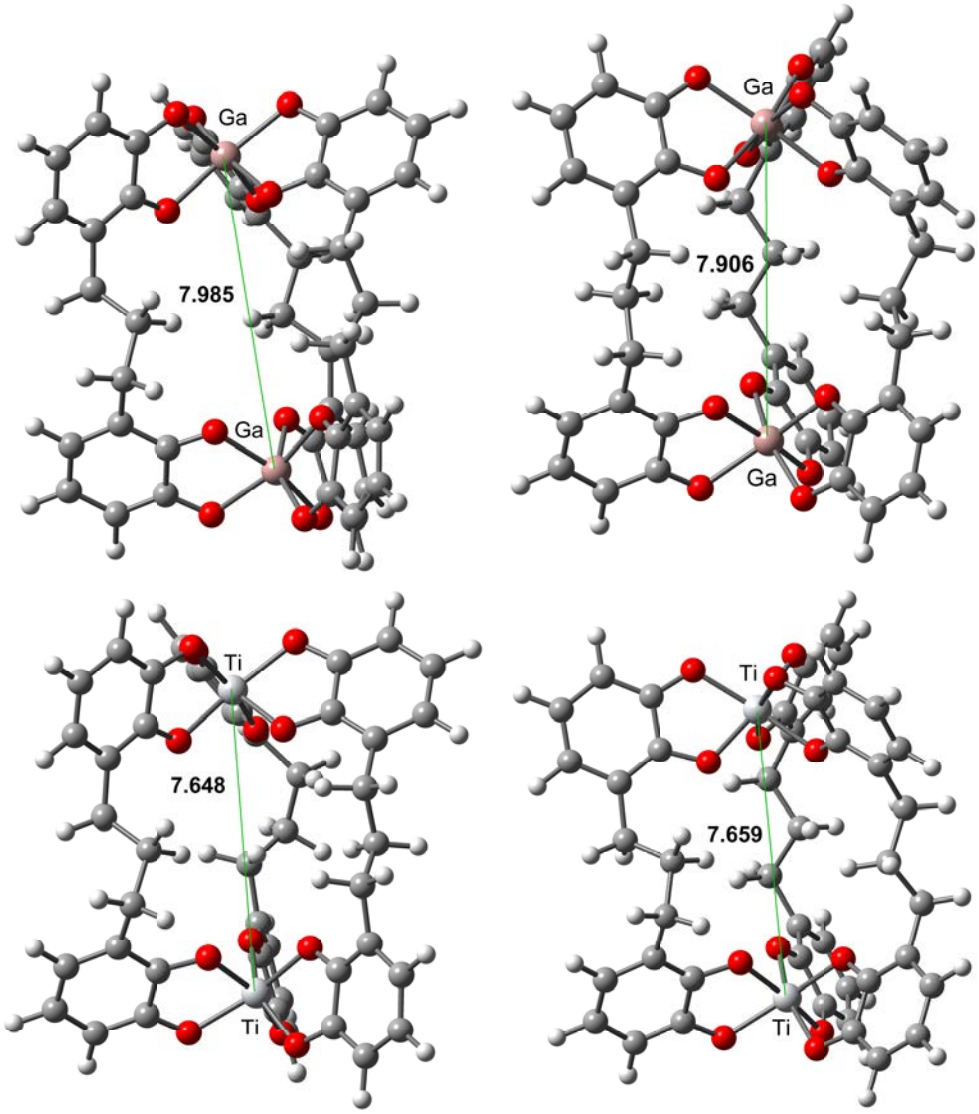

Fig. 187: *Structurally optimized ΔΔ and ΔΛ form of the complexes with Ga(III) (pink) or Ti(IV) (white) and a propylene spacer; method: cam-B3LYP/TZVP.*

Comparison of the ΔΔ and ΔΛ form of the complexes with Ga(III) or Ti(IV) and a propylene spacer (Figure 187) shows that the metal-metal distances are different. With Ga(III) the distances are 7.985 Å (helicate) and 7.906 Å (*meso*-helicate). With Ti(IV) instead of Ga(III) the distances are smaller. Here the distance within the helicate is 7.648 Å and within the *meso*-helicate 7.659 Å. The shape of the three spacers of the ΔΔ and ΔΛ form are very similar with both metals.

All in all, the complexes with Ga(III) leave more space for potential guests (cations like K^+) as the distances between the two metal centers are larger than with Ti(IV). The shape of the alkyl bridged complex seems not to depend strongly on the choice of the metal.

form	Donor NBO	Acceptor NBO	E in kcal/mol	average E in kcal/mol
ΔΔ	LP O 1	LP* Ga 1	51.15	
ΔΔ	LP O 2	LP* Ga 1	54.43	
ΔΔ	LP O 3	LP* Ga 1	56.30	
ΔΔ	LP O 4	LP* Ga 1	48.32	
ΔΔ	LP O 5	LP* Ga 1	48.14	
ΔΔ	LP O 6	LP* Ga 1	53.64	52.00
ΔΔ	LP O 7	LP* Ga 2	51.42	
ΔΔ	LP O 8	LP* Ga 2	48.18	
ΔΔ	LP O 9	LP* Ga 2	48.17	
ΔΔ	LP O 10	LP* Ga 2	48.47	
ΔΔ	LP O 11	LP* Ga 2	56.29	
ΔΔ	LP O 12	LP* Ga 2	47.00	49.92
ΔΛ	LP O 1	LP* Ga 1	54.48	
ΔΛ	LP O 2	LP* Ga 1	49.63	
ΔΛ	LP O 3	LP* Ga 1	47.87	
ΔΛ	LP O 4	LP* Ga 1	54.62	
ΔΛ	LP O 5	LP* Ga 1	55.04	
ΔΛ	LP O 6	LP* Ga 1	52.04	52.28
ΔΛ	LP O 7	LP* Ga 2	46.94	
ΔΛ	LP O 8	LP* Ga 2	53.46	
ΔΛ	LP O 9	LP* Ga 2	55.51	
ΔΛ	LP O 10	LP* Ga 2	50.42	
ΔΛ	LP O 11	LP* Ga 2	51.23	
ΔΛ	LP O 12	LP* Ga 2	54.86	52.07

Table 36: *NBO analysis of the optimized structures with Ga(III) and a butylene spacer, basis set: TZVP, ECP: MWB28.*

The second order energies of interaction between the metal center and the O-atoms (Table 37) reveal that the Ti(IV)−O interactions are much stronger than the interactions between Ga(III) and the O-atoms (Table 36). This result correlates with the smaller Ti−O distances, and the ionic radii are quite similar with 62 pm for Ga(III) and 68 pm for Ti(IV).[80] In both cases the ΔΛ form shows higher energies of the interaction than the ΔΔ form, which leads to a lower energy of the *meso*-helicate.

form	Donor NBO	Acceptor NBO	E in kcal/mol	average E in kcal/mol
ΔΔ	LP O 1	LP* Ti 1	63.24	
ΔΔ	LP O 2	LP* Ti 1	92.26	
ΔΔ	LP O 3	LP* Ti 1	90.02	
ΔΔ	LP O 4	LP* Ti 1	55.64	
ΔΔ	LP O 5	LP* Ti 1	93.30	
ΔΔ	LP O 6	LP* Ti 1	93.64	81.35
ΔΔ	LP O 7	LP* Ti 2	86.51	
ΔΔ	LP O 8	LP* Ti 2	82.91	
ΔΔ	LP O 9	LP* Ti 2	97.39	
ΔΔ	LP O 10	LP* Ti 2	69.84	
ΔΔ	LP O 11	LP* Ti 2	57.44	
ΔΔ	LP O 12	LP* Ti 2	55.34	74.91
ΔΛ	LP O 1	LP* Ti 1	102.26	
ΔΛ	LP O 2	LP* Ti 1	96.07	
ΔΛ	LP O 3	LP* Ti 1	101.18	
ΔΛ	LP O 4	LP* Ti 1	51.41	
ΔΛ	LP O 5	LP* Ti 1	88.23	
ΔΛ	LP O 6	LP* Ti 1	55.64	82.47
ΔΛ	LP O 7	LP* Ti 2	104.74	
ΔΛ	LP O 8	LP* Ti 2	79.48	
ΔΛ	LP O 9	LP* Ti 2	101.38	
ΔΛ	LP O 10	LP* Ti 2	76.81	
ΔΛ	LP O 11	LP* Ti 2	66.92	
ΔΛ	LP O 12	LP* Ti 2	63.21	82.09

Table 37: *NBO analysis of the optimized structures with Ti(IV) and a butylene spacer, basis set: TZVP, ECP: MDF10.*

The computational study of the ΔΔ and ΔΛ forms of the Ti(IV) and Ga(III) complexes with different alkyl spacers led to the result that a spacer with an odd number of methylene units forms a *meso*-helicate and one with an even number leads to a helicate. The energetically optimized structures also provide an answer to the question why either the ΔΔ or the ΔΛ form is preferred. In general, a less twisted ligand within the complex leads to an energetically favored structure.

4.1.1 Transition State Studies on Alkyl-Bridged Dichatecholate-Ligands

The studies presented above only reveal the energy differences between the helicate and meso-helicate form of the alkyl-bridged complexes and do not provide any insight into the dynamics of the complexes. If these dynamical aspects should be further investigated, it is of great importance to study the intra molecular conversion of the ΛΛ into the ΛΔ form. To obtain the barrier of interconversion calculations on the "Bailar-Twist" transition state have to be performed.

Figure 188 presents the first results on the B3LYP/TZVP level of theory. The green arrows indicate the twist from the ΛΔ form to the transition state and further from this point to the ΛΛ form. With butylene as a spacer, the helicate is energetically favored.

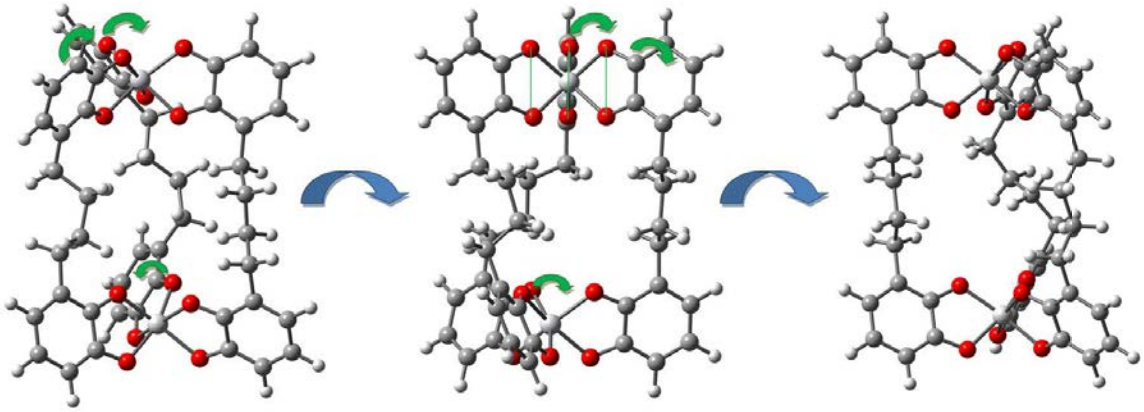

Fig. 188: *"Bailar-Twist"-transition state from the ΛΔ form to the ΛΛ form of the complexes with Ti(IV), butylene as a spacer, method: B3LYP.*

The reaction path connecting the ΛΔ and the ΛΛ form is depicted in Figure 189. The calculations were performed at the cam-B3LYP/TZVP level of theory. The resulting energy of the transition state is 2.63 kcal/mol above the ΛΔ form.

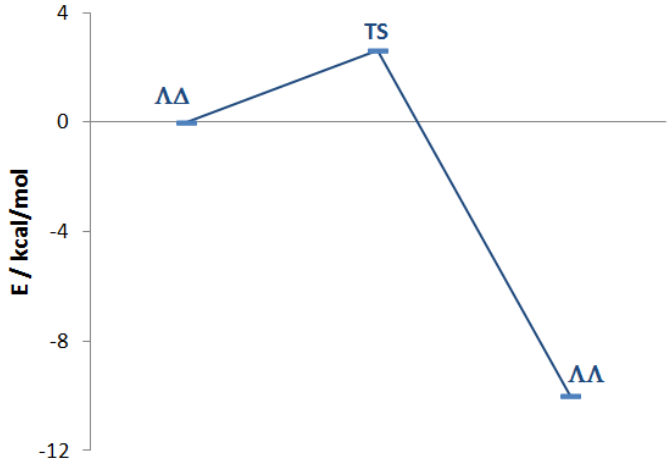

Fig. 189: *Energies of the Bailar-Twist from the ΛΔ form to the ΛΛ form of the complexes with Ti(IV) with butylene as a spacer.*

The transition state calculations on the B3LYP/TZVP level of theory of the complexes with propylene, butylene and pentylene as spacers result in different imaginary frequencies: for propylene in 5.52i cm^{-1}, for butylene in 57.49i cm^{-1} and for pentylene in 50.38i cm^{-1}. They can be correlated with the energy differences between the ΔΔ and ΛΔ form of 12.149 kcal/mol, 9.994 kcal/mol, and 10.124 kcal/mol. The correlation between the two results is inversely proportional; the lower the energy difference

between the two forms is, the higher the imaginary frequency. Figure 190 shows the resulting structures of the complexes with the different spacers.

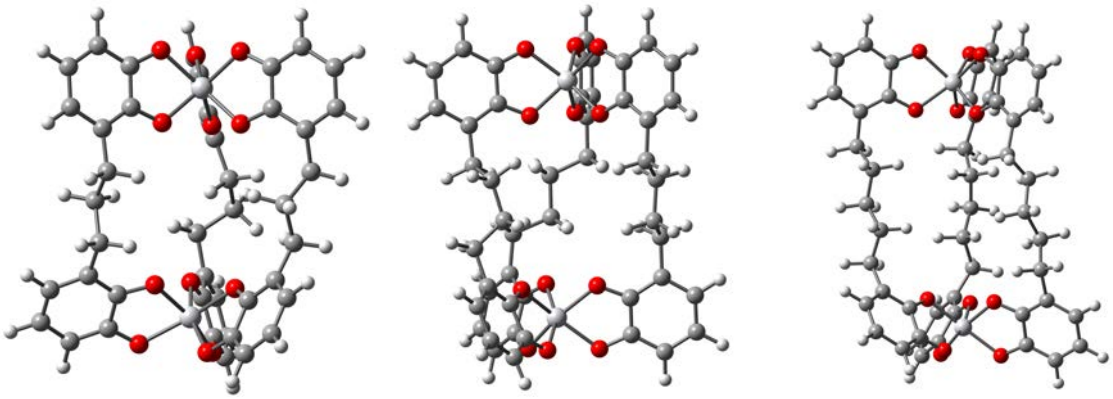

Fig. 190: *Optimized structures of the "Bailar-Twist"-transition state of the complexes with Ti(IV), propylene, butylene and pentylene as spacers, functional: B3LYP.*

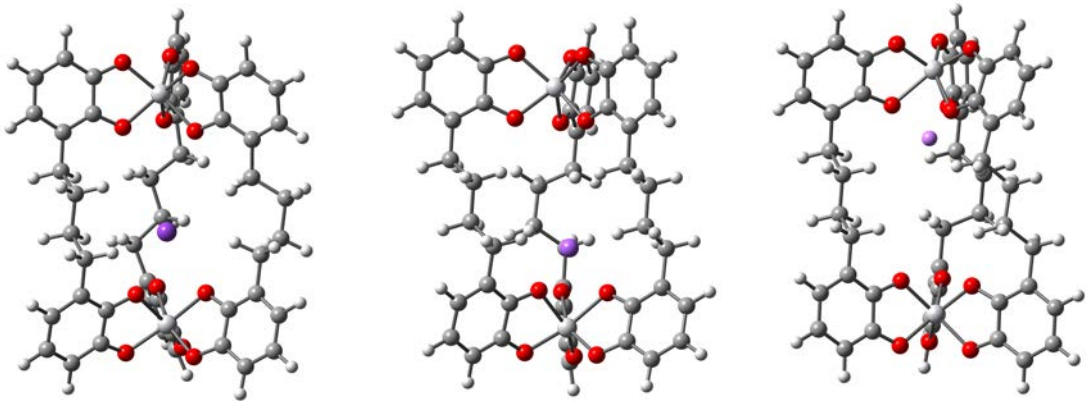

Fig. 191: *Optimized structures of the "Bailar-Twist"-transition state of the complexes with Ti(IV) with butylene as a spacer and K^+, Na^+, or Li^+ as a template, functional: B3LYP.*

ion	energy in a.u.	energy without template in a.u.	energy difference in a.u.
-	−2875.159473	−2875.159473	0.000
K^+	−3475.332868	−2875.572558	0.413
Na^+	−3037.694208	−2875.602276	0.408
Li^+	−2882.925136	−2875.639093	0.480

Table 38: *Energy difference of the transition state structures with butylene as a spacer and K^+, Na^+, or Li^+ as a template to the complex without a template, functional: B3LYP.*

In Table 38 the energies of the "Bailar-Twist" transition states for the ΛΔ/ΛΛ interconversion of the complexes with butylene as a spacer and K^+, Na^+, or Li^+ as a template are listed. The energies of the ions ($E(K^+)$ = −599.760310 a.u., $E(Na^+)$ = −162.091932 a.u. and $E(Li^+)$ = −7.286043 a.u.) were subtracted to compare the energies of the different complexes. The energy difference to the complex without a template grows in the order Na^+, K^+, and Li^+. Therefore, Li^+ has the biggest stabilization effect on the transition state. This result is surprising, because a bigger ion

like K^+ should have a more significant influence. In contrast to this, the calculations in the gas phase show that the Li^+ ion which is closest to the metal center has the most significant influence on the transition state. This might indicate that the stabilizing effect on the transition state is due to the coordination of the three O atoms and the metal center to the Li^+ ion.

As a conclusion, the analysis of the "Bailar-Twist" transition state of the alkyl-bridged dicatecholate-ligands shows that the conversion to the energetically more favored form is possible and it takes about 2.63 kcal/mol in the case of butylene as a spacer. Templates have a significant influence on the energy of the transition state. Therefore, the choice of the counter ion might be a way to influence the reaction barrier.

4.2 Homodinuclear Complexes with Imino-Bridged Ligands

With imino-bridged instead of alkyl-bridged dicatecholate ligands, the same dependence on the structure of the spacer was obtained. Earlier experimental studies showed that complex **17** adopts the $\Delta\Lambda$ with a central CH_2-unit and complex **18** having a central $(CH_2)_2$-unit adopts the $\Delta\Delta$ form.[40] The structure of both complexes is presented in Figure 192.

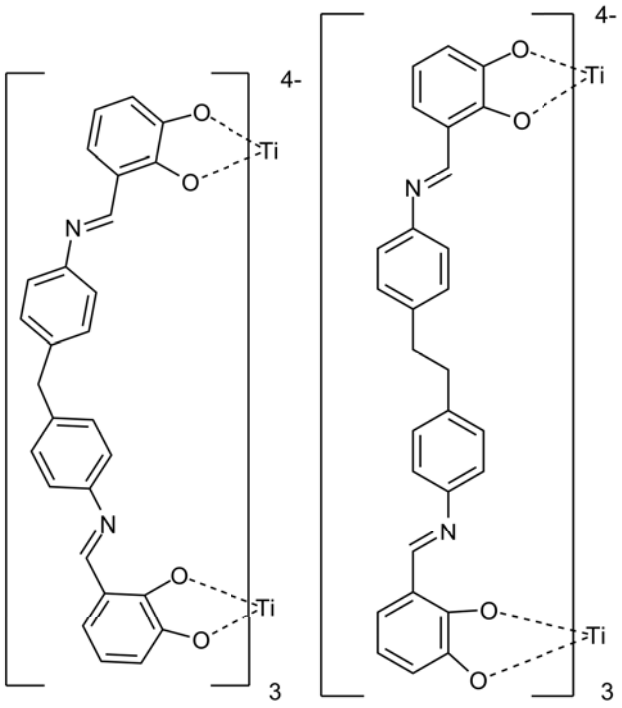

Fig. 192: *Structure of complex **17** and **18** with an imino spacer.*

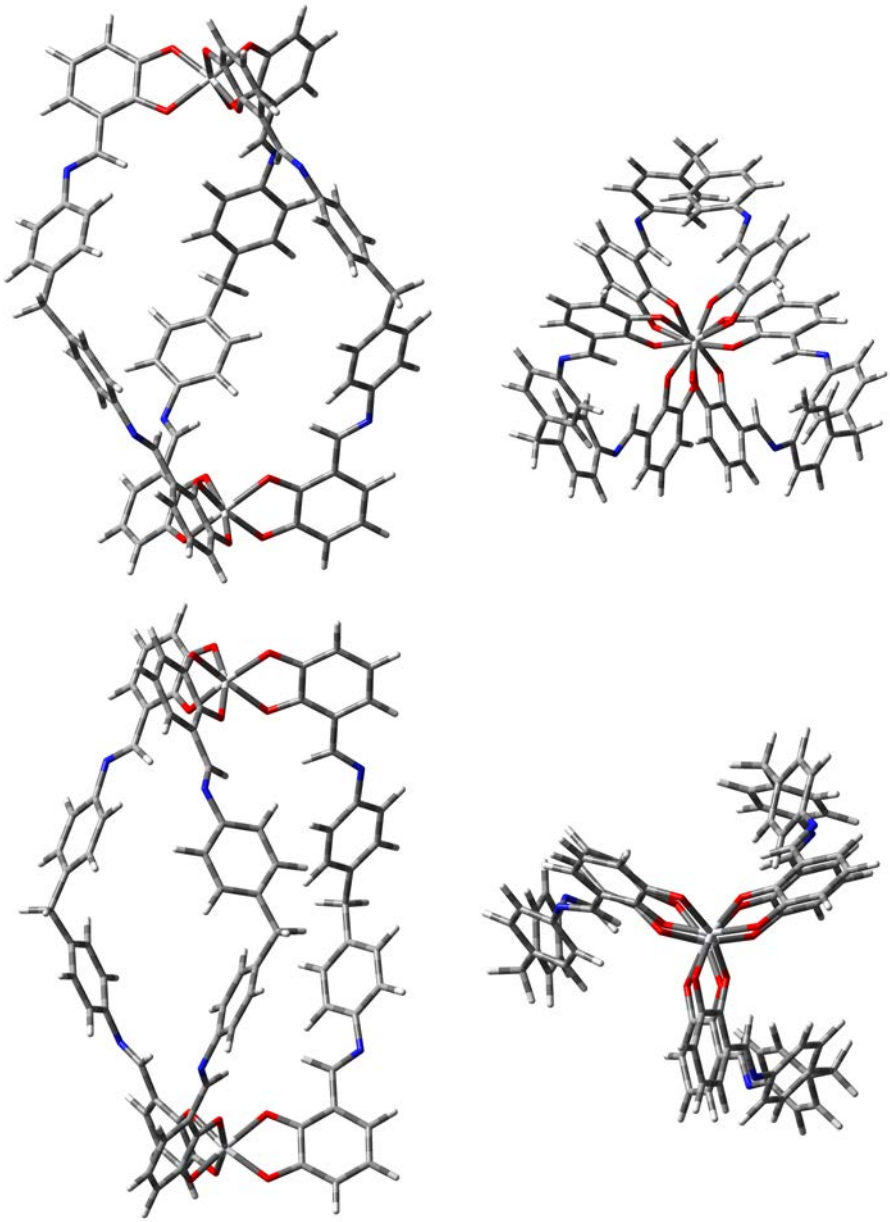

Fig. 193: *Optimized structures of the ΔΔ form of complex **17** with an imino spacer and one CH_2-unit, white: Ti. blue: N, red: O; method: cam-B3LYP/TZVP.*

configuration	Ti−Ti distance in Å	Energy in a.u.	difference in kcal/mol
ΔΛ	16.680	−4466.714593	−7.846
ΔΔ	15.551	−4466.702090	

Table 39: *Energies of the ΔΛ and ΔΔ configuration of complex **17**, functional: cam-B3lyp, basis set: TZVP.*

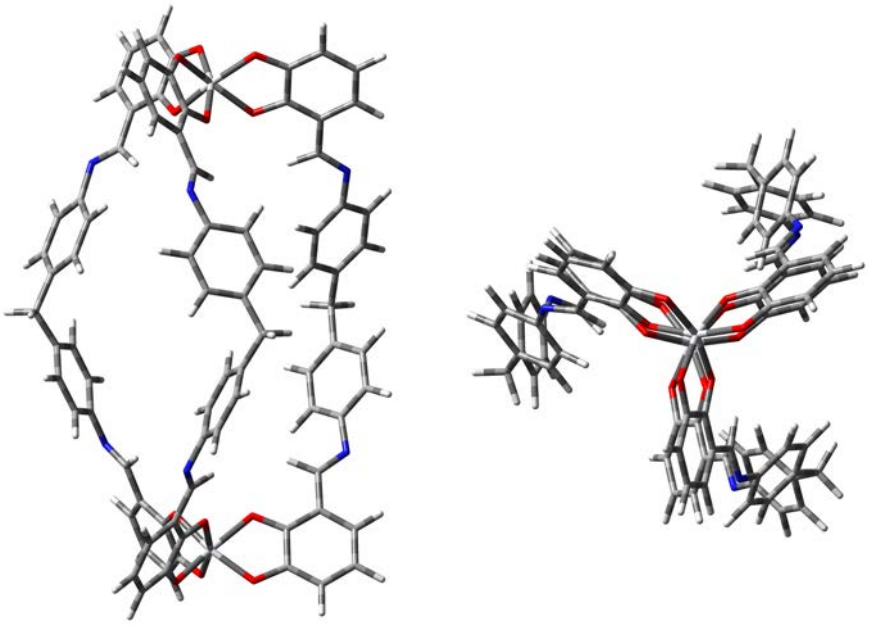

Fig. 194: *Optimized structures of the* $\Delta\Lambda$ *form of complex* ***17*** *with an imino spacer and one* CH_2*-unit, white: Ti. blue: N, red: O; method: cam-B3LYP/TZVP.*

The computational results underline the earlier studies, in that the energy of the $\Delta\Lambda$ form is lower than the energy of the $\Delta\Delta$ form (Table 39). In the more stable form, the ligand has a less twisted geometry. In Figure 195 the dihedral angles are shown. The ligand of the $\Delta\Lambda$ form has an angle of 94.30° and the $\Delta\Delta$ an angle of 64.76°.

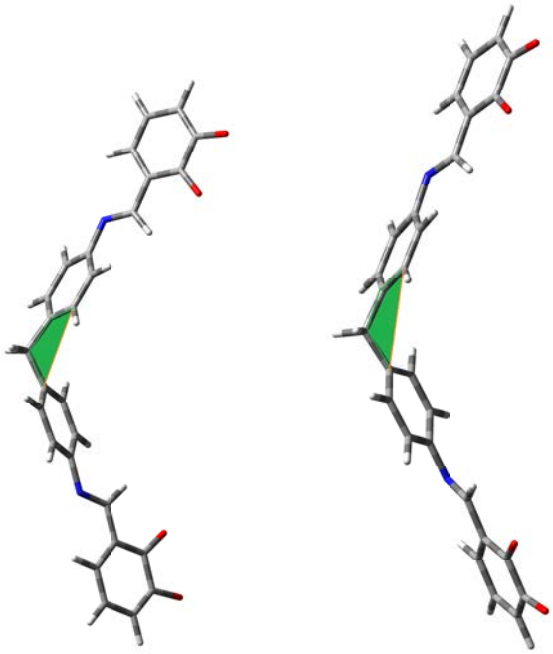

Fig. 195: $\Delta\Delta$ *(left) and* $\Delta\Lambda$ *(right) form of the ligand of the complex with an imino spacer, green: dihedral angle.*

In the next step computational studies on complex **18** were performed, which has a central $(CH_2)_2$-unit instead of a CH_2-unit. The resulting structures are presented in Figure 196 and 197.

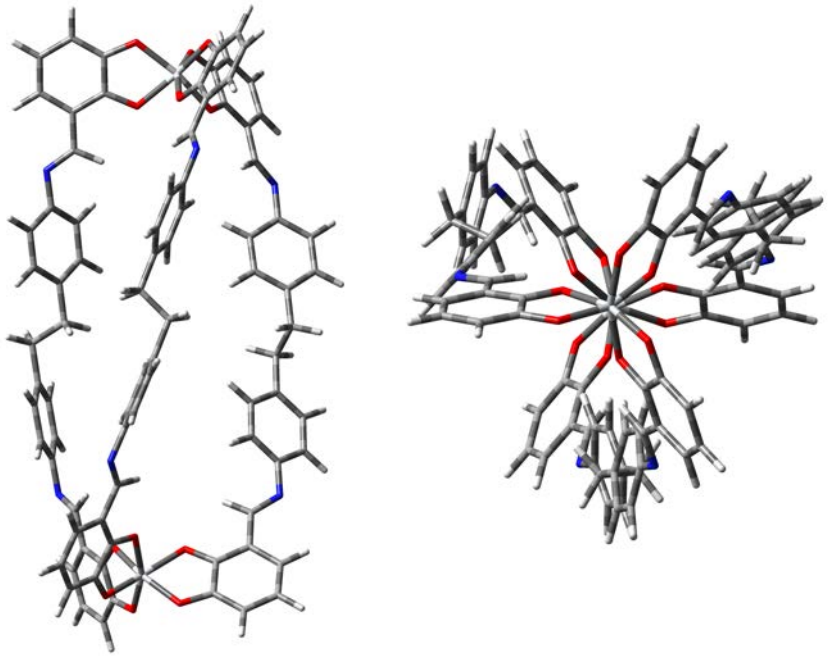

Fig. 196: *Structurally optimized ΔΔ form of the ligand of the complex with a $(CH_2)_2$-unit, white: Ti. blue: N, red: O; method: cam-B3LYP/TZVP.*

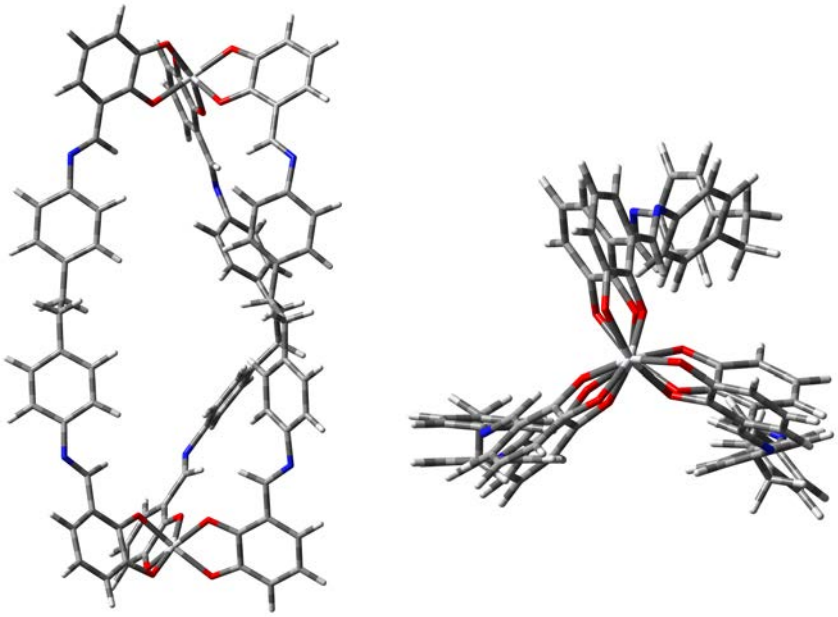

Fig. 197: *Structurally optimized ΔΛ form of the ligand of the complex with a $(CH_2)_2$-unit, white: Ti. blue: N, red: O; method: cam-B3LYP/TZVP.*

The ΔΛ form of the complex with a $(CH_2)_2$-unit results in a more eclipsed conformation. The comparison of the energies of the two forms reveal that the helicate form is favored (Table 40).

configuration	Ti−Ti distance in	Energy in a.u.	difference in kcal/mol
ΔΛ	18.644	−4584.622753	10.466
ΔΔ	18.907	−4584.639431	

Table 40: *Energies of the* ΔΛ *and* ΔΔ *configuration of complex* ***18****, functional: cam-B3lyp, basis set: TZVP.*

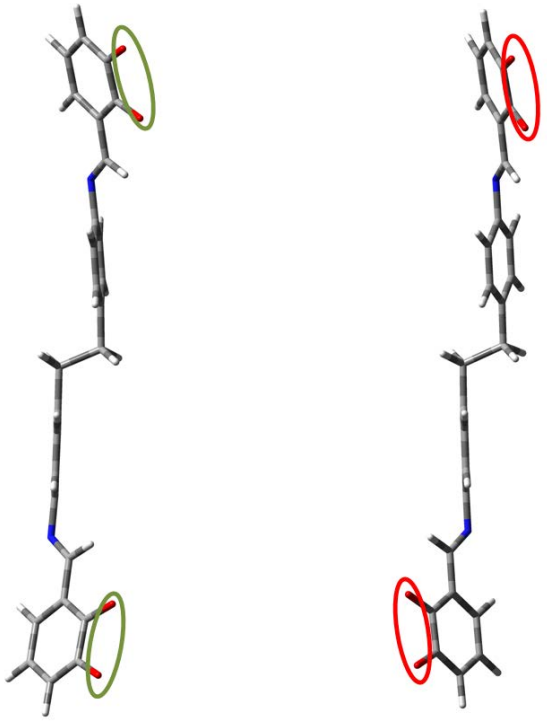

Fig. 198: ΔΛ *(left) and* ΔΔ *(right) form of the ligand of the complex with an imino spacer.*

The comparison of the two ligands from the optimized structures of complex **18** (Figure 198) reveals that the ligand in the ΔΔ complex is much stronger twisted. The dicatecholate parts of the ΔΔ complex marked in red even point into different directions.

Complex **19** is presented in Figure 199. This complex is very similar to complex **17** but has a sterically more demanding sterical rest. Due to its size the theoretical treatment of the complex demands the use of the *multi-layer ONIOM method*. Therefore, the complex has been divided into two parts: the high layer (metal centers and the spacer) and the low layer (sterically demanding rest). For the high layer, cam-B3LYP was used in combination with the TZVP basis set. For the low layer, HF/6-31g* was chosen. The *ONIOM* calculation reveals a very symmetrical structure. Additionally, calculations on the MMFF level show that the helicate form is favored for complex **19**, which corresponds to the result of the calculations with complex **17**.

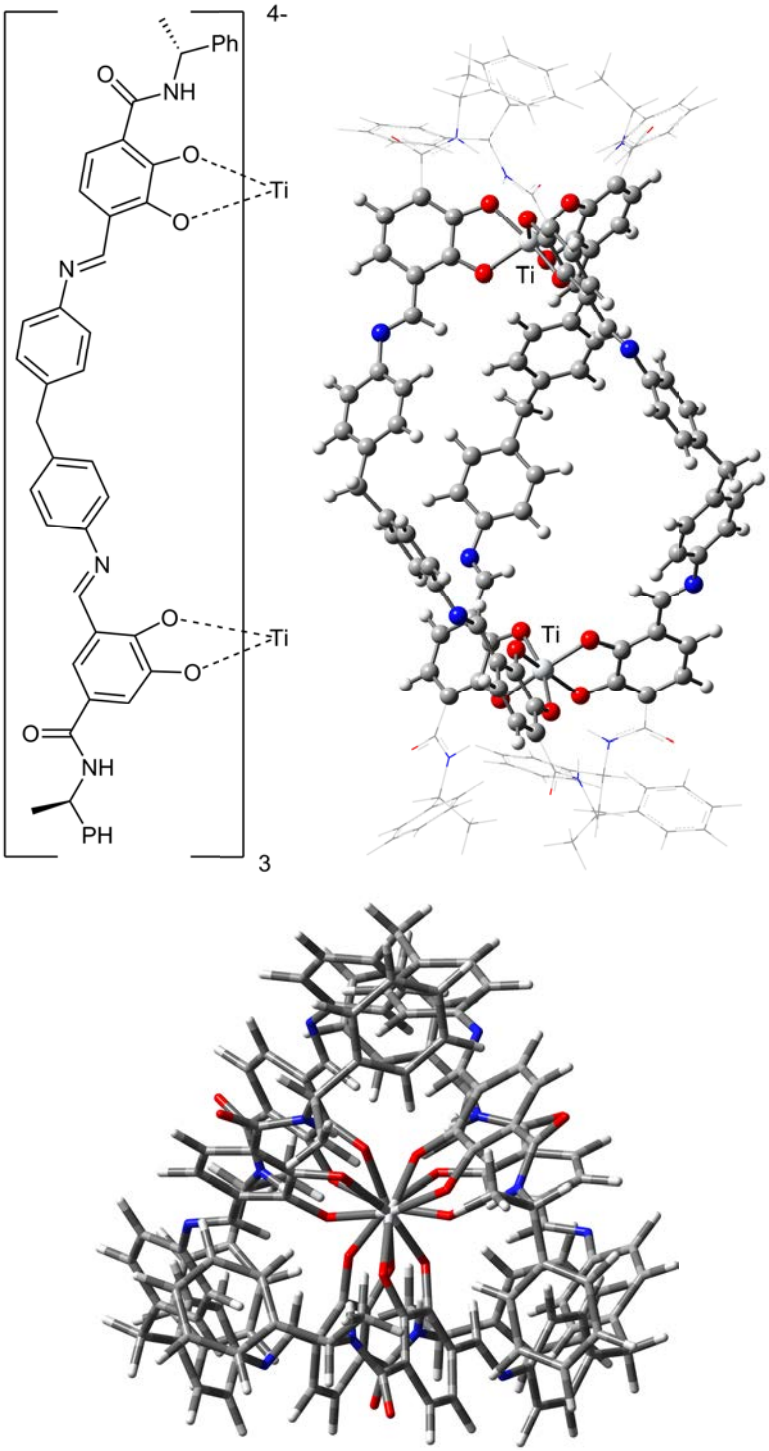

Fig. 199: *Structure of complex **19** with an imino spacer and a sterical demanding rest, right: with B3LYP/HF optimized structure, white: Ti, blue: N, red: O.*

As a result, the computational study of imino-bridged ligands with either a CH_2- or a $(CH_2)_2$-unit provides an answer to the question, which configuration of the complexes is preferred. Comparison of the energies shows that complex **17** with one CH_2 unit prefers the helicate form and complex **18** with a $(CH_2)_2$ unit occurs as a *meso*-helicate. A closer look at the geometrical structure of the complex reveals that the twisting of the ligand is essential for the formation of the helicate or *meso*-helicate. With a central

CH_2 unit the helicate leads to the less twisted geometry, and with a central $(CH_2)_2$ unit the *meso*-helicate has a energetically more favored structure. In general, the less twisted structure of the ligand leads to the energetically favored complex.

4.3 Heterodinuclear Complexes with Bishydroxychinoline-Based Ligands

The complexes with isobutinylidene-bridged bishydoxychinoline ligands have been studied before.[86] The first complex with two Al(III) cations as metal centers (Figure 200) forms a *meso*-helicate while the complex with two Yb(III) cations adopts the helicate form.[87] With the help of computational methods the question, which form the complex with Al(III) and Yb(III) adopts, should be answered.

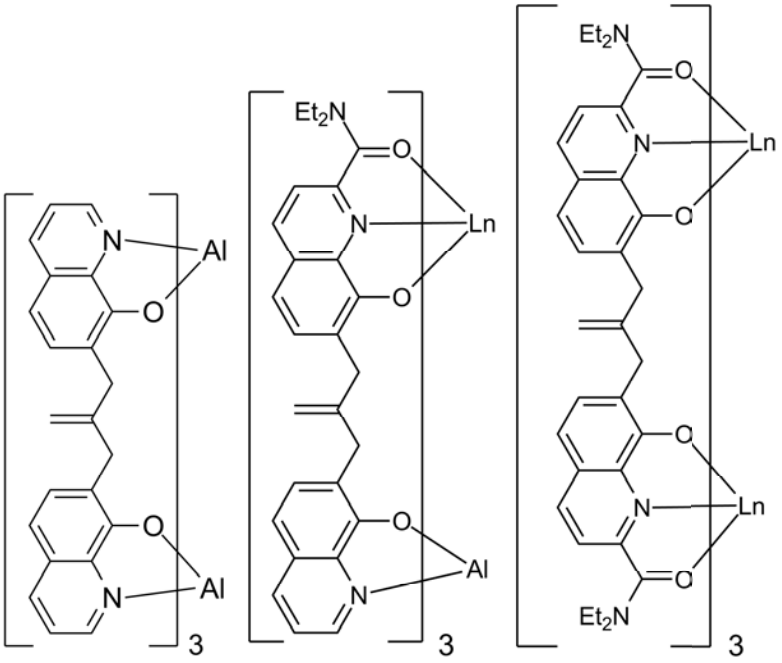

Fig. 200: *Complex **20** with two Al(III), Complex **21** with Al(III) and Ln(III) and Complex **22** with two Ln(III).*

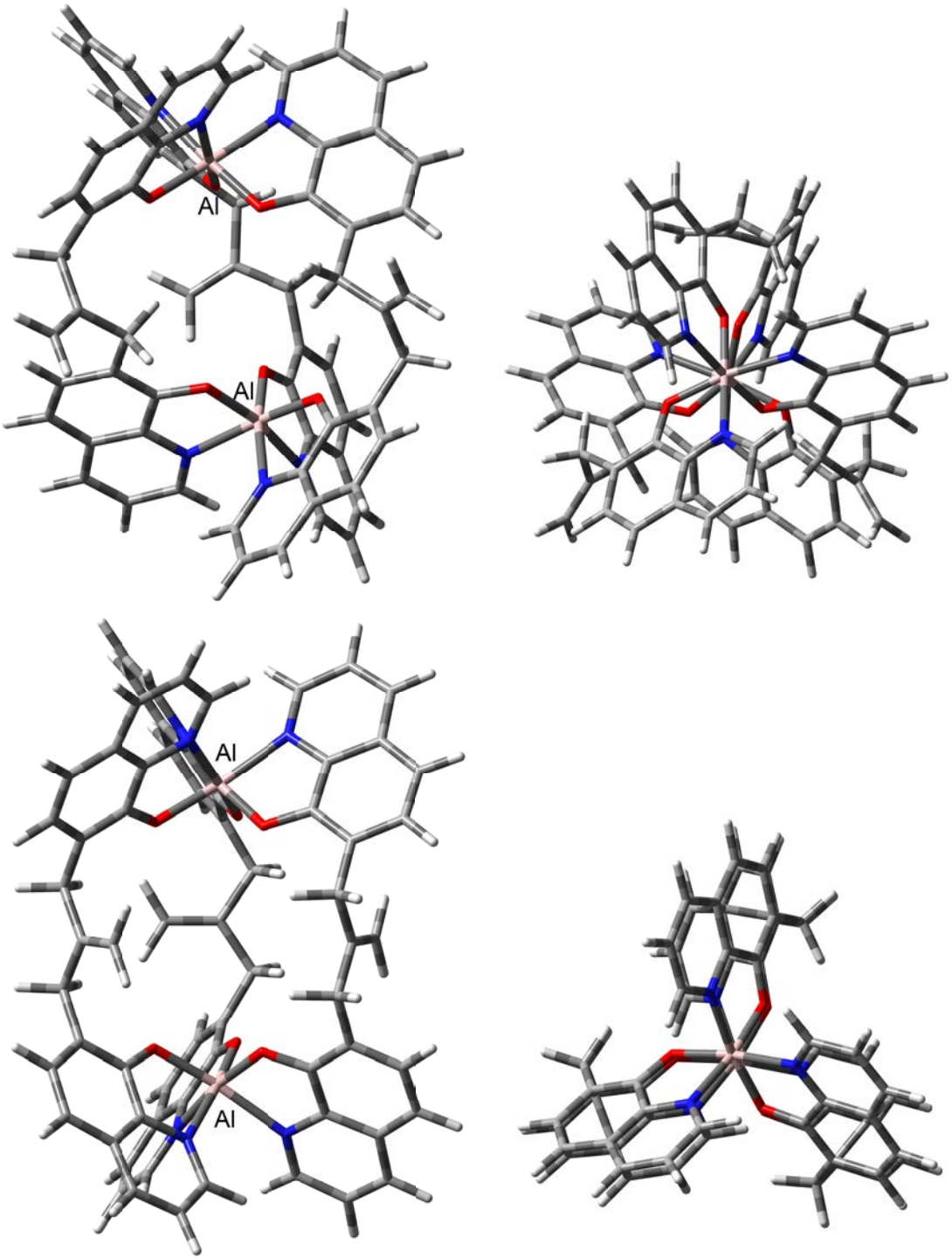

Fig. 201: *Geometrically optimized* $\Delta\Delta$ *(above) and* $\Delta\Lambda$ *(below) form of complex* ***20*** *with Al(III) but without a template; blue: N, red: O, pink: Al; functional: PBE1PBE, basis set: TZVP.*

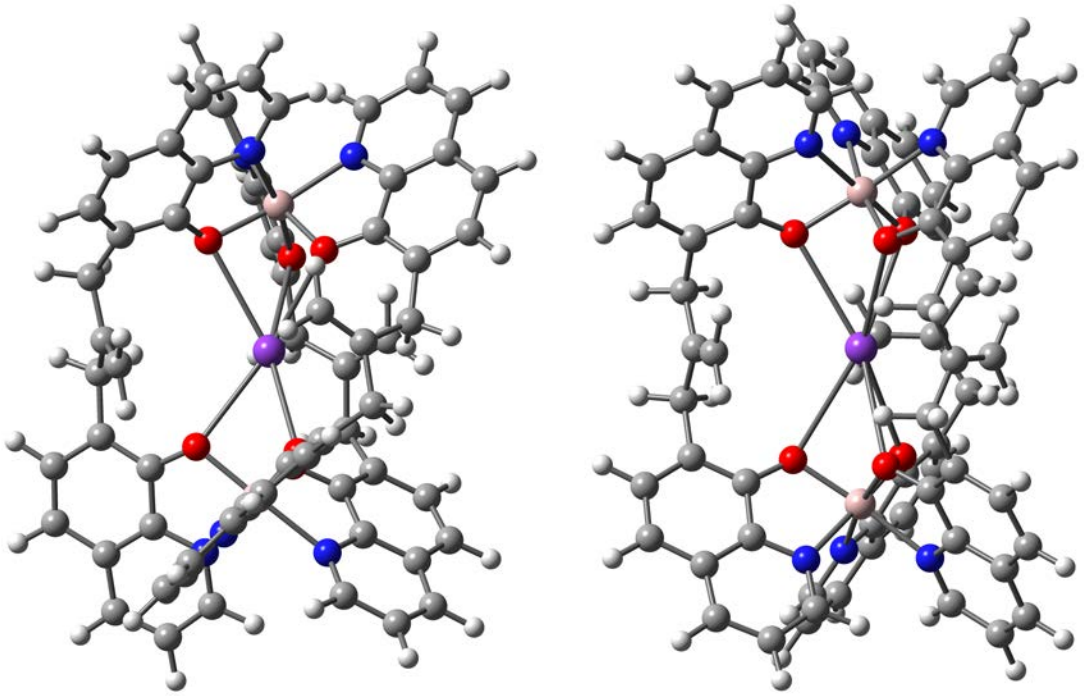

Fig. 202: *Geometrically optimized ΔΔ (left) and ΔΛ (right) form of complex **20a** with Al(III) and K^+ as spacer; blue: N, red: O, pink: Al, purple: K; functional: PBE1PBE, basis set: TZVP.*

A calculation on the ΔΔ form of complex **20** (with two Al(III) cations) results in an energy of −4405.844045 a.u. while the ΔΛ form of complex **20** gives −4405.877474 a.u.. Therefore, the ΔΛ form is energetically favored (ΔE = 20.977 kcal/mol). With K^+ as a spacer the ΔΔ of complex **20a** has an energy of −4405.844045 a.u. and the ΔΛ form has an energy of −4405.877474 a.u.. Thus the energy difference of ΔE = 20.977 kcal/mol is the same as without the spacer. As the cation K^+ has the same distance to both metal centers of 3.42 Å the cavity formed by the three ligands has an appropriate size.

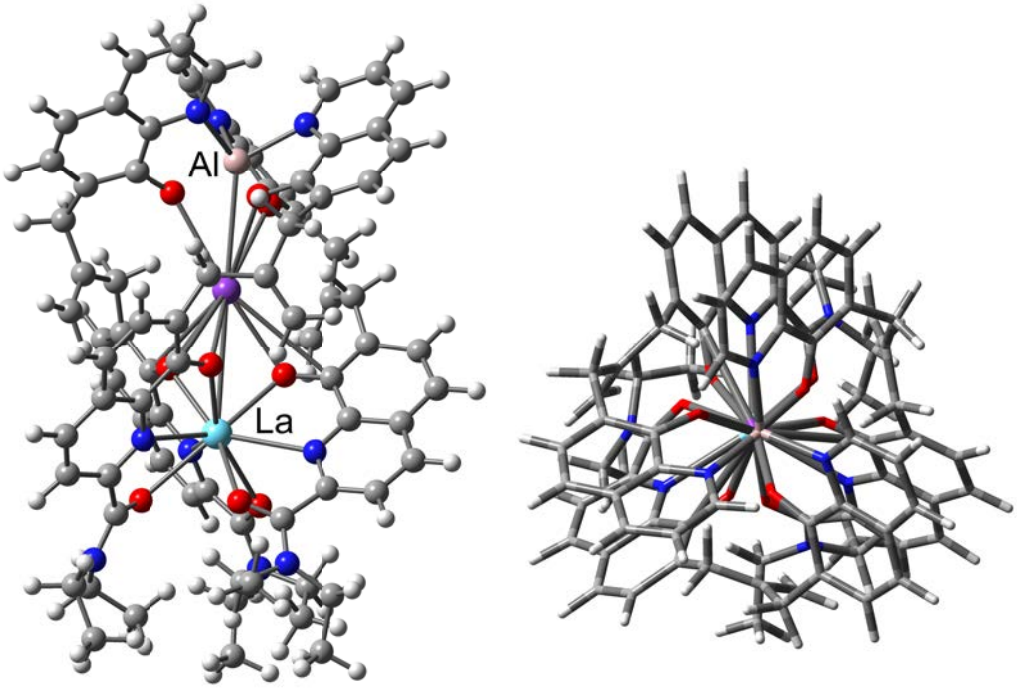

Fig. 203: *Geometrically optimized ΔΔ form of complex **21** with Al(III) and La(III) and K^+ as template, energy: −5341.093131 a.u.; light blue: La, pink: Al, purple: K, blue: N, red: O; functional: B3LYP, basis set: TZVP.*

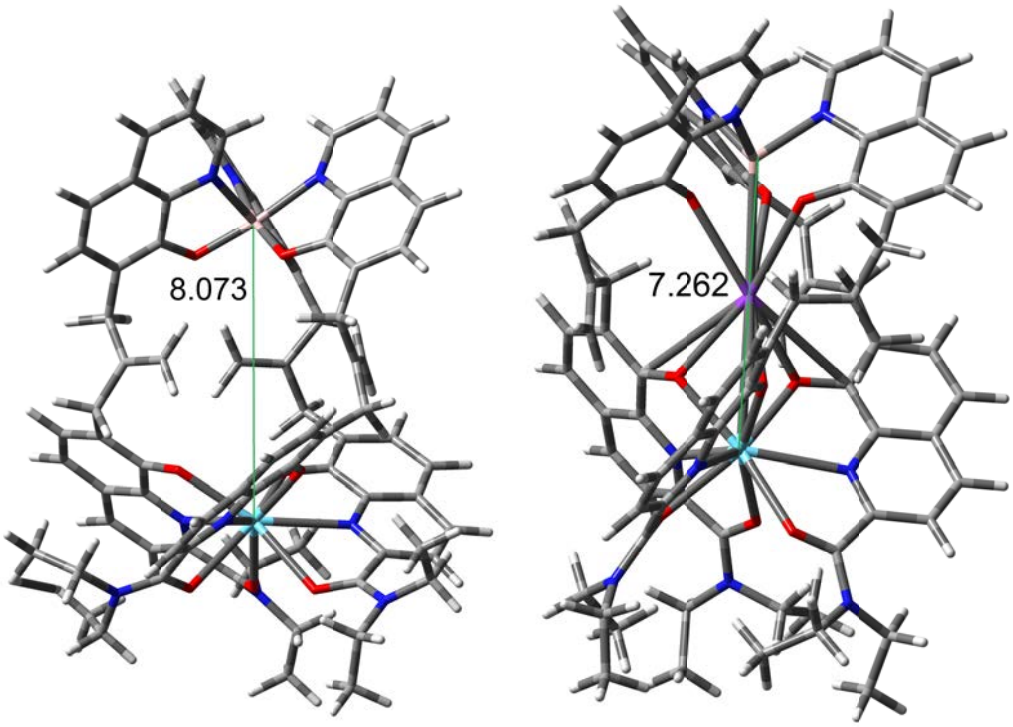

Fig. 204: *Geometrically optimized ΔΔ form of complex **21** with Al(III) and La(III) with and without K^+ as template; light blue: La, pink: Al, purple: K, blue: N, red: O; functional: B3LYP, basis set: TZVP.*

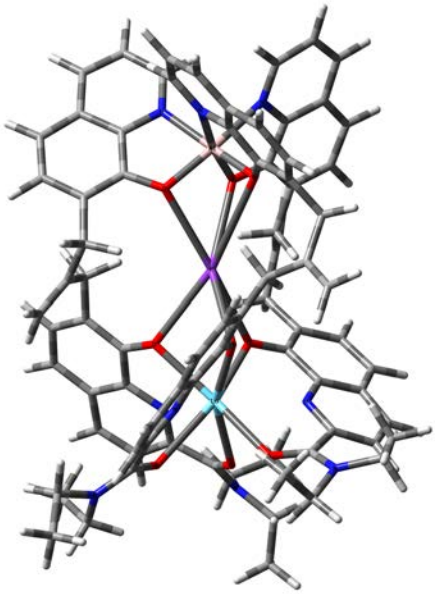

Fig. 205: *Geometrically optimized ΔΛ form of complex **21** with Al(III) and La(III) and K^+ as template, energy: −5341.134416 a.u.; light blue: La, pink: Al, purple: K, blue: N, red: O; functional: B3LYP, basis set: TZVP.*

Complex **21** with Al(III) and La(III) results in an energy of −5341.093131 a.u. for the ΔΔ form at the B3LYP/TZVP level of theory. The energetically optimized structure of the ΔΛ form results in an energy of −5341.134416 a.u.. Therefore, the ΔΛ form is energetically favored (25.907 kcal/mol). In the next step, complex **22** was energetically optimized with La(III) as metal center.

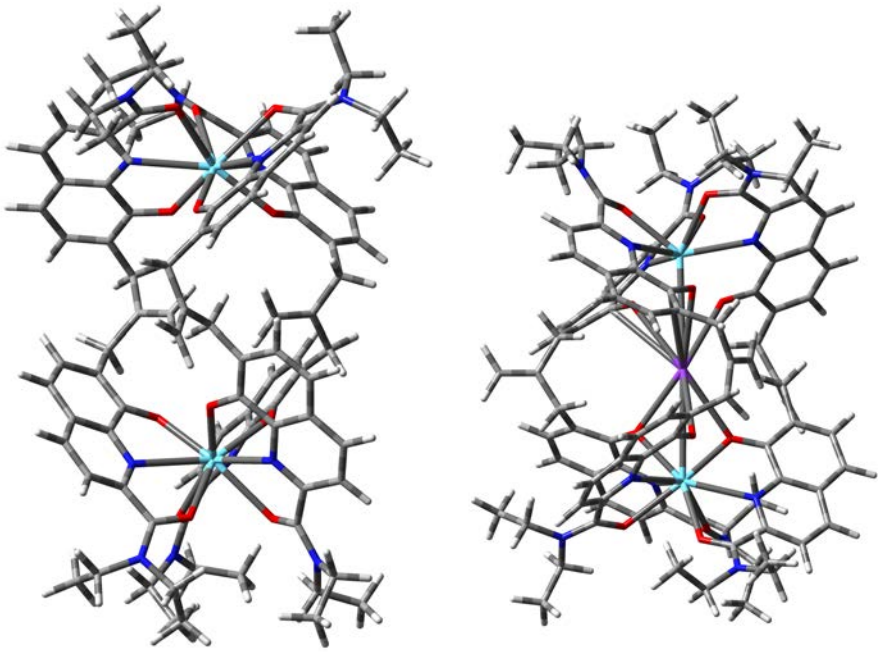

Fig. 206: *Geometrically optimized ΔΛ form of complex **22** with La(III) with (right) and without K^+ (left) as template; light blue: La, purple: K, blue: N, red: O; functional: B3LYP, basis set: TZVP.*

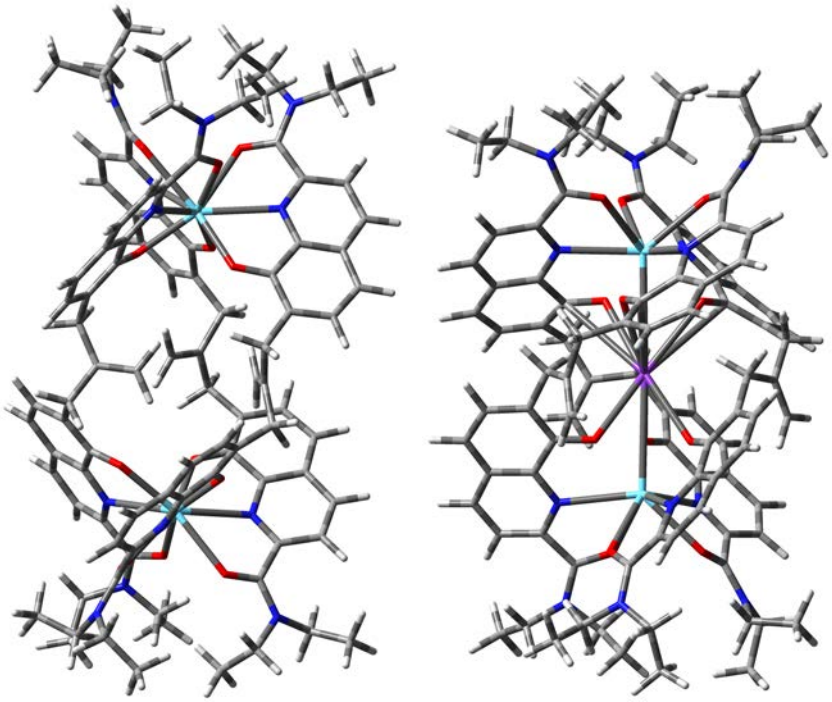

Fig. 207: *Geometrically optimized ΔΔ form of complex **22** with La(III) with and without K^+ as template; light blue: La, purple: K, blue: N, red: O; functional: B3LYP, basis set: TZVP.*

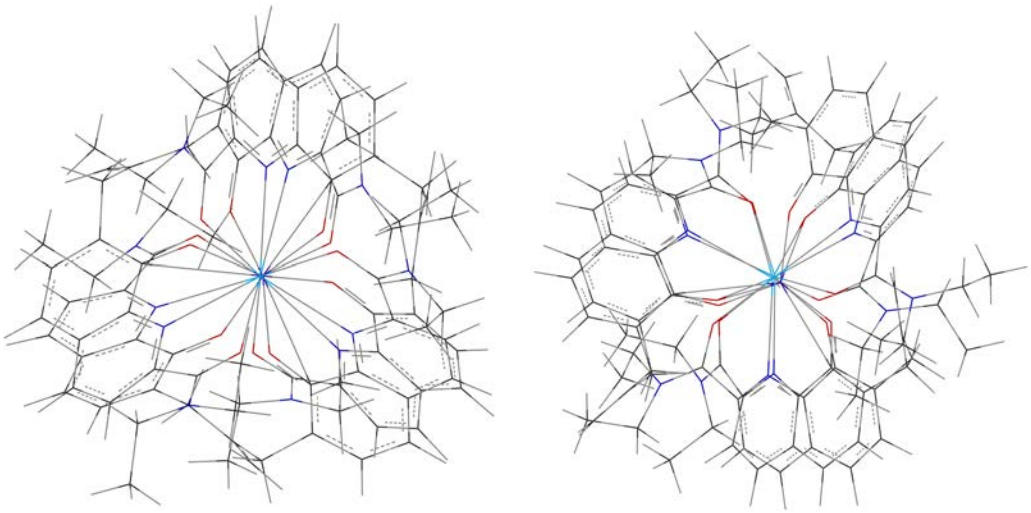

Fig. 208: *Geometrically optimized ΔΔ (left) and ΔΛ (right) form of complex **22** with La(III) with K^+ as template; light blue: La, purple: K, blue: N, red: O; functional: B3LYP, basis set: TZVP.*

configuration	metal center	Energy in a.u.	difference in kcal/mol
ΔΛ	Al, Al	−4405.877474	−20.977
ΔΔ	Al, Al	−4405.844045	
ΔΛ	La, La	−6753.019467	−11.099
ΔΔ	La, La	−6753.001779	

Table 41: *Total and relative energies of the ΔΛ and ΔΔ form of complexes **20** (with Al(III)) and **22** (with La(III)) with K^+ as template, functional: B3LYP, basis set: TZVP.*

Optimization of the structure of complex **22** with La(III) results in a *meso*-helicate ($\Delta\Lambda$). The energy difference to the helicate form ($\Delta\Delta$) is −11.099 kcal/mol. As earlier studies with Yb(III) and the same ligand as in complex **22** showed that the helicate form is adopted, additional calculations with Yb(III) instead of La(III) were performed. The structure of the *meso*-helicate with Yb(III) could not be optimized on the B3LYP level of theory as no energetical minimum could be found on this level of theory. Therefore, the complex **22** with Yb(III) was energetically optimized with the HF method (Figure 210).

In Figure 209 the structures of the optimized complexes with Yb(III) and La(III) are compared in their helicate form. The ligands within both complexes show the same twist. In contrast to this, the ligands within the $\Delta\Lambda$ form are very different (Figure 210). As Yb(III) has a smaller ionic radius (86 pm) than La(III) (122 pm),[80] the metal−O distances are smaller. This results in a more compact structure in which the ligand in the *meso*-helicate adopts a more twisted form with more repulsions than in the complex with La(III).

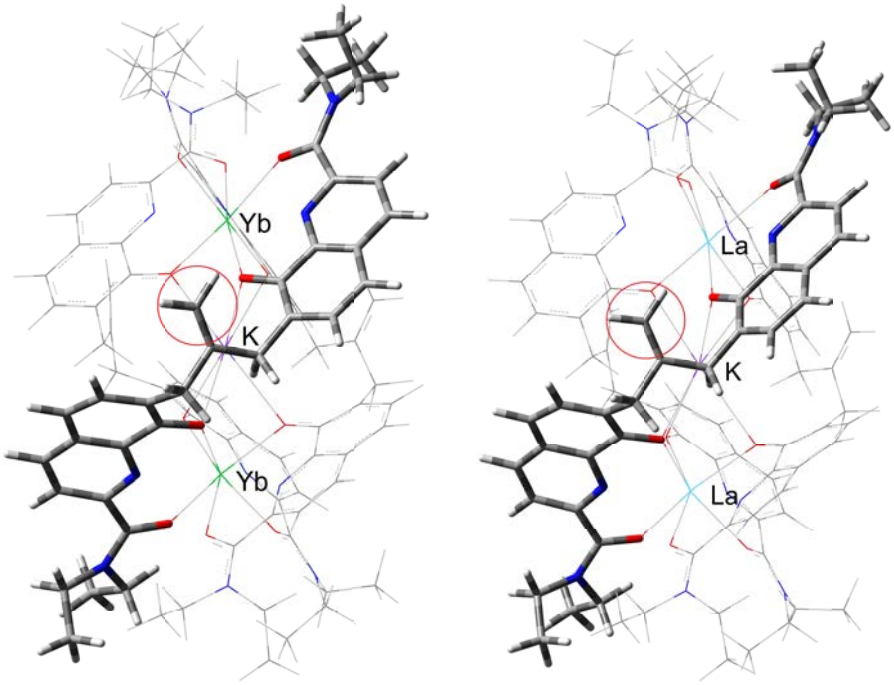

Fig. 209: *Geometrically optimized $\Delta\Delta$ form of complex **22** with Yb(III) (left) and La(III) (right) with K^+ as template; green: Yb, light blue: La, purple: K, blue: N, red: O; functional: B3LYP, basis set: TZVP.*

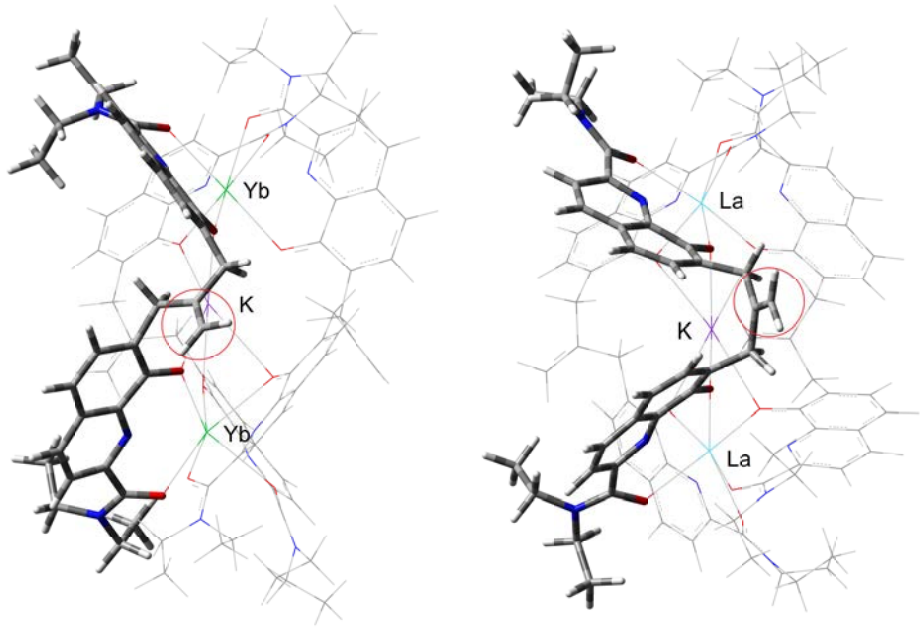

Fig. 210: *Geometrically optimized ΔΛ form of complex **22** with Yb(III)* (left) and La(III)** (right) with K^+ as template; green: Yb, light blue: La, purple: K, blue: N, red: O; *method: HF, **functional: B3LYP, basis set: TZVP.*

To answer the question, which form (ΔΔ or ΔΛ) is preferred, if complex **21** is formed with the combination of Yb(III) and Al(III), both structures were calculated on the B3LYP/6-31g* level of theory. The resulting relative energies are listed in Table 42. The energy difference between both forms is 25.655 kcal/mol, where the ΔΛ form is energetically favored.

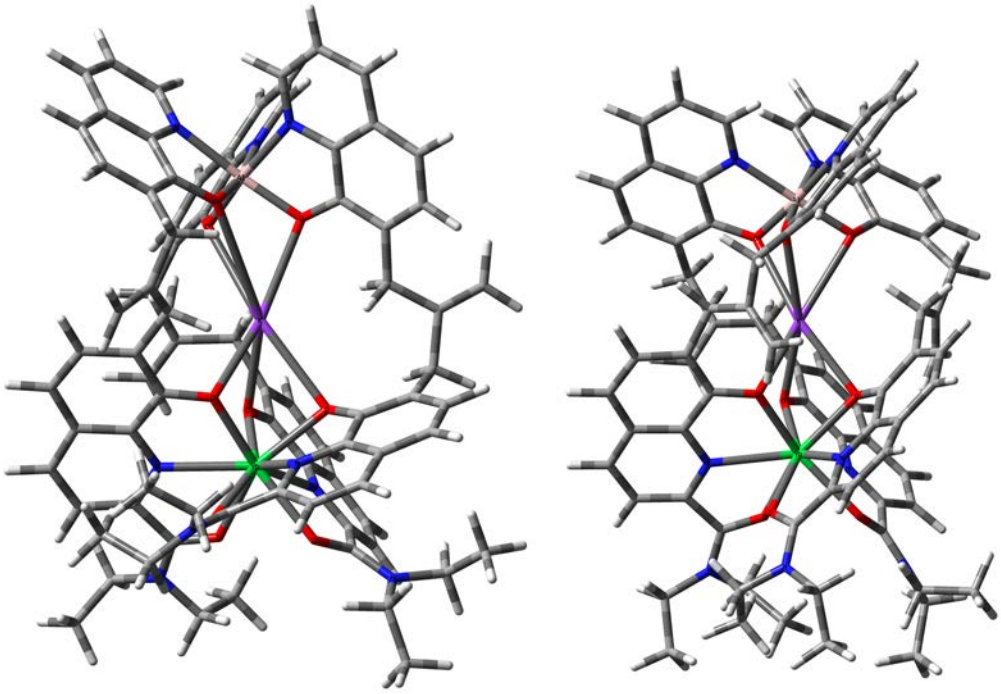

Fig. 211: *Geometrically optimized ΔΛ form of complex **21** with Yb(III) and Al(III) with K^+ as template; green: Yb, pink: Al, purple: K, blue: N, red: O; B3LYP, basis set: 6-31g*.*

configuration	metal center	Energy in a.u.	difference in kcal/mol
ΔΛ	Al, Yb	−6063.353311	25.655
ΔΔ	Al, Yb	−6063.312428	

Table 42: *Total and relative energies of the ΔΛ and ΔΔ form of complex **21** with K^+ as template, functional: B3LYP, basis set: 6-31g*.*

All in all, the calculations on the heterodinuclear complexes with bishydroxychinoline-based ligands could answer the question, which form (ΔΛ or ΔΔ) is preferred. Complex **20** with Al(III) prefers the ΔΛ form, complex **21** with the combination of Al(III) and Yb(III) adopts the ΔΛ form, and complex **22** with La(III) also favors the ΔΛ form. Only complex **22** with Yb(III) instead of La(III) energetically favors the helicate form, which can be seen in Figure 209 and 210.

4.4 Heterodinuclear Complexes with Dicatecholate-Based Ligands

Helicates with two or more different metals are of special interest, as interactions between the metals are possible. Al(III), Ga(III), Ti(IV) and La(III) were chosen as metal centers and different dicatecholate-acylhydrazone-based ligands were used. The resulting structures are presented in Figure 212.[89]

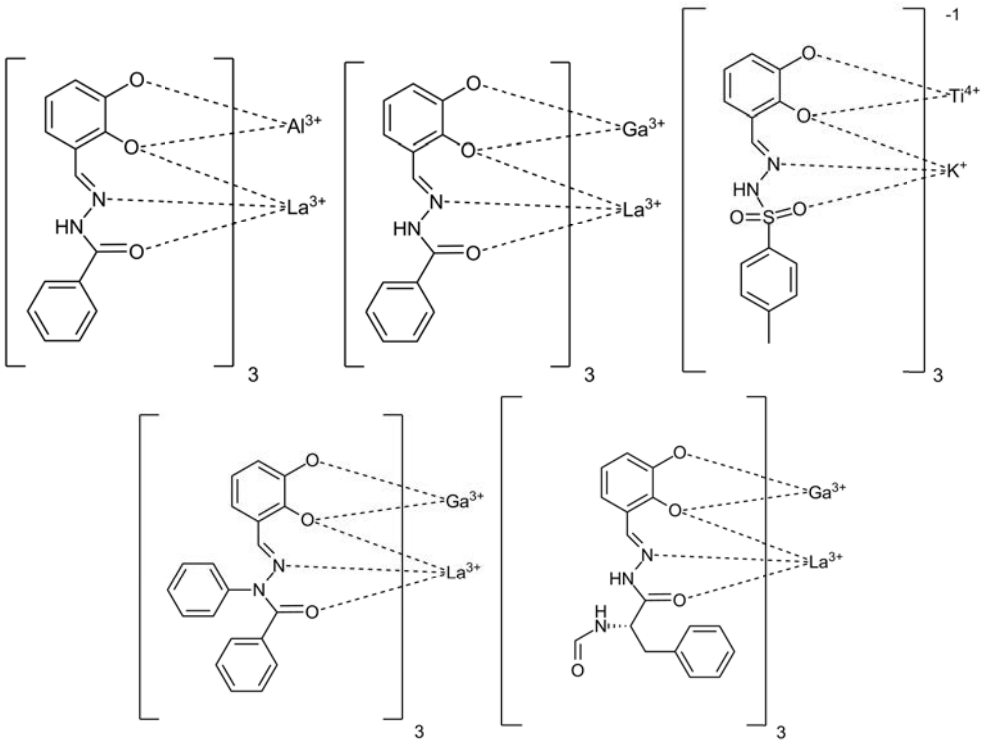

Fig. 212: *Structure of the chosen complexes **23** to **27** with dicatecholate-based ligands.*

4.4.1 Comparison to the solid state structure

The first step of this study is the comparison of the calculated structure of complex **23** with the experimentally obtained structure in the solid state. This study enables the choice of an appropriate functional. Figure 213 depicts different views of the structure of complex **23** in the solid state, where the complex adopts the Δ configuration.

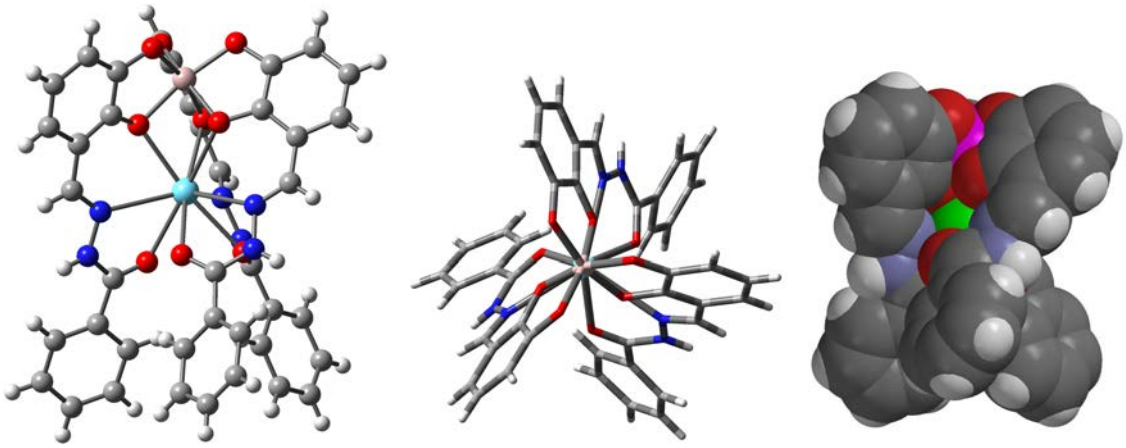

Fig. 213: *Different views of the solid state structure of complex **23**, Δ configuration.*

The functionals, B3LYP, cam-B3LYP and PBE1PBE were tested. Comparison of some important resulting structural parameters of complex **23** is made in Table 43. The distances within the solid state structure are: d(Al−La)= 3.360(18) Å, d(Al−O)= 1.909(5) Å, d(La−O)= 2.552(4) Å, and d(La−N)= 2.805(5) Å.[90] The largest deviation from the solid state structure occurs with B3LYP. Use of the functionals cam-B3LYP and PBE1PBE result in similar distances. With cam-B3LYP, the difference between the calculated and measured metal-metal distances is slightly larger and the metal−O distances have a smaller deviation to the solid state structures than those obtained with the PBE1PBE functional.

Method	d(Al−La)*	Dev.**	d(Al−O)	Dev.	d(La−O)	Dev.	d(La−N)	Dev.
B3LYP	3.409	0.049	1.949	0.040	2.545	0.006	2.806	0.001
cam-B3LYP	3.372	0.012	1.938	0.029	2.530	0.022	2.779	0.026
PBE1PBE	3.366	0.006	1.936	0.027	2.524	0.027	2.766	0.039

Table 43: *Optimized structural parameters of the complexes with La(III) and Al(III), basis set: TZVP, ECP: MWB28, *distances in Å, **deviation from the solid state structure of complex **1**.*

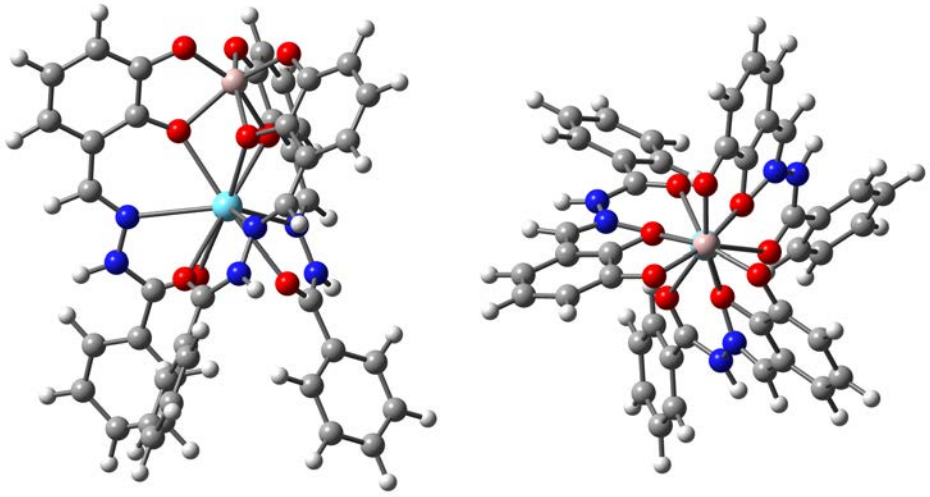

Fig. 214: *Different views of the energetically optimized structure of complex* ***23****,* Δ *configuration; pink: Ga, light blue: La, blue: N, red: O; method: cam-B3LYP/TZVP.*

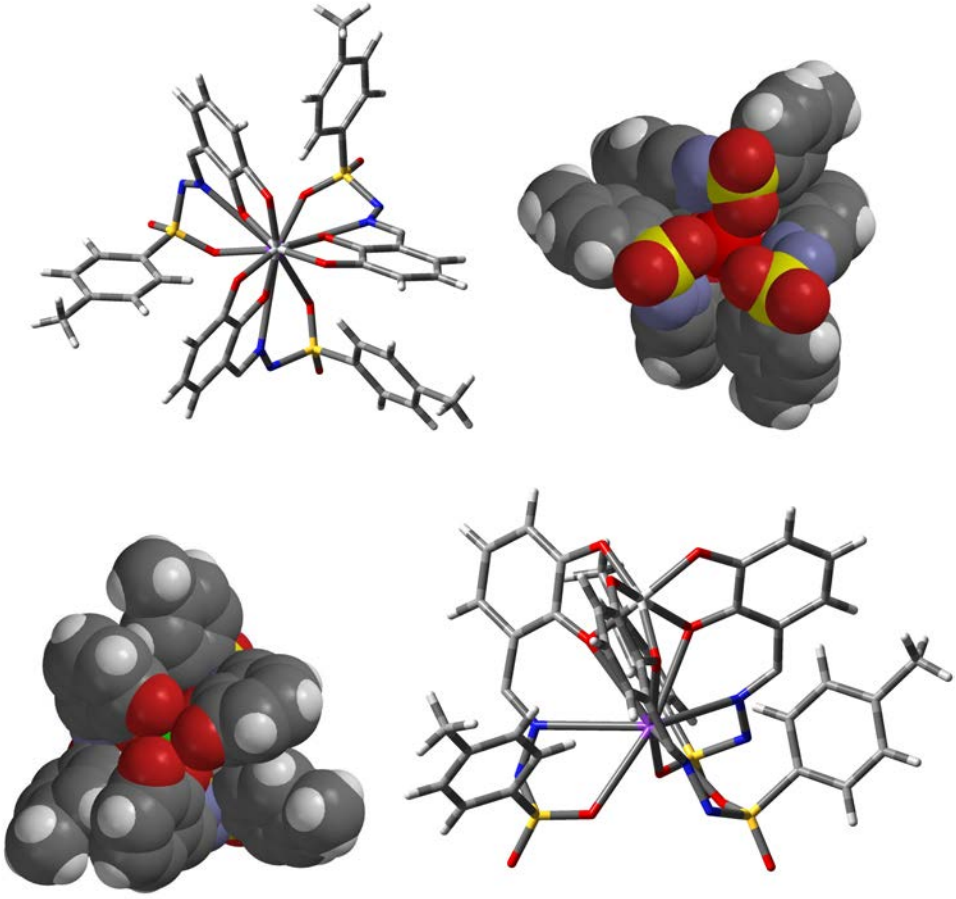

Fig. 215: *Different views of the solid state structure of complex* ***25****,* Λ *configuration; white: Ti, purple: K, red: O, yellow: S.*

The second known solid state structure is the one of complex **25**. It reveals a Λ configuration of the complex (Figure 215).

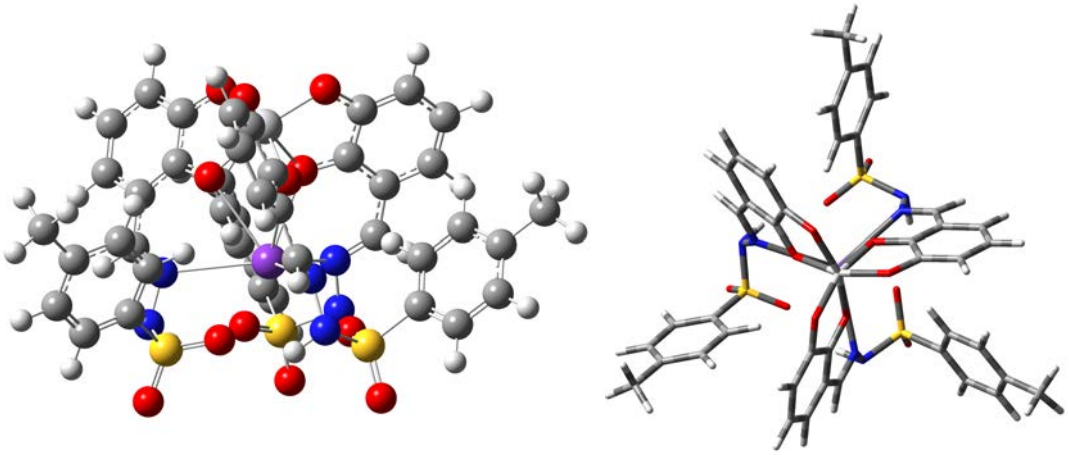

Fig. 216: *Energetically optimized structure of complex **25** with Ti(IV) and K(I); white: Ti, purple: K, red: O, yellow: S; method: cam-B3LYP/TZVP.*

As the comparison of calculated parameter with the first solid state structure shows that cam-B3LYP is a good choice as a functional for heterodinuclear complexes, this method is used in the following calculations as well. Comparison with the second solid state structure results in relatively small differences (Table 44). The distances within the solid state structure are d(Ti−K)= 3.512 Å, d(Ti−O)= 1.964 Å, d(K−O)= 2.772 Å, and d(K−N)= 3.131 Å (with a R1 factor of 0.0913).[90]

Method	d(Ti−K)*	Dev.**	d(Ti−O)	Dev.	d(K−O)	Dev.	d(K−N)	Dev.
cam-B3LYP	3.597	0.085	1.963	0.001	2.800	0.028	2.881	0.025

Table 44: *Optimized structures of complexes with Ti(IV) and K(I), basis set: TZVP, ECP: MDF10, *distances in Å, **Deviation from the solid state structure of Complex **25**.*

4.4.2 Comparison of the different metal-metal distances

In the next part of the study, the influence of different ligands on the metal-metal distances was studied. This distance is a good indicator for the structure of the complex and, therefore, for the possible metal-metal interactions. The first two complexes, which were studied, are complex **23** with Al(III) and La(III) and complex **24** with the same ligand but Ga(III) instead of Al(III). The geometry of the energetically optimized structure of complex **24** is presented in Figure 217.

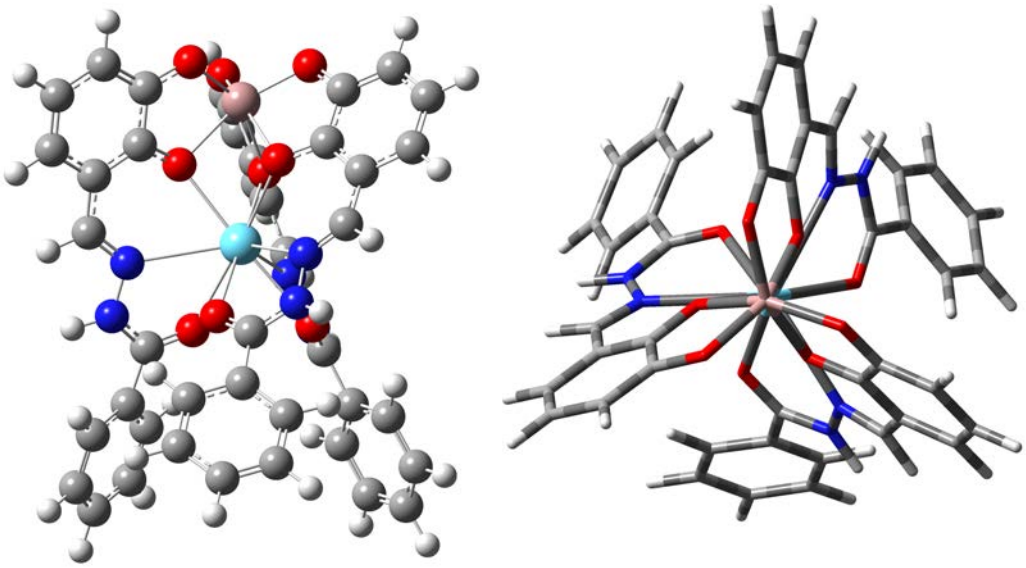

Fig. 217: *Different views of the geometrically optimized structure of complex **24** with Ga(III) and La(III), Δ configuration; pink: Ga, light blue: La, blue: N, red: O; method: cam-B3LYP/TZVP.*

Complex 1 − atom	distance*	average	Complex 2 − atom	distance	average
Ga−La	3.470		Al−La	3.383	
Ga−O	1.908	1.908	Al−O	1.856	1.856
	1.908			1.856	
	1.908			1.856	
	2.162	2.162		2.051	2.050
	2.163			2.051	
	2.162			2.050	
La−O	2.424	2.424	La−O	2.429	2.429
	2.424			2.430	
	2.424			2.428	
	2.629	2.630		2.623	2.623
	2.630			2.622	
	2.629			2.623	
La−N	2.794	2.795	La−N	2.787	2.789
	2.796			2.789	
	2.795			2.790	

Table 45: *Optimized structures of complexes **23** and **24**, ionic radii of the cations: La(III)= 1.22 Å, Ga(III)=0.62 Å, Al(III)= 0.57 Å; *distances in Å; method: cam-B3LYP, basis set: TZVP, ECP: MWB28.*

Although the ionic radii of Al(III) and Ga(III) are quite similar, the distance between Ga(III) and La(III) is much larger than the one between Al(III) and La(III). Likewise, the Ga(III)−O distances are larger than the Al(III)−O distances. Therefore, Al(III) seems to have a higher affinity to oxygen than Ga(III).

The next Figures 216 and 219 show the optimized geometries of the complexes **25** and **26**. Both complexes have Ga(III) and La(III) as metal centers.

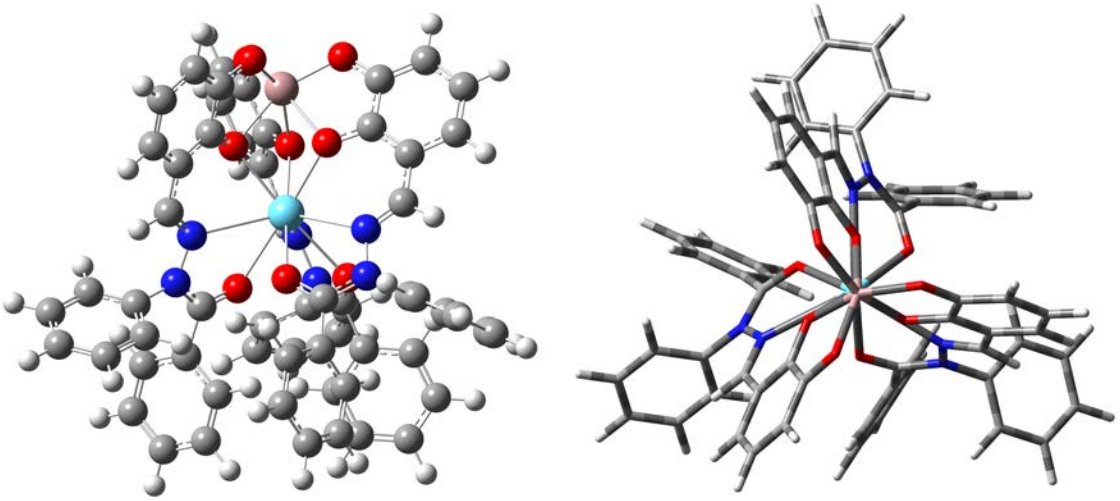

Fig. 218: *Energetically optimized structure of complex **26**, Δ configuration, d(Ga-La)=3.451; method: cam-B3LYP/TZVP.*

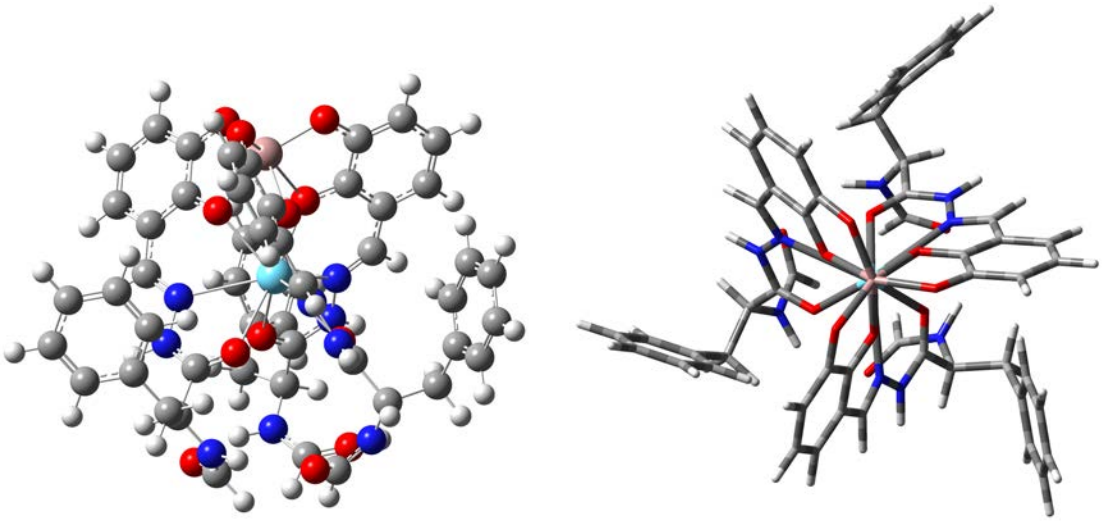

Fig. 219: *Energetically optimized structure of complex **27**, Λ configuration, d(Ga-La)=3.479; method: cam-B3LYP/TZVP.*

The analysis of the distances between the metal centers and the O- as well as the N-atoms can help to reveal some more aspects of the different complexes. The Ga(III)−La(III) distance of complex **27** (3.479 Å) for example is slightly larger than the same distance in complex **23** (3.470 Å). The La(III)-O and La(III)-N distances of complex **26** are shown in Figure 220 (distance La(III)-O: 2.599 and 2.416 Å, distance La(III)-N: 2.829 Å).

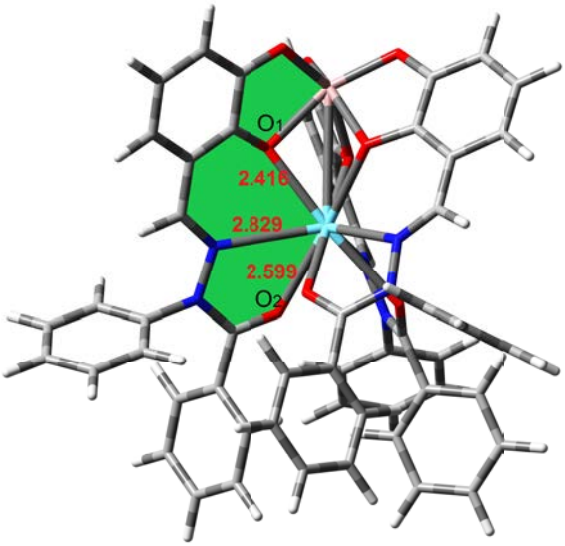

Fig. 220: *Optimized geometry of complex **26**, Λ configuration, with the distances La(III)-O and La(III)-N.*

As a conclusion, the analysis of the various distances reveals that the metal-metal distances tend to remain the same, if slight changes of the ligand are made. Only the distances between the metal centers and the O- and N-atoms depend significantly on the choice of the ligand. Therefore, the metal-metal interactions supposedly remain the same if the ligand is replaced by a slightly different ligand.

4.4.3 CD Measurements on Heterodinuclear Helicates

To further analyze the heterodinuclear helicates with dicatecholate-based ligands, TD-DFT calculations were performed. For these calculations, the ligand shown in Figure 221 was chosen. As metal centers, Ga(III) and La(III) were selected.[90]

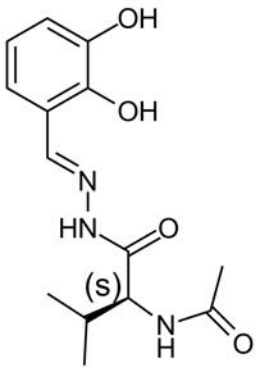

Fig. 221: *Ligand for the CD measurements.*

The bare ligand only shows a very small Cotton effect in the CD spectrum measured in DMSO and the spectrum is very noisy. The measurement of the ligands is important, because the result can be compared to the CD spectrum of the complex afterwards. This comparison is made in Figure 223. The complexes with Ga(III) and La(III) and

ligand **23** show spectra which differ significantly from the spectrum of the ligand. The spectrum of the complex in DMSO shows two minima and two maxima. The two maxima are located at 282 and 322 nm, and the two minima at 300 and 376 nm.

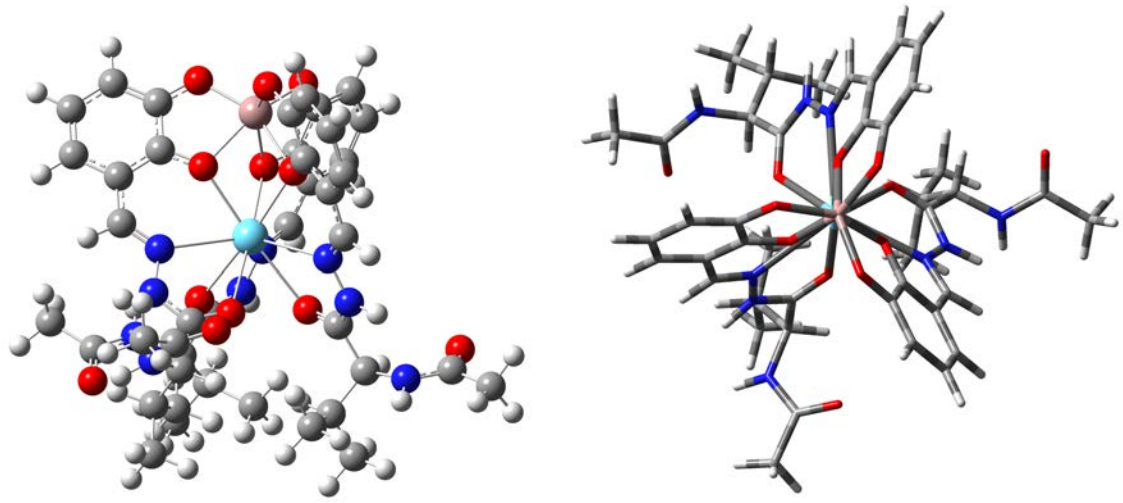

Fig. 222: *Geometrically optimized structure of complex **23** with Ga(III) and La(III), Λ configuration; pink: Ga, light blue: La, red: O, blue: N; method: cam-B3LYP/TZVP.*

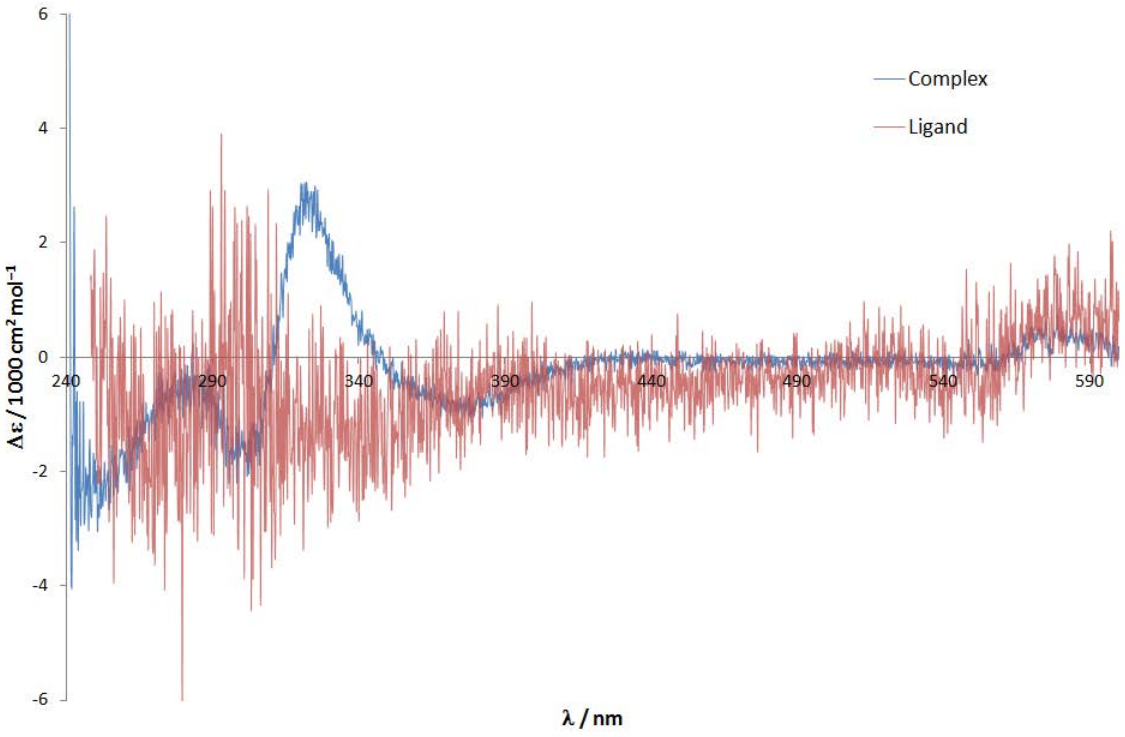

Fig. 223: *CD spectra of ligand **23** and the complex with Ga(III) and La(III), red: ligand **23**, blue: complex **23**, solvent = DMSO.*

The geometry of complex **23** with Ga(III) and La(III) was optimized. The resulting structure in the Λ form is shown in Figure 222. Important intermolecular distances are 3.480 Å (Ga(III)-La(III)), the Ga(III)-O distance 2.031 Å, and the La(III)-O dis-

tances 2.431 and 2.647 Å. Subsequently, TD-DFT calculations were performed on the B3LYP/TZVP level of theory. The outcome is presented in Figure 224.

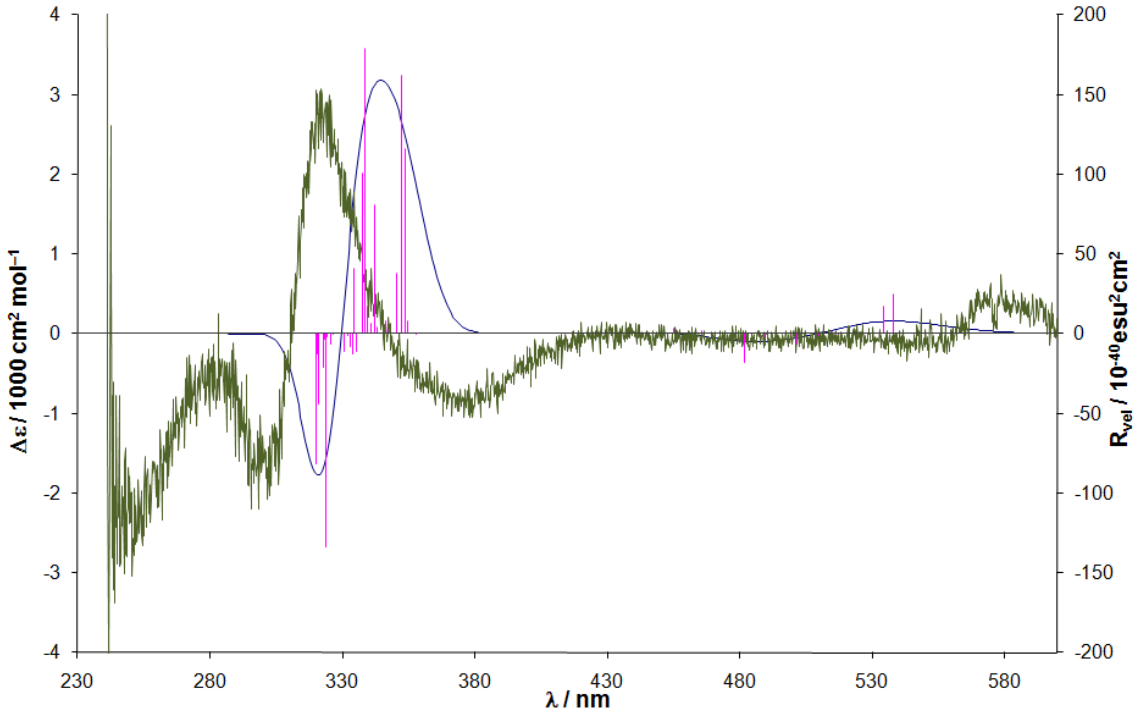

Fig. 224: *Ligand **23** with Ga(III) and La(III), comparison of the measured and calculated CD spectra; method: TDDFT/B3LYP/TZVP//cam-B3LYP/TZVP, number of excited states: 40.*

The calculated spectrum shows two minima, a very weak one at 480 nm and a much stronger at 320 nm. The most intense maximum is located at 354 nm and an additional smaller one at 538 nm. The calculated and measured CD bands can be assigned as follows 530/575, 480/380, 354/330, and 320/300 nm, which would imply different strong shifts in different parts of the spectrum.

wavelength	transitions	rotational strength	kind
537.93	247 → 248	25.2339	$\pi \rightarrow \pi^*$, np-metal(La(III))
534.50	247 → 249	16.9057	$\pi \rightarrow \pi^*$, np-metal(La(III))
352.56	244 → 249	162.3339	$\pi \rightarrow \pi^*$, np-metal(La(III))
338.47	243 → 249	178.7944	n,$\pi \rightarrow \pi^*$, np-metal(La(III))
323.85	247 → 260	−133.8066	$\pi \rightarrow \sigma^*$, np-metal(La(III))

Table 46: *The four excited states with the biggest rotational strength, their major components, and calculated rotational strength.*

Listing the four excited states with the biggest rotational strength Table 46 that reveals that the main configurations involve transitions between the ligand and the metal center (La(III)). The HOMO and the LUMO are presented in Figure 225. The

HOMO-LUMO transition is between the catecholate-part of the ligand and the La(III) ion.

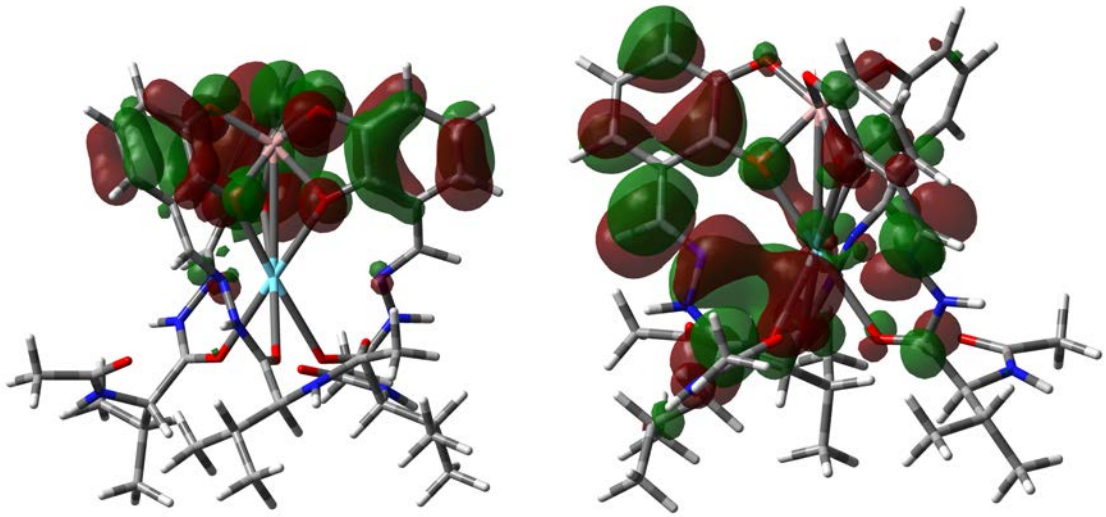

Fig. 225: *Energetically optimized structure of ligand **23** with Ga(III) and La(III), left: Ψ=247 (HOMO), right: Ψ=248 (LUMO) .*

To decide which form (Δ or Λ) is adopted in the solvent the spectrum was interpolated (Figure 226).[88] A better fit could only be achieved by multiplying the whole calculated spectrum by 0.77 (y-axes) and subtracting 21 nm (x-axes), which could indicate that the calculated spectrum does not properly reproduce the measured spectrum. The next Figure 227 shows the mirror image of the calculated spectrum. This spectrum was multiplied by -1.20 (y-axes) and 20 nm were added. Comparison of the two figures reveal that the original curve of the calculated spectrum (Figure 226) fits better than the mirror image. Therefore, the Λ form is most likely adopted in the solvent, although there remains uncertainty regarding the assignment of the strongly negative band observed at about 380 nm.

The TD-DFT calculations can be used to elucidate, which configuration (Δ or Λ) is adopted in the chosen solvent. Moreover, they provide a tool for the analysis of the transitions within the complex. If the transitions involve the metal center a dependence of the spectral curve on the nature of the metal can be expected.

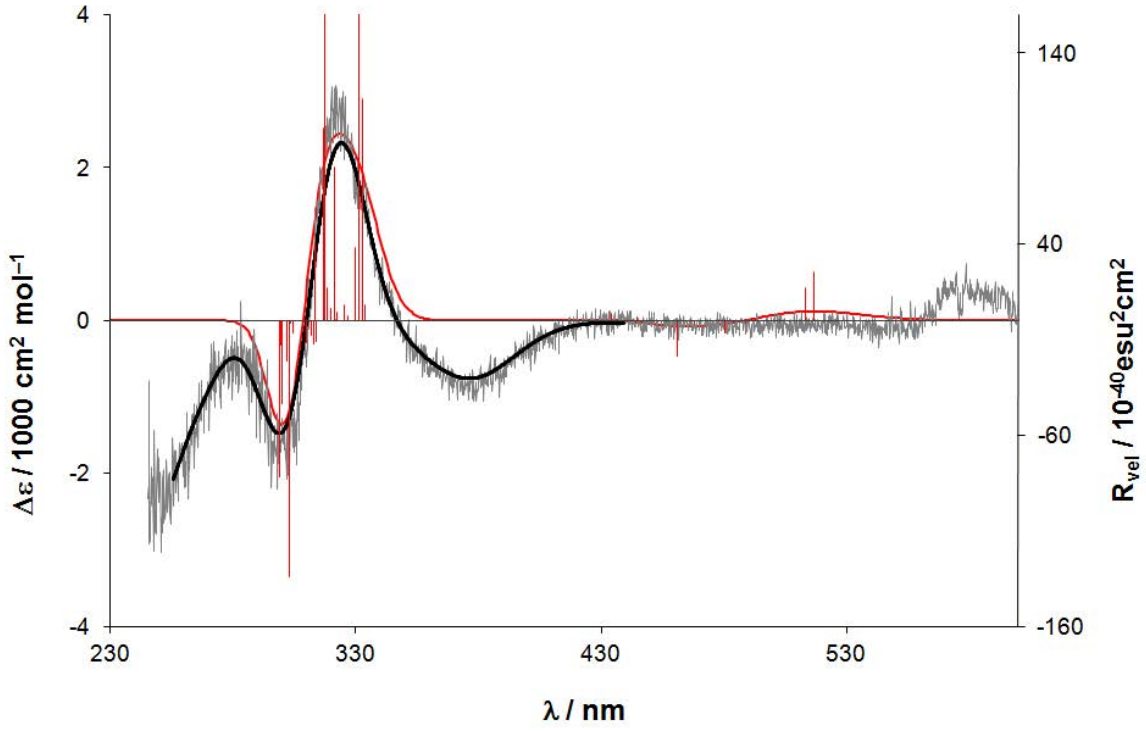

Fig. 226: *Ligand 23 with Ga(III) and La(III), comparison of the measured (interpolated spectrum, black) and calculated CD spectra (red); the calculated spectrum was multiplied by 0.77 (y-axes), and 21 nm were subtracted (x-axes); method: TDDFT/B3LYP/TZVP//cam-B3LYP/TZVP, number of excited states: 40.*

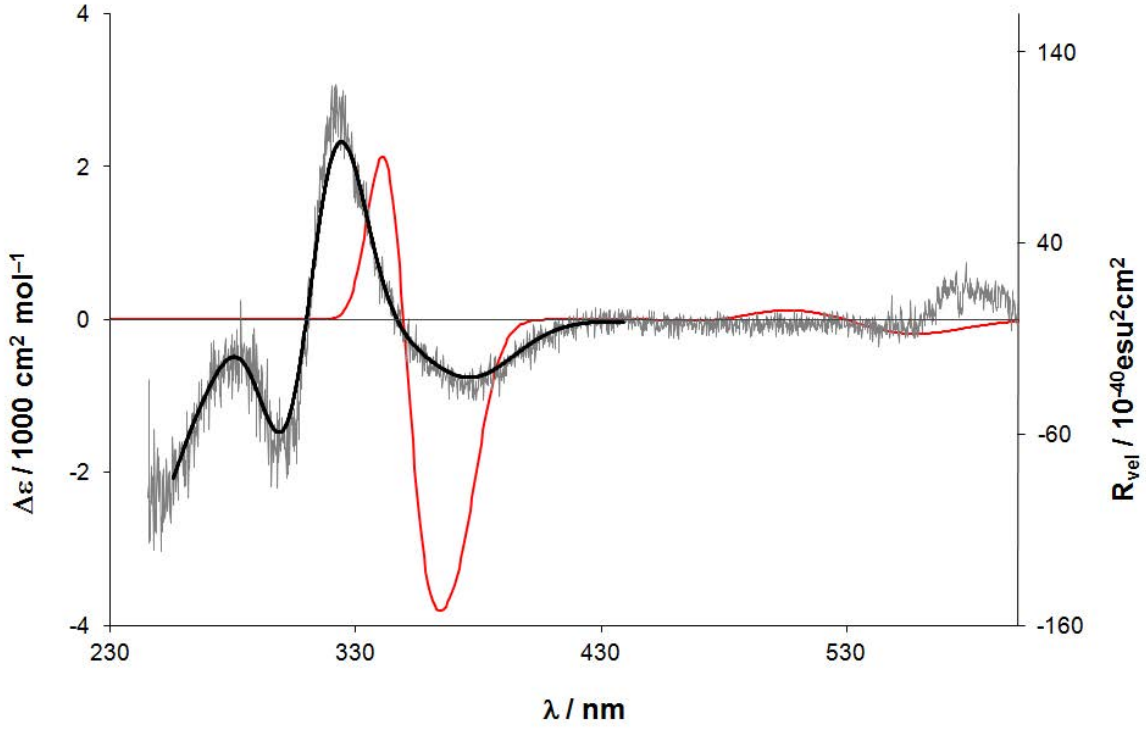

Fig. 227: *Ligand 23 with Ga(III) and La(III), comparison of the measured (interpolated spectrum, black) and calculated CD spectra (red); the calculated spectrum was multiplied by -1.20 (y-axes), and 20 nm were added (x-axes); method: TDDFT/B3LYP/TZVP//cam-B3LYP/TZVP, number of excited states: 40.*

5 Tetranuclear Complexes

5.1 Tetranuclear Helicates

Having the possibility of several metal-metal interactions, tetranuclear helicates are of great interest. The dinuclear helicates analyzed before are model compounds for the complexes with more than two metal centers. Figure 228 shows the differences between the complexes with two and four metal centers. The part with the dicatecholate-acylhydrazone remains unchanged while the phenyl groups at the periphery of the ligand are replaced by a second dicatecholate-acylhydrazone moiety.

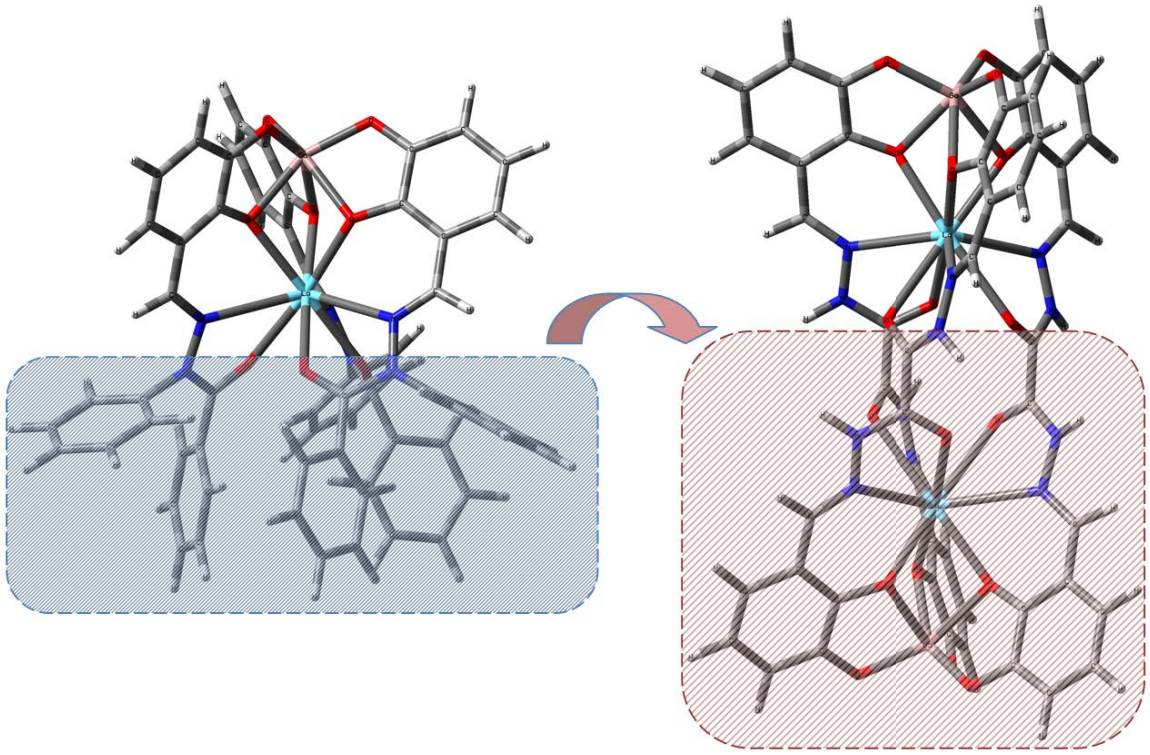

Fig. 228: *Relationship between the structure with two metal centers and four metal centers, metal: Ga(III) and La(III); pink: Ga, light blue: La, blue: N, red: O.*

For the study of tetranuclear helicates, the following ligands were chosen:

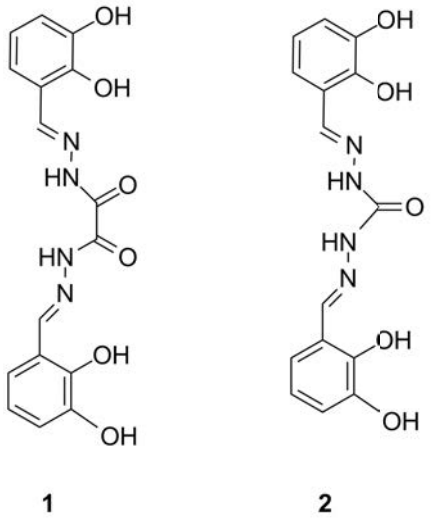

Fig. 229: *Structures of the ligands one and two.*

The two ligands in Figure 229 have very similar structures. They only differ in the numbers of carbonyl groups in the center of the spacer. Computational analysis of the resulting complexes can show the impact of this difference on the electronic structure.[91] NBO analyses will help to understand, why a certain combination of different metals and either ligand **28** or **29** is the most favored one and, thereby, provide a strategy for further synthetic work in the laboratory.

5.1.1 Calculations with ligand 28

With ligand **28** different combinations of metal ions were chosen: Ti(IV) and Y(III), Ti(IV) and La(III), Ga(III) and La(III), Ga(III) and Y(III).

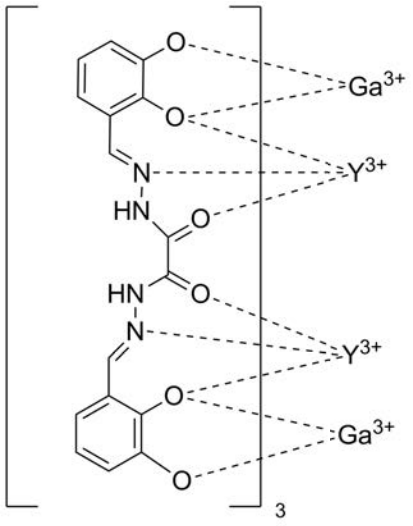

Fig. 230: *Complex with ligand **28**.*

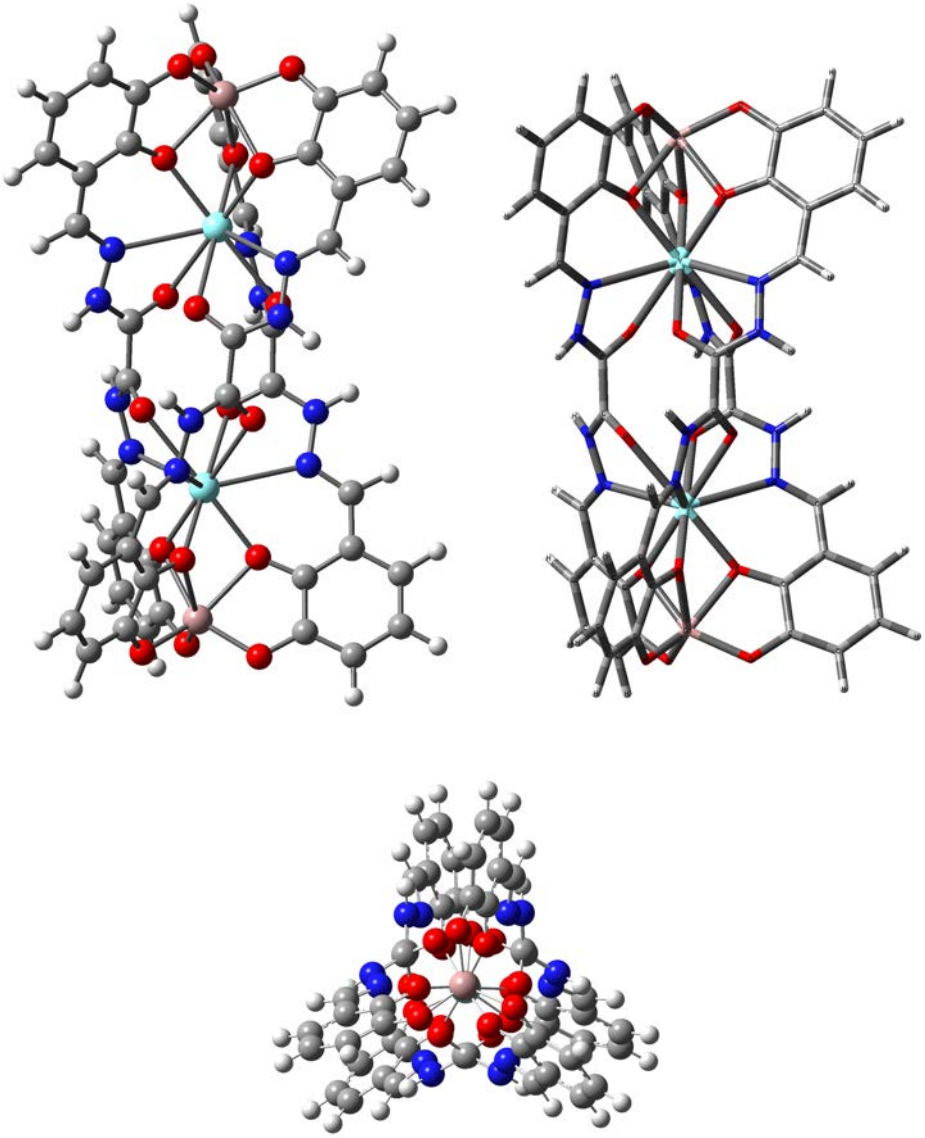

Fig. 231: *Geometrically optimized complex with ligand **28** and Ga(III) and Y(III), ΔΔ configuration; pink: Ga, light blue: Y, blue: N, red: O; method: cam-B3LYP/TZVP.*

For the complex with ligand **28** and the combination of Ga(III) and Y(III), the geometries of both the ΔΔ as well as the ΔΛ form were optimized. The ΔΔ form turned out to be slightly (1.31 kcal/mol) more stable than the ΔΛ isomer.

configuration	Energy in a.u.	difference in kcal/mol
ΔΛ	−3939.21040	
ΔΔ	−3939.21249	−1.31

Table 47: *Energies of the ΔΛ and ΔΔ configuration of complex **29** with Ga(III) and Y(III).*

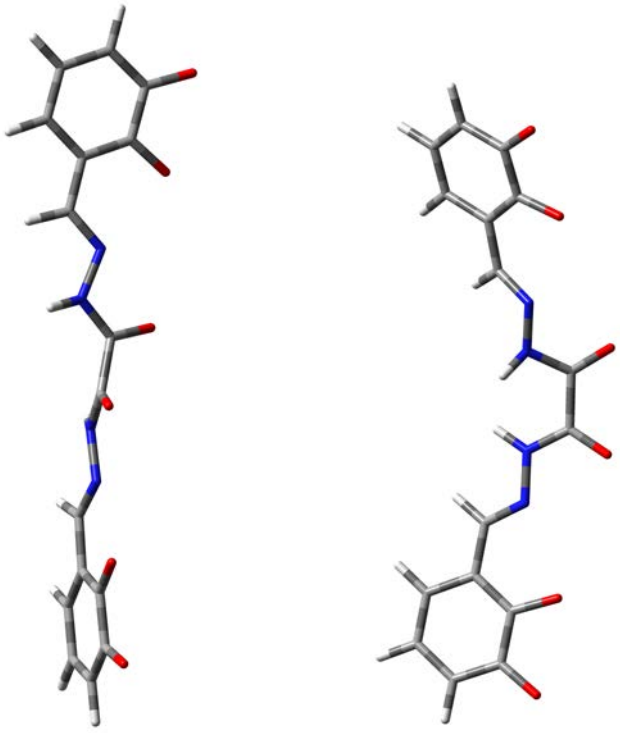

Fig. 232: *Ligand **28** from the complexes with Ga(III) and Y(III),* $\Delta\Delta$ *(left) and* $\Delta\Lambda$ *(right) configuration.*

form	energy in a.u.	energy difference in kcal/mol
$\Delta\Delta$	−1285.504912	−14.175
$\Delta\Lambda$	−1285.482323	

Table 48: *Energies of Ligand **28** from the complexes with Ga(III) and Y(III) in its* $\Delta\Delta$ *and* $\Delta\Lambda$ *configuration.*

The ligands of the $\Delta\Delta$ and $\Delta\Lambda$ form of the complex with Ga(III) and Y(III) are shown in Figure 232. The energy difference between the two configurations might be caused by the different twisting of the ligand (Table 48). The favored $\Delta\Delta$ form has larger distances between the O atoms of the α-diceto group.

atom	distance in Å	average in Å
Ga−Y	3.3426	
	3.3426	
Y-Y	6.6118	
Ga_1−O	1.8975	1.8976
	1.8978	
	1.8976	
	2.1904	2.1912
	2.1906	
	2.1926	
Y_1−O	2.2633	2.2626
	2.2619	
	2.2626	
	2.5645	2.5632
	2.5605	
	2.5646	
Y_1−N	2.7551	2.7556
	2.7538	
	2.7580	
Ga_2−O	1.8978	1.8976
	1.8976	
	1.8975	
	2.1906	2.1912
	2.1904	
	2.1926	
Y_2−O	2.2619	2.2626
	2.2626	
	2.2633	
	2.5646	2.5632
	2.5605	
	2.5645	
Y_2−N	2.7538	2.7556
	2.7551	
	2.7580	

Table 49: *Metal-metal distances and metal-O distances of complex **28** with Ga(III) and Y(III).*

The identical distances of the metals Y_1, Y_2 and Ga_1, Ga_2 to the ligands demonstrate the symmetric architecture of the complexes. To further analyze the electronic structure of the complex, a NBO (Natural Bond Orbital) analysis was carried out. The strongest interactions of the O atoms occur with Ga(III) resulting in an energy of about 63 kcal/mol (Table 50).

Donor NBO	Acceptor NBO	E in kcal/mol	average in kcal/mol
LP (3) O 31	LP*(1)Ga 109	62.32	62.65
LP (3) O 53	LP*(1)Ga 109	62.81	
LP (3) O 86	LP*(1)Ga 109	62.83	
LP (2) O 10	LP*(4)Ga 109	17.09	17.16
LP (2) O 27	LP*(4)Ga 109	17.20	
LP (2) O 42	LP*(4)Ga 109	17.18	
LP (1) O 10	LP*(4) Y 111	24.48	23.21
LP (1) O 27	LP*(5) Y 111	26.34	
LP (1) O 42	LP*(6) Y 111	18.82	
LP (1) N 37	LP*(2) Y 111	37.95	31.71
LP (1) N 14	LP*(3) Y 111	29.41	
LP (1) N 93	LP*(2) Y 111	27.77	
LP (2) O 51	LP*(1) Y 111	13.16	14.67
LP (1) O 52	LP*(2) Y 111	15.99	
LP (2) O 54	LP*(3) Y 111	14.86	

Table 50: *Complex **28** with Ga(III) and Y(III), donor and acceptor NBO with the corresponding energy in kcal/mol.*

Y(III) was then replaced by La(III) and the complex with ligand **28** was geometrically optimized. The resulting structure is presented in Figure 233.

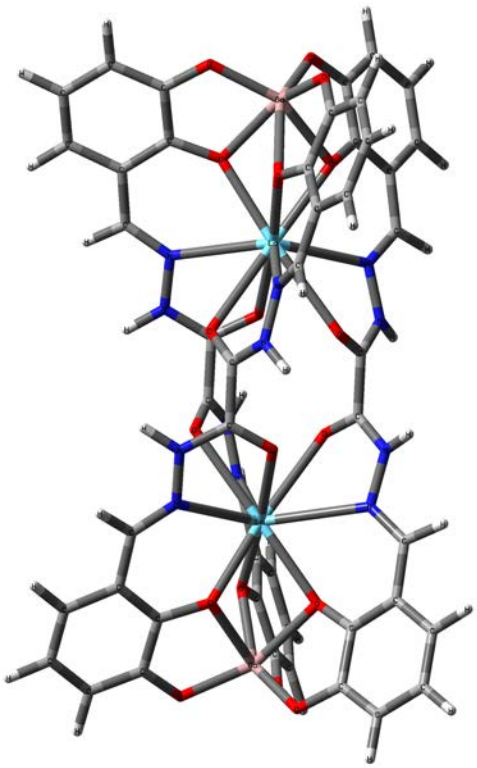

Fig. 233: *Geometrically optimized complex with ligand **28** and Ga(III) and La(III), ΔΔ configuration; pink: Ga, light blue: La, blue: N, red: O; method: cam-B3LYP/TZVP.*

configuration	Energy in a.u.	difference in kcal/mol
ΔΛ	−4733.786667	
ΔΔ	−4733.796975	−6.47

Table 51: *Energies of the* ΔΛ *and* ΔΔ *configuration of complex* ***28*** *with Ga(III) and Y(III).*

Again the ΔΔ configuration is the energetically favored one and has the stronger twisted ligand with larger O−O distances (Figure 234) and a higher energy (Table 52. The O−O distance of the ΔΔ form is 3.19 Å and the one of the ΔΔ is 2.68 Å.

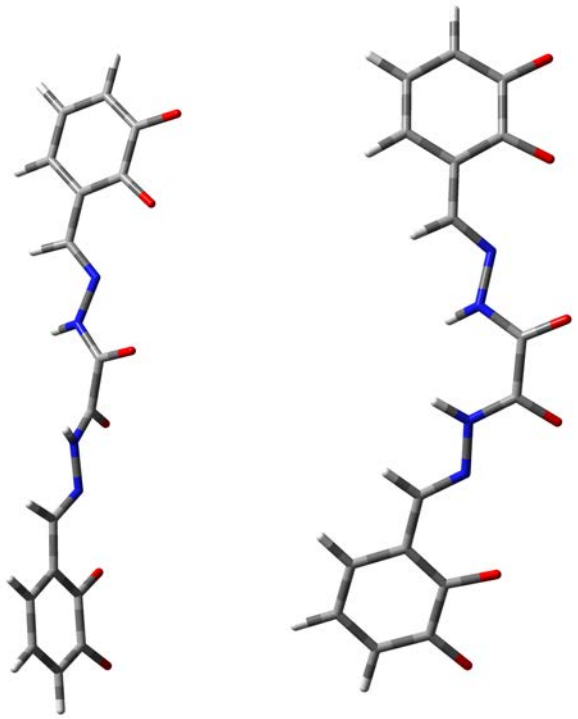

Fig. 234: *Ligand* ***28*** *from the complex with Ga(III) and La(III),* ΔΔ *and* ΔΛ *configuration.*

form	energy in a.u.	energy difference in kcal/mol
ΛΛ	−1285.515253	−3.005
ΔΛ	−1285.510465	

Table 52: *Energies of Ligand* ***28*** *from the complexes with Ga(III) and La(III) in its* ΛΛ *and* ΔΛ *configuration.*

The distances to La(III) are larger than the distances to Y(III) (Table 53). The $Y(III)_1$-O distances are about 0.13 Å and the $Y(III)_1$-N distances about 0.03 Å smaller than the corresponding distances to La(III). The ionic radii of La(III) and Y(III) are 115 and 93 pm, which corresponds to the smaller distances to Y(III).

atom	distance in Å	average in Å	atom	distance in Å	average in Å
Ga−La	3.4455		Ga-Y	3.3426	
	3.4455			3.3426	
La−La	6.7021		Y-Y	6.6118	
Ga_1−O	1.8967	1.8967	Ga_1−O	1.8975	1.8976
	1.8967			1.8978	
	1.8967			1.8976	
	2.2036	2.2038		2.1904	2.1912
	2.2038			2.1906	
	2.2038			2.1926	
La_1−O	2.3792	2.3792	Y_1−O	2.2633	2.2626
	2.3792			2.2619	
	2.3791			2.2626	
	2.7025	2.7028		2.5645	2.5632
	2.7025			2.5605	
	2.7033			2.5646	
La_1−N	2.7854	2.7854	Y_1−N	2.7551	2.7556
	2.7853			2.7538	
	2.7856			2.7580	

Table 53: *Comparison of selected bond lengths within complex **28**, Ga(III) + La(III), and Ga(III) + Y(III).*

Donor NBO	Acceptor NBO	E in kcal/mol	average in kcal/mol
LP (3) O 10	LP*(1)Ga 52	66.46	66.45
LP (3) O 31	LP*(1)Ga 52	66.27	
LP (3) O 48	LP*(1)Ga 52	66.62	
LP (2) O 11	LP*(4)Ga 52	12.17	12.17
LP (2) O 26	LP*(4)Ga 52	12.18	
LP (2) O 44	LP*(4)Ga 52	12.17	
LP (2) O 11	LP*(5)La 51	22.18	23.23
LP (2) O 26	LP*(5)La 51	22.58	
LP (2) O 44	LP*(4)La 51	24.92	
LP (1) N 14	LP*(3)La 51	35.87	31.34
LP (1) N 36	LP*(1)La 51	22.14	
LP (1) N 21	LP*(4)La 51	36.02	
LP (2) O 53	LP*(9)La 51	12.05	15.39
LP (2) O 54	LP*(2)La 51	18.17	
LP (2) O 56	LP*(8)La 51	15.95	

Table 54: *Complex **28** with Ga(III) and La(III), donor and acceptor NBO with the corresponding energy in kcal/mol.*

Within this complex the interactions between Ga(III) and the ligand are a little bit weaker than the interactions within the complex with Ga(III) and Y(III). Apart from

this, the interactions between La(III) or Y(III) and the ligands are very similar. The larger distances of La(III) to the ligands do not seem to have a significant effect on the interactions. The difference regarding the interactions within the complex with Ga(III) and La(III) compared to the other analyzed complexes might be due to the fact that Ga(III) has the smallest ionic radius of the chosen metal ions and La(III) has the largest radius. Therefore, the difference between the two metal ions is the most significant one. This seems to lead to the weaker interactions within the complex.

The next combination of metals to form a complex with the same ligand **28** is Ti(IV) and Y(III). The geometrically optimized structure of the ΔΔ form is shown in Figure 235.

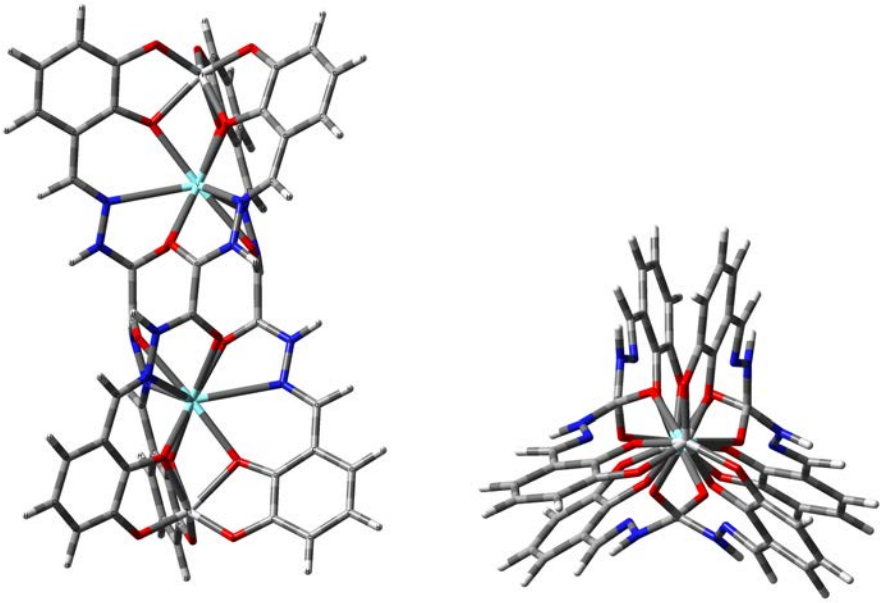

Fig. 235: *Geometrically optimized complex with ligand **28** and Y(III) and Ti(IV), ΔΔ configuration, white: Ti, light blue: Y, red: O, blue: N; method: cam-B3LYP/TZVP.*

configuration	Energy in a.u.	difference in kcal/mol
ΔΛ	-4051.414528	
ΔΔ	-4051.430946	−10.302

Table 55: *Energies of the ΔΛ and ΔΛ configuration of complex **28** with Y(III) and Ti(IV).*

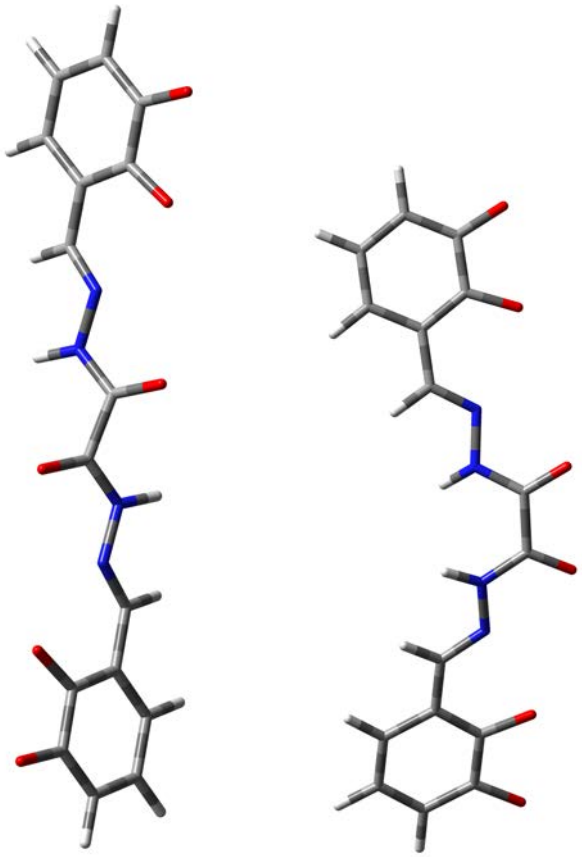

Fig. 236: *Structurally optimized ligand **28** from the complex with Ti(IV) and Y(III),* $\Delta\Delta$ *(left) and* $\Delta\Lambda$ *(right) configuration.*

form	energy in a.u.	energy difference in kcal/mol
$\Delta\Delta$	−1285.475834	
$\Delta\Lambda$	−1285.476444	−0.383

Table 56: *Energies of Ligand **28** from the complexes with Ti(IV) and Y(III) in its* $\Delta\Delta$ *and* $\Delta\Lambda$ *configuration.*

The energy difference of ligand **28** from the complexes with Ti(IV) and Y(III) in its $\Delta\Delta$ and $\Delta\Lambda$ configuration shows that the ligand for the $\Delta\Lambda$ form is energetically favored (Table 56). Despite this result, the complex prefers the $\Delta\Delta$ form. This can be explained by the very small energy difference of 0.383 kcal/mol.

atom	distance in Å	average in Å	atom	distance in Å	average in Å
Ti−Y	3.3522		Ti−Y	3.3294	
	3.3517			3.3294	
Y−Y	6.6295		Y−Y	6.4599	
Ti_1−O	1.8423	1.8419	Ti_1−O	1.8439	1.8441
	1.8399			1.8442	
	1.8435			1.8441	
	2.1236	2.1159		2.1084	2.1080
	2.1144			2.1074	
	2.1098			2.1081	
Y_1−O	2.3029	2.3049	Y_1−O	2.2992	2.2992
	2.3076			2.2988	
	2.3043			2.2995	
	2.5340	2.5418		2.4894	2.4890
	2.5113			2.4878	
	2.5801			2.4898	
Y_1−N	2.7983	2.7661	Y_1−N	2.7675	2.7669
	2.8045			2.7649	
	2.6954			2.7683	
Ti_2−O	1.8407	1.8426	Ti_2−O	1.8442	1.8441
	1.8447			1.8439	
	1.8425			1.8441	
	2.1224	2.1154		2.1074	2.1080
	2.1045			2.1084	
	2.1193			2.1081	
Y_2−O	2.3042	2.3023	Y_2−O	2.2988	2.2992
	2.3004			2.2995	
	2.3024			2.2992	
	2.5340	2.5418		2.4898	2.4890
	2.5113			2.4894	
	2.5801			2.4878	
Y_2−N	2.8204	2.7346	Y_2−N	2.7649	2.7669
	2.6793			2.7675	
	2.7042			2.7683	

Table 57: *Selected structural parameter from the structurally optimized complex **28** with Y(III) and Ti(IV), metal-metal distances and metal-O distances.*

As the ΔΔ form adopts a symmetrical structure, bonds like Y_1-O and Y_2-O are of identical average lengths, and this form is energetically favored. In contrast, the ΔΛ form has different distances between the metal and the ligands as well as different metal-metal distances. Especially noticeable is the large Ti−Y distance, which results from the Ti(IV) position, which is located on top of the complex. The Ti−O distances to the external O atoms is very small (1.8426 and 1.8419 Å).

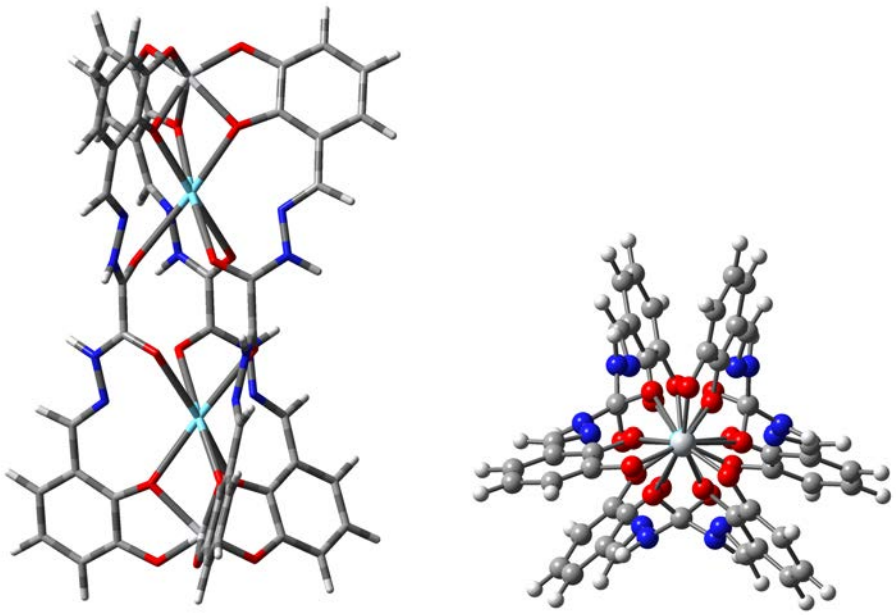

Fig. 237: *Geometrically optimized structure of the complex with ligand **28** and La(III) and Ti(IV), ΔΔ configuration; method: cam-B3LYP/TZVP.*

configuration	Energy in a.u.	difference in kcal/mol
ΔΛ	−4846.003415	
ΔΔ	−4846.016219	−8.035

Table 58: *Energies of the ΔΛ and ΔΛ configuration of complex **28** with La(III) and Ti(IV).*

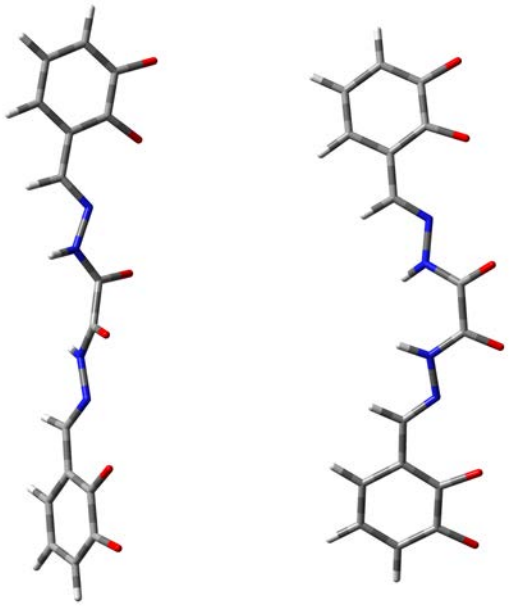

Fig. 238: *Structurally optimized ligand **28** of the complex with Ti(IV) and La(III), ΔΔ (left) and ΔΛ (right) configuration.*

form	energy in a.u.	energy difference in kcal/mol
ΔΔ	−1285.486252	−2.465
ΔΛ	−1285.482323	

Table 59: *Energies of Ligand **28** from the complexes with Ti(IV) and La(III) in its* ΔΔ *and* ΔΛ *configuration.*

atom	distance in Å	average in Å
Ti−La	3.4399	
	3.4399	
La−La	6.6121	
Ti_1-O	1.8437	1.8438
	1.8437	
	1.8439	
	2.1237	2.1233
	2.1228	
	2.1233	
La_1−O	2.4134	2.4140
	2.4148	
	2.4139	
	2.6395	2.6430
	2.6448	
	2.6447	
La_1−N	2.8028	
	2.8018	
	2.8003	2.8016
Ti_2−O	1.8437	1.8438
	1.8439	
	1.8437	
	2.1237	2.1233
	2.1233	
	2.1228	
La_2−O	2.4134	2.4140
	2.4139	
	2.4148	
	2.6395	2.6430
	2.6448	
	2.6447	
La_2−N	2.8028	2.8016
	2.8003	
	2.8018	

Table 60: *Selected structural parameters from complex **28** with Ti(IV) and La(III), metal-metal distances and metal-O distances.*

The *meso* form of the complex **28** with Ti(IV) and Y(III) as metal centers has a Ti(IV)−Y(III) distance of 3.3522 Å and a Y(III)−Y(III) distance of 6.6295 Å. In the

energetically favored ΔΔ form with Ti(IV) and La(II) the distances are longer. The Ti(IV)−La(III) bond is 3.4399 Å and the La(III)−La(III) distance is 6.6121 Å. In both cases, the ΔΔ form is energetically favored.

metals	energetically favored configuration
Ti(IV), Y(III)	ΔΔ
Ti(IV), La(III)	ΔΔ
Ga(III), La(III)	ΔΔ
Ga(III), Y(III)	ΔΔ

Table 61: *Comparison of the different complexes with ligand **28**.*

With ligand **28** the ΔΔ-form is energetically favored in all the analyzed metal combinations.

5.1.2 Calculations with ligand 29

The structures of the complexes with ligand **29** and the same combinations of metal atoms were geometrically optimized in order to analyze the effect of the change of the ligand. The resulting complex with Ga(III) and Y(III) is presented schematically in Figure 239.

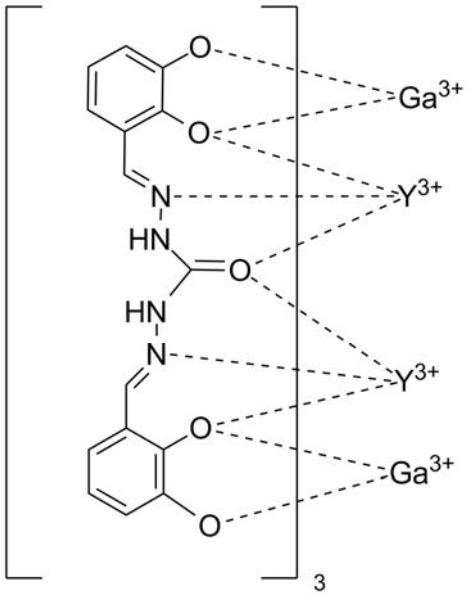

Fig. 239: *Complex with ligand **29** and Ga(III) and Y(III).*

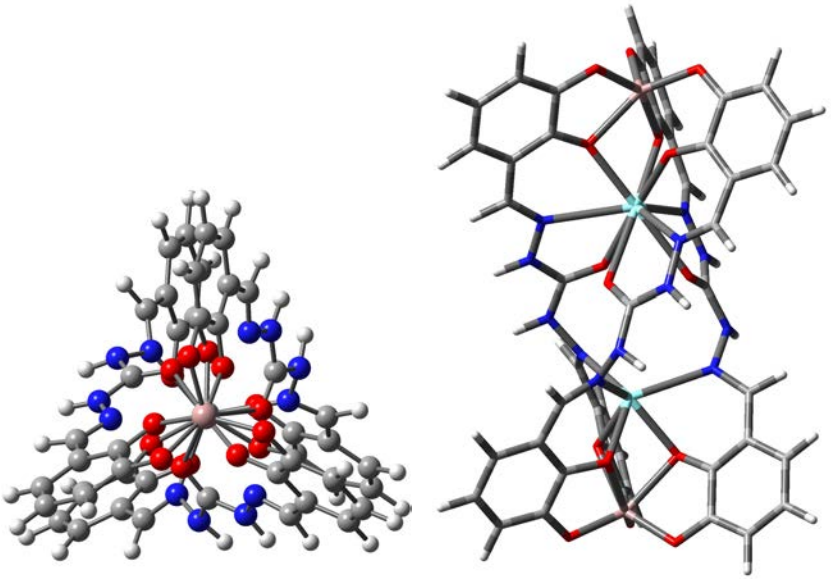

Fig. 240: *Geometrically optimized structure of the complex with ligand **29** and Ga(III) and Y(III), ΔΔ configuration.; method: cam-B3YLP/TZVP*

configuration	Energy in a.u.	difference in kcal/mol
ΔΛ	−3599.163356	
ΔΔ	−3599.189008	−16.097

Table 62: *Total and relative energies of the ΔΛ and ΔΔ form of complex **29** with Ga(III) and Y(III).*

The ΔΔ configuration of the complex with ligand **29** is energetically more favorable. Within this complex, one Y(III) is coordinated by six O and three N atoms and the other Y(III) by only three O and three N atoms. Despite the result that the energy of Ligand **29** from the complex with Ga(III) and Y(III) in its ΔΛ configuration is lower than the energy for the ΔΔ form (Table 63), the ΔΔ configuration is energetically favored (Table 62). This might indicate that in this case the coordination of the metal centers has a stronger effect on the energy of the complex than the structure of the ligand.

form	energy in a.u.	energy difference in kcal/mol
ΔΔ	−1172.145295	
ΔΛ	−1172.154615	−5.848

Table 63: *Energies of Ligand **29** from the complexes with Ga(III) and Y(III) in its ΔΔ and ΔΛ configuration.*

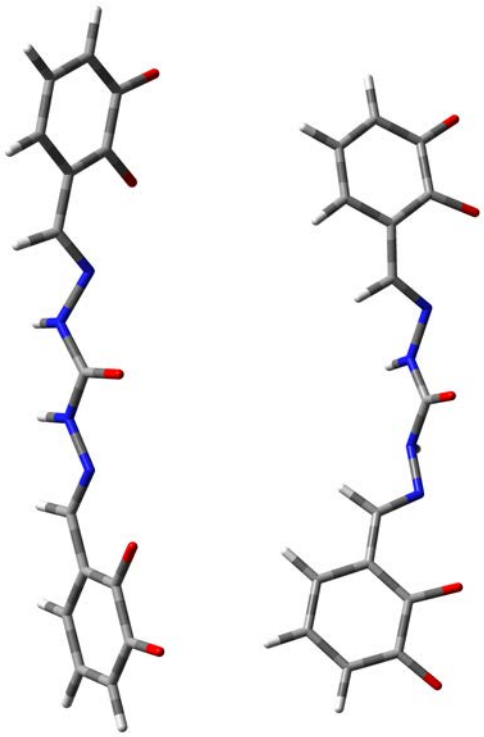

Fig. 241: *Structurally optimized ligand **29** from the complexes with Ga(III) and Y(III), ΔΔ (left) and ΔΛ (right) configuration.*

The next complex, which was geometrically optimized is the one with ligand **29** and Ga(III) but with La(III) instead of Y(III). Figure 242 shows the resulting structure of the ΔΛ form.

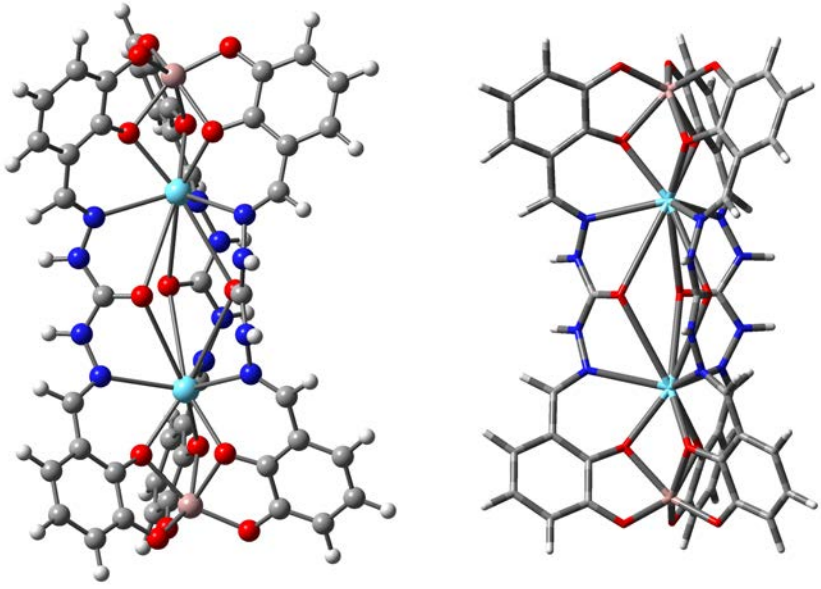

Fig. 242: *Geometrically optimized complex with ligand **29** and Ga(III) and La(III), ΔΛ configuration, light blue: La, pink: Ga, blue: N, red: O; method: cam-B3LYP/TZVP.*

Only for the ΔΛ form of the complex with Ga(III) and La(III) an energetical minimum could be obtained. No minimum structure for the ΔΔ form could be obtained,

since the geometry optimization did not converge.

atom	distance in Å
Ga−La	3.4746
	3.4746
La−La	5.8951
La_1-O_{center}	3.3764
	3.3764
	3.3764
La_2-O_{center}	3.3764
	3.3764
	3.3764

Table 64: *Selected structural parameters of the ΔΛ configuration of complex **29** with Ga(III) and La(III).*

The distances of La(III) to the inner O atoms (O_{center}) reveals the symmetric structure of the complex. In contrast to the complex with Y(III) and Ga(III) in the molecule with La(III) and Ga(III) each metal center is coordinated by six O atoms. Due to the larger ionic radius of 1.15 Å La(III) is able to bind more distant O atoms much better than Y(III) with a radius of 0.93 Å.

The third complex to be analyzed is the one with Ti(IV) and La(III). The most stable configuration is the ΔΛ form of the complex. The resulting structure is presented in Figure 243. Again no minimum could be located for the ΔΔ form as the geometry optimization did not converge.

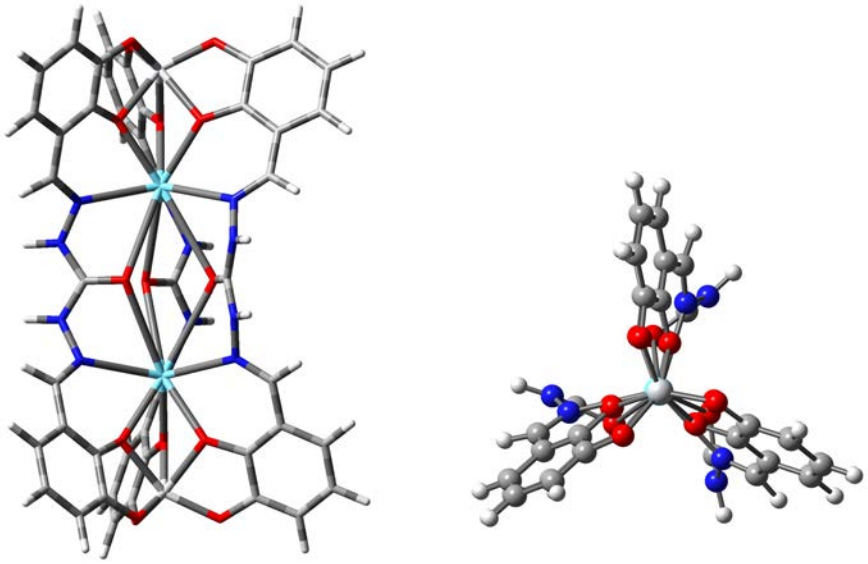

Fig. 243: *Geometrically optimized complex with ligand **29** and Ti(IV) and La(III), white: Ti, light blue: La, red: O, blue: N, ΔΛ configuration, white: Ti, light blue: La, red: O, blue: N; method: cam-B3LYP/TZVP.*

Selected interatomic distances of the structurally optimized ΔΛ form of the complex are listed in Table 65. The values of the La_1-O_{center} and La_2-O_{center} distances, which are the same (3.25 Å) at both positions of the metal ion, underline the symmetric structure of the complex.

atom	distance in Å
Ti−La	3.4842
	3.4842
La−La	5.6525
La_1-O_{center}	3.2500
	3.2500
	3.2500
La_2-O_{center}	3.2500
	3.2500
	3.2500

Table 65: *Selected inter atomic distances of the ΔΛ configuration of complex **29** with Ti(IV) and La(III).*

The last complex being studied with ligand **29** was the one with Ti(IV) and Y(III) (Figure 244). The ΛΛ results in a much lower energy than the ΔΛ form (Table 66).

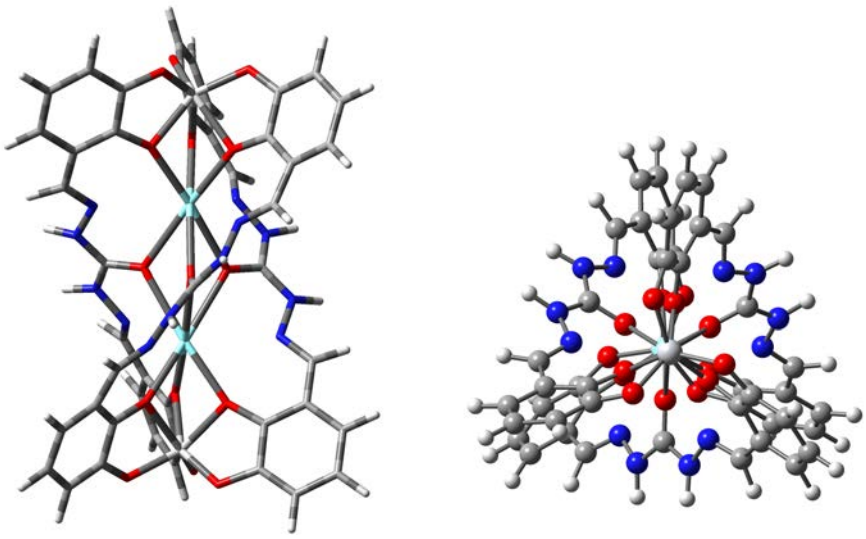

Fig. 244: *Geometrically optimized complex with ligand **29** and Ti(IV) and Y(III), ΛΛ configuration, white: Ti, light blue: Y, red: O, blue: N; method: cam-B3LYP/TZVP.*

configuration	Energy in a.u.	difference in kcal/mol
ΔΛ	−3711.315461	
ΛΛ	−3711.374800	−37.236

Table 66: *Total and relative energies of the ΔΛ and ΛΛ configuration of complex **29** with Ti(IV) and Y(III).*

Comparison of the two resulting forms of the ligands from the ΛΛ and ΔΛ form explain why the ΛΛ conformer is energetically favored. The ligand of the ΔΛ complex is strongly twisted, presumably resulting in a tension within the complex (Figure 245).

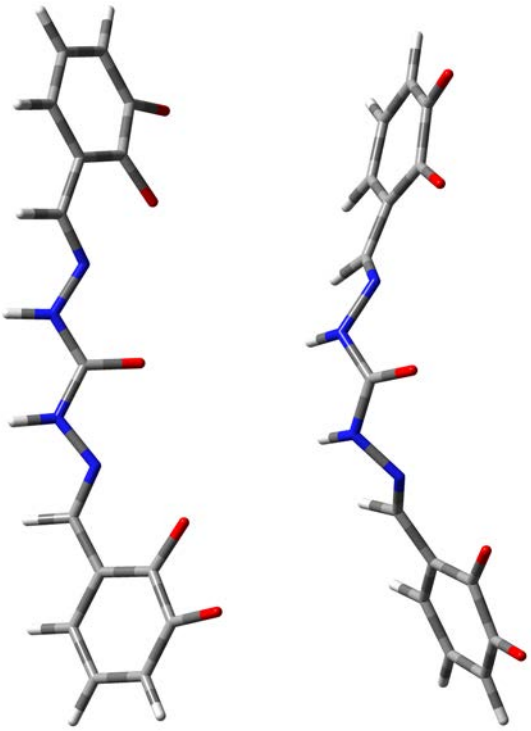

Fig. 245: *Structurally optimized ligand **29** from the complexes with Ti(IV) and Y(III),* ΛΛ *(left) and* ΔΛ *(right) configuration.*

form	energy in a.u.	energy difference in kcal/mol
ΛΛ	−1172.083214	
ΔΛ	−1172.096117	−8.097

Table 67: *Energies of Ligand **29** from the complexes with Ti(IV) and Y(III) in its* ΛΛ *and* ΔΛ *configuration.*

The energy of Ligand **29** from the complex with Ti(IV) and Y(III) in its ΔΛ configuration is 8.097 kcal/mol lower than the energy for the ΔΔ form (Table 67), but the ΔΔ configuration of the complex is energetically favored (Table 66). This might indicate that like in the case of the complex with Ga(III) and Y(III) the coordination of the metal centers has a stronger effect on the energy of the complex than the structure of the ligand.

atom	distance in Å
Ti−Y	3.3276
	3.3276
Y−Y	4.1666
Y_1−O_{center}	2.5416
	2.5416
	2.5416
Y_2−O_{center}	2.5416
	2.5416
	2.5416

Table 68: *Selected inter atomic distances of the ΛΛ configuration of complex **29** with Ti(IV) and Y(III).*

As a conclusion, the energetically favored configurations of the different complexes are summarized:

metal	favored configuration
Ti(IV), Y(III)	ΛΛ
Ti(IV), La(III)	ΛΔ
Ga(III), La(III)	ΛΔ
Ga(III), Y(III)	ΔΔ

Table 69: *Favored configuration of complex **29** with different combinations of metals.*

The numbers in table 69 show that with Y(III) the complex with ligand **29** leads to a ΔΔ or ΛΛ helicate and with La(III) to a *meso*-helicate.

5.1.3 Comparison of the Complexes with ligand 28 and 29

In general, complexes which are able to form helicates, have an energy difference between their Λ and Δ form if there is a chiral substituent or a second metal center with a spacer between the two. One example for the last case are tetranuclear helicates as they have not only a spacer but also four metal centers. Table 70 presents the results of the calculations for several complexes with ligand **28** and **29**.

ligand	metal	favored configuration	
1	Ti(IV), Y(III)	ΛΔ	*meso*-helicate
2	Ti(IV), Y(III)	ΛΛ	helicate
1	Ti(IV), La(III)	ΔΔ	helicate
2	Ti(IV), La(III)	ΛΔ	*meso*-helicate
1	Ga(III), La(III)	ΔΔ	helicate
2	Ga(III), La(III)	ΛΔ	*meso*-helicate
1	Ga(III), Y(III)	ΔΔ	helicate
2	Ga(III), Y(III)	ΔΔ	helicate

Table 70: *Favored configuration of complex **28** and **29** with different metals.*

With ligand **28**, the complexes tend to form helicates. With ligand **29**, the helicate form is adopted two times and the *meso*-helicate form as well. The result can be explained by the involved ionic radii: Ti(IV): 61 pm, Ga(III): 62 pm,Y(III): 106 pm and La(III): 122 pm.[80]

As Ti(IV) has a strong affinity to bind O atoms and a small ionic radius, the formed Ti(IV)-O distances are very short. With Y(III) as the second metal center, the short Y(III)-O distances lead to the favored ΔΛ structure in complex **28**. With Ti(IV) in combination with La(III) the helicate form is obtained, as the longer La(III)-O distance lead to a more "open" structure.

Complex with ligand **29** shows a stronger dependence on the choice of the metal ion. The *meso*-helicate is formed with Ti(IV) + La(III), and Ga(III) + La(III). With Y(III) instead of La(III) in the cavity of the complex, the helicate form is adopted.

As a conclusion, the computationally obtained results in the studies on tetranuclear helicates demonstrate the possibility to predict the geometric structure of a complex. The total energies obtained for the structurally optimized complexes provide answers to the question why depending on the ligand and the combination of metals in some cases a *meso*-helicate is formed while in others the helicate is the energetically favored structure.

5.2 Molecular Tetrahedra

One of the most interesting structural features of molecular tetrahedra are their internal cavities. The performed calculations allow an analysis of the structure of the different complexes and, therefore, provide an insight into the size of the cavity. Possible configurations of the tetrahedra are the ΔΔΔΔ, ΔΔΔΛ, ΔΔΛΛ, ΔΛΛΛ and the ΛΛΛΛ form. The corresponding interconversions will be studied as well.

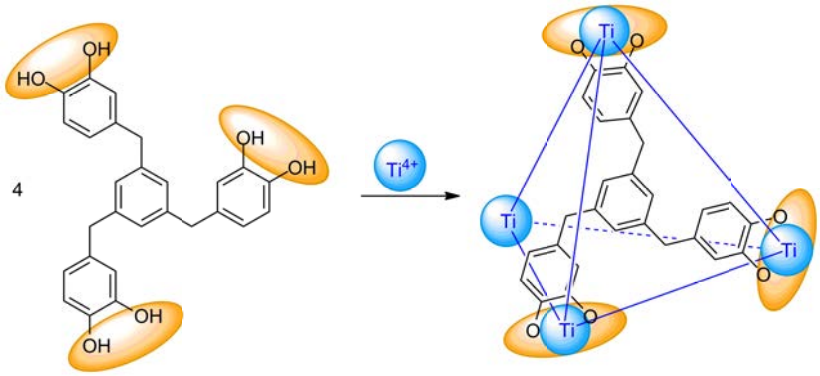

Fig. 246: *Reaction to the M_4L_4 tetrahedra with ligand **30**.*

Figure 246 schematically illustrates the reaction of four ligands with four metal ions to a M_4L_4 tetrahedra.[93] The first simulation of the complex has been performed with the semi-empirical PM6 method[92] (Figure 247). The resulting structures with ligand **30** are presented in Figure 248.

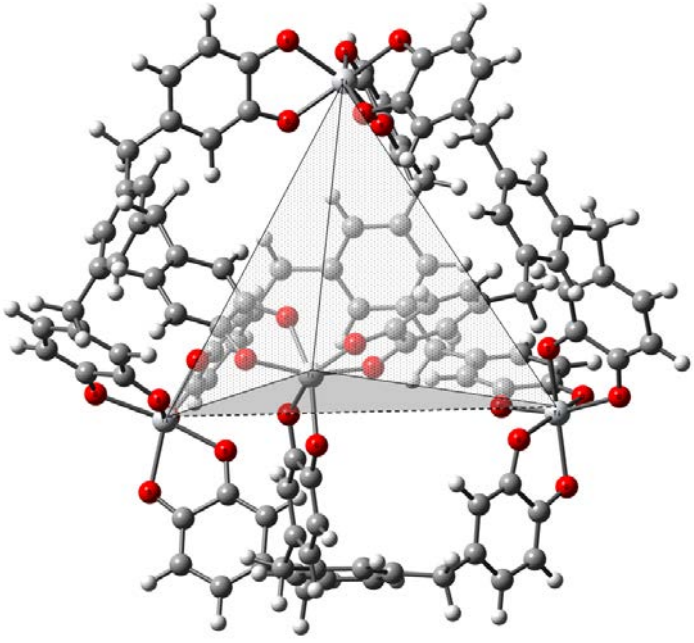

Fig. 247: *With PM6 optimized M_4L_4 tetrahedra with ligand **30**; Grey: internal cavity.*

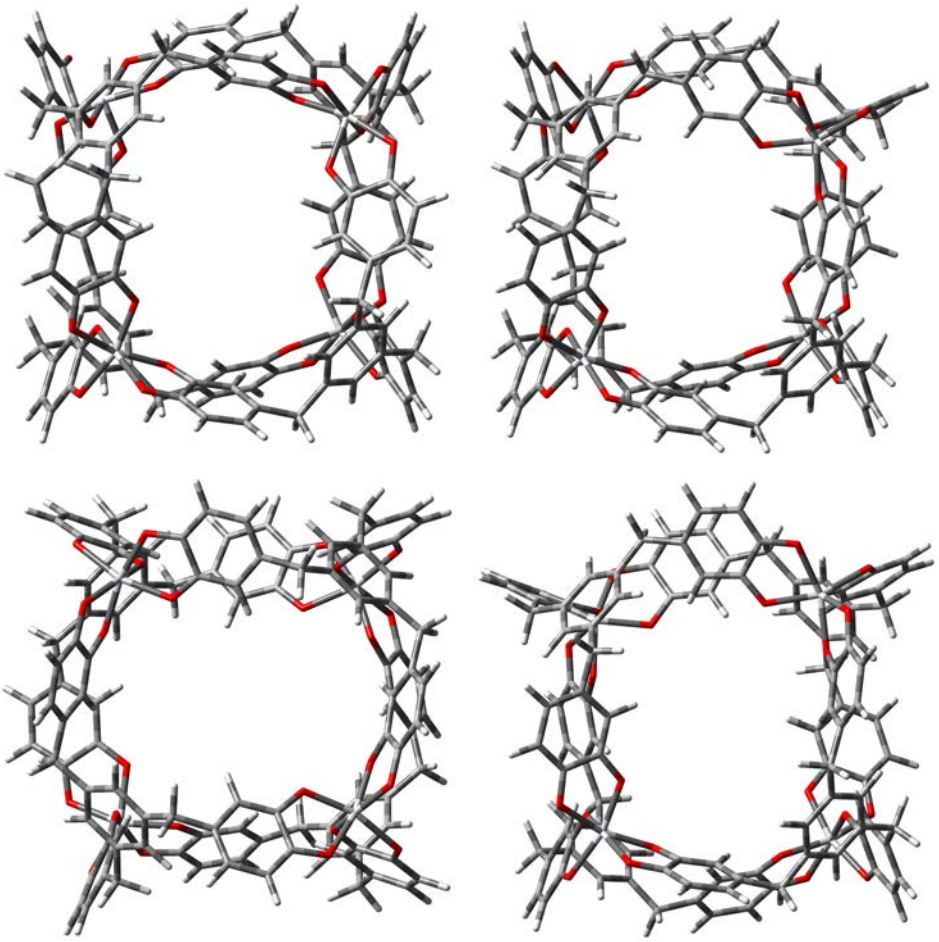

Fig. 248: *With PM6 optimized structures of complex **30**,* ΔΔΔΔ, ΔΔΔΛ, ΔΔΛΛ, *and* ΔΛΛΛ *form.*

Table 71 gives the results of the calculation on the different configurations of the molecular tetrahedra with ligand **30**. The largest energy difference is obtained between the ΔΔΔΔ and the ΔΛΛΛ form (6.93 kcal/mol). The ΔΔΔΛ and the ΔΔΛΛ form result in the same relative energy. The average Ti−Ti distance is about 11.494 Å for the ΔΔΔΔ form.

configuration	energy in a.u.	difference in kcal/mol*
ΔΔΔΔ	−0.940094	0.00
ΔΔΔΛ	−0.934407	3.57
ΔΔΛΛ	−0.929047	6.93
ΔΛΛΛ	−0.934407	3.57

Table 71: *Comparison of the energies (PM6) of the different configurations of the complex with ligand **30**, *difference to the most stable form.*

configuration	energy in a.u.	difference in kcal/mol
ΔΔΔΔ	−6161.160324	0.00
ΔΔΔΛ	−6161.144305	10.05
ΔΔΛΛ	−6161,129323	19.45
ΔΛΛΛ	−6161.144305	10.05

Table 72: *Comparison of the energies of the different configurations of the complex with ligand **30**; method: HF/TZVP, ECP for Ti(IV): MDF10.*

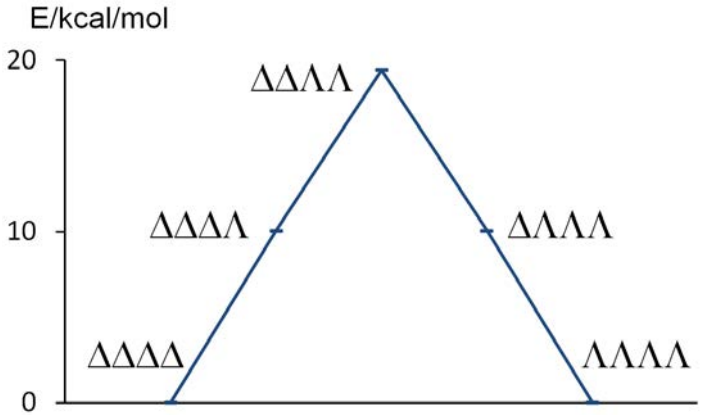

Fig. 249: *Energy profile of the conversion (ΔΔΔΔ into ΛΛΛΛ) for complex **30**, method: HF.*

With ab inito (HF) instead of PM6, the energy differences between the ΔΔΔΔ, ΔΔΔΛ, ΔΔΛΛ and ΔΛΛΛ form are larger. But the tendency remains the same: the energy of the ΔΔΔΛ and the ΔΔΛΛ form are higher than the energy of the ΔΔΔΔ form. The energy difference between the ΔΔΔΔ and the ΔΔΛΛ form is the largest. The average metal-metal distance is 11.173 Å instead of 11.494 Å for the ΔΔΔΔ form.

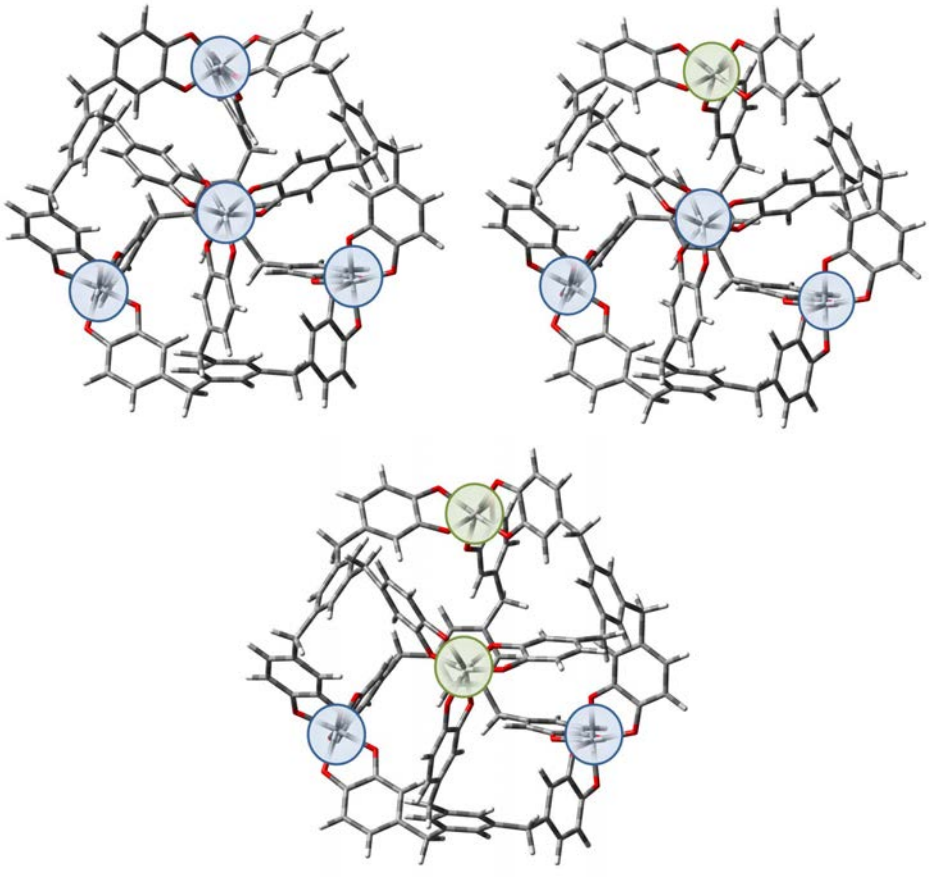

Fig. 250: *Geometrically optimized structure of the complex with ligand **30**, ΔΔΔΔ, ΔΔΔΛ and ΔΔΛΛ form, blue: Δ configuration, green: Λ configuration, method: HF/TZVP.*

The ligand studied next is similar to ligand **30** but spatially less demanding. It contains four phenyl groups without a methylene group between the aromatic rings. Therefore the flexibility of the ligand is limited.

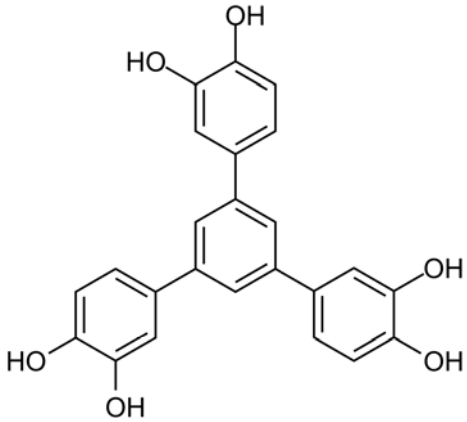

Fig. 251: *Ligand **31** with three possible coordination sides.*

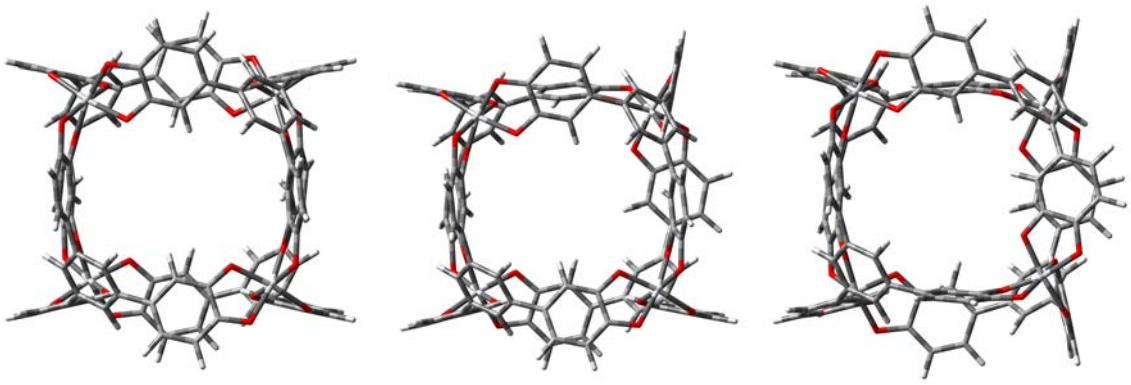

Fig. 252: *Geometrically optimized structure of the complex with ligand **31**, ΔΔΔΔ, ΔΔΔΛ and ΔΔΛΛ form, method: HF/TZVP.*

The internal cavity of the ΔΔΔΔ form is larger than the cavity formed by ligand **30**.

Calculations on the conversion of the ΔΔΔΔ form into the ΛΛΛΛ form results in a similar energy profile like the one shown before. The ΔΔΔΔ form is the most stable configuration and the ΔΔΛΛ form has the highest energy. Only the values of the energy differences are smaller (Table 73). This effect might be due to the inflexible ligand, which causes the complex to be tense even in the most stable ΔΔΔΔ form.

configuration	energy in a.u.	difference in kcal/mol
ΔΔΔΔ	−5692.433927	0.00
ΔΔΔΛ	−5692.433152	0.49
ΔΔΛΛ	−5692.432896	0.65
ΔΛΛΛ	−5692.433152	0.49

Table 73: *Comparison of the energies of the different configurations of the complex with ligand **31**, method: HF/TZVP, ECP for Ti(IV): MDF10.*

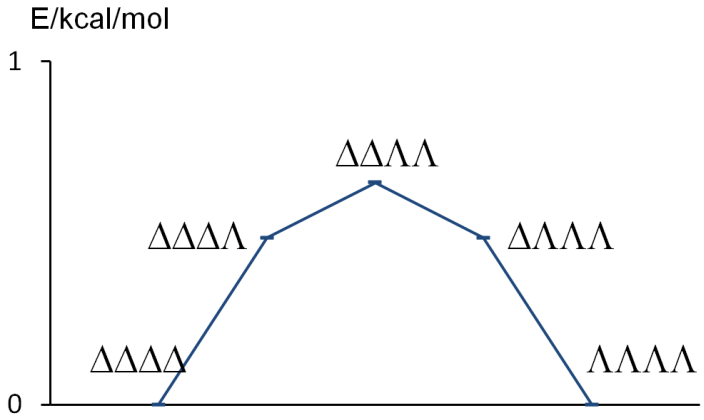

Fig. 253: *Energy profile of the conversion (ΔΔΔΔ into ΛΛΛΛ) for the complex with ligand **31**, method: HF/TZVP.*

Calculations on the B3LYP level of theory with ligand **31** (Figure 254) also lead to the result that the ΔΔΔΔ form is the most stable one:
E(ΔΔΔΔ)= −5727.783482 a.u. and E(ΔΔΔΛ)= −5727.783371 a.u.

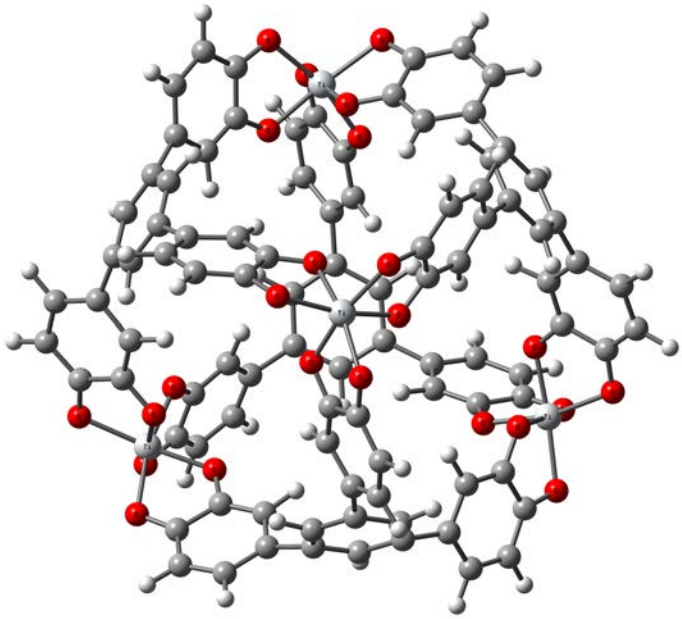

Fig. 254: *Optimized structure of the ΔΔΔΔ form of the complex with ligand **31**, method: B3LYP/TZVP.*

The influence of small changes of the ligand can be analyzed with the help of ligands **33** and **34** (Figure 255). The first ligand connects with its catechol part through 3-position and the second ligand through 4-position.

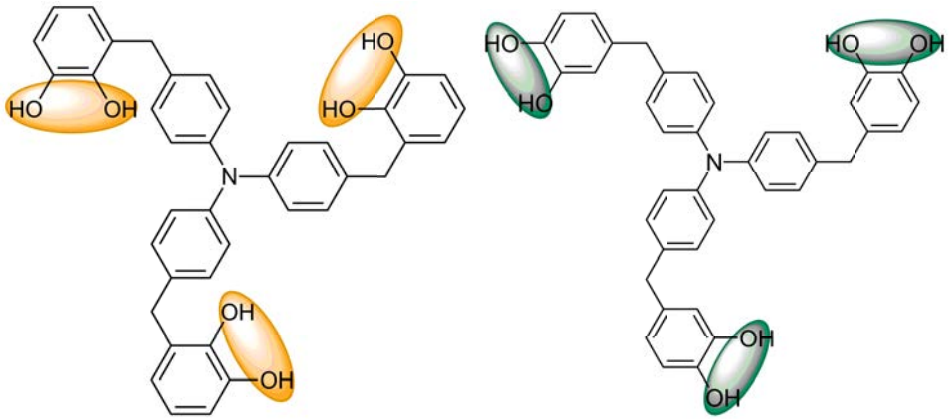

Fig. 255: *Ligand **33** and **34** with three possible coordination sides, connection of the catechol part through 3- (left) and 4-position (right).*

The catechol ligands connected in 3-position leads to a smaller internal cavity than the connection in 4-position. As ligand **33** is curved inwards the space for a potential guest becomes even smaller. The resulting structure is compact (Figure 256) with an average N−N distance of 10.133 Å. The optimized structure of the complex with ligand

34 is presented in Figure 257. The 4-position of the catechol forces the spacer to bend outwards, leaving a huge cavity for potential guests. The average N−N distance is about 13.479 Å. The difference to the N−N distance within complex **33** is 3.35 Å.

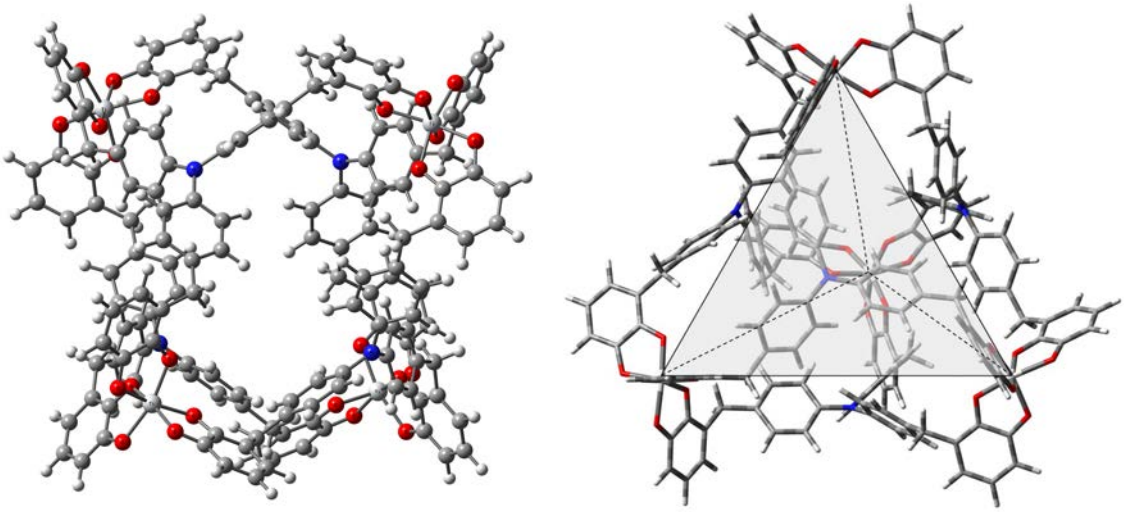

Fig. 256: *Geometrically optimized structure of the complex with ligand **33**, connection of the catechol part through 3-position, method: HF/TZVP.*

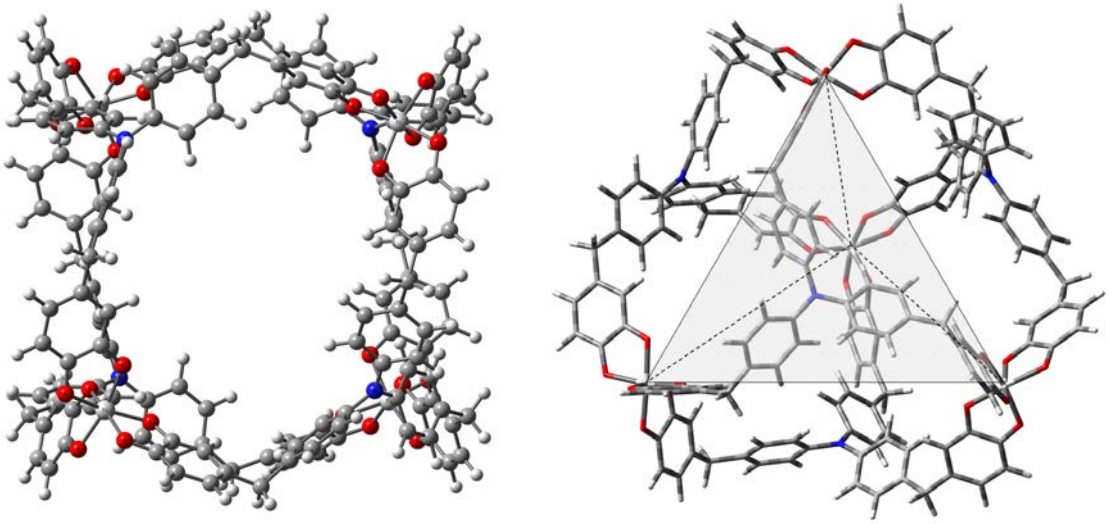

Fig. 257: *Geometrically optimized structure of the complex with ligand **34**, connection of the catechol part through 4-position, method: HF/TZVP.*

The last ligand forming complex **35** (Figure 258) has the catechol unit in 3-position. This complex was chosen to analyze the influence of the missing methylene group acting as a spacer within complex **33**. Ligand **35** leads to a less flexible tetrahedron and, therefore, resulted in a complex with a larger cavity. Calculations on the HF/TZVP level of theory resulted in an average N-N distance of 9.03 Å. Due to the smaller size of ligand **35** compared to ligand **33**, the internal cavity is smaller. But the N-N distance is only 1.1 Å smaller than the one in the complex with ligand **33**. Figure 259 shows the cavity of the complex with ligand **35** for potential guests.

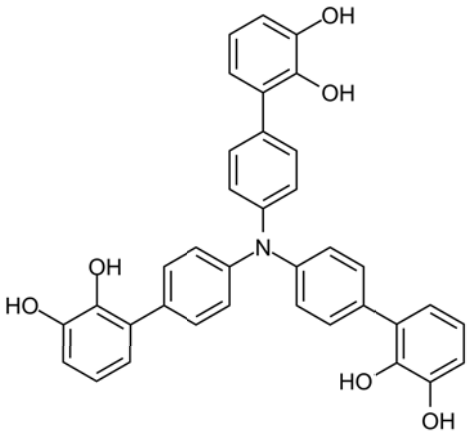

Fig. 258: *Ligand **35** with three possible coordination sides, connection of the catechol part through 3-position.*

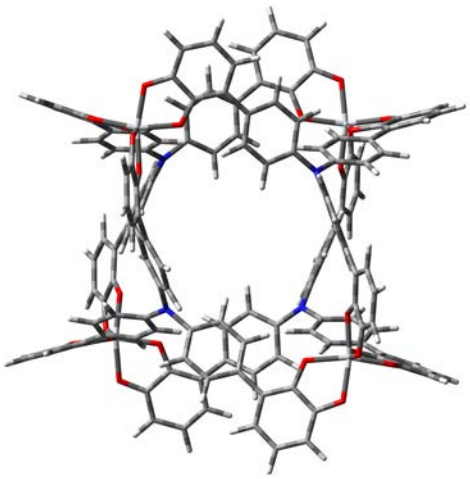

Fig. 259: *Geometrically optimized structure of the complex with ligand **35**, method: HF/TZVP.*

The calculated energy profile (Figure 260) shows only a small energy difference between the ΔΔΔΛ and ΔΔΛΛ configuration. This might be due to small structural differences between both forms (Figure 261).

configuration	energy in a.u.	difference in kcal/mol
ΔΔΔΔ	−7749.843780	0.00
ΔΔΔΛ	−7749.832058	7.36
ΔΔΛΛ	−7749.831692	7.59
ΔΛΛΛ	−7749.832058	7.36

Table 74: *Comparison of the total and relative energies of the different configurations of the complex with ligand **35**, method: HF/TZVP, ECP for Ti(IV): MDF10.*

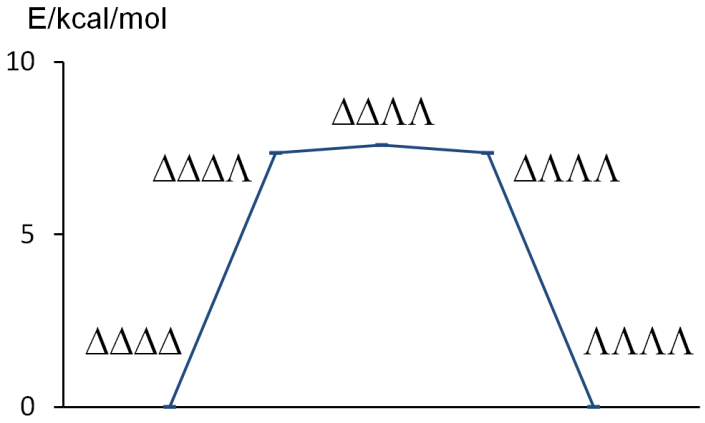

Fig. 260: *Energy profile of the conversion (ΔΔΔΔ into ΛΛΛΛ) for complex **35**, method: HF/TZVP.*

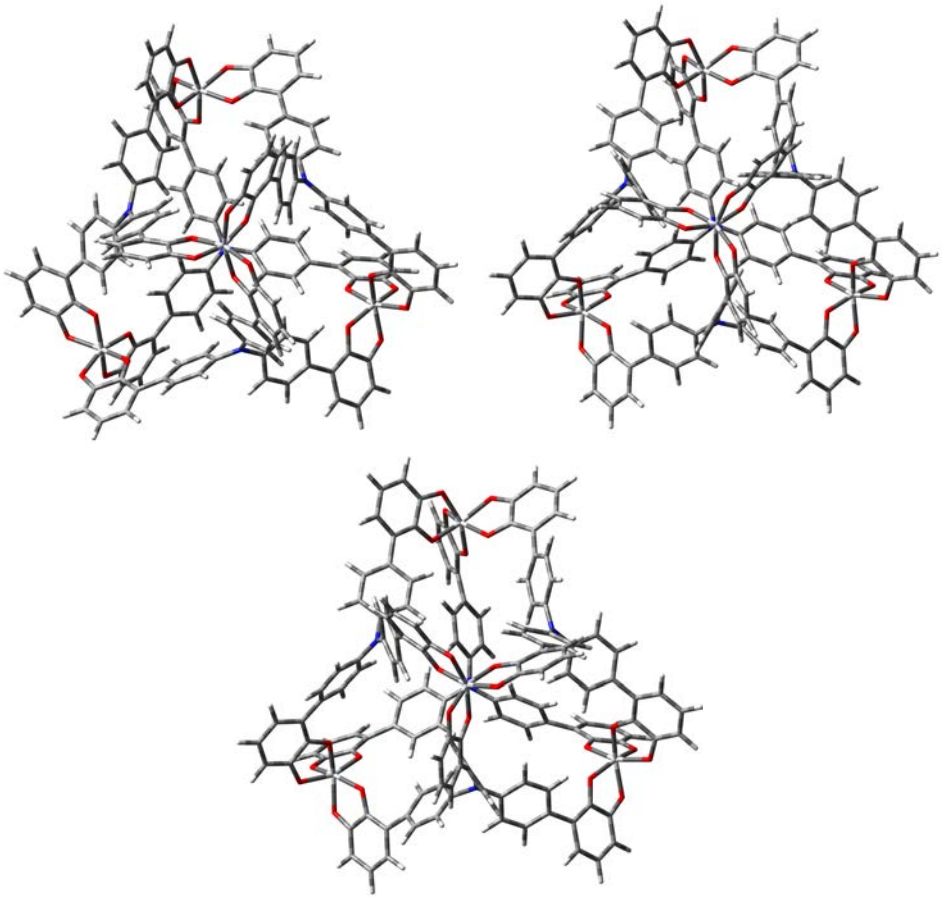

Fig. 261: *Calculated structure of the complex with ligand **35**, ΔΔΔΔ, ΔΔΔΛ and ΔΔΛΛ form, method: HF/TZVP.*

In conclusion, the performed analyses of molecular tetrahedra reveal that the ΔΔΔΔ configuration is clearly favored. Only the energies of the conversion of ΔΔΔΔ, ΔΔΔΛ, ΔΔΛΛ, ΔΛΛΛ into ΛΛΛΛ differ, depending on the sterical demands of the spacers. A great influence of the catechol position was found. To obtain larger cavities, the 4-position should be preferred. Therefore, the size of the internal cavity strongly depends on the structure of the ligand. Small changes can cause the complex to "collapse" leaving very small space for guests.

6 Summary

The task of this thesis is a computer-aided study of supramolecular systems with the help of *ab initio* as well as DFT methods. The structure, different conformers, the behavior in different solvents and reaction paths of supramolecules were studied. As supramolecular chemistry is a very wide field the basic idea was to start with rather small molecules and enlarge the system step by step. Therefore, this work is divided into four main parts.

The beginning of this thesis was devoted to the study of anion-π interactions. These systems are small enough to use accurate calculation methods like MP2 in combination with the basis set 6-311++g**. After the validation of the chosen level of theory, two different aspects were analyzed.

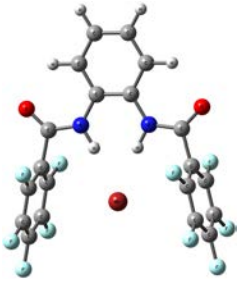

The first goal was to study the interaction of an anion with a chosen molecule and determine its energetically favored conformation in the present of the anion. This was achieved by comparison of the energies of the possible conformers. Having a lower energy, the more symmetrical geometry of the chosen interacting system of molecule and anion was formed. The second goal was to study interactions with dianions. A tweezer-type diphosphonium salt with two electron demanding pentafluorophenyl units was synthesized. This molecule has the ability to stabilize I_4^{2-} anions. This finding was obtained on the MP2/LANL2DZ level of theory. The calculations analyze the weakly bonded character of the dianion and a very low barrier of fragmentation to I_3^- and I^-. The computationally obtained results underline the stabilizing effect of the cavity of the chosen tweezer-like molecule. As the two goals could be fulfilled, the MP2 *ab initio* method proved to be an important tool for analyzing the interactions of anions with π-systems. The next part of this thesis deals with larger systems, and to reduce the computation time to an acceptable level, DFT calculations were performed. With this method, the scale factor of the MP2 method of N^4 is avoided and supramolecular complexes can be treated within reasonable time.

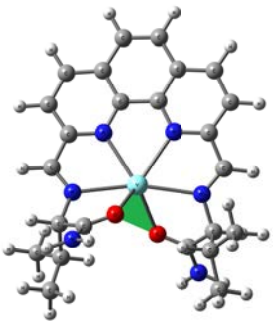

The mononuclear complexes studied initially have pincertype ligands and lanthanide metal centers. A special focus was on the interaction of the chosen complexes with solvent molecules or anions. Additional TD-DFT calculations provide CD spectra, which depend on the choice of the metal center. As a conclusion, the performed computational analysis reveals the importance of the choice of the ligand and the metal center as the structure of the complex shows a "bending" which depends on the sterical demand of the ligand and the size of the metal ion.

Mononuclear complexes with a metal center coordinated by triscatecholate-based ligands were also studied. The metal cations chosen were Ti(IV) and Ga(III). As the metal center has an octahedral coordination, a Λ or Δ configuration can occur. To understand which form is adopted, TD-DFT calculations were performed to obtain CD spectra. These calculations show that the shape of the CD curve strongly depends on the choice of the metal center. In the next step, the dimerization of trischatecholate-based helicates was studied as the monomer often forms a dimer. To analyze this process, points on the reaction path to the dimer were calculated. The computationally obtained results show that the Λ *mer* form can switch to the Δ *mer* form through a "*Bailar-Twist*" transition state. Then, the *mer*-Δ form adopts a *fac*-Δ form through the "*Ray-Dutt*" transition state and finally the dimer is formed.

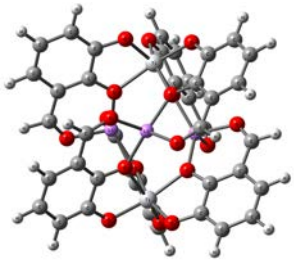

The next section deals with homodinuclear and hetereodinuclear helical complexes. Homodinuclear complexes with alkyl-bridged dicatecholate-ligands and Ti(IV) or Ga(III) as a metal center tend to form a helicate with an odd number and a *meso*-helicate with an even number of methylene units. Different degrees of deformation of the ligands in the different forms of the structurally optimized complexes might account for this. Complexes with an imino-bridge also showed a preference to form either a helicate or *meso*-helicate. If a central $(CH_2)_2$-unit exists, the complex adopts the $\Delta\Delta$ form and with a single CH_2-unit, the *meso*-helicate is obtained. The performed geometry optimizations confirm that the preference of a certain form depends on the shape or "twisting" of the ligand in the resulting complex.

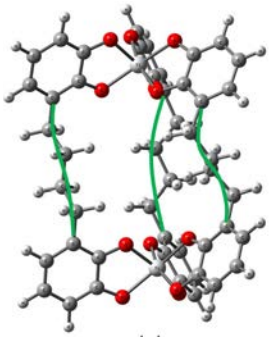

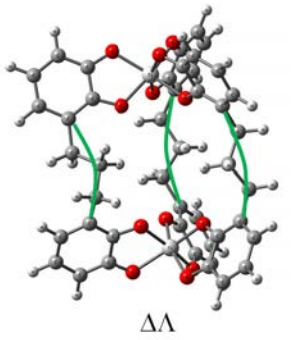

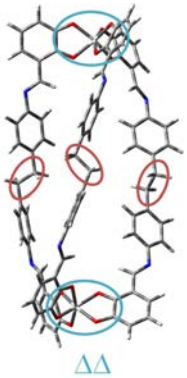

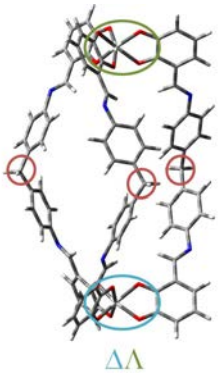

Heterodinuclear complexes with isobutinylidene-bridged bishydroxychinlin ligands were also studied. The chosen complex forms the *meso*-helicate with Al(III). While earlier studies resulted in a helicate with two Yb(III), with La(III) instead of Yb(III), the resulting energies from the geometry optimizations indicate that the *meso*-helicate would energetically be favored.

Another class of heterodinuclear complexes studied within this thesis were dicatecholate-based compounds. The chosen structures have

Al(III), Ga(III) or La(III) as metal centers and different substituents at the ligands. The comparison of the different distances within the complexes was one of the main parts of this study as they reveal the dependence of the structure of the complex on the different ligands. Since the structure of the ligands has no profound effect on the metal-metal distance, the metal-O and metal-N distances were studied as well. These distances strongly depend on the spatial demands of the ligand. Therefore, the structure of the ligand strongly determines the geometry of the complex.

The concluding part of this thesis has tetranuclear complexes as a topic. The previously performed calculation on heterodinuclear complexes was a model study for the compounds, which are chosen in this chapter. Initially, complexes with two slightly different ligands were studied. The structures of the resulting complexes with Ga(III), Y(III), La(III) or Ti(IV) as metal centers were geometrically optimized in their $\Delta\Delta$ as well as in their $\Delta\Lambda$ form both resulting in helical structures. The calculations on these complexes show that the choice of the combination of the metal centers has a significant influence, because the different ionic radii of the metal cations lead to different distances within the complex which influences the twist of the ligand and, therefore, the complex in general.

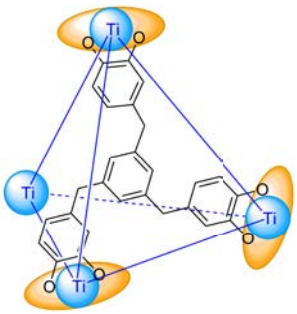

The last family of complexes which were analyzed is also the biggest one. They are called molecular containers, as their internal cavity is big enough to host guest molecules. Each metal center has an octahedral environment leading to four possible configurations: $\Delta\Delta\Delta\Delta$, $\Delta\Delta\Delta\Lambda$, $\Delta\Delta\Lambda\Lambda$, and $\Delta\Lambda\Lambda\Lambda$. The corresponding interconversions are studied. The performed calculations reveal that the $\Delta\Delta\Delta\Delta$ is energetically preferred. The size of the internal cavity strongly depends on the structure of the ligand. Small changes can cause the complex to "collapse" leaving very small space for guests.

In summary, the comparison of experimentally accessible structural information and computationally obtained results proved that the chosen theoretical methods are a good tool to analyze the molecules. Especially the question, which geometry the structure of a certain complex adopts can be answered. For this task, not only measured and calculated CD spectra were compared but also the energies of the different possible configurations of the complexes were evaluated. In addition to this, a performed NBO analyses provide further information concerning the electronic structure of the complex. The most important essence of this thesis is the importance of the cooperation between the work in the laboratory and the theoretical studies, as only the combination of both gives a realistic view of a supramolecular system.

A References

[1] J. D. van der Waals, *The equation of state for gases and liquids*, Nobel Lecture, **1919**.

[2] H. Kunz, *Angew. Chem.* **2002**, *41*, 4439.

[3] J. M. Lehn, *Science* **1993**, *260* (5115), 1762.

[4] G. A. Jeffrey, W. Saenger, *Hydrogen Bonding in Biological Systems*, Springer Verlag, Berlin **1991**; C.-I. Branden, J. Tooze, *Introduction to Protein Structure*, Garland Publishing, New York **1998**; J. D. Watson, F. H. C. Crick, *Nature* **1953**, *171*, 737; J. D. Watson, F. H. C. Crick, *Nature 1953*, *171*, 964.

[5] C. J. Pedersen, *Angew. Chem.* **1988**, *100*, 1053.

[6] D. C. Sherrington, K. A. Taskinen, *Chem. Soc. Rev.* **2001**, *30*, 83; G. Cooke, V. M. Rotello, *Chem. Soc. Rev.* **2002**, *31*, 275; L. J. Prins, D. N. Reinhoudt, P. Timmerman, *Angew.Chem.* **2001**, *113*, 2446; J. Atwood et al, *J. Am. Chem. Soc.* **2002**, *124*, 2122; Leung et al, *J. Am. Chem. Soc.* **2002**, *124*, 4287.

[7] F. Vögtle, O. Safarowsky, C. Heim, A. Affeid, O. Braun, A. Mohry, *Pure Appl. Chem.* **1999**, *77*, 247.

[8] G. Wenz, *Angew. Chem.* **1994**, *106*, 851; H. Dugas, Bioorganic Chemistry, Springer- Verlag, New York **1999**.

[9] G. Ebert, Biopolymere, Teubner Verlag, Stuttgart **1993**; Z. A. Sabarova, *Advanced Organic Chemistry of Nucleic Acids*, VCH, Weinheim **1994**.

[10] L. Fabbrizzi, A. Poggi (Hrsg.), *Transition Metals in Supramolecular Chemistry*, Kluwer Academic Publishers, Dordrecht **1994**; E. C. Constable, *Chem. Ind. (London)* **1994**, 56; E. C. Constable, *Metals and Ligand Reactivity*, VCH, Weinheim **1995**, 183; A. F. Williams, C. Floriani, A. E. Merbach, *Perspectives in Coordination Chemistry*, VCH, Weinheim **1992**.

[11] J. W. Steed, J. L. Atwood, *Supramolecular Chemistry*, Wiley, Chichester, **2000**.

[12] E. Fischer, *Ber. Deutsch. Chem. Ges.* **1894**, *27*, 2985.

[13] P. Ehrlich, *Studies on Immunity*, Wiley **1906**.

[14] D. Koshland, Proc Natl Acad Sci U S A. **1958 February**, *44*(*2*), 98.

[15] J. M. Lehn, *Angew. Chem.* **1990** *29* (11), 1304.

[16] *The Nobel Prize: The First 100 Years*, A. W. Levinovitz, N. Ringertz, Imperial College Press and World Scientific Publishing Co. Pte. Ltd., **2001**.

[17] H. M. Schmeck, *The New York Times* 10/15/1987.

[18] R. W. Saalfrank, H. Maid, A. Scheurer, *Angew. Chem.* **2008**, *120*, 8924.

[19] E. A. Meyer, R. K. Castellano, F. Diederich, *Angew. Chem.* **2003**, *115*, 1244.

[20] Non-Covalent Interactions: Theory and Experiment (RSC Theoretical and Computational Chemistry), P. Hobza, K. Müller-Dethlefs, Royal Society of Chemistry, Cambridge, **2010**.

[21] G. R. Desiraju, A. Gavezzotti, *J. Chem. Soc., Chem. Commun.* **1989**, *621*; S. K. Burley, G. A. Petsko, *Ado. Protein Chem.* **1988**, *39*, 125; C. A. Hunter, J. K. M. Sanders, *J. Am. Chem. Soc.* **1990**, *112*, 5525; C. Janiak, *J. Chem. Soc. Dalton. Trans.* **2000**, 3885.

[22] P. D. Beer, P. A. Gale, *Angew. Chem.* **2001**, *113*, 502; R. Vilar, *Angew. Chem.* **2003**, *115*, 1498.

[23] C. Garau, A. Frontera, D. Quinonero, P. Ballester, A.Costa, P. M. Deyà, *J. Phys. Chem. A* **2004**, *108*, 9423.

[24] A. Frontera, D. Quinonero, A. Costa, P. Ballester, P. M. Deyà, *New J. Chem.* **2007**, *31*, 556; M. Albrecht, C. Wessel, M. de Groot, K. Rissanen, A. Lüchow, *J. Am. Chem. Soc.* **2008**, *130*, 4600; Research report, C. N. Bannwarth, RWTH Aachen, **2010**; M. Giese, M. Albrecht, C. Bannwarth, G. Raabe, A. Valkonen, K. Rissanen, *Chem. Commun.* **2011**, *47*, 8542.

[25] S. W. Hawking, *Eine kurze Geschichte der Zeit*, Spiegel-Verlag Rudolf Augstein GmbH and Co KG, Hamburg, **2006**.

[26] L. Pauling, R. B. Corey, H. R. Branson, *Proc. Natl. Acad. Sci. U. S. A.* **1951**, *37*, 205.

[27] P. X. Gao, Y. Ding, W. Mai, W. L. Hughes, C. Lao, Z. L. Wang, *Science* **2005**, *309*, 1700.

[28] J. D. Watson, F. H. C. Crick, *Nature* **1953**, *171*, 737.

[29] B. Linton, A. D. Hamilton, *Chem. Rev.* **1997**, *97*, 1669.

[30] M. Albrecht, *Naturwissenschaften* **2007**, *94*, 951.

[31] A. F. Williams, C. Piguet, G. Bernardinelli, *Angew. Chem.* **1991**, *103*, 1530.

[32] G. T. Morgan, F. H. Burstall, *J. Chem. Soc.* **1937**, 1649.

[33] E. C. Constable, F. M. Elder, M. J. Hannon, A. Martin, P. R. Raithby, D. A. Tocher, *J. Chem. Soc., Dalton Trans.* **1996**, 2423.

[34] W. J. Stratton, D. H. Busch, *J. Chem. Soc.* **1958**, 1286.

[35] G. Struckmeier, U. Thewalt, J.-H. Fuhrhop, *J. Am. Chem. Soc.* **1976**, *98*, 278.

[36] 32 R. C. Scarrow, D. L. White, K. N. Raymond, *J. Am. Chem. Soc.* **1985**, *107*, 6540.

[37] M. Albrecht, *Chem. Rev.* **2001**, *101*, 3457.

[38] M. Albrecht, I. Janser, H. Houjou, R. Fröhlich, *Chem. Eur. J.* **2004**, *10*, 2839.

[39] M. Albrecht und S. Kotila, *Angew. Chem.* **1996**, *108*, 1299; M. Albrecht und S. Kotila, *Angew. Chem.* **1995**, *107*, 2285.; M. Albrecht, *Chem. Eur. J.* **2000**, *6*, 3485.

[40] M. Albrecht, I. Janser, H. Houjou, R. Fröhlich, *Chem. Eur. J.* **2004**, *10*, 2839.

[41] D. L. Caulder, R. E. Powers, T. N. Parac, K. N. Raymond, *Angew. Chem.* **1998**, *110*, 1940; D. J. Cram, J. M. Cram, *Container molecules and their guests*, RSC, Cambridge **1994**.

[42] D. L. Caulder, C. Bru1ckner, R. E. Powers, S. Ko1nig, T. N. Parac, J. A. Leary, K. N. Raymond *J. Am. Chem. Soc.* **2001**, *123*, 8923.

[43] M. Albrecht, I. Janser, S. Meyer, P. Weis, R. Fröhlich, *Chem. Commun.* **2003**, 2854; M. Albrecht, I. Janser, S. Burk, P. Weis, *Dalton Trans.* **2006**, 2875; M. Albrecht, S. Burk, P. Weis, *Synthesis* **2008**, 2963.

[44] A. Jasat, J. C. Sherman, *Chem. Rev.* **1999**, *99*, 931; R. C. Helgeson, K. Paek, C. B. Knobler, E. F. Maverick, D. J. Cram, *J. Am. Chem. Soc.* **1996**, *118*, 5590; J. C. Sherman, D. J. Cram, *J. Am. Chem. Soc.* **1989**, *111*, 4527.

[45] B. R. Beno, C. Sheu, K. N. Houk, R. Warmuth, D. J. Cram, *Chem. Commun.* **1998**, 301.

[46] D. Fiedler, R. G. Bergman, K. N. Raymond, *Angew. Chem.* **2004**, *116*, 6916; M. Yoshizawa, M. Tamura, M. Fujita, *Science* **2006**, *312*, 251.

[47] W. Kohn, L. J. Sham, *Phys. Rev.* **1965**, *140*, A1133.

[48] M. Albrecht, M. Schneider, H. Röttele, *Chem. Ber.* **1997**, *130*, 615; M. Albrecht, M. Schneider, *Chem. Commun.* **1998**, 137.

[49] Spartan '02, Wavefunction Inc., Irvine, CA.

[50] ChemBioOffice, CambridgeSoft Corporation, **2010**.

[51] Gaussian 09, Revision C.04, M. J. Frisch, G. W. Trucks, H. B. Schlegel, G. E.Scuseria, M. A. Robb, J. R. Cheeseman, J. A. Montgomery, Jr., T. Vreven, K. N. Kudin, J. C. Burant, J. M. Millam, S. S. Iyengar, J. Tomasi, V. Barone, B. Mennucci, M. Cossi, G. Scalmani, N. Rega, G. A. Petersson, H. Nakatsuji, M. Hada, M. Ehara, K. Toyota, R. Fukuda, J. Hasegawa, M. Ishida, T. Nakajima,Y. Honda, O. Kitao, H. Nakai, M. Klene, X. Li, J. E. Knox, H. P. Hratchian, J.B. Cross, V. Bakken, C. Adamo, J. Jaramillo, R. Gomperts, R. E. Stratmann, O. Yazyev, A. J. Austin, R. Cammi, C. Pomelli, J. W. Ochterski, P. Y. Ayala, K. Morokuma, G. A. Voth, P. Salvador, J. J. Dannenberg, V. G. Zakrzewski, S. Dapprich, A. D. Daniels, M. C. Strain, O. Farkas, D. K. Malick, A. D. Rabuck, K. Raghavachari, J. B. Foresman, J. V. Ortiz, Q. Cui, A. G. Baboul, S. Cliord, J. Cioslowski, B. B. Stefanov, G. Liu, A. Liashenko, P. Piskorz, I. Komaromi, R. L. Martin, D. J. Fox, T. Keith, M. A. Al-Laham, C. Y. Peng, A. Nanayakkara, M. Challacombe, P. M. W. Gill, B. Johnson, W. Chen, M. W. Wong, C. Gonzalez and J. A. Pople, Gaussian, Inc., Wallingford CT, **2009**.

[52] TURBOMOLE, V6.1 **2009**, University of Karlsruhe und Forschungszentrum Karlsruhe GmbH, **1989-2007**.

[53] T. A. Halgren, *J. Comp. Chem.* **1996**, *17*, 490.

[54] C. Møller, M.S. Plesset, *Phys. Rev.* **1934**, *46*, 618.

[55] D. J. Tozer, R. D. Amos, N. C. Handy, B. O. Roos, L. Serrano-Andres *Mol. Phys.* **1999**, *97*, 859; A. Dreuw, J. L. Weisman, M. Head-Gordon *J. Chem. Phys.* **2003**, *119*, 2943; L. Bernasconi, M. Sprik, J. Hutter *J. Chem. Phys.* **2003**, *119*, 12417.

[56] R. G. Parr, W. Yang *Density-functional theory of atoms and molecules* Oxford Univ. Press, Oxford, **1989**.

[57] Y. Tawada, T. Tsuneda, S. Yanagisawa, T. Yanai, K. Hirao, *J. Chem. Phys.* **2004**, *120*, 8425.

[58] T. Yanai, D. Tew, and N. Handy,*Chem. Phys. Lett.* **2004**, *393*, 51.

[59] J. D. Chai, M. Head-Gordon, *Phys. Chem.* **2008**, *10*, 6615.

[60] C. J. Cramer *Essentials of Computational Chemistry* John Wiley and Sons, Chichester, **2002**; J. Reinhold *Quantentheorie der Moleküle - Eine Einführung* B.G. Teubner Verlag, Wiesbaden, **2004**.

[61] J. Reinhold *Quantentheorie der Moleküle, Eine Einführung* Teubner, Wiesbaden **2006**.

[62] M. J. Frisch, M. Head-Gordon, J. A. Pople *Chem. Phys. Lett.* **1990**, *275*, 166; M. Head-Gordon, T. Head-Gordon *Chem. Phys. Lett.* **1994**, *220*, 122; S. Dapprich, I. Komáromi, K. S. Byun, K. Morokuma, M. J. Frisch, *J. Mol. Struct.* (Theochem) **1999**, *462*, 1.

[63] P. Hohenberg, W. Kohn *Phys. Rev.* **1964**, *136*, B864; F. Jensen *Introductio to Computational Chemistry* Wiley, West Sussex, **2008**.

[64] W. Koch, M. C. Holthausen *A Chemist's Guide to Density Functional Theory* Wiley-VCH, Weinheim, **2000**.

[65] W. Kohn, L. J. Sham *Phys. Rev.* **1965**, *140*, A1133.

[66] J. C. Slater, *Phys. Rev.* **1929**, *34*, 1293-1322.

[67] E. Fermi *Z. Phys.* **1928**, *48*, 73 ; L. H. Thomas, *Proc. Camb. Phil. Soc.* **1927**, *23*, 542; E. Wigner *Phys. Rev.* **1934**, *46*, 1002.

[68] R. M. Dreizler, E. K. U. Gross, *Density Functional Theory* Springer Verlag, Berlin, **1990**.

[69] Y. Yang, J. P. Perdew, J. A. Cevary, L. D. Macdonald and S. H. Vosko, *Phys. Rev.* A **1990**, *41*, 78.

[70] P. Atkins, J. de Paula *Elements of Physical Chemistry* 4th edn., Oxford University Press, Oxford, **2005**.

[71] R. W. Woody, N. Sreerama, Methods in Enzymology, Numerical Methods part D, **2004**.

[72] M. Albrecht, C. Wessel, M. de Groot, K. Rissanen, A. Lüchow, *J. Am. Chem. Soc.* **2008**, *130*, 4600.

[73] M. Giese, Dissertation **2011**, RWTH Aachen.

[74] D. Quinonero, C. Garau, C. Rotger, A. Frontera, P. Ballester, A. Costa, P. M. Deya, *Angew. Chem.* **2002**, *114*, 3539.

[75] L. J. Sæthre, O. Gropen, J. Sletten, *Acta Chem. Scan.* **1988**, *A42*, 16.

[76] M. Müller, M. Albrecht, V. Gossen, T. Peters, A. Hoffmann, G. Raabe, A. Valkonen, K. Rissanen, *Chem. Eur. J.* **2010**, *16*, 12446.

[77] M. Müller, M. Albrecht, V. Gossen, T. Peters, A. Hoffmann, G. Raabe, A. Valkonen, K. Rissanen, *Chem. Eur. J.* **2010**, *16*, 12446.

[78] C. Adamo and V. Barone, *J. Chem. Phys.* **1999**, *110*, 6158.

[79] J. P. Foster, F. Weinhold, *J. Am. Chem. Soc.* **1980**, *102*, 7211; A. E. Reed, F. Weinhold, *J. Chem. Phys.* **1983**, *78* , 4066.

[80] A. F. Hollemann, E. Wiberg, N. Wiberg *Lehrbuch der Anorganischen Chemie*, Gruyter, New York, **1995**.

[81] M. Albrecht, I. Janser, J. Fleischhauer, Y. Wang, G. Raabe, R. Fröhlich, *Mendeleev Commun.* **2004**, *14*, 250.

[82] M. Albrecht, S. Mirtschin, M. de Groot, I. Janser, J. Runsink, G. Raabe, M. Kogej, C. A. Schalley, R. Fröhlich, *J. Am. Chem. Soc.* **2005**, *127*, 10371.

[83] M. Albrecht, E. Isaak, M. Baumert, V. Gossen, G. Raabe,R. Fröhlich, *Angew. Chem.* **2011**, *50*, 2850.

[84] E. Isaak, Diplomarbeit **2010**, RWTH Aachen.

[85] Römpp, Georg Thieme Verlag **2006**.

[86] C. A. Schalley, F. Vögtle, K.H. Dötz, *Templates in Chemistry I* Springer, Berlin, **2004**.

[87] M. Albrecht, O. Osetska, R. Fröhlich, J.-C. G. Bünzli, A. Aebischer, F. Gumy, J. Hamacek, *J. Am. Chem. Soc.* **2007**, *129*, 14178. M. Albrecht, O. Osetska, J.-C. Bünzli, F. Gumy, R. Fröhlich, *Chem. Eur. J.* **2009**, *15*, 8791.

[88] R. Moha, Seminararbeit **2012**, FH Aachen.

[89] M. Albrecht, I. Latorre, Y. Liu, R. Fröhlich, *Z. Naturforsch.* **2010**, *65b*, 311.

[90] I. C. Latorre Martinez, Dissertation **2011**, RWTH Aachen.

[91] Rafal Kozik, Bachelor thesis **2010**, RWTH Aachen.

[92] J. J. P. Stewart, *J. Mol. Model.* **2007**, *13*, 1173.

[93] Y. Shang, Dissertation **2011**, RWTH Aachen.